



HAL
open science

Heterogeneous catalysts for acceptor-less alcohol dehydrogenation - joined experimental and theoretical studies

Kamila Maria Kazmierczak

► **To cite this version:**

Kamila Maria Kazmierczak. Heterogeneous catalysts for acceptor-less alcohol dehydrogenation - joined experimental and theoretical studies. Catalysis. Université de Lyon, 2019. English. NNT : 2019LY-SEN045 . tel-03270783

HAL Id: tel-03270783

<https://theses.hal.science/tel-03270783v1>

Submitted on 25 Jun 2021

HAL is a multi-disciplinary open access archive for the deposit and dissemination of scientific research documents, whether they are published or not. The documents may come from teaching and research institutions in France or abroad, or from public or private research centers.

L'archive ouverte pluridisciplinaire **HAL**, est destinée au dépôt et à la diffusion de documents scientifiques de niveau recherche, publiés ou non, émanant des établissements d'enseignement et de recherche français ou étrangers, des laboratoires publics ou privés.



Numéro National de Thèse : 2019LYSEN045

THESE de DOCTORAT DE L'UNIVERSITE DE LYON

opérée par

l'Ecole Normale Supérieure de Lyon

Ecole Doctorale N° 206

Ecole Doctorale de Chimie

Spécialité de doctorat : Catalyse

Discipline : Chimie

Soutenue publiquement le 30/09/2019, par :

Kamila Maria KAŻMIERCZAK

**Heterogeneous catalysts for
acceptor-less alcohol dehydrogenation -
joined experimental and theoretical studies**

Catalyseurs hétérogènes pour la déshydrogénation d'alcool
sans accepteur - études expérimentales et théoriques
conjointes

Devant le jury composé de :

PIDKO Evgeny	Professeur TU Delft, Faculty of Applied Sciences	Rapporteur
PIRAULT-ROY Laurence	Professeure des universités Université de Poitiers	Rapporteuse
VIAU Guillaume	Directeur de recherche INSA Toulouse	Examineur
MICHEL Carine	Chargée de recherche ENS de Lyon	Directrice de thèse
PERRET Noémie	Chargée de recherche Université Lyon 1	Co-encadrante de thèse
BESSION Michèle	Directrice de recherche Université Lyon 1	Membre

Acknowledgements

For the last three years I shared my professional life between Laboratoire de Chimie of ENS de Lyon and Institut de Recherches sur la Catalyse et l'Environnement de Lyon (IRCELYON). At the beginning I would like to thank my PhD advisors Carine Michel and Noemie Perret. Carine, thank you for introducing me to the DFT world, which I truly love. Thank you for all the discussions we had, for pushing me, for encouraging me, and most of all for supporting me. Noemie, thank you for giving me the opportunity to work experimentally. This made my work completed, and me feel fulfilled. Thank you for your time, thank you for trying, thank you for allowing me to decide.

I also would like to thank other people involved in the project. Michele Besson, thank you for sharing your broad knowledge, for answering even the most naïve questions, for having the time when I needed it. You were always very involved and ready to help in every moment. Catherine Pinel, thank you for all the consultations about organic chemistry, for all the suggestions, and for the interest in my work, even when we just pass each other on the corridor. Stephane Loridant, thank you for help with analysis of gases, which was tricky, especially at the beginning. Guillaume Viau and Katerina Soulantica from LPCNO in Toulouse, thank you for introducing me into the amazing world of shaped nanoparticles, for all the discussions, shared information, interest and curiosity. Raj Ramamoorthy, thank you for all the samples, all the characterization data, and more characterization data while I requested. Jean-Yves Piquemal from ITODYS in Paris, thank you for coordinating this project and motivating us to want more. Arnaud Viola, Brandon Azeredo, Marion Giraud, Lorette Sicard, Jennifer Peron - it was a pleasure to work with you.

I cannot forget about my colleagues, among which many become my friends. Marwa and Natalia, thank you for all the chats we had, for all the support, for all the experience exchange, for laughing together and crying together. I do not know how I will survive without you :) Lama, my GC mate, it was always fun with you. Maxime, Achraf, Aleks, Oleksandra, Lucie, Dian, Sarah, Zahraa, Miguel every time it was a pleasure to talk with you. Thibaut and Ruben, thank you for all the technical help. People from scientific services - Yoann, Pascale, Nicolas, Bernadette, Chantal – thank you for all the analyses of my samples. Qingyi (Chris), you were always so kind, friendly and helpful – I am lucky to know you. Nina, two polish girls talking in English between each other seems weird for others, but for us it just works. Enza and

Emanuele, thank you for all the Friday evenings, for all the board games, for talks about literally everything. Christian and Tao, thank you for all your help with hardware and software. Stephan, thank you for accepting to be the member of my “comité de thèse” every year, it was a pleasure to discuss with you. Chen, Sarah, Ruben, Paul, Benjamin, Pauline, Antton, Masoud, Daniel, Akif, Adrian thank you for all the lunches, for all the chats, you make the atmosphere of the lab. Edwige, Damien, Marie-Francoise, Christelle – thank you for all the administrative help.

There is still a lot of people I would like to thank for supporting me. Sergio, thank you for all the walks we had around Lyon - you kept me sane. Konrad, you know me too long, just thank you for being. Magda, Michał, Norbert, Beata, Darek, Piotrek, Marta, Robert, Marysia, Konrad, Patrycja, Kasia, Kasia, Marta, Sebastian, Janek, Maciek, Kasia, Radek thank you for all your encouragements, even though physically far I know you were with me. Last, but not least, I would like to thank my family. My parents, for accepting my choices and motivating to want more. My brother, uncles, aunts, cousins – thank you all for the support and believe that I can do it.

Table of Contents

<i>Introduction</i>	1
<i>Chapter 1 Bibliographic study</i>	7
<i>1.1</i> <i>Acceptor-less alcohol dehydrogenation</i>	7
1.1.1. Catalysts for the acceptor-less monoalcohol dehydrogenation	9
1.1.2. Reaction conditions	11
1.1.3. Activity towards different alcohols dehydrogenation	16
1.1.4. Dehydrogenation of diols	19
1.1.5. Side reactions in acceptor-less alcohol dehydrogenation	22
<i>1.2</i> <i>Towards the understanding of catalytic activity</i>	26
1.2.1. Insight into metal activity	26
1.2.2. Effect of NPs size and support	31
1.2.3. Shape effect.....	34
1.2.4. Ligand effect.....	40
<i>1.3</i> <i>Approaching the acceptor-less alcohol dehydrogenation with shaped metal NPs</i>	44
<i>1.4</i> <i>Conclusions</i>	46
<i>Bibliography</i>	48
<i>Chapter 2 Experimental part</i>	57
<i>2.1. List of products used</i>	57
<i>2.2. Synthesis protocols</i>	57
2.2.1. Synthesis of catalysts by wet impregnation method	57
2.2.2. Synthesis of TiO ₂ “home made”	58
2.2.3. Synthesis of unsupported catalysts	58
<i>2.3. Characterization techniques</i>	59
2.3.1. Elemental analysis by ICP-OES	59
2.3.2. Specific surface area measurement	60

2.3.3. X-ray diffraction	61
2.3.4. Thermogravimetric analysis	62
2.3.5. Transmission Electron Microscopy	63
2.3.6. Surface coverage with ligands for unsupported Co particles	64
2.3.7. X-ray Photoelectron Spectroscopy	64
2.4. Catalytic tests	65
2.4.1. Reaction equipment and catalytic tests conditions	65
2.4.2. Reaction results analysis	70
2.4.3. Catalyst pre-treatment	71
2.5. Density Functional Theory	72
Bibliography	76
Chapter 3 Activity of cobalt supported catalysts towards alcohol dehydrogenation	79
3.1. Characterization of supported catalysts	80
3.1.1. Elemental analysis of metal content and specific surface area measurements	81
3.1.2. X-ray diffraction analysis	82
3.1.2.1. Catalyst treatment	82
3.1.2.2. Different metal precursors	84
3.1.2.3. Different supports	84
3.1.3. Thermogravimetry analysis under H ₂	88
3.1.3.1. Influence of heating rate on the catalyst reducibility	88
3.1.3.2. Influence of the support on cobalt reducibility	92
3.1.3.3. Influence of aging on the removal of the passivation layer	95
3.1.4. Transmission Electron Microscopy imaging	97
3.1.5. X-ray Photoelectron Spectroscopy analysis	97
3.1.6. Characterization – summary	99
3.2. Catalytic tests results	100
3.2.1. Solvent effect	101
3.2.2. Catalyst post-treatment, aging and activation	103
3.2.3. Cobalt precursor	106
3.2.4. Support effect in catalytic dehydrogenation of 2-octanol	106
3.2.5. Catalyst recyclability	109

3.2.6. Catalytic dehydrogenation of 1-octanol	110
3.2.7. Catalytic dehydrogenation of 1,2-octanediol	111
3.2.8. Towards dehydrogenation of other diols	112
3.3. Conclusions	113
Bibliography	115
Chapter 4 Activity of different cobalt hcp and fcc type surfaces toward alcohol dehydrogenation – DFT investigations	119
4.1. Population of different surfaces on unsupported Co NPs.....	120
4.2. Alcohol dehydrogenation mechanisms	125
4.2.1. Mechanisms description.....	125
4.2.2. EtOH dehydrogenation on Co (0001) – determining the preferred reaction mechanism.	126
4.3. Alcohol dehydrogenation on different surfaces	130
4.3.1. Adsorption of molecules and intermediates.....	130
4.3.2. Bonds dissociation.....	131
4.3.3. Activity of different surfaces	136
4.4. Towards understanding and predicting(?) catalytic activity.....	140
4.4.1. Kinetics vs thermochemistry of elementary reaction	140
4.4.1.1. Bell-Evans-Polanyi (BEP) principle	140
4.4.1.2. Checking the relations between E_{act} and ΔE for OH and CH bond breakings on different Co surfaces	142
4.4.2. Linking surface geometric arrangements with their adsorption properties.....	144
4.4.2.1. Geometry descriptors.....	144
4.4.2.2. Relation between adsorption strength and geometry properties of adsorption site....	146
4.5. Selectivity – primary vs secondary alcohol dehydrogenation	150
4.5.1. Activity of Co nanorods	150
4.5.2. Towards explaining the chemoselectivity.....	151
4.5.2.1. Electronic energy vs Gibbs Free Energy profiles.....	151
4.5.2.2. Primary vs secondary alcohol dehydrogenation	155
4.6. Conclusions	157
Bibliography	159

Chapter 5 Activity of cobalt unsupported nanoparticles of well-defined shapes towards alcohol dehydrogenation.....	163
5.1. Preparation and characterization of Co NPs of different shapes	164
5.2. Catalytic activity of shaped Co NPs.....	169
5.3. Importance of the ligand decoration	172
5.3.1. Factor(s) guiding the catalytic activity.....	172
5.3.2. Attempts to improve the catalysts activity.....	175
5.3.3. Post-reaction analysis.....	176
5.3.4. Back to structure sensitivity	178
5.4. DFT computational insight – towards understanding of the role of ligands.....	180
5.4.1. Chosen molecule and surface models and preferred reaction mechanism.....	180
5.4.2. Activity	181
5.5. Activity towards primary alcohol and diol	188
5.6. Conclusions	189
Bibliography	191
Conclusions	193
Annex.....	197

Abbreviations

AAD – acceptor-less alcohol dehydrogenation

1,2-BDO – 1,2-butanediol

1,3-BDO – 1,3-butanediol

b.p. – boiling point

DFT – Density Functional Theory

DMF – N,N-dimethylformamide

DMSO – dimethyl sulfoxide

EtOH - ethanol

hcp – hexagonal close packed

HT - hydrotalcite

fcc – face centered cubic

ML - monolayer

NPs - nanoparticles

iPrOH – isopropanol, 2-propanol

1-PrOH – 1-propanol

TOF – turnover frequency

TON – turnover number

Introduction

Considering the unavoidable depletion of fossil fuels in the future, it is necessary to find new and renewable source(s) of energy and chemicals. Huge potential is located in biomass. Lignocellulosic biomass is composed mainly of three substances: cellulose (14-69% of dry mass), hemicelluloses (8-22%) and lignin (8-29%).¹ At first it is necessary to separate them and then to transform them into smaller/simpler building chemical blocks. This requires mechanical pre-treatment of the biomass, enzymatic or chemical (acidic) hydrolysis, fermentation, separation/purification of products. Cellulose and hemicelluloses are good sources of sugars like glucose, mannose, xylose and arabinose, whereas, lignin can serve as reservoir of aromatic compounds.² By further transformations different acids, aldehydes, ketones, polyalcohols, monoalcohols, esters etc. can be obtained.

Among the biomass-derived substances some mono- and polyalcohols can be found: glycerol, butanediols, propanediols, ethylene glycol and fatty alcohols, to name the most popular ones. Their dehydrogenated products – aldehydes and ketones - are high value-added products. They are already used in pharmaceuticals, in perfumes as flavorings, as food additives, as solvents, in polymer production, and as disinfectants.

Acceptor-less alcohol dehydrogenation (AAD) is an atom efficient reaction, allowing for the production of carbonyl compounds from (biomass-derived) alcohols. As the only by-product in the reaction, H₂ in gaseous form is obtained, which generation is of high interest, as it can be used as a highly-energetic fuel (Figure I.1).

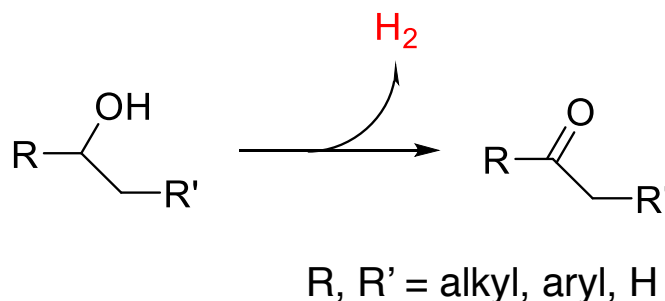


Figure I.1. Scheme of the acceptor-less alcohol dehydrogenation (AAD) reaction.

However, the reaction is not thermodynamically favored at room temperature (e.g. for isopropanol dehydrogenation³ $\Delta H^{298K} = 55.2 \text{ kJ mol}^{-1}$, $\Delta S^{298K} = 150 \text{ J mol}^{-1} \text{ K}^{-1}$ and therefore $\Delta G^{298K} = 10.5 \text{ kJ mol}^{-1} = 0.11 \text{ eV}$; and for 2-octanol dehydrogenation⁴ $\Delta H^{298K} = 53.0 \text{ kJ mol}^{-1}$, $\Delta S^{298K} = 124 \text{ J mol}^{-1} \text{ K}^{-1}$ what gives $\Delta G^{298K} = 16.0 \text{ kJ mol}^{-1} = 0.17 \text{ eV}$), hence it requires elevated temperatures (over 100°C) to proceed.

To facilitate the reaction, different catalysts can be used. This opens the door to improve its efficiency, and to guide its selectivity towards the desired carbonyl products. As will be detailed in Chapter 1, in the literature, examples of utilization of homogeneous and heterogeneous metal catalysts can be found. It is well-known, that the homogeneous catalysts suffer from problems of stability and recyclability. Moreover, they often require the presence of additives (like bases) to be efficient. Alternative for them constitutes heterogeneous catalysts. They are easy to recover after the experiment, can be more stable and the addition of base can be avoided thanks to the acid-basic properties of the catalyst support. Up to now, the most investigated catalysts in the AAD reaction are the noble metal catalysts. Due to their high costs, the replacements are sought. The chance lies in the use of non-noble metal catalysts. Some examples of the utilization of Cu, Ni and Co supported catalysts can be found, however, they are not always entirely selective to the desired carbonyl product. To improve the chemoselectivity in the reaction, heterogeneous unsupported (shaped) metal nanoparticles are postulated as good candidates for this purpose.⁵

Biomass derived reactants can be complex substances. Hence, it is important to find a catalyst which will be active and selective in a given reaction. To do this more efficiently (avoiding trial and error approach) it is important to understand the catalyst performance in terms of its structural properties.^{6,7,8,9} For this purpose, joining experimental (synthesis, catalytic tests, sample characterization) and theoretical (chemical modeling) attitudes is useful. The controlled synthesis allows to obtain the catalyst of well-defined properties. It is possible to synthesize metal supported catalysts for which the nature of support is known, or the NPs size is controlled. Also, unsupported shaped NPs for which the exposed crystallographic facets are defined can be obtained. In the catalytic tests it is possible to investigate the activity and selectivity, starting from substances with one functional group, through the ones of higher complexity, to finish with biomass-derived substrates. Thanks to the different characterization techniques it is possible to learn about the structural properties of materials, and

by computations, the reaction can be investigated on the molecular level. It is possible to study the reaction mechanism, the influence of metal nature and the type of exposed surface on the activity, or the role of surface co-adsorbates. Joining all of them allows to determine the main factor(s) guiding the activity and/or selectivity and by this to better design the catalysts.

The main purpose of my thesis was to investigate the structure-activity relations of acceptor-less alcohol dehydrogenation, starting with cobalt catalysts. For better understanding of the issue we joined experimental (catalytic tests and characterizations) and theoretical (Density Functional Theory calculations) approaches.

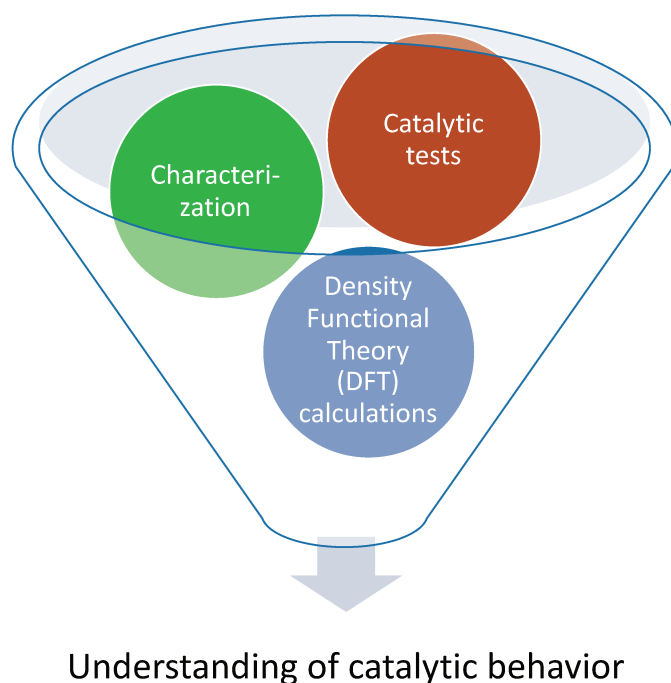


Figure I.2. Schematic of the beneficial cooperation between different approaches, towards a better understanding of structure-sensitivity of heterogeneous catalysts.

Chapter 1 will refer to the literature background about the acceptor-less alcohol dehydrogenation. Different catalysts reported as active in this reaction will be considered and their catalytic activity towards dehydrogenation of different alcohols and the reported reaction conditions will be compared. Moreover, in the second part of this chapter, different

structural parameters, influencing the catalysts performance, will be discussed. It will be demonstrated, how the type of metal, nature of support, the shape of nanoparticles and the presence of ligands on the metal surfaces, can influence the catalytic activity and/or selectivity.

The following **Chapter 2** will refer to the technical details of the characterization techniques, catalytic tests equipment and conditions, and results analysis. Furthermore, the technical details of DFT computations will be indicated.

At the beginning of this work, as the project was new in our group, it was necessary to set-up the reaction equipment and establish the reaction conditions. For this purpose, we used Co/TiO₂ as a benchmark catalyst, which is reported in the literature as active in AAD reaction.¹⁰ Afterwards, we investigated the effects of: solvent, catalyst post-treatment, aging and activation, recyclability, used metal precursor, and nature of support, on the catalytic performance of cobalt catalysts towards model secondary (2-octanol) alcohol dehydrogenation. Moreover, for chosen catalysts, their activity towards the dehydrogenation of primary alcohol (1-octanol) and diol (1,2-octanediol) was investigated. By this, we established their selectivity towards dehydrogenation of primary vs secondary alcohols. This will be described in details in **Chapter 3**.

At the same time, we started our DFT investigations about the activity of different Co surfaces towards the dehydrogenation of primary and secondary alcohols. The aim was to assess the preferred reaction mechanism and to understand the catalytic behavior of the Co facets of different nature. As Co can exist in hexagonal close packed (hcp) and face center cubic (fcc) crystallographic forms metal surfaces of both types were considered. We modeled the reaction pathway on 5 different hcp type surfaces and 4 different fcc type facets. Furthermore, the relations between kinetic and thermochemistry of the elementary reactions were checked and the adsorption strength of different reaction species in term of the adsorption position was studied. At this point the chemoselectivity exhibited by Co nanorods (preliminary catalytic tests conducted by our project partners), towards the preferential dehydrogenation of secondary alcohol over primary alcohol, were also explained. This work will be described in **Chapter 4**.

The last **Chapter 5** is focused on the catalytic activity of the unsupported cobalt nanoparticles (NPs) of different shapes, protected with carboxylic ligands of different lengths, for

the dehydrogenation of 2-octanol. Different characterization techniques allowed us to identify the intrinsic properties of the unsupported metal NPs (such as the specific surface area, type and amount of exposed facets, amount of ligands protecting the samples). By the combined analysis of NPs characteristics, their catalytic activity and DFT investigations, the main factors guiding their catalytic performance were identified. To finish with, the chemoselectivity of a chosen catalyst towards dehydrogenation of different types of alcohols (primary, secondary and diol) was checked.

Chapter 1

Bibliographic study

The aim of this chapter is to give the literature background for these studies. The first part of it refers to the acceptor-less alcohol dehydrogenation (AAD) in liquid phase. To begin with, different types of catalysts used for monoalcohols dehydrogenation are presented. Furthermore, the reaction conditions are analyzed in a critical way and the comparison of the catalyst's activity towards dehydrogenation of different alcohols, particularly octanols, is made. Afterward, the examples of dehydrogenation of diols are discussed, what brings us closer to biomass-derived polyalcohols. This part finishes with the explanation of the formation of by-products observed in AAD reaction. Second part of this chapter refers to the influence of the catalyst's structural parameters on the catalytic activity. It starts with the insight into activity of different metals. Then, it refers to the NPs size effect and support effect, the shape effect, and the ligand effect. The Chapter finishes with the considerations about possible use of shaped NPs in AAD reaction.

1.1. Acceptor-less alcohol dehydrogenation

The oxidation of alcohols is an important reaction in organic chemistry. In the past, strong oxidants such as permanganate (MnO_4^-) or dichromate ($\text{Cr}_2\text{O}_7^{2-}$) were used in order to convert alcohols into useful carbonyl compounds.¹¹ However, with these oxidants harmful by-products are obtained and it is hard to avoid the overoxidation of primary alcohols to acids. Metal-catalyzed oxidation allows to use milder oxidants (Figure 1.1.a), such as O_2 ^{12,13,14,15} and H_2O_2 ,^{12,13} but still the selectivity to the desired product may be an issue. The reaction can be as well facilitated by the presence of hydrogen acceptors (Figure 1.1.b), like olefins (e.g. styrene)^{16,17} and ketones,¹⁸ but the separation of the obtained by-products is unavoidable in such strategy, which increases the costs of the process. The most attractive reaction for the production of carbonyl compounds seems to be the acceptor-less alcohol dehydrogenation. It does not require the use of toxic reagents and the overoxidation is

avoided. Moreover, only H₂ in gaseous form is obtained as a by-product, which is of high interest, as it can be used as a highly-energetic fuel.^{19,20}

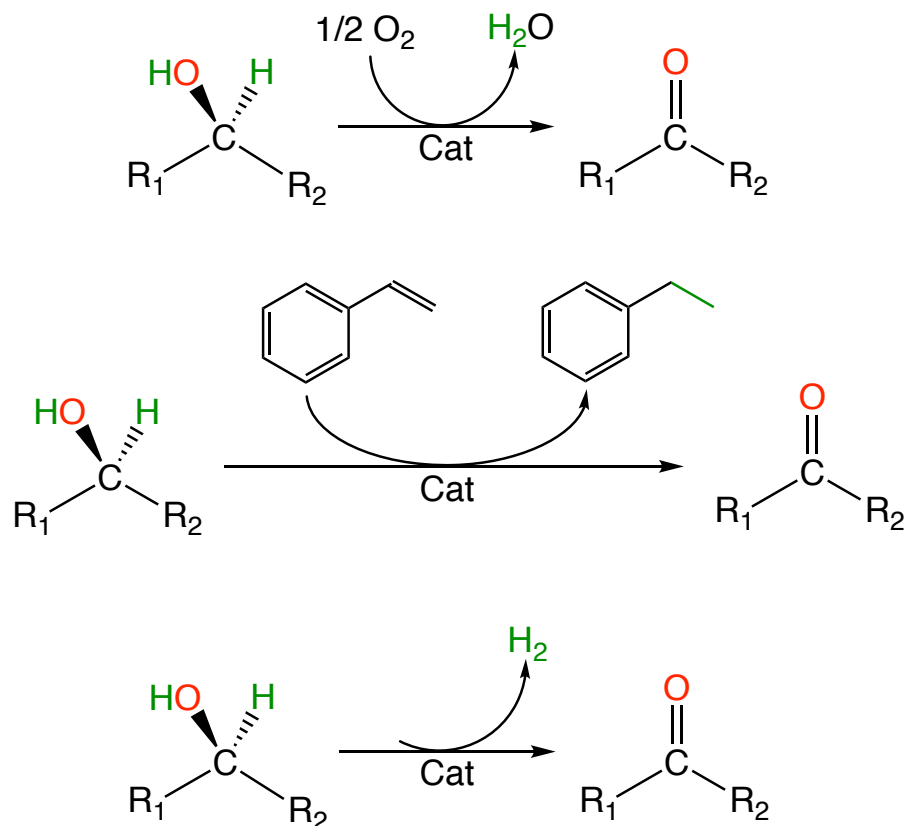


Figure 1.1. Schematics of alcohol oxidation reactions (a) with mild(er) oxidant (e.g. O₂), (b) with H₂-accepting molecule (e.g. styrene) and (c) acceptor-less alcohol dehydrogenation.

From the thermochemical point of view, acceptor-less alcohol dehydrogenation is not favored at room temperature (e.g. for isopropanol dehydrogenation³ $\Delta H^{298K} = 55.2 \text{ kJ mol}^{-1}$, $\Delta S^{298K} = 150 \text{ J mol}^{-1} \text{ K}^{-1}$ and therefore $\Delta G^{298K} = 10.5 \text{ kJ mol}^{-1} = 0.11 \text{ eV}$; and for 2-octanol dehydrogenation⁴ $\Delta H^{298K} = 53.0 \text{ kJ mol}^{-1}$, $\Delta S^{298K} = 124 \text{ J mol}^{-1} \text{ K}^{-1}$ what gives $\Delta G^{298K} = 16.0 \text{ kJ mol}^{-1} = 0.17 \text{ eV}$). Hence, it requires an elevated reaction temperature (over 100°C) to proceed, and because of this, it is called thermal alcohol dehydrogenation. Another way to drive the reaction equilibrium towards the products is to remove the generated H₂ from the reaction environment. It can be achieved by conducting the reaction under constant flow of gases²¹ or at low pressure (e.g. 0.01 atm).²² Catalysts are used to facilitate the proceeding

of the reaction. In the literature examples of homogeneous and heterogeneous (supported and unsupported) catalysts can be found, which will be discussed in the following sections.

1.1.1. Catalysts for the acceptor-less monoalcohol dehydrogenation

Some examples of the homogeneous catalysts used in the acceptor-less alcohol dehydrogenation are reported in the literature, and also are collected in reviews.^{23,24,25} Among them the complexes of Ru,^{26,27,28,23} Os,²⁶ Rh,²⁹ Ir,³⁰ Fe,³¹ and Co^{32,33} can be found. Nowadays, the most common in use are pincer complexes. They are composed of tridentate (pincer) ligands, bound to metal center at coplanar sites (Figure 1.2). Their activity is based on the cooperation between metal and the ligand, and therefore can be influenced by the modification of both.

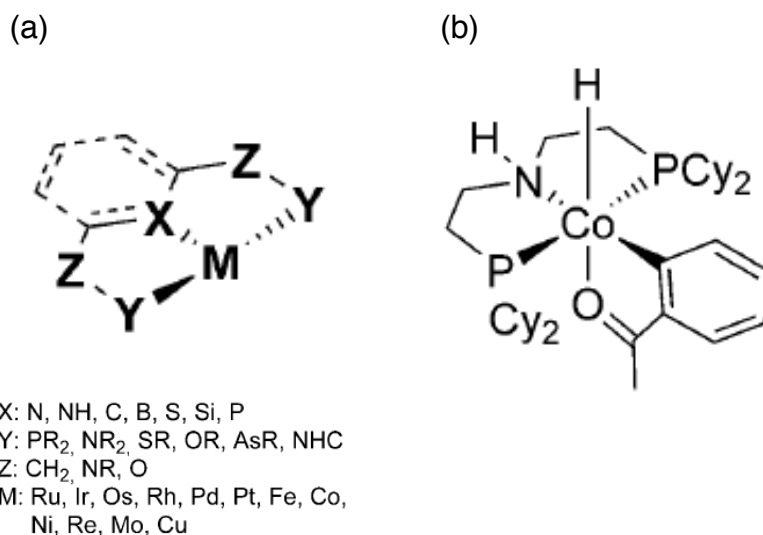


Figure 1.2. (a) General structure of a pincer complex (b) Example of Co pincer complex used in alcohol dehydrogenation.²⁴

As it was summarized by Filonenko et al. the presence of additives and promoters is often decisive for the good activity of homogeneous metal complexes.²⁵ They can be Lewis acid additives and/or basic promoters (non-anionic, or anionic organic and inorganic). Notably, the complexes of base metals (Fe, Co, Mn) often require higher base concentration

in comparison with the noble metal complexes. Considering the performance of homogeneous catalysts,^{23,24} they are active and selective towards secondary alcohols dehydrogenation. Also, some examples of primary alcohol dehydrogenation can be found, but they are less common, as some catalysts (like Ru) can be deactivated by CO coming from the aldehyde decarbonylation.

As it is commonly known, homogeneous catalysts often suffer from the problems with stability, recyclability, and necessity of additive use. Therefore, the attention is paid towards finding active and selective heterogeneous catalysts. They are easy to recover after experiment and can be more stable. As well the necessity of base or acid addition can be circumvented by the use of supports with acid-basic properties.

Among the heterogeneous supported catalysts, mostly noble metal catalysts are reported, such as Pt,³⁴ Ru,^{35,36} Re,³⁷ Rh,³⁸ Au,^{39,40,41} Ag.^{21,42,43,44,45} But, it is also possible to find examples of non-noble transition metal catalysts, such as Cu,^{46,47,48,49} Ni,^{50,51} and Co,¹⁰ being active for this reaction. Moreover, some heterogeneous unsupported nanoparticles have also been studied, like Re NPs,⁵ Mo₂N,⁵² Mo₂C.⁵³ Unsupported metal nanoparticles are considered as a new (sub)class of heterogeneous catalysts. Due to their unique properties (e.g. metal-ligand cooperation), they are thought to be good candidates to improve activity and/or selectivity of the reaction.

As it can be seen, variety of metals has already been tested in AAD reaction. Based only on the amount of publications Ag and Cu catalysts seem to be the most investigated. However, this does not necessarily mean that they are the most active and/or selective catalysts. To compare the performance of different catalysts, at first, the reaction conditions in which they were tested have to be scrutinized. Also, the attention has to be paid if they were appropriate for the reaction to adapt acceptor-less mechanism. This will be done in part 1.1.2. of this Chapter. Most of the catalysts were tested towards the dehydrogenation of a broad range of alcohols. Secondary and primary, aromatic and aliphatic alcohols were used as substrates. The comparison of their activity and selectivity will be done in part 1.1.3. In many of the reports the importance of the nature of support and/or size of NPs are highlighted. Their influence and connection with the reaction mechanism will be discussed in the second part of this chapter, in a context of understanding and improving catalytic performance.

1.1.2. Reaction conditions

The catalytic test conditions used for the liquid-phase acceptor-less alcohol dehydrogenation are gathered in Table 1.1. When comparing them, it can be noticed that there are five popular solvents for the reaction: o-xylene, p-xylene, toluene, dimethylformamide (DMF) and dimethyl sulfoxide (DMSO). With o-xylene (boiling point 144°C) and toluene (b.p. 110°C) the reaction is usually performed at the boiling temperature of the solvent. For p-xylene, DMF and DMSO the reaction temperature is lower (by 10°C to 70°C) than the boiling temperature of the solvent (b.p. 138°C, 153°C and 189°C, respectively). Also, one example in H₂O (reaction temp. 100°C) and one in solvent-free conditions (reaction temp. 180°C) can be found. For all of them the reaction temperature is exceeding 100°C, what is dictated by the thermochemistry of the reaction.

To assure the acceptor-less conditions, an inert atmosphere (Ar or N₂) is introduced in the reactors. According to the reports, usually it is a steady inert atmosphere and not often a flow of inert gas. In many cases it is not reported if the reactor and the reaction mixture were purged with the inert gas before the experiment, which implies that some air might still be remaining. Moreover, H₂ production is checked in only half of the cases, which questions the proceeding of acceptor-less reaction, and implies the possibility of oxidation reaction. As it was shown at the beginning of the Chapter, in addition to the corresponding carbonyl product, H₂O molecule is formed as a by-product during oxidation. This reaction is strongly exothermic, what makes it favored over dehydrogenation. For example, oxidation of ethanol (EtOH, CH₃CH₂OH) with O₂, leading to the formation of acetaldehyde (CH₃CHO) and H₂O, has $\Delta H^{298K} = -259.2 \text{ kJ mol}^{-1}$, $\Delta S^{298K} = 63.3 \text{ J mol}^{-1} \text{ K}^{-1}$, and hence $\Delta G^{298K} = -278.1 \text{ kJ mol}^{-1}$ (values are established based on the heat of formation for the substances, taken from chemical tables).⁵⁴ In contrast, the ΔG^{298K} is $> 0 \text{ kJ mol}^{-1}$ for the dehydrogenation of alcohols. Up to date, all the reported reactions were conducted in the solution volume not exceeding 10 mL of liquid, therefore they can be considered as small-scale reactions.

Liu et al.²¹ conducted an interesting study, dealing with the influence of the reaction atmosphere on the acceptor-less benzyl alcohol dehydrogenation over Ag/ γ -Al₂O₃, to establish the adapted reaction mechanisms in the presence of different mixtures of gases. The reactions were conducted at 120°C, in 5.0 mL of p-xylene, in a 25 mL round-bottomed flask equipped with a vapor condenser. In the first experiment the vapor condenser was open

to air, and the obtained conversion was >99%. In the second experiment O₂ was bubbled through the reactor (2 mL min⁻¹), and again the obtained conversion was >99%. In the third experiment conducted with constant flow of inert gas (N₂, 4 mL min⁻¹) through the reactor, the obtained conversion was only 13%. When the flushing with N₂ was started 30 min before the reaction, only traces of desired benzaldehyde were observed. This led to the conclusion that the reaction atmosphere is very important for the catalytic performance. If the inert atmosphere is assured, and no hydrogen accepting molecule is present in the reaction environment, the alcohol dehydrogenation takes place via an acceptor-less route. However, when even traces of O₂, being H₂ acceptor, are present in the reaction environment, the reaction mechanism changes into oxidation, which is thermodynamically favored over dehydrogenation. Therefore, the H₂ production monitoring during the reaction is of great importance, as it proves the adapted reaction mechanism.

Table 1.1. Comparison of the reaction conditions employed in acceptor-less alcohol dehydrogenation in liquid phase.

Catalyst	$n_{\text{alcohol}} : n_{\text{metal}}$	Solvent	Reaction atmosphere	Reactor	Temperature (°C)	Monitoring of H ₂ production	Reference
5 wt% Pt/Al₂O₃	200 - 10 000	o-Xylene (1.15 mL)	N ₂	Closed batch-type	144	Generated quantitatively - GC analysis	34
1.4 wt% Ru/γ-Al₂O₃	25	Toluene (2.0 mL)	Ar	Closed batch-type	110	Not mentioned	35
2.5 wt% Ru/AlO(OH)	15 - 30	Toluene (5.0 mL)	Ar	Closed batch-type	80 - 100	Not mentioned	36
5 wt% Re/Al₂O₃	100	o-Xylene (1.0 mL)	N ₂	Closed batch-type	144	Not mentioned	37
10 wt% Rh/C	5	H ₂ O (1.0 mL)	Ar	Closed batch-type	100	Considered as proceeding – not confirmed	38
0.06-0.5 wt% Au/HT	200 - 1 670	p-Xylene (5.0 mL)	Ar or N ₂ (flow)	Batch-type reaction vessel with a reflux condenser	120	Not mentioned	39,40,41
0.005 wt% Ag/HT	22 220	p-Xylene (5.0 mL)	Ar	Batch-type reaction vessel with a reflux condenser	130	Generated quantitatively – GC analysis	42
5 wt% Ag/Al₂O₃	50	Toluene (3.0 mL)	N ₂	Batch-type reaction vessel with a reflux condenser	100	Generated quantitatively – GC analysis	45,43
1.5 wt% Ag/SiO₂-Fe₂O₃	500	Toluene (3.0 mL)	N ₂	Batch-type reaction vessel with a reflux condenser	110	Not mentioned	44

Table 1.1. cont.

Catalyst	$n_{\text{alcohol}} : n_{\text{metal}}$	Solvent	Reaction atmosphere	Reactor	Temperature (°C)	Monitoring of H ₂ production	Reference
4.6 wt% Cu/HT	15	p-Xylene (5.0 mL)	Ar	Batch-type reaction vessel with a reflux condenser	130-160	Generated quantitatively – GC analysis	47
8 wt% Cu/Al₂O₃	30	DMF (3.0 mL)	N ₂	Closed batch-type	120	Not mentioned	48
7.4 wt% Cu/Cr₂O₃	50	DMF (3.0 mL)	N ₂	Closed batch-type	120	Not mentioned	49
5 wt% Ni/θ-Al₂O₃	100	o-Xylene (1.15 mL)	N ₂	Closed batch-type	144	Generated quantitatively – GC analysis	50
23 wt% Ni/NiAl-MMO¹	30	o-Xylene (7.15 mL)	Ar	Closed batch-type	170	Not mentioned	51
5 wt% Co/TiO₂	100	o-Xylene (1.15 mL)	N ₂	Closed batch-type	144	Generated quantitatively – GC analysis	10
Re	50	Solvent-free (~0.8 mL)	Not mentioned	Batch-type reaction vessel with a reflux condenser, open to air	180	Determined for one reaction ³	5
Mo₂N	3	DMSO (4.0 mL)	N ₂	Batch-type reaction vessel with a reflux condenser	150	Not mentioned	52
Mo₂C	n.a. ²	DMSO (4.0 mL)	N ₂	Closed batch-type	120	Not mentioned	53

n.a. – not available

¹ – refers to the Ni content in the whole sample

² – the Mo₂C and Mo content in the catalyst was not determined, hence, the determination of substrate-metal ratio is not possible

³ – determined by coupling the reaction with hydrogenation of 1-decene

Table 1.2. Yields of carbonyl products obtained in the dehydrogenation of primary and secondary alcohols over varied heterogeneous catalysts.

The results are gathered only for the systems for which the H₂ production was confirmed.

Entry	Catalyst	n _{alcohol} : n _{metal}	Secondary alcohols		Primary alcohols		Reference
			Aromatic – yield (%)	Aliphatic – yield (%)	Aromatic – yield (%)	Aliphatic – yield (%)	
1	5 wt% Pt/Al ₂ O ₃	200 - 10 000	---	78 - 97	---	---	34
2	10 wt% Rh/C	5	66	---	---	---	38
3	0.005 wt% Ag/HT	22 220	98 - >99	58 - >99	83 - 98	17	42
4	5 wt% Ag/Al ₂ O ₃	50	93	50 - 94	70 - 93	16	43,45
5	4.6 wt% Cu/HT	15	81 – 97	69 - >99	55	9	47
6	5 wt% Ni/θ-Al ₂ O ₃	100	---	74 - 99	---	2	50
7	5 wt% Co/TiO ₂	100	---	78 - 99	8	10	10
8	Re	50	---	>99	61	0 - 5	5

Table 1.3. Catalytic test results for dehydrogenation of 1-octanol and 2-octanol with different catalysts. The results are gathered only for the systems for which the H₂ production was confirmed.

Entry	Catalyst	n _{alcohol} : n _{metal}	Sovent	Reaction temperature (°C)	2-octanol – yield (%)	1-octanol – yield (%)	Reference
1	5 wt% Pt/Al ₂ O ₃	10 000	o-Xylene	144	84	---	34
2	0.005 wt% Ag/HT	22 220	p-Xylene	130	58	17	42
3	5 wt% Ag/Al ₂ O ₃	50	Toluene	100	50	16	43,45
4	4.6 wt% Cu/HT	15	p-Xylene	130	96	---	47
5	5 wt% Ni/θ-Al ₂ O ₃	100	o-Xylene	144	82	---	50
6	5 wt% Co/TiO ₂	100	o-Xylene	144	78	10	10

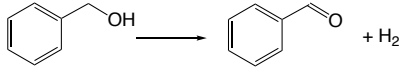
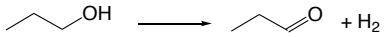
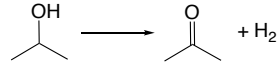
1.1.3. Activity towards different alcohols dehydrogenation

Aiming at dehydrogenating biomass-derived polyalcohols, we need to ensure a good selectivity either in secondary alcohol or in primary alcohol, and to avoid the formation of complicated product mixtures through secondary reactions. Most catalytic tests in the past years have been focusing on monoalcohols, which will provide a first insight into catalysts performance, as we will see later in this subsection. We will focus more specifically on the few studies on diols in the next part.

As it was described in the previous section 1.1.2, supported and unsupported metal catalysts were tested towards alcohol dehydrogenation, but the H₂ production was not confirmed for some catalytic systems. And by this, the acceptor-less alcohol dehydrogenation mechanism is not proved for them. Therefore, only the examples for which it was checked are chosen to compare the activity and selectivity, and the corresponding results are collected in Table 1.2.

It can be seen that usually the catalysts exhibit better activity towards dehydrogenation of aromatic alcohols. Their activity towards primary and secondary aromatic alcohols dehydrogenation is usually better for secondary alcohols (entries 3-5 in Table 1.2) and the same trend is observed for aliphatic alcohols (entries 3-8 in Table 1.2). Usually for aliphatic alcohols the difference in activity is significant and we can say that the catalysts are chemoselective towards secondary alcohols dehydrogenation vs primary alcohols. Very good examples of such behavior are Ni/ θ -Al₂O₃ supported catalyst and Re unsupported NPs, for which the yields of ketones are over 70% and yields of aldehydes are under 5%.

Table 1.4. Thermochemical data for the dehydrogenation reaction of chosen alcohols. The reaction enthalpies, entropies and Gibbs free energies are calculated based on the enthalpies and entropies of formation for appropriate species, available in NIST database.

Reaction	ΔH^{298K} (kJ mol ⁻¹)	ΔS^{298K} (J mol ⁻¹ K ⁻¹)	ΔG^{298K} (kJ mol ⁻¹)	T at which $\Delta G = 0$ (°C)
	67.5	135.2	27.2	226
	84.2	150.8	39.3	285
	67.6	150.5	21.9	176

In Table 1.4 the thermochemical data for dehydrogenation of chosen alcohols are collected. Based on them, the preferential dehydrogenation of aromatic alcohol over aliphatic alcohol can be explained by value of reaction enthalpy, which indicates the better stability of aromatic aldehyde vs aliphatic aldehyde. Even though the entropy value for dehydrogenation of benzyl alcohol is lower than for dehydrogenation of 1-propanol, the difference is not large enough to reverse the activity trend. While comparing the dehydrogenation of primary vs secondary aliphatic alcohol, it also can be clearly seen that the activity difference results from the reaction enthalpies. Obtained ketone (2-octanone) is more stable than aldehyde (octanal), what is in favor of secondary alcohol dehydrogenation.

Cyclic and linear molecules are among the tested secondary aliphatic alcohols. For cyclic alcohols, the size of the ring can influence their reactivity. According to the results of Shimizu⁵⁰ using Ni/ θ -Al₂O₃, when cyclooctanol, cycloheptanol and cyclohexanol were tested as substrates, longer reaction times of 3 h, 24 h and 72 h, respectively, were required to achieve conversions over 90%. Considering the linear aliphatic alcohols, the position of hydroxyl group in some cases can influence the reactivity of the molecule. It was observed for Co/TiO₂¹⁰ catalyst that 4-octanol was dehydrogenated more efficiently than 2-octanol (98% vs 85% of conversion, respectively). However, it was not the case for Pt/Al₂O₃³⁴ catalyst, as under the same reaction conditions, 4-octanol and 2-octanol were dehydrogenated with almost the same efficiency (86% vs 84% of conversion, respectively).

In general, the catalytic activity strongly depends on the alcohol used as a substrate. Similarly, the selectivity is sensitive to the type of alcohols. For secondary alcohols, the reported selectivity is always good (>75%) to excellent (>99%) towards the desired ketone, while for primary alcohols, the selectivity towards the aldehyde varied from 40% to >99%, depending on the catalyst. The formed by-products usually are not identified. However, for example for dehydrogenation with Re NPs, they were recognized as coming from aldol condensation reaction (condensation reaction with C-C bond formation) and this will be discussed later in part 1.1.5 of this Chapter.

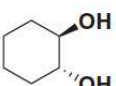
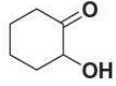
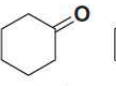
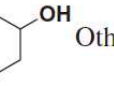
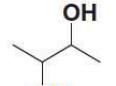
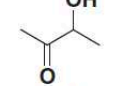
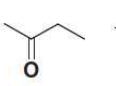
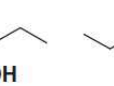

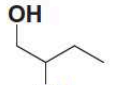
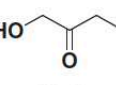
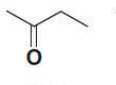
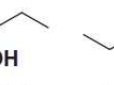

1-octanol and 2-octanol are often chosen as model primary and secondary linear aliphatic alcohols. As dehydrogenation of aliphatic alcohols is more hindered in comparison with aromatic alcohols, the comparison of catalysts activity towards their dehydrogenation will elucidate their relative activity. Also, the alcohols are good first choice molecules to determine the catalysts selectivity, and further test the chosen catalyst toward biomass-derived aliphatic linear polyalcohols. The results for 1-octanol and 2-octanol dehydrogenation with different catalysts were collected in Table 1.3. In agreement with previous observations on a wide range of alcohols, the activity towards 2-octanol dehydrogenation (>50% of yield) is systematically better than the activity towards 1-octanol when considered (yields under 20%). Due to the very differentiated reaction conditions it is not straightforward to determine the most active catalyst. Nevertheless, it can be stated that Co/TiO₂ catalyst is more chemoselective than Ag/HT and Ag/Al₂O₃, based on the ratio of activities towards different alcohols dehydrogenation (yield of 2-octanone to yield of octanal). Hence, it is a good candidate for polyalcohol dehydrogenation, even though it is not the most active catalyst. The available reports of diol dehydrogenation will be discussed in the following part.

1.1.4. Dehydrogenation of diols

Dehydrogenation of diols is one step closer to the dehydrogenation of biomass-derived polyalcohols. They possess 2 OH functional groups, which can be primary and/or secondary, and differently separated from each other. Hence, they are more complex molecules than monoalcohols. In the literature, examples of diols dehydrogenation with heterogeneous catalysts in liquid phase are scarce. To the best of our knowledge only 6 reports are available,^{22,36,44,55,56,57} among which 2 were already discarded, as the acceptor-less mechanism was not confirmed for them.^{36,44}

Both Sato et al.⁵⁶ and Tamura et al.⁵⁷ conducted the diol dehydrogenation in water, using batch reactor, pressurized with Ar (10 atm.), at elevated temperatures (220°C and 160°C, respectively). The aims of the two investigations were different. The purpose of the first group was to dehydrogenate vicinal diols (diols with neighboring OH groups) with Ir-ReO_x/SiO₂ catalyst, whereas the second group wanted to transform (hydrogenate) diols into monoketones by hydrogen borrowing methodology (dehydrogenation - intermediate reaction - hydrogenation reaction sequence) with different metals supported on SiO₂. As the main product obtained by Tamura et al. was in some cases α -hydroxyketone we will include it in the discussion.

Three different aliphatic vicinal diols were tested with the Ir-ReO_x/SiO₂ catalyst: 1,2-cyclohexanediol, 2,3-butanediol and 1,2-butanediol. The main reaction product was α -hydroxyketone, but monoketone, monoalcohol and alkane were also observed (Figure 1.3). Their formation will be discussed in the following section of this Chapter, dedicated to the by-products formation. The two first diols possess two secondary OH group, and dehydrogenation of any of them was leading to the same carbonyl product (Figure 1.3, entry 1 and 2). However, as 1,2-butanediol possesses primary and secondary hydroxyl group, its dehydrogenation could have led to different products. As it was observed, only the secondary OH group was dehydrogenated, whereas primary one was preserved (Figure 1.3, entry 3). It is in agreement with the activity towards primary vs secondary alcohol dehydrogenation, described in previous section. What is also worth to notice, the conversions were under 20%, and the obtained selectivity to hydroxyketone was better in the case of linear alcohols.

Entry	Substrate	Conv./%	Selectivity/%			
1		17.1	 56.2	 16.5	 20.9	Others ^b 6.3
2		19.1	 84.9	 13.9	 0	 1.2
3		12.6	 83.0	 8.2	 7.2	 1.5

^aReaction conditions: Ir-ReO_x/SiO₂ 0.1 g, substrate 4.3 mmol, water 10 g, $T = 453$ K, $t = 1$ h, $P_{Ar} = 1$ MPa. ^bOthers: phenol + linear alkanes + cyclohexane + benzene + cyclopentanecarbaldehyde + 1,2-cyclohexanedione.

Figure 1.3. Vicinal diols dehydrogenation with Ir-ReO_x/SiO₂ catalyst.⁵⁶

As it was already mentioned, the aim of the investigations of Tamura et al. was to obtain monoketones from vicinal diols by hydrogen borrowing strategy.⁵⁷ They tested different metal catalysts supported on SiO₂. In the reaction with 2,4-pentanediol Pt/SiO₂, Pd/SiO₂, Ru/SiO₂, Ir/SiO₂ and Ru/C occurred to be more selective towards α -hydroxyketone than towards monoketone (36-59% selectivity). Among them the most active occurred to be Ru/C, giving 68% of conversion (with the selectivity to hydroxyketone of 57%), while for the other catalysts the conversion was <20%.

All in all, as the above two examples illustrated, it was possible to dehydrogenate alcohol in closed system. However, as the reactor was pressurized and H₂ was not removed from the reactor, it was accelerating the subsequent reactions, leading to the by-products formation.

Vu et al.⁵⁵ and Guicheret et al.²² used other reaction conditions for the dehydrogenation of diols. The catalytic tests were performed under solvent-free conditions, at 160-180°C, and the produced H₂ was removed from the reactor by reducing the pressure (to 0.1 atm. and 0.01 atm, respectively). In the first paper, oleochemical 1,2-diols were dehydrogenated with commercially available Pd, Pt and Ru catalysts. The first screening in the reaction with 9,10-dihydroxyoctadecanoate allowed to determine Ru/C as the most active catalyst, whereas

Pd and Pt catalysts were not active. The chosen catalyst was also active in the dehydrogenation of oleochemical 1,2-diols with different functionalities. The obtained conversions were ranging 50-99% with the selectivities towards α -hydroxyketone of 81-92%. As a by-product monoketone, coming from dehydration reaction, was observed (Figure 1.4).

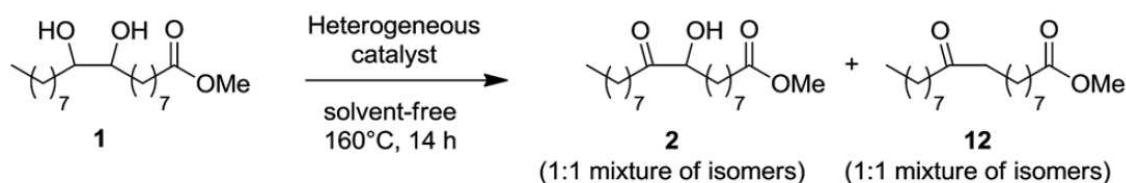


Figure 1.4. Scheme of dihydroxyoctadecanoate dehydrogenation.⁵⁵

In the second paper, Guicheret et al.²² studied dehydrogenation of 1,2-diols over 64 wt% Ni/SiO₂.²² The catalyst occurred to be very active towards fatty-alcohol derived vicinal diols, giving conversions of 87-93%, with selectivity to α -hydroxyketone of 88-90%. Diketone and monoketone were observed as by-products. In the dehydrogenation of cyclic aliphatic diol, the activity was dependent on the ring size. For the C12-ring diol (1,2-cyclododecanediol), which is not under strong steric tension, the conversion was equal to 82%, whereas for diol with C6 ring (1,2-cyclohexanediol) the conversion was equal only to 10%. Such dependency between the activity and the size of the carbon ring was already noticed in the dehydrogenation of monoalcohols. In the catalytic test with linear aliphatic diol (1,2-octanediol) the conversion was equal to 25%, what is much lower than result for the fatty-alcohols derived diols. Also, the selectivity towards α -hydroxyketone in the dehydrogenation of linear aliphatic diol was lower than in the dehydrogenation of fatty-alcohol derived diols (60% vs 88-90%, respectively). This may result from the activation of molecule by the presence of ester groups in fatty alcohols. To better understand the activity and selectivity of 1,2-octanediol dehydrogenation, the catalytic tests with 1-octanol and 2-octanol were conducted. The catalyst occurred to be highly active towards secondary monoalcohol (99% of conversion and 99% selectivity), and not active towards primary monoalcohol dehydrogenation (1-2% conversion). Hence, it showed the excellent chemoselectivity towards dehydrogenation of secondary monoalcohol vs primary monoalcohol. It was in good

agreement with 1,2-octanediol dehydrogenation, for which secondary OH group was dehydrogenated preferentially over primary OH group (no product of primary OH group dehydrogenation was reported).

Even though scarce, the available examples of diol dehydrogenation demonstrate that conducting the reaction in closed system is possible, but accelerates the secondary product formation, hence diminishing the amount of desired hydroxyketone product. While H₂ is removed from the reactor, the selectivity is significantly improved. Considering the chemoselectivity in diol dehydrogenation it was demonstrated that a secondary OH group is preferentially dehydrogenated over a primary hydroxyl group. As was shown on the example of 1,2-octanediol, 1-octanol and 2-octanol, it could have been deduced based on the reactions with monoalcohols.

1.1.5. Side reactions in acceptor-less alcohol dehydrogenation

The main, expected product in the dehydrogenation of mono- and polyalcohols is the corresponding carbonyl product. However, the formation of some small amounts of by-products is also observed. In the following paragraphs, the formation of side substances in the reactions of monoalcohols and diols will be discussed.

The by-products formed during the monoalcohol dehydrogenation in liquid phase are not often identified. However, while they are, they are ascribed to come from the aldol condensation reaction.⁵ Moreover, the experimental and theoretical (DFT) results of 1,3-propanediol deoxygenation (involving propanol hydrogenation-dehydrogenation in the reaction network) with Cu supported catalyst showed that also the esterification reaction is possible.^{58,59} Both of these reactions belong to the family of hydrogen transfer reactions.^{23,60}

The strategy involves three consecutive transformations:

- (1) Dehydrogenation of hydrogen donating molecule (e.g. alcohol, amine, alkane),
- (2) Intermediate reaction, in which a new bond is formed (e.g. C=C, C-O, C=N),
- (3) Subsequent hydrogenation reaction, utilizing the H₂ produced in the first step.

Alcohol molecules are not very active substances. However, while they are transformed into carbonyl compounds, their activity increases significantly. They can act as nucleophiles (while

they are involved in the reaction via O) or electrophiles (while they are involved in the reaction via C). In such transformations new C-C or C-O bond can be formed.

Hydrogen borrowing reaction sequence, which involves aldol condensation, leads to the formation of new C-C bond (Figure 1.5). At first, the corresponding carbonyl compound is formed from an alcohol. Then, the carbonyl compound, in equilibrium with an enol (carbonyl compound possessing H in C_α position to carbonyl group) reacts with another carbonyl compound (which can be an aldehyde or a ketone). This leads to formation of a new C=C bond. In the following step, the C=C bond is hydrogenated into C-C bond, by H₂ produced in the first step of the sequence.

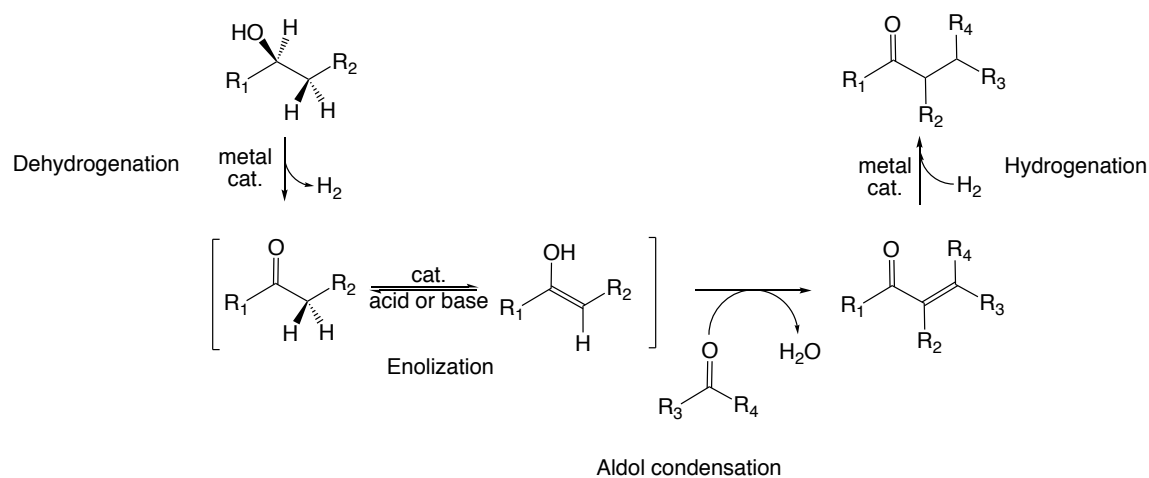


Figure 1.5. Hydrogen borrowing reaction sequence, involving the aldol condensation reaction.

The formation of new C-O bond is also possible in the dehydrogenative coupling sequence of reactions.^{23,60} It starts with the dehydrogenation of alcohol molecule (Figure 1.6). When primary alcohols are used as substrate, the coupling between aldehydes takes place, leading directly to ester formations (Tishchenko reaction). Per one molecule of ester, two H₂ molecules are liberated. To the best of our knowledge no report is describing the esterification coupling between two secondary alcohol molecules. But in our opinion, such possibility, in the presence of metal catalyst cannot be excluded.

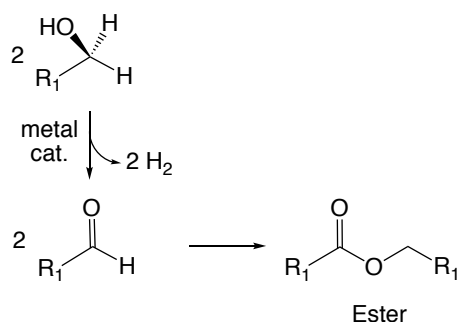


Figure 1.6. Esterification reaction sequence for primary alcohols.

In the literature some examples of metal catalyzed aldol condensation^{60,61} and esterification⁶¹ reactions are available. For both of them, it was shown that the acid-basic properties are important for the catalyst activity. Aldol condensation was favored with the basic supports (Cu/HT and Pd/HT),⁶² what allowed to avoid the basic additives reported for other catalysts.^{63,64,65} The esterification reaction was reported to be preferred on the catalysts with support possessing basic (Pt/SnO₂)⁶⁶ or amphoteric properties (Cu/ZrO₂).⁶⁷ Moreover, as Sad et al.⁵⁸ and Neurock et al.⁵⁹ showed, the reactions can proceed with the involvement of metal exclusively. The electronic properties of adsorbates (reaction intermediates) can change the properties of the surface, due to electron withdrawing abilities from the metal surfaces, and hence facilitate the aldol condensation and esterification reactions.

The by-products are also reported for the dehydrogenation of diols, however their origin is different. As it was schematically shown by Sato et al.⁵⁶ (Figure 1.7), after the hydroxyketone is formed, it can undergo the subsequent dehydration-hydrogenation reactions, which leads to the monoketone product. Further, the monoketone can be hydrogenated, what will result in the formation of monoalcohol.

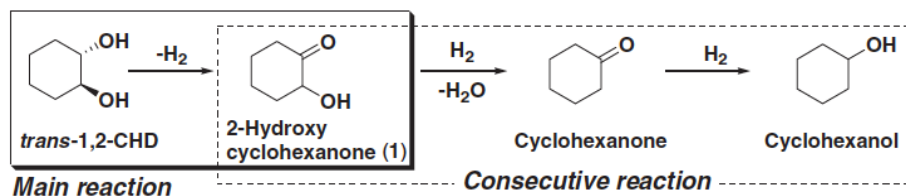


Figure 1.7. Proposed reaction pathway for 1,2-cyclohexanediol dehydrogenation with Ir-ReO_x/SiO₂ catalyst.⁵⁶

For diol dehydrogenation over Ni/SiO₂ catalyst²² the formation of diketone as a by-product is additionally reported. It results from the dehydrogenation of second OH group. But its formation was not observed while the second OH group in diol was primary OH – it was not dehydrogenated. Instead, larger amount of monoalcohol, from dehydration reaction was notified as side product.

There are not enough examples of diol dehydrogenation to assess the influence of catalysts structural parameters on the by-product formation. Nevertheless, the conclusion can be made that the presence of H₂, formed in the dehydrogenation reaction, favors the formation of side products in sequential reaction.

1.2. Towards the understanding of catalytic activity

To achieve better catalytic performance, the understanding of the influence of different structural parameters of catalyst, together with the comprehension of reaction mechanism, is necessary. The effect of: the type of metal by itself, nanoparticles size effect, influence of the support nature, type of exposed facets (shape effect), and the surface ligands will be discussed in the following parts. The dominant influence of a given parameter will be described on the chosen examples. However, what has to be kept in mind is that the catalyst possesses all its structural parameters at the same time, and even though one of them is usually the most decisive for the catalytic activity, the other parameters cannot be totally forgotten.

The understanding of the role of catalysts structural parameters is possible by (combining) different techniques: catalytic tests, material characterization, DFT computations. They allow to identify the most relevant sample parameter, but also to make conclusions about the tendencies of the change of given feature and outline the path for improvement.

1.2.1. Insight into metal activity

Metals differ in their properties, like for example oxophilicity. Due to this, they may exhibit different activity and favor different reaction mechanisms, what may imply different reaction selectivity (while different mechanisms are leading to different products). DFT calculations can help to explain and understand their catalytic behavior. Alcohol dehydrogenation is usually computed using MeOH, EtOH or iPrOH as model alcohols. Most of the time, computations are performed only on the metal surfaces, not including the support, however, examples of such calculations can also be found (see section 1.2.2). To model the metal surfaces the supercells composed of few metal layers (usually 4) and vacuum (usually over 10 Å) over them are used and repeated periodically to mimic the extended crystallographic facets. Very often close packed (111) facet for fcc (face centered cubic) type metals and (0001) surface for hcp (hexagonal close packed) type metals are chosen to represent the metals. However, it is also possible to find reaction pathways modeled on stepped and open type metal surfaces (see subchapter 1.2.3). In the literature, reports about activity of: Pt,^{68,69,70,71} Pd,^{69,70,72} Rh,^{68,69,73,74} Ru,⁷⁰ Ir,⁶⁹ Au,⁶⁹ Ag,⁶⁹ Cu,^{69,70,75} Ni⁶⁹ and Co^{69,76} are available.

To assess the catalytic activity of different metals for the same reaction, two types of energies have to be compared: adsorption energies of reaction species and activation energies for bond dissociations.^{77,78,79} The adsorption should not be too weak, as in such case the contact time between the molecule and the surface may be not long enough for the transformation to occur. It cannot be also too strong, as in such case the blocking of catalysts active sites takes place. For the activation energy, the lower it is, the easier it is for the molecule to undergo the elementary reaction.

Every catalytic cycle starts with the contact between substrate and catalyst surface. Therefore, in the case of alcohol dehydrogenation, it starts with the adsorption of alcohol molecule on the metal surface (Figure 1.8). It is widely accepted that at first the OH or α -CH bond dissociation occurs (marked as OH and CH on the Figure 1.8, respectively), leading to the corresponding alkoxy or hydroxyalkyl intermediate, respectively. As a subsequent step, CH bond breaking can take place for alkoxy intermediate (through TS OH-CH), leading to the formation of carbonyl product and two H^* atoms. For hydroxyalkyl intermediate, OH bond dissociation occurs (via TS CH-OH), leading to the formation of the same products. The catalytic cycle finishes with desorption of carbonyl product and H_2 molecule from the surface. For metals of different nature, the preferred dehydrogenation mechanism can be different.

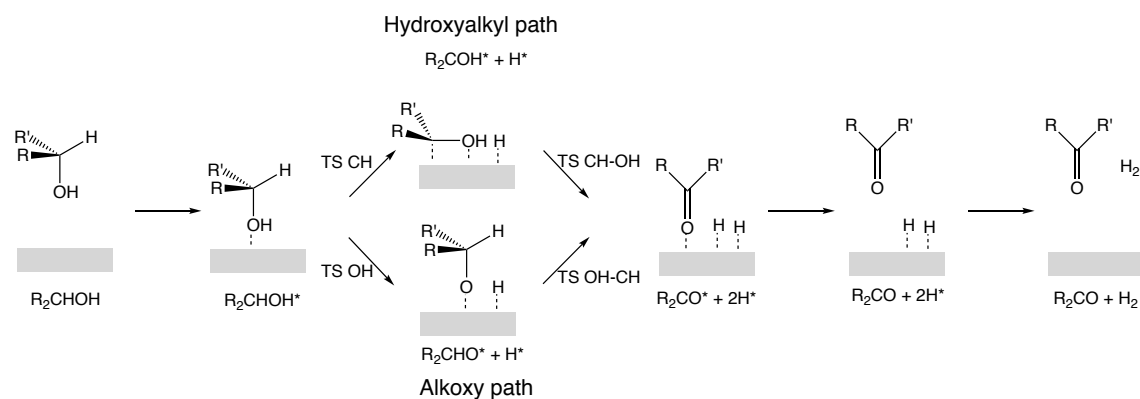


Figure 1.8. Mechanisms schematic of catalytic alcohol dehydrogenation.

Some examples of alcohol dehydrogenation reaction modeled by DFT calculation on different metals are available in the literature. Mostly, they focus on the activity of one metal. To compare the performance of different metal surfaces the calculations should be performed

on the same computational level (i.e. with the same functional and dispersion correction), and the energy reference state should be the same for them (i.e. the adsorption energy can be referred to the sum of energy of given species in gas phase and pure surface, or to the energy of substrate in gas phase and surface). Two studies in which the reaction pathways were computed for few elements were chosen to compare the activities of different metals, and they will be discussed in the following paragraphs.

Garcia-Muelas et al.⁷⁰ modeled the methanol decomposition reaction for four different metals on their close-packed surfaces: Cu(111), Ru(0001), Pd(111) and Pt(111). The computations were performed applying PBE functional with Grimme D2 dispersion correction. Adsorption energies of species refer to the difference between the energy of the adsorbate on the surface and the energy of adsorbate in gas phase and surface. The preferred reaction pathway was assessed by comparing the activation energies for the bond breakings and the adsorption strengths of subsequently formed reaction intermediates (Table 1.5). According to the results, the alcohol decomposition starting with OH bond dissociation is preferred on Cu and Ru surfaces, whereas CH bond breaking was favored on Pd and Pt facets. Such preference may be connected with oxophilicity of metals, as Cu and Ru are more oxophilic than Pd and Pt.⁸⁰

Table 1.5. Adsorption energies and activation energies for the chosen states among methanol decomposition pathways on Cu(111), Ru(0001), Pd(111) and Pt(111) facets.⁷⁰ Computations were performed with PBE functional with D2 dispersion correction. Adsorption energies of species refer to the difference between the energy of the adsorbate on the surface and the energy of adsorbate in gas phase and surface. Negative energy means stabilizing interactions.

	Cu(111)	Ru(0001)	Pd(111)	Pt(111)
	Adsorption energy (eV)			
CH₃OH	-0.38	-0.61	-0.48	-0.46
CH₃O*	-0.48	-1.23	-0.27	0.16
*CH₂OH	0.42	-0.84	-0.75	-0.68
	Activation energy (eV)			
OH	1.20	0.83	0.95	0.87
CH	1.33	0.64	0.64	0.81

For Cu(111), Pd(111) and Pt(111) the chosen reaction pathway is undoubtful, as the most stable reaction intermediate is reached by the transition state, requiring lower activation energy. However, for Ru(0001) the situation is not as obvious. CH bond breaking requires less energy to be reached, thus we could have expected the reaction to proceed through hydroxyalkyl pathway. But, this transformation is leading to the less thermodynamically favored intermediate (*CH_2OH is 0.39 eV less stable than CH_3O^* , whereas the difference in activation energies is equal only to 0.19 eV). Therefore, on Ru(0001) facet we can expect methanol decomposition to proceed via methoxy intermediate.

Syu et al.⁶⁹ systematically modeled EtOH dehydrogenation, for 9 different metals (Co(111), Ni(111), Cu(111), Rh(111), Pd(111), Ag(111), Ir(111), Pt(111) and Au(111)). The computations were performed with PW91 functional, and no dispersion correction. Similarly, adsorption energies were considered as the energy difference between the energy of species on the surface and energy of species in gas phase and pure surface. The aim of the work was to understand the catalytic activity of Cu, Ag and Au metals by analyzing their chemical properties. For all of the metals CH_3CH_2OH (ethanol) and CH_3CHO (acetaldehyde) were weakly bounded with the surfaces ($E_{ads} > -0.5$ eV). On the other hand, $CH_3CH_2O^*$ (ethoxy), CH_3CHOH^* (hydroxyethyl) and H^* species were adsorbed much stronger. For example, ethoxy intermediate was adsorbed the weakest on Au (-1.33 eV) and the strongest on Co (-2.91 eV), indicating different oxophilicity of investigated metals. Moreover, it may be expected that Co will be blocked by alkoxy intermediate, whereas this should not occur for Au. Activation energies for bond breakings also differed depending on the nature of metal. The OH bond dissociation required only 0.44 eV on Co(111) (the lowest activation energy among different metals) and 1.13 eV on Au(111) (the highest among different metals). However, subsequent OH-CH bond dissociation seemed to be less influenced by the metal nature with no systematic change. Starting from ethoxy intermediate, this type of scission requires 1.64 eV on Cu(111) and 0.94 eV on Pt(111).

All in all, according to the computational results, Cu, Ag and Au are expected to be inert in direct (acceptor-less) alcohol dehydrogenation. However, this is not in agreement with the experimental results (see Table 1.2 for comparison). Therefore, it can be suspected that other factors are responsible for the catalyst activity, like the size of metal nanoparticles and/or nature of support, which will be discussed in the following parts of the Chapter.

On the other hand, the metals such as Co and Ni, are predicted to be endangered by blocking of active sites by the reaction intermediates and by this their activity is supposed to be suppressed. Apparently, it does not take place, as they are reported as being active. In the calculations, the entropy correction was not included (energies are reported as electronic energies, not Gibbs Free Energies), what is the reason of predicted overstabilization of species.

Despite of the classical dehydrogenation mechanism, involving OH and α -CH bond breakings, also the pathway involving β -CH bond scission is reported in the literature. Experimentally, it was confirmed by kinetic isotope effect for Re unsupported NPs⁵ (Figure 1.9). It starts with OH bond scission, after which the Re NP gains a partial positive charge. Then, β -CH bond dissociation occurs, increasing the partial positive charge of metal, and leading to the formation of enol intermediate. At the end of the cycle, the H₂ and enol are desorbed from the metal surface, and interconversion of enol into carbonyl product takes place. From the computational side, it was shown by Michel et al.⁷⁴ that the β -CH and α -CH bond breaking from EtOH molecule on Rh(111) surface, require the same energy input and lead to the intermediates of similar stability. Hence, they can be assessed as occurring with very similar probability. The above results suggest that the reaction mechanism involving β -CH bond breaking may be preferred on some of the metals, and should not be forgotten.

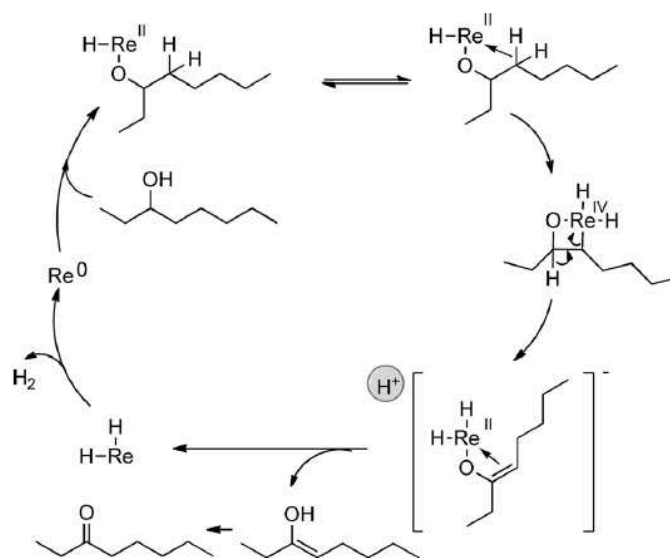


Figure 1.9. Proposed mechanism of 3-octanol dehydrogenation with unsupported Re NPs.⁵

1.2.2. Effect of NPs size and support

As it was stated in the previous part 1.2.1, the metal activity predicted by DFT calculations for Au, Ag and Cu does not agree with the activity observed experimentally. This implies the participation of other factors, like NPs size and/or support in the activity. They may be concomitantly involved, if the reaction occurs on the metal-support interface. It is very challenging to disentangle these two parameters. To assess it properly, the support effect should be compared for the NPs of similar size, and the size effect should be compared for the samples of the same metal content and total surface area of samples. In the following paragraphs the two effects will be discussed.

The metal atoms exposed on the corners, edges and terraces of a NP are differently coordinated. The lower coordinated atoms are considered to be more active than the ones more coordinated. Hence, the corner and edges atoms are expected to be more active than the terrace atoms, what was shown already for the CO oxidation.^{81,82} The amount and ratio between them depend of the NP size. The bigger it is the more of the terraces and the less of the edges and corners occurs.

Acceptor-less dehydrogenation of benzyl alcohol, with Au/HT catalysts, is reported as sensitive to the size of metal NPs.⁴¹ The investigated catalysts possess NPs of size ranging from 2.1 nm to 12 nm, with the same Au loading of 0.4 wt%. According to the catalytic tests results, the reaction rate per surface Au atom was decreasing with increase of the size of metal NPs. This behavior was ascribed to the differences in the activity of different types of metal atoms in the NP. According to the calculated optimal intrinsic reaction rates, the corners and edges (reaction rates $1016 \text{ mmol mol}_{\text{Au}}^{-1} \text{ s}^{-1}$ and $795 \text{ mmol mol}_{\text{Au}}^{-1} \text{ s}^{-1}$, respectively) were responsible for the catalytic performance, while the contribution of terraces was negligible (reaction rate $5 \text{ mmol mol}_{\text{Au}}^{-1} \text{ s}^{-1}$).

Kon et al.³⁴ also investigated NPs size effect for the activity of 5 wt% Pt/Al₂O₃ catalyst in acceptor-less alcohol dehydrogenation. The NPs size was varied by the treatment of samples at different temperatures, ranging from 500°C to 670°C, what resulted in the formation of NPs of 1.4-12 nm in diameter. According to the obtained TOF (turnover frequency) values, the larger were the NPs the lower was the activity. This is in agreement with the just described findings for Au/HT.

However, the effect of NPs size does not exclude the effect of support. The influence of support nature was investigated in many reports concerning alcohol dehydrogenation.^{34,37,39,40,45,47,50,10} The most active occurred to be: Pt/ γ -Al₂O₃, Re/Al₂O₃, Au/HT, Ag/Al₂O₃, Cu/HT, Ni/ θ -Al₂O₃, Co/TiO₂. It can be noticed that for Au and Cu the most appropriate was basic hydrotalcite (HT), whereas for the remaining metals the use of supports of amphoteric nature (Al₂O₃ and TiO₂) resulted in the best activity. This connects with the proposed reaction mechanism, which involves the participation of metal NP and support, as illustrated on Figure 1.10.

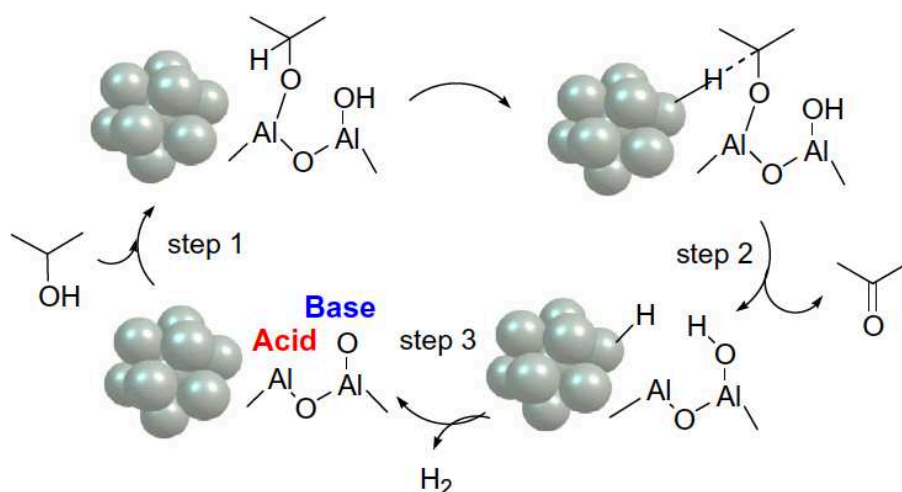


Figure 1.10. Proposed reaction mechanism for alcohol dehydrogenation with Pt/ γ -Al₂O₃.³⁴

It is proposed that the reaction starts with the interaction of OH group from alcohol with the acid-basic site of support. O interacts with positively charged acidic site (e.g. Al^{δ+}), whereas H interacts with negatively charged basic site on the support (e.g. Al-O^{δ-}).³⁴ This results in dissociation of H atom from alcohol molecule, and creation of alkoxy reaction intermediate. In the following, rate limiting step, α -CH interacts with metal nanoparticle (e.g. Pt⁰),³⁴ and another H atom is separated from the substrate species, leading to the formation of corresponding carbonyl product. As the final stage of the reaction, H atom present on the support surface and H atom present on the metal surface, combine into H₂

molecule, which is the second reaction product. Such mechanism justifies the necessity of the basic support properties, which are enhancing the catalytic performance.

The presence of the catalyst support is usually not taken into consideration in DFT computations, due to high computational demands. Nevertheless, the example of such modeling, with reaction proceeding on the interface between oxide support and metal nanoparticle, can be found in the literature for Ni/ θ -Al₂O₃.⁸³ The computations were performed with PBE functional, and no dispersion correction was applied. iPrOH dehydrogenation (through alkoxy pathway) was modeled at first only on Ni cluster composed by 13 atoms, and subsequently on Ni₁₃ cluster, adsorbed on θ -Al₂O₃(010) surface. The corresponding energy profiles are presented on Figure 1.11. For the dehydrogenation proceeding on metal cluster, the OH bond dissociation required 0.95 eV and was the rate determining step. Subsequent OH-CH bond scission demanded only 0.41 eV. For the Ni₁₃/ θ -Al₂O₃ reaction started with the adsorption of OH group on Al₂O₃, close to the metal cluster. As the first one OH bond dissociation took place, for the preferred pathway requiring only 0.05 eV. To subsequently break the OH-CH bond an input of 0.38 eV of energy was needed. As it can be seen, the presence of metal-support interface has decisive meaning for the OH bond breaking. Hence, it is showing the importance of the support for heterogeneous metal supported catalysts, what is in agreement with the experimental results reported by Shimizu et al.⁵⁰

of alcohol dehydrogenation on different type of surfaces was already reported. The differences in their activity will be discussed on such calculation examples.

Xu et al. reported the shape-dependency of oxidation of styrene with silver nanoparticles.⁸⁹ Truncated triangular Ag nanoplatelets were synthesized by solvothermal method (DMF – solvent and reducing agent, AgNO_3 – metal precursor, PVP – poly(vinylpyrrolidone) – stabilizing agent, at 140°C). Near-spherical NPs were synthesized by reducing water solution of AgNO_3 by N_2H_4 (hydrazine), in the presence of PVP (at room temperature). Nanocubes were synthesized by modified silver-mirror reaction (with CTAB – cetyltrimethylammonium bromide – as capping agent). Cubic NPs exposed uniquely (100) facets, near-spherical NPs exposed a mixture of (111) (mainly) and (100) facets, whereas truncated triangular platelets were exposing (111) planes. The corresponding TEM images and geometrical models are presented on Figure 1.12.

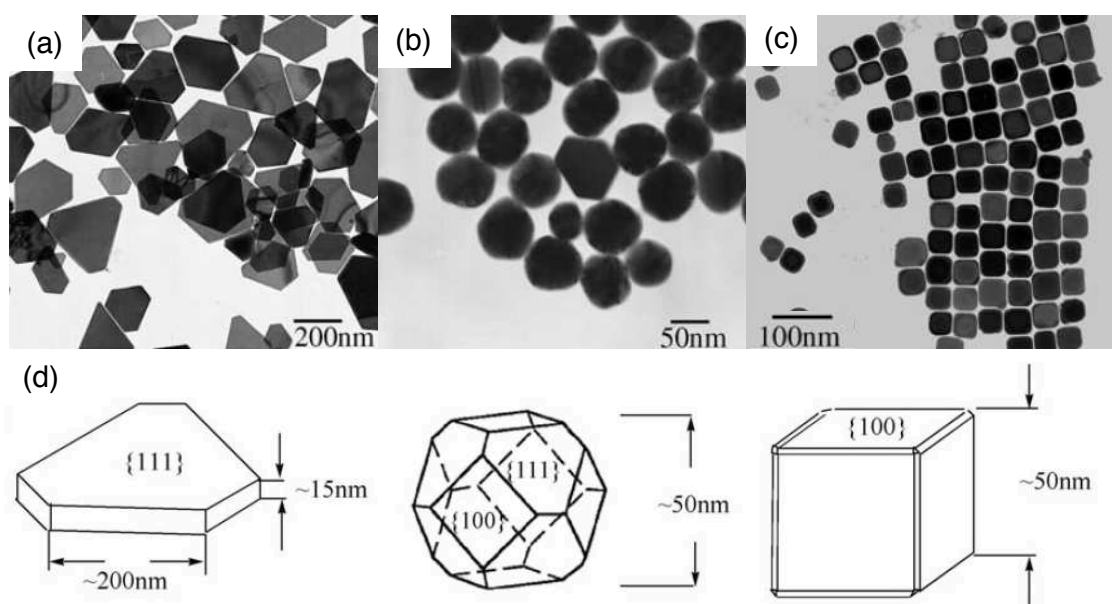


Figure 1.12. TEM images of (a) nanoplatelets, (b) near-spherical NPs, and (c) nanocubes, (d) their structural models.⁸⁹

In the oxidation of styrene, nanocubes were more active than near-spherical NPs (~4 times more active), and platelets (~14 times more active). Selectivity was not influenced by the shape of NPs. The factor which could be decisive for the catalytic activity of samples was

the type of exposed surfaces. As it is considered that the facets with higher surface energies are more active,⁹⁰ therefore (100) surface is supposed to be more active than (111) facet. For better comparison, the activity was expressed by specific reaction rate, equal to the ratio between amount (in mol) of converted styrene to the surface area of Ag NPs. This comparison clearly showed that the nanocubes possessing (100) facets were outperforming the NPs with (111) surfaces exposed, what agreed with the catalytic tests results. The specific reaction rates were equal to $9.53 \cdot 10^{-3} \text{ mol m}^{-2} \text{ h}^{-1}$ for nanocubes, $1.98 \cdot 10^{-3} \text{ mol m}^{-2} \text{ h}^{-1}$ for near spherical NPs, and $0.66 \cdot 10^{-3} \text{ mol m}^{-2} \text{ h}^{-1}$ for platelets. This confirmed the importance of the type of exposed surface for the catalytic activity, and by this the significance of NPs shape.

The example of selectivity conditioned by the type of exposed crystallographic facet was investigated for benzene hydrogenation by Bratlie et al.⁹¹ The Pt NPs were prepared by reducing aqueous solution of metal precursor (K_2PtCl_4) and capping agent (TTAB – tetradecyltrimethylammonium bromide) with NaBH_4 and gaseous H_2 , at 50°C . The variation of preparation conditions allowed to obtain cubic and cuboctahedral NPs. The cubic NPs were exposing only (100) facets, whereas cuboctahedral NPs were exposing both (100) and (111) facets. For the catalytic tests the NPs were assembled on a silicon wafer. Both catalysts were similarly active in the benzene hydrogenation (turnover rates $\sim 0.95 \text{ molecules Pt sites}^{-1} \text{ s}^{-1}$ at 107°C). However, they differed in selectivity. In the reaction with cubic Pt NPs cyclohexane were formed exclusively, whereas in the reaction with cuboctahedral NPs both cyclohexane and cyclohexene were obtained. The difference in the reaction selectivity resulted from different types of facets exposed by NPs. (100) facets, present on both cubic and cuboctahedral NPs, lead to the formation of cyclohexane, and (111) surface, present on cuboctahedral NPs, promoted the formation of cyclohexene (Figure 1.13).

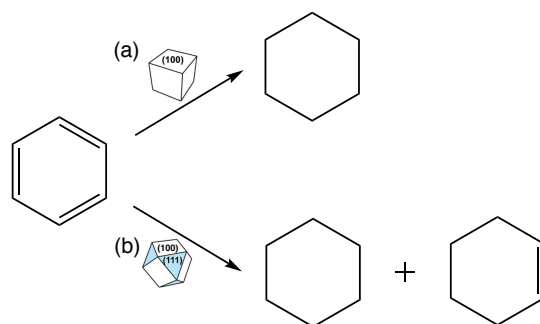


Figure 1.13. Reaction schematic for benzene hydrogenation with (a) cubic and (b) cuboctahedral NPs.⁹¹

Very recently (in 2019) He et al. examined the influence of surface restructuring of Cu catalysts on their activity in EtOH dehydrogenation.⁹² Cu/SiO₂ catalyst was used for the gas phase ethanol dehydrogenation. The restructuring of metal nanoparticles was induced by oxidation with N₂O, applied under the reaction conditions. It influenced only the metal NPs surfaces, not altering other structural parameters (like size, dispersion, oxidation state). Catalyst with the modified surface was 4 times more active than the catalyst before the oxidative treatment (TOF equal to 15 h⁻¹ and 60 h⁻¹ for reactions conducted before and after the Cu/SiO₂ treatment with N₂O, respectively). TEM structural analysis revealed that the NPs before the treatment possessed faceted shape, exposing mainly (111) and (100) surfaces, whereas the NPs after the treatment became more spherical, and exposed more of small (in dimensions) (111), (100) and (110) facets. Hence, the surface of NPs after the treatment became rougher and possessed more less coordinated sites, like edges and corners.

For better understanding of the improvement in catalytic activity, the reaction kinetic studies and DFT calculations were performed. The kinetic isotope effect investigations together with the examination of influence of alcohol pressure, revealed that the reaction proceed via CH₃CH₂O* intermediate (alkoxy pathway), and α-CH bond dissociation is the rate determining step in the reaction, what is in line with the DFT findings, already described in part 1.2.1 of this Chapter. By DFT computations, the authors investigated the activity of Cu(111) and Cu(211) surfaces. The calculations were performed with PBE functional and D3 dispersion correction. The close-packed (111) facet was used to simulate the surface of the NPs before the restructuring, while stepped (211) surface was mimicking the surface of the NPs after N₂O treatment. The adsorption of molecules and intermediates is found to be stronger on open (211) facet, and the activation energies for OH and OH-CH bond breakings are lower for it. Hence, it is expected to be more active than the close-packed (111) facet, in accordance with the better activity of Cu/SiO₂ catalyst after treatment.

MeOH and EtOH dehydrogenation on Cu were also investigated by DFT computations by Hoyt et al.⁷⁵ The modeling was performed with PBE functional, and van der Waals corrections were calculated with Tkatchenko-Scheffler method. As model surfaces were used: Cu(111) terrace facet and (111) and (100) step edges (for illustration see Figure 1.14), what allowed to understand, on a molecular level, the catalytic behavior of highly stepped Cu(111) sides present on the metal nanoparticles of the catalyst.

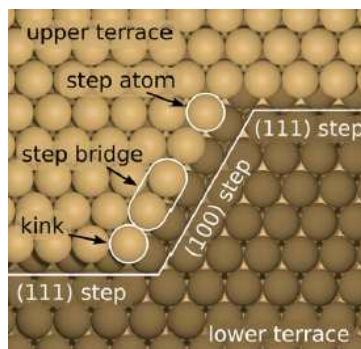


Figure 1.14. Illustration of the surfaces used in computations by Hoyt et al.⁷⁵

The reaction was considered as proceeding via alkoxy pathway. (For the obtained energy profiles see Figure 1.15) Among the reaction species, the alkoxy intermediate is adsorbed stronger than alcohol and aldehyde molecules, therefore, it is the most stable species among the reaction pathway. As it was observed, the adsorption strength for all the reaction species on steps is larger than on terrace (111) side (by ~ 0.30 eV), what might suggest the weaker activity of steps, due to the blocking of active sites by molecules and (especially) intermediates of the reaction. However, the activation energies for OH and OH-CH bond dissociations are lower on the stepped surfaces, than on terrace (111) facet (for OH by 0.31-0.43 eV and for OH-CH by 0.19-0.36 eV), what makes them more active. The proceeding of reaction is strongly limited by product desorption from the metal surfaces. Especially for stepped surfaces, the hydrogenation of aldehyde to alkoxy intermediate is more favored than the desorption of molecule from the surface. Hence, the reaction has to be conducted at temperature high enough to allow desorption of the products from the metal surface, and by this directing the reaction towards products.

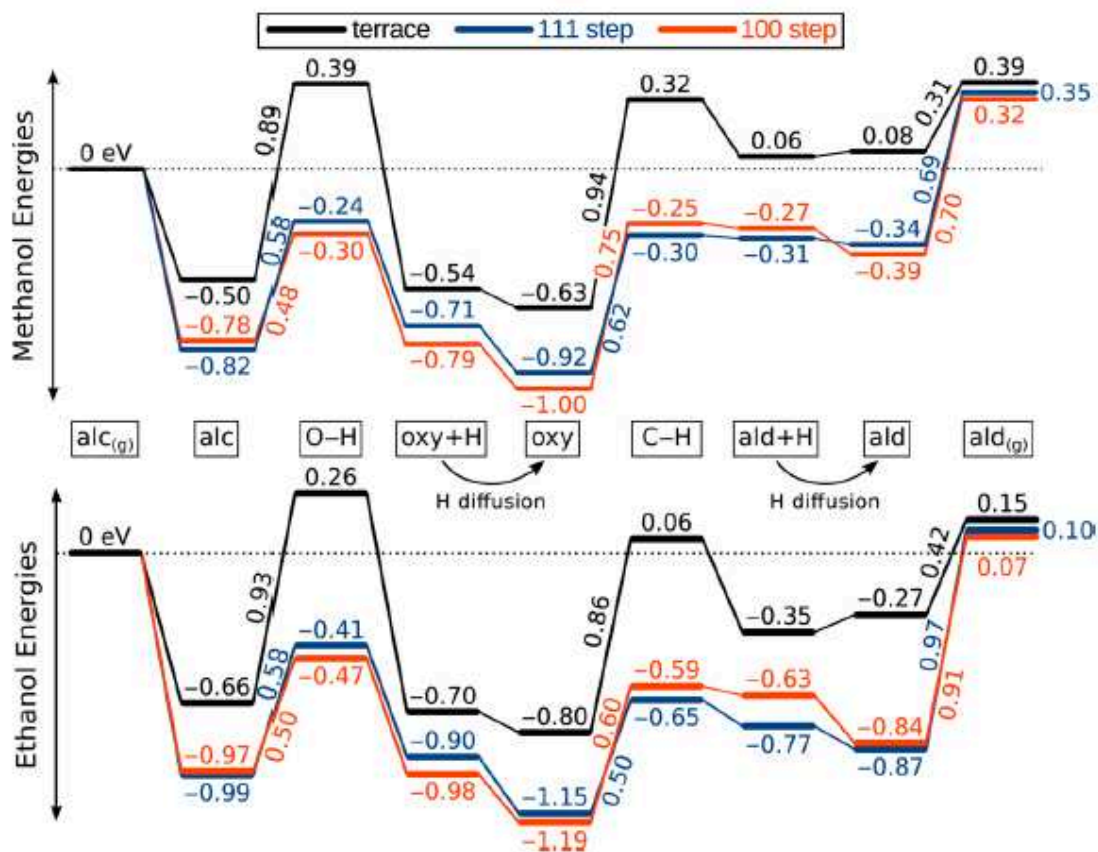


Figure 1.15. Energy profiles for MeOH and EtOH dehydrogenation on Cu(111) terrace (black), (111) step (blue), and (100) step (red).⁷⁵

Comparison between energetic profiles of MeOH and EtOH dehydrogenation suggested that OH bond scission activation energy was not influenced by the length of alcohol. Therefore, similar activation energies for this bond breaking are expected for alcohols with longer alkyl chains. On the other hand, the OH-CH bond breaking activation energy for ethoxy intermediate was lower than for methoxy intermediate (by 0.08-0.15 eV, depending on the surface), suggesting its facilitation for longer alcohols. However, the adsorption energies for EtOH dehydrogenation reaction species were higher than for MeOH, that may suggest a possible blocking of active sites for higher alcohols. Hence, the reaction conditions will have to be adjusted to improve the efficiency.

As just demonstrated, better catalytic activity and/or selectivity can be achieved with shaped metal NPs, exposing defined crystallographic facets. However, as it was mentioned, some

capping agents are used in their synthesis, which also can influence the material activity, as they stay on the metal surface after the synthesis. This will be discussed in details in the following part.

1.2.4. Ligand effect

To rationally design the size, shape and morphology of metal nanoparticles (both supported and unsupported ones), different ligands can be used during the synthesis of catalysts. They can be for example: amines,⁹³ carboxylic acids,⁹⁴ thiols,^{95,96,97,98} phosphines,^{99,100} polymers.^{93,100} They are considered mainly as stabilizers and growth rate regulators for various crystallographic facets.¹⁰¹ But they can also modify the nature and concentrations of species consisting reservoir for (unsupported) NPs formation.^{101,102} Additionally, the presence of ligands on the surface can modify catalysts activity and selectivity towards desired products.

The catalyst coverage with ligands is important for its performance in the reaction, as it was illustrated by Yoskamtorn et al.⁹⁸ Au₂₅ clusters supported on porous carbon and protected with dodecanethiolate ligands (SC₁₂H₂₅), were tested in aerobic oxidation of benzyl alcohol. The coverage with thiolate ligands was modified by calcination under vacuum – the longer the calcination was (2-4 h) and the higher the temperature was (400-500°C), the less ligands remained present on the catalyst surface. (For the calcination conducted at 500°C, for 4 h it became negligible.) The activity of catalysts was decreasing as the amount of ligands was increasing (from 98% conversion for Au₂₅ – catalyst with negligible amount of ligands, to 0% conversion for Au₂₅(SC₁₂H₂₅)₁₈ – catalyst fully covered with ligands). However, the selectivity to the desired benzaldehyde was improved, as the amount of ligands on the surface was higher (see Figure 1.16 for illustration). The role of thiolate ligands present on the Au₂₅ cluster surface is dual. From one side, they are blocking the catalytically active sites, and are reducing the oxidation ability of metal cluster, due to the electron withdrawal, what results in lower conversions. On the other hand, by the steric effect (site isolation), they are preventing the side reaction (esterification).

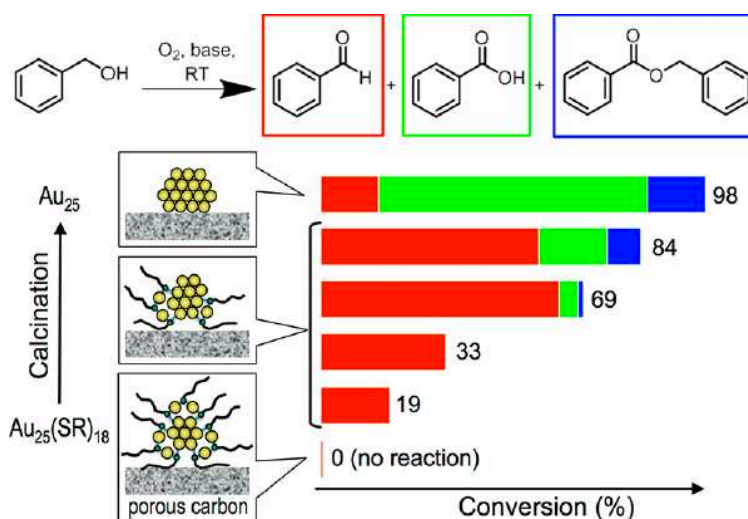


Figure 1.16. Activity and selectivity of Au_{25} clusters, covered with thiolate ligands, supported on carbon, in the aerobic oxidation of benzyl alcohol, in term of surface coverage with ligands.⁹⁸

There are three possible roles of ligands in binding of reactants and transition states: steric effect, orientation effect, and influence on surface charge state.⁹⁵ Steric effect can limit the adsorption and desorption of reaction species on a given plain surface, thus favoring the adsorption on edges and corners, where the density of ligands is lower. For structure sensitive reactions this effect can change the product selectivity. It was showed by Medlin et al. that hydrogenation of furfural can proceed in different ways depending on the thiol ligand.⁹⁶ When 1-octadecanethiol (C18) was used, the binding of furfural to surface was possible only on surface defects, like edges and corners. In this case reaction proceeded preferentially to furfuryl alcohol and methylfuran, with a combined selectivity to these products above 70%. In contrast, when the bulky cage 1-adamantanethiol was used, furfural could bind to the surface terraces lying flat on them. In this case, the selectivity of reaction was directed towards the formation of tetrahydrofuran and furan, with a selectivity >90%.

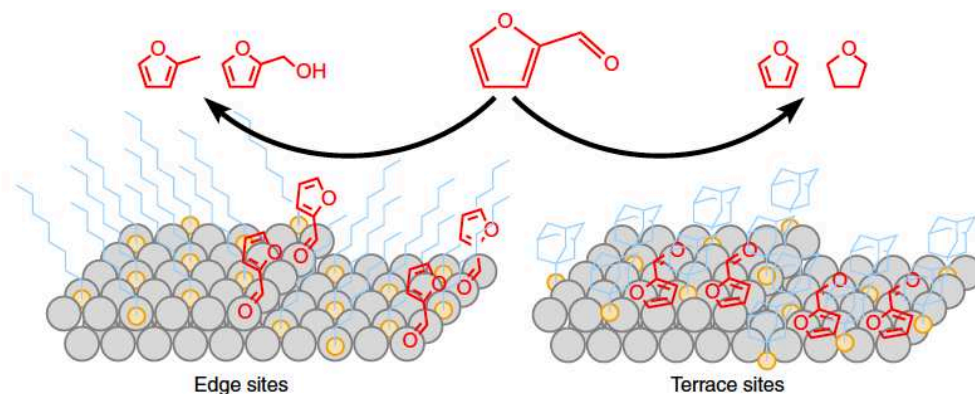


Figure 1.17. Furfural hydrogenation on the surface covered with 1-octadecanethiol (on left) and 1-adamantanethiol (on right).⁹⁶

In orientation effect the crowdedness of ligands can impose the steric hindrance. Hence, the binding of molecules with more complicated geometries and/or more functional groups, will be limited only to scope of positions. It also can cause the binding of molecules in restricted direction, while non-covalent interactions, like hydrogen bonding or π - π interactions, between surface ligands and reactants occur. The example of steric effect can be observed in hydrogenation of cinnamaldehyde occurring on Pt/Al₂O₃ coated by 3-phenylpropanethiol ligands.⁹⁷ As the structures of this thiol and aldehyde are similar, the aromatic rings of both substances can interact forming π - π bonds. Therefore, the bonding of aldehyde to the surface takes place only via aldehyde functional group. This leads to hydrogenation of cinnamaldehyde to cinnamyl alcohol (selectivity >90%), whereas hydrogenation of C=C in aldehyde is limited.

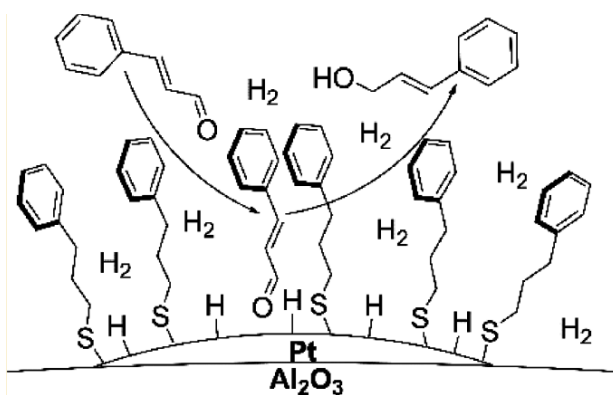


Figure 1.18. Selective hydrogenation of cinnamaldehyde to cinnamyl alcohol on Pt/Al₂O₃ surface coated with 3-phenylpropanethiol ligands.⁹⁷

The presence of surface ligands can also vary the charge density of metal surface atoms, which influences the binding affinity of reaction species to active sites. Tuning of the surface charge density can change the surface activity, as well as mechanism of reaction, favoring formation of specific intermediate. Different mono- and diphosphine ligands were used in the synthesis of Ru unsupported NPs⁹⁹. These ligands were expected to interact strongly with metal surface and form π - π interactions between aromatic backbone and metal atoms, and thus change the electronic state of the surface. Such particles were tested in hydrogenation of *o*-methylanisole. Ru NPs with alkyl substituted phosphines (Alk₂ArP) showed better activity (up to >99.9% of conversion) than NPs with only aryl substituted ligands (Ar₃P, conversion <12%). Since Alk₂ArP are stronger electron donor ligands than Ar₃P, more electronically rich NPs are formed when alkyl substituted phosphines are used, resulting in better catalytic activity in hydrogenation of *o*-methylanisole aromatic ring.

As we saw in the two previous parts, the activity and/or selectivity of metal NPs can be influenced by their shape and the presence of ligands on the surfaces. They can have positive effect, improving the catalytic performance, or negative, hindering the activity of samples. In practice, it may not be easy to distinguish their influence, as the shaped NPs are often covered with ligands. Therefore, it is important to precisely control the synthesis parameters to obtain catalysts of defined structural properties.

1.3. Approaching the acceptor-less alcohol dehydrogenation with shaped metal NPs

As described, many metals were tested towards acceptor-less alcohol dehydrogenation, among them Co/TiO₂ catalyst.¹⁰ It was also discussed that the type of exposed facet^{89,91} and presence of surface ligands^{95,97,98,103} can improve the activity and selectivity in a given reaction. Up to now, the use of the shaped metal nanoparticles in the acceptor-less alcohol dehydrogenation has not been reported. The potential is located in the shaped Co NPs, which can be synthesized by the polyol process, what will be described in the following paragraphs.

Synthesis of Co nanorods by polyol method was reported by Soumare et al.¹⁰⁴ In the process, cobalt carboxylate metal precursor is reduced by diol (e.g. 1,2-butanediol) which serves also as a solvent in the synthesis. It is necessary to use a nucleating agent (e.g. Ru or Ir seeds), to start the NPs nucleation, and to conduct the process in basic medium (e.g. solution containing NaOH), to solubilize the metal precursor. The formation of NPs takes place during the heating. The control of the nanoparticles shape is achieved by controlling the growth rate, which is dependent (at least) on three parameters: the nature of cobalt carboxylate, heating rate, and the basicity of the medium.

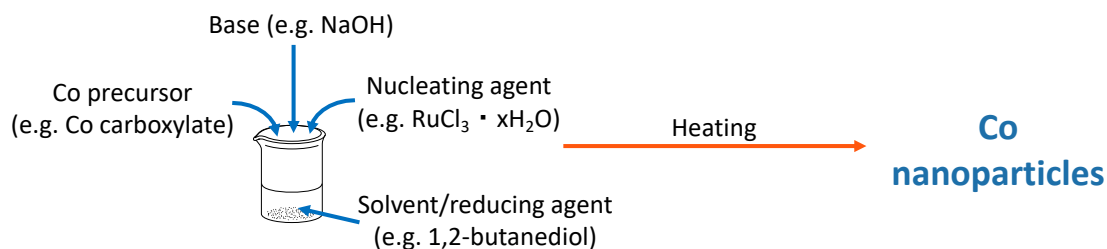


Figure 1.19. Schematic of the Co NPs by polyol method.

Synthesis of Co NPs of different shapes was possible by changing the metal precursor. When cobalt acetate was used as cobalt source, sea-urchin-like particles were obtained. Such result is attributed to the higher growth rate than nucleation rate. Nanorods were formed when Co(C_nH_{2n+1}COO)₂, where n ≥ 7, were used as metal precursors. The mean diameter was

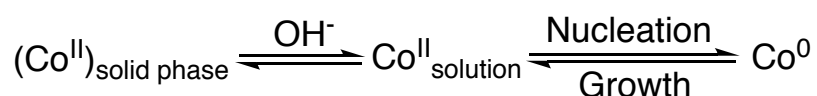
in the range of 10-30 nm and the mean length in the range of 100-250 nm, depending on the other experimental conditions. It was also observed that the mean diameter slightly increases with increasing carboxylate chain length.

Basicity of the synthesis medium was likewise important for the control of nanoparticles shape. When concentration of NaOH was in the range of 0.02-0.10 mol L⁻¹ the rods were formed. The mean diameter and mean length were decreasing with increasing the basicity. With higher NaOH concentration, e.g. 0.20 mol L⁻¹, cubic nanoparticles were formed instead of rods.

Furthermore, the heating rate also influenced the morphology of NPs. The decrease from 7 °C min⁻¹ to 3.5 °C min⁻¹ caused the increase in the mean dimension of rods. The ratio between mean length and mean diameter decreased from 10 to 4. When the ramp was below 2 °C min⁻¹ hexagonal platelets were formed instead of rods.

The synthesized rods possessed hexagonal close packed type of structure. On the other hand, hexagonal platelets crystallized in mixed hcp and fcc phases. The cubic nanoparticles were built of hcp and ε-Co phases.

The proposed mechanism of nanoparticle formation is as followed:



Cobalt precursor is solubilized in the basic reaction medium (the presence of OH⁻ ions is required). As Co^{II} species are present in the solution, the nucleation, initiated by the seeds of another metal, and growth may take place. When the growth rate was low, the formation of fcc and ε-Co phases were favored, whereas when growth rate was high hcp types structures were formed.

Synthesis of Co unsupported NPs is conducted with diol as a solvent. Atmane et al.¹⁰⁵ used 1,2-butanediol (1,2-BDO), and observed that during the formation of metal NPs, 1,2-BDO is transformed into 1-hydroxy-2-butanone. Moreover, the hydroxyketone was still generated after the formation of NPs was finished. This finding demonstrated an activity of formed NPs towards the diol dehydrogenation, and motivated the beginning of this project.

1.4. Conclusions

Acceptor-less alcohol dehydrogenation is highly interesting reaction, as from alcohol corresponding carbonyl product and gaseous H₂ are obtained exclusively. However, it has some limitations. It is not thermodynamically favored at room temperature, therefore, it has to be conducted in elevated temperature (over 100°C). Also, it requires inert atmosphere to adopt the acceptor-less mechanism. Hence, monitoring H₂ production is of high importance. However, it was not reported systematically. Better reaction performances can be achieved by removing the produced H₂ from reactor, which can be done by decreasing the pressure or constantly flowing the gases through reactor.

Many heterogenous metal catalysts have been tested for monoalcohol dehydrogenation, among which noble and non-noble metals can be found. They all occurred to be more active towards dehydrogenation of aromatic alcohols vs aliphatic alcohols. And also, they showed better activity towards secondary alcohols dehydrogenation over primary alcohols, which is conditioned by reaction thermochemistry. Among the reported metals, Co appeared to exhibit good activity and selectivity, which makes it good candidate for dehydrogenation of our targeted diols and polyalcohols. Selectivity can be an issue in these reactions. In the case of monoalcohols, the observed by-products are coming from the aldol condensation and/or esterification reactions which can be followed by hydrogenation, leading to the formation of mixture of side substances.

Not much is reported considering catalytic dehydrogenation of diols. However, secondary OH group is usually dehydrogenated preferentially over primary OH group, leading to the formation of hydroxyketone. The by-products are then resulting from sequential dehydration – hydrogenation reactions, leading to monoketone and monoalcohol formation. Removing H₂ from reactor hinders these side reactions.

To avoid trial-and-error approach in searching for active and selective catalysts, the understanding of the relation between their structural features and performance is indispensable. These relations can be established using DFT computations to determine the preferred reaction mechanism, and compare the activity of different metals. Oxophilic metals like Co and Ni are predicted to be active in the alcohol dehydrogenation, but they may be endangered by blocking of active sites by reaction intermediates. On the other hand, Au, Ag and Cu were predicted to be not active, which is not in agreement with the experimental

observations, and implies the participation of support in the reaction mechanism. Another structural factor influencing the catalytic performance is the type and amount of exposed crystallographic facet. This was illustrated on the example of styrene oxidation and benzene hydrogenation. So far, no experimental studies about the activity of shaped NPs in alcohol dehydrogenation have been reported. But as it was shown by DFT calculations with Cu, the reaction is facilitated on open type and stepped surfaces in comparison with close packed facet. This suggests structure sensitivity of the reaction. It cannot be forgotten that different ligands are used during the preparation of shaped NPs, and they remain on their surface after the synthesis. Therefore, they can influence the samples activity and/or selectivity, as it was reported in the literature for benzyl alcohol oxidation, furfural, cinnamaldehyde and methylanisole hydrogenation.

Nowadays, it is possible to obtain unsupported shape Co NPs by polyol method. This metal is reported to be active in acceptor-less alcohol dehydrogenation. Moreover, during the synthesis of these unsupported NPs, they showed some activity towards the dehydrogenation of the diol, used as the solvent in the synthesis protocol. This inspired us to investigate the activity, and structure-activity relations of shaped Co NPs in acceptor-less dehydrogenation of mono- and polyalcohols, which had not been done until now.

Bibliography

1. Mosier, N. Features of promising technologies for pretreatment of lignocellulosic biomass. *Bioresource Technology* **96**, 673–686 (2005).
2. Werpy, T. & Petersen, G. *Top Value Added Chemicals from Biomass: Volume I -- Results of Screening for Potential Candidates from Sugars and Synthesis Gas*. (2004). doi:10.2172/15008859
3. Buckley, E. & Herington, E. F. G. Equilibria in some secondary alcohol + hydrogen + ketone systems. *Transactions of the Faraday Society* **61**, 1618–1625 (1965).
4. Cubberley, A. H. & Mueller, M. B. Equilibrium studies on the dehydrogenation of primary and secondary alcohols. I. 2-butanol, 2-octanol, cyclopentanol and benzyl alcohol. *J. Am. Chem. Soc.* **68**, 1149–1151 (1946).
5. Yi, J. *et al.* A reusable unsupported rhenium nanocrystalline catalyst for acceptorless dehydrogenation of alcohols through γ -C-H activation. *Angew. Chem. Int. Edit.* **53**, 833–836 (2014).
6. Dai, Y., Wang, Y., Liu, B. & Yang, Y. Metallic nanocatalysis: an accelerating seamless integration with nanotechnology. *Small* **11**, 268–289 (2015).
7. Zhou, K. & Li, Y. Catalysis based on nanocrystals with well-defined facets. *Angew. Chem. Int. Ed.* **51**, 602–613 (2012).
8. Cuenya, B. R. Synthesis and catalytic properties of metal nanoparticles: Size, shape, support, composition, and oxidation state effects. *Thin Solid Films* **518**, 3127–3150 (2010).
9. Huang, W. & Li, W.-X. Surface and interface design for heterogeneous catalysis. *Phys. Chem. Chem. Phys.* **21**, 523–536 (2019).
10. Shimizu, K. *et al.* Heterogeneous cobalt catalysts for the acceptorless dehydrogenation of alcohols. *Green Chem.* **15**, 418–424 (2013).
11. John McMurry. *Organic chemistry*. (Cengage Learning, 2011).
12. Sheldon, R. A. & Kochi, J. K. *Metal-catalyzed oxidations of organic compounds*. (Academic Press, 1981).
13. Sheldon, R. A., Arends, I. W. C. E. & Hanefeld, U. *Green chemistry and catalysis*. (Wiley-VCH Verlag GmbH & Co. KGaA, 2007).
14. Mallat, T. & Baiker, A. Oxidation of alcohols with molecular oxygen on solid catalysts. *Chem. Rev.* **104**, 3037–3058 (2004).

15. Besson, M. & Gallezot, P. Selective oxidation of alcohols and aldehydes on metal catalysts. *Catal. Today* **57**, 127–141 (2000).
16. Zaccheria, F., Ravasio, N., Psaro, R. & Fusi, A. Synthetic scope of alcohol transfer dehydrogenation catalyzed by Cu/Al₂O₃: a new metallic catalyst with unusual selectivity. *Chem-Eur J.* **12**, 6426–6431 (2006).
17. Gerez, T., Besson, M., Pinel, C., Joerger, J.-M. & Henryon, V. Catalytic transfer dehydrogenation of geraniol to geranial over palladium and copper supported catalysts. *Top. Catal.* **57**, 1498–1504 (2014).
18. Bäckvall, J.-E. Transition metal hydrides as active intermediates in hydrogen transfer reactions. *J. Organomet. Chem.* **652**, 105–111 (2002).
19. Angelici, R. J. Hydrogen storage and energy recovery using aldehydes and ketones: a key role for catalysis. *ACS Catal.* **1**, 772–776 (2011).
20. Dalebrook, A. F., Gan, W., Grasemann, M., Moret, S. & Laurenczy, G. Hydrogen storage: beyond conventional methods. *Chem. Commun.* **49**, 8735 (2013).
21. Liu, H., Tan, H.-R., Tok, E. S., Jaenicke, S. & Chuah, G.-K. Dehydrogenation of alcohols over alumina-supported silver catalysts: the role of oxygen in hydrogen formation. *ChemCatChem* **8**, 968–975 (2016).
22. Guicheret, B. *et al.* A two-step oxidative cleavage of 1,2-diol fatty esters into acids or nitriles by a dehydrogenation-oxidative cleavage sequence. *ChemSusChem* **11**, 3431–3437 (2018).
23. Gunanathan, C. & Milstein, D. Applications of acceptorless dehydrogenation and related transformations in chemical synthesis. *Science* **341**, 1229712-1-1229712–11 (2013).
24. Werkmeister, S., Neumann, J., Junge, K. & Beller, M. Pincer-type complexes for catalytic (de)hydrogenation and transfer (de)hydrogenation reactions: recent progress. *Chem. Eur. J.* **21**, 12226–12250 (2015).
25. Filonenko, G. A., van Putten, R., Hensen, E. J. M. & Pidko, E. A. Catalytic (de)hydrogenation promoted by non-precious metals – Co, Fe and Mn: recent advances in an emerging field. *Chem. Soc. Rev.* **47**, 1459–1483 (2018).
26. Dobson, Alan. & Robinson, S. D. Complexes of the platinum metals. 7. Homogeneous ruthenium and osmium catalysts for the dehydrogenation of primary and secondary alcohols. *Inorg. Chem.* **16**, 137–142 (1977).

27. Jung, C. W. & Garrou, P. E. Dehydrogenation of alcohols and hydrogenation of aldehydes using homogeneous ruthenium catalysts. *Organometallics* **1**, 658–666 (1982).
28. Nielsen, M. *et al.* Efficient hydrogen production from alcohols under mild reaction conditions. *Angew. Chem. Int. Ed.* **50**, 9593–9597 (2011).
29. Simpson, M. C. & Cole-Hamilton, D. J. Catalytic applications of rhodium complexes containing trialkylphosphines. *Coordin. Chem. Rev.* **155**, 163–207 (1996).
30. Choi, J., MacArthur, A. H. R., Brookhart, M. & Goldman, A. S. Dehydrogenation and related reactions catalyzed by iridium pincer complexes. *Chem. Rev.* **111**, 1761–1779 (2011).
31. Moyer, S. A. & Funk, T. W. Air-stable iron catalyst for the Oppenauer-type oxidation of alcohols. *Tetrahedron Lett.* **51**, 5430–5433 (2010).
32. Zhang, G. & Hanson, S. K. Cobalt-catalyzed acceptorless alcohol dehydrogenation: synthesis of imines from alcohols and amines. *Org. Lett.* **15**, 650–653 (2013).
33. Zhang, G., Vasudevan, K. V., Scott, B. L. & Hanson, S. K. Understanding the mechanisms of cobalt-catalyzed hydrogenation and dehydrogenation reactions. *J. Am. Chem. Soc.* **135**, 8668–8681 (2013).
34. Kon, K., Hakim Siddiki, S. M. A. & Shimizu, K. Size- and support-dependent Pt nanocluster catalysis for oxidant-free dehydrogenation of alcohols. *J. Catal.* **304**, 63–71 (2013).
35. Karvembu, R. & Priyarega, S. Ru/ γ -Al₂O₃ as reusable catalyst for dehydrogenation of alcohols without hydrogen acceptor. *React. Kinet. Catal. Lett.* **88**, 333–338 (2006).
36. Kim, W.-H., Park, I. S. & Park, J. Acceptor-free alcohol dehydrogenation by recyclable ruthenium catalyst. *Org. Lett.* **8**, 2543–2545 (2006).
37. Kon, K., Onodera, W., Toyao, T. & Shimizu, K. Supported rhenium nanoparticle catalysts for acceptorless dehydrogenation of alcohols: structure–activity relationship and mechanistic studies. *Catal. Sci. Technol.* **6**, 5864–5870 (2016).
38. Sawama, Y. *et al.* Rhodium-on-carbon catalyzed hydrogen scavenger- and oxidant-free dehydrogenation of alcohols in aqueous media. *Green Chemistry* **16**, 3439 (2014).
39. Fang, W., Zhang, Q., Chen, J., Deng, W. & Wang, Y. Gold nanoparticles on hydrotalcites as efficient catalysts for oxidant-free dehydrogenation of alcohols. *Chem. Commun.* **46**, 1547–1549 (2010).
40. Fang, W., Chen, J., Zhang, Q., Deng, W. & Wang, Y. Hydrotalcite-supported gold catalyst for the oxidant-free dehydrogenation of benzyl alcohol: studies on support and gold size effects. *Chem-Eur J.* **17**, 1247–1256 (2011).

41. Chen, J., Fang, W., Zhang, Q., Deng, W. & Wang, Y. A comparative study of size effects in the Au-catalyzed oxidative and non-oxidative dehydrogenation of benzyl alcohol. *Chem. Asian J.* **9**, 2187–2196 (2014).
42. Mitsudome, T. *et al.* Oxidant-free alcohol dehydrogenation using a reusable hydrotalcite-supported silver nanoparticle catalyst. *Angew. Chem. Int. Edit.* **47**, 138–141 (2008).
43. Shimizu, K. & Satsuma, A. Silver cluster catalysts for green organic synthesis. *J. Jpn. Petrol. Inst.* **54**, 347–360 (2011).
44. Bayat, A., Shakourian-Fard, M., Ehyaei, N. & Mahmoodi Hashemi, M. Silver nanoparticles supported on silica-coated ferrite as magnetic and reusable catalysts for oxidant-free alcohol dehydrogenation. *RSC Advances* **5**, 22503–22509 (2015).
45. Shimizu, K., Sugino, K., Sawabe, K. & Satsuma, A. Oxidant-free dehydrogenation of alcohols heterogeneously catalyzed by cooperation of silver clusters and acid-base sites on alumina. *Chem-Eur J.* **15**, 2341–2351 (2009).
46. Conesa, J. M., Morales, M. V., López-Olmos, C., Rodríguez-Ramos, I. & Guerrero-Ruiz, A. Comparative study of Cu, Ag and Ag-Cu catalysts over graphite in the ethanol dehydrogenation reaction: Catalytic activity, deactivation and regeneration. *Appl. Catal. A-Gen.* **576**, 54–64 (2019).
47. Mitsudome, T. *et al.* Copper nanoparticles on hydrotalcite as a heterogeneous catalyst for oxidant-free dehydrogenation of alcohols. *Chem. Commun.* 4804–4806 (2008). doi:10.1039/b809012b
48. Damodara, D., Arundhathi, R. & Likhar, P. R. Copper nanoparticles from copper aluminum hydrotalcite: an efficient catalyst for acceptor- and oxidant-free dehydrogenation of amines and alcohols. *Adv. Synth. Catal.* **356**, 189–198 (2014).
49. Zhu, Y., Shen, M., Xia, Y. & Lu, M. Copper nanoparticles on dichromium trioxide: a highly efficient catalyst from copper chromium hydrotalcite for oxidant-free dehydrogenation of alcohols: Nano-copper particles from hydrotalcite for alcohol dehydrogenation. *Appl. Organomet. Chem.* **29**, 152–156 (2015).
50. Shimizu, K., Kon, K., Shimura, K. & Hakim, S. S. M. A. Acceptor-free dehydrogenation of secondary alcohols by heterogeneous cooperative catalysis between Ni nanoparticles and acid–base sites of alumina supports. *J. Catal.* **300**, 242–250 (2013).
51. Chen, H. *et al.* Promoted synergic catalysis between metal Ni and acid–base sites toward oxidant-free dehydrogenation of alcohols. *ACS Catal.* **7**, 2735–2743 (2017).

52. Li, Z., Chen, C., Zhan, E., Ta, N. & Shen, W. Mo₂N nanobelts for dehydrogenation of aromatic alcohols. *Catal. Commun.* **51**, 58–62 (2014).
53. Leng, Y. *et al.* N-Doped carbon encapsulated molybdenum carbide as an efficient catalyst for oxidant-free dehydrogenation of alcohols. *J. Mater. Chem. A* **5**, 17580–17588 (2017).
54. Weast, R. C. *Handbook of chemistry and physics*. (RCS Press Inc., 1974).
55. Vu, N. D., Guicheret, B., Duguet, N., Méta y, E. & Lemaire, M. Homogeneous and heterogeneous catalytic (dehydrogenative) oxidation of oleochemical 1,2-diols to α -hydroxyketones. *Green Chem.* **19**, 3390–3399 (2017).
56. Sato, H., Tamura, M., Nakagawa, Y. & Tomishige, K. Synthesis of α -hydroxy ketones from vicinal diols by selective dehydrogenation over Ir–ReO_x/SiO₂ catalyst. *Chem. Lett.* **43**, 334–336 (2014).
57. Tamura, M., Arai, T., Nakagawa, Y. & Tomishige, K. Transformation of diols to ketones via intramolecular borrowing hydrogen mechanism. *Chem. Lett.* **46**, 1333–1336 (2017).
58. Sad, M. E., Neurock, M. & Iglesia, E. Formation of C–C and C–O bonds and oxygen removal in reactions of alkanediols, alkanols, and alkanals on copper catalysts. *J. Am. Chem. Soc.* **133**, 20384–20398 (2011).
59. Neurock, M., Tao, Z., Chemburkar, A., Hibbitts, D. D. & Iglesia, E. Theoretical insights into the sites and mechanisms for base catalyzed esterification and aldol condensation reactions over Cu. *Faraday Discussions* **197**, 59–86 (2017).
60. Corma, A., Navas, J. & Sabater, M. J. Advances in one-pot synthesis through borrowing hydrogen catalysis. *Chem. Rev.* **118**, 1410–1459 (2018).
61. Hamid, M. H. S. A., Slatford, P. A. & Williams, J. M. J. Borrowing hydrogen in the activation of alcohols. *Adv. Synth. Catal.* **349**, 1555–1575 (2007).
62. Onyestyák, Gy. *et al.* Acetone alkylation with ethanol over multifunctional catalysts by a borrowing hydrogen strategy. *RSC Advances* **5**, 99502–99509 (2015).
63. Yamada, Y. M. A. & Uozumi, Y. Development of a convoluted polymeric nanopalladium catalyst: α -alkylation of ketones and ring-opening alkylation of cyclic 1,3-diketones with primary alcohols. *Tetrahedron* **63**, 8492–8498 (2007).
64. Cho, C. S., Ren, W. X. & Shim, S. C. Pd/C-Catalyzed oxidative alkylation of secondary alcohols with primary alcohols. *Bull. Korean Chem. Soc.* **26**, 1611–1613 (2005).
65. Carlini, C. *et al.* Selective synthesis of isobutanol by means of the Guerbet reaction. *J. Mol. Cat. A-Chem.* **206**, 409–418 (2003).

66. Moromi, S. K., Hakim Siddiki, S. M. A., Ali, Md. A., Kon, K. & Shimizu, K. Acceptorless dehydrogenative coupling of primary alcohols to esters by heterogeneous Pt catalysts. *Catal. Sci. Technol.* **4**, 3631–3635 (2014).
67. Miura, H., Nakahara, K., Kitajima, T. & Shishido, T. Concerted functions of surface acid–base pairs and supported copper catalysts for dehydrogenative synthesis of esters from primary alcohols. *ACS Omega* **2**, 6167–6173 (2017).
68. Loffreda, D., Michel, C., Delbecq, F. & Sautet, P. Tuning catalytic reactivity on metal surfaces: Insights from DFT. *J. Catal.* **308**, 374–385 (2013).
69. Syu, C.-Y., Yang, H.-W., Hsu, F.-H. & Wang, J.-H. The chemical origin and catalytic activity of coinage metals: from oxidation to dehydrogenation. *Phys. Chem. Chem. Phys.* **16**, 7481–7490 (2014).
70. García-Muelas, R., Li, Q. & López, N. Density Functional Theory comparison of methanol decomposition and reverse reactions on metal surfaces. *ACS Catal.* **5**, 1027–1036 (2015).
71. Wang, H.-F. & Liu, Z.-P. Selectivity of direct ethanol fuel cell dictated by a unique partial oxidation channel. *J. Phys. Chem. C* **111**, 12157–12160 (2007).
72. Wang, E. D., Xu, J. B. & Zhao, T. S. Density Functional Theory studies of the structure sensitivity of ethanol oxidation on palladium surfaces. *J. Phys. Chem. C* **114**, 10489–10497 (2010).
73. Caglar, B., Olus Ozbek, M., Niemantsverdriet, J. W. (Hans) & Weststrate, C. J. (Kees-J. The effect of C–OH functionality on the surface chemistry of biomass-derived molecules: ethanol chemistry on Rh(100). *Phys. Chem. Chem. Phys.* **18**, 30117–30127 (2016).
74. Michel, C., Auneau, F., Delbecq, F. & Sautet, P. C–H versus O–H bond dissociation for alcohols on a Rh(111) surface: a strong assistance from hydrogen bonded neighbors. *ACS Catal.* **1**, 1430–1440 (2011).
75. Hoyt, R. A., Montemore, M. M., Sykes, E. C. H. & Kaxiras, E. Anhydrous methanol and ethanol dehydrogenation at Cu(111) step edges. *J. Phys. Chem. C* **122**, 21952–21962 (2018).
76. Ma, Y., Hernández, L., Guadarrama-Pérez, C. & Balbuena, P. B. Ethanol reforming on Co(0001) surfaces: a Density Functional Theory study. *J. Phys. Chem. A* **116**, 1409–1416 (2012).
77. Medford, A. J. *et al.* From the Sabatier principle to a predictive theory of transition-metal heterogeneous catalysis. *J. Catal.* **328**, 36–42 (2015).

78. Kozuch, S. & Martin, J. M. L. The rate-determining step is dead. Long live the rate-determining state! *ChemPhysChem* **12**, 1413–1418 (2011).
79. Kozuch, S. Steady state kinetics of any catalytic network: graph theory, the energy span model, the analogy between catalysis and electrical circuits, and the meaning of “mechanism”. *ACS Catal.* **5**, 5242–5255 (2015).
80. Kepp, K. P. A quantitative scale of oxophilicity and thiophilicity. *Inorg. Chem.* **55**, 9461–9470 (2016).
81. Lopez, N. On the origin of the catalytic activity of gold nanoparticles for low-temperature CO oxidation. *J. Catal.* **223**, 232–235 (2004).
82. Overbury, S., Schwartz, V., Mullins, D., Yan, W. & Dai, S. Evaluation of the Au size effect: CO oxidation catalyzed by Au/TiO₂. *J. Catal.* **241**, 56–65 (2006).
83. Lyalin, A., Shimizu, K. & Taketsugu, T. Interface effects in hydrogen elimination reaction from isopropanol by Ni₁₃ cluster on θ -Al₂O₃ (010) surface. *J. Phys. Chem. C* **121**, 3488–3495 (2017).
84. Lee, A. F., Gawthorpe, D. E., Hart, N. J. & Wilson, K. A fast XPS study of the surface chemistry of ethanol over Pt{111}. *Surface Science* **548**, 200–208 (2004).
85. Rodríguez de la Fuente, O., Borasio, M., Galletto, P., Rupprechter, G. & Freund, H.-J. The influence of surface defects on methanol decomposition on Pd(111) studied by XPS and PM-IRAS. *Surface Science* **566–568**, 740–745 (2004).
86. Shorthouse, L. J., Roberts, A. J. & Raval, R. Propan-2-ol on Ni(111): identification of surface intermediates and reaction products. *Surface Science* **480**, 37–46 (2001).
87. Shekhar, R. & Barteau, M. A. Structure sensitivity of alcohol reactions on (110) and (111) palladium surfaces. *Catal Lett* **31**, 221–237 (1995).
88. Doyle, A. M., Shaikhutdinov, S. K., Jackson, S. D. & Freund, H.-J. Hydrogenation on metal surfaces: why are nanoparticles more active than single crystals? *Angew. Chem. Int. Ed.* **42**, 5240–5243 (2003).
89. Xu, R., Wang, D., Zhang, J. & Li, Y. Shape-dependent catalytic activity of silver nanoparticles for the oxidation of styrene. *Chem. Asian J.* **1**, 888–893 (2006).
90. Sun, Y. & Xia, Y. Shape-controlled synthesis of gold and silver nanoparticles. *Science* **298**, 2176–2179 (2002).
91. Bratlie, K. M., Lee, H., Komvopoulos, K., Yang, P. & Somorjai, G. A. Platinum nanoparticle shape effects on benzene hydrogenation selectivity. *Nano Lett.* **7**, 3097–3101 (2007).

92. He, X. *et al.* Controllable in situ surface restructuring of Cu catalysts and remarkable enhancement of their catalytic activity. *ACS Catal.* **9**, 2213–2221 (2019).
93. Hu, J., Chen, Z., Li, M., Zhou, X. & Lu, H. Amine-capped Co nanoparticles for highly efficient dehydrogenation of ammonia borane. *ACS Appl. Mater. Interfaces* **6**, 13191–13200 (2014).
94. Vu, K. B., Bukhryakov, K. V., Anjum, D. H. & Rodionov, V. O. Surface-bound ligands modulate chemoselectivity and activity of a bimetallic nanoparticle catalyst. *ACS Catal.* **5**, 2529–2533 (2015).
95. Jin, L., Liu, B., Duay, S. & He, J. Engineering surface ligands of noble metal nanocatalysts in tuning the product selectivity. *Catalysts* **7**, 44 (2017).
96. Pang, S. H., Schoenbaum, C. A., Schwartz, D. K. & Medlin, J. W. Directing reaction pathways by catalyst active-site selection using self-assembled monolayers. *Nat. Commun.* **4**, 1–6 (2013).
97. Kahsar, K. R., Schwartz, D. K. & Medlin, J. W. Control of metal catalyst selectivity through specific noncovalent molecular interactions. *J. Am. Chem. Soc.* **136**, 520–526 (2014).
98. Yoskamtorn, T. *et al.* Thiolate-mediated selectivity control in aerobic alcohol oxidation by porous carbon-supported Au₂₅ clusters. *ACS Catal.* **4**, 3696–3700 (2014).
99. González-Gálvez, D., Nolis, P., Philippot, K., Chaudret, B. & van Leeuwen, P. W. N. M. Phosphine-stabilized ruthenium nanoparticles: the effect of the nature of the ligand in catalysis. *ACS Catal.* **2**, 317–321 (2012).
100. Martínez-Prieto, L. M. & Chaudret, B. Organometallic ruthenium nanoparticles: synthesis, surface chemistry, and insights into ligand coordination. *Acc. Chem. Res.* **51**, 376–384 (2018).
101. Amiens, C., Ciuculescu-Pradines, D. & Philippot, K. Controlled metal nanostructures: Fertile ground for coordination chemists. *Coordin. Chem. Rev.* **308**, 409–432 (2016).
102. Liakakos, N. *et al.* The big impact of a small detail: cobalt nanocrystal polymorphism as a result of precursor addition rate during stock solution preparation. *J. Am. Chem. Soc.* **134**, 17922–17931 (2012).
103. Schoenbaum, C. A., Schwartz, D. K. & Medlin, J. W. Controlling the surface environment of heterogeneous catalysts using self-assembled monolayers. *Accounts Chem. Res.* **47**, 1438–1445 (2014).
104. Soumare, Y. *et al.* Kinetically controlled synthesis of hexagonally close-packed cobalt nanorods with high magnetic coercivity. *Adv. Funct. Mater.* **19**, 1971–1977 (2009).

105. Atmane, K. A. *et al.* Control of the anisotropic shape of cobalt nanorods in the liquid phase: from experiment to theory... and back. *Nanoscale* **6**, 2682–2692 (2014).

Chapter 2

Experimental part

2.1. List of products used

Compound	Systematic name	Supplier	Purity
Co(NO₃)₂ · 6H₂O	cobalt nitrate hexahydrate	Aldrich	99%
CoCl₂ · 6H₂O	cobalt chloride hexahydrate	Aldrich	98%
Ti[O(CH₂)₃CH₃]₄	titanium isopropoxide	Aldrich	98%
(±)-2-octanol	2-octanol	Alfa Aesar	98%
1-octanol	1-octanol	Alfa Aesar	99%
1,2-octanediol	1,2-octanediol	Aldrich	98%
1,2-butanediol	1,2-butanediol	Fluka	≥98%
1,3-butanediol	1,3-butanediol	Aldrich	99%
2-octanone	2-octanone	Aldrich	≥99.5%
octanal	octanal	Alfa Aesar	98%
1-hydroxy-2-butanone	1-hydroxy-2-butanone	Aldrich	n.g.
n-decane	n-decane	Carl Roth	≥99%
diisopentyl ether	diisopentyle ether	Alfa Aesar	96%
o-xylene	o-xylene	Alfa Aesar	99%
GVL	γ-valerolactone	Aldrich	99%
DMSO	dimethyl sulfoxide	Acros Organics	99.7%

n.g. – not given

2.2. Synthesis protocols

2.2.1. Synthesis of catalysts by wet impregnation method

All cobalt supported catalysts were synthesized by wet impregnation method. Either Co(NO₃)₂ · 6H₂O or CoCl₂ · 6H₂O were used as precursors. Different materials were used as supports: TiO₂ P25 (62 m² g⁻¹, Degussa), TiO₂ P90 (122 m² g⁻¹, Evonik), TiO₂ DT51D (85 m² g⁻¹, Millenium Chemicals), TiO₂ SGNH (117 m² g⁻¹, obtained thanks to the kindness of H.Mutin, J.Alauzun and M.Bouchneb from Institut Charles Gerhardt Montpellier; oxide synthesized by non-hydrolytic sol-gel method), TiO₂ “home made” (121 m² g⁻¹, synthesized by sol-gel method), ZrO₂ (137 m² g⁻¹, MEL Chemicals), C (1095 m² g⁻¹, size 40-80 μm, CECA ARKEMA),

γ -Al₂O₃ (119 m² g⁻¹, Degussa), ZnO (16 m² g⁻¹, Alfa Aesar). All the catalysts contained 5 wt% of metal.

Typically, 4.75 g of support and 28.28 mL of precursor solution (0.15 mol L⁻¹) and ultra-pure water (75 mL) were put into a flask and stirred for 2 h (600 rpm, room temperature). The solution was then evaporated with rotary evaporator for 4 h (120 rpm, 50°C H₂O, p ~ 0.05-0.06 atm). To remove the remaining moisture, the catalyst was dried overnight at 80°C, under N₂ flow. The obtained solid was crushed in order to homogenize it as a powder. The sample was subsequently calcined (air, 40 mL min⁻¹, 1 °C min⁻¹, 300°C, 1 h), reduced (H₂, 40 mL min⁻¹, 1 °C min⁻¹, 400°C, 0.5 h) and passivated (1% v/v O₂/N₂, 50 mL min⁻¹, room temperature, 0.5 h). For Co/C the calcination step was omitted.

2.2.2. Synthesis of TiO₂ “home made”

TiO₂ “home made” was synthesized by low temperature sol-gel method,¹ the procedure reported for the synthesis of high surface area TiO₂ rutile. At first titanium isopropoxide (37.1 mL) was hydrolyzed by aqueous solution of HCl (2 mol L⁻¹; 62.5 mL), under vigorous stirring, and then aged for 48 h at room temperature. Subsequently, polyethyleneglycol (used as porogen) was added to the solution, under vigorous stirring. The resulting mixture was evaporated with rotary evaporator (120 rpm, 30°C, p ~ 0.08 atm, 1.5 h → 120 rpm, 50°C, p ~ 0.06 atm, 1.5 h → 120 rpm, 70°C, p ~ 0.05 atm, 1.5 h), dried for 24 h under air in 110°C, and calcined under air flow at 400°C, for 2 h, with heating rate 2 °C min⁻¹. Such obtained support possessed specific surface area of 121 m² g⁻¹.

2.2.3. Synthesis of unsupported catalysts

The unsupported shaped nanoparticles were synthesized by our project partners from LPCNO in Toulouse and ITODYS in Paris, using adapted polyol method.² It consisted in reacting a cobalt (II) carboxylate compound in a basic polyol (NaOH in 1,2-propanediol or 1,2-butanediol) using RuCl₃ as a seeding agent, at 175°C. During the heating, the reduction of Co(II) into Co⁰ took place what was signalized by the change of solution color into black. The formed NPs were recovered from the solution, washed 3 times with EtOH and subsequently dried. The morphologies and mean dimensions of the particles can be varied depending on several

reaction parameters such as the nature of the polyol, the nature of the Co(II) carboxylate, its drying procedure and the concentration of the long-chain carboxylate. In such way rods, diabolos and platelets were prepared. The samples are named according to the role: type of ligand – shape – order number (if necessary), where the type of ligand corresponds to the nature of the carboxylate (L – laurate, C12, P – palmitate, C16, H – heptanoate, C7, O – octanoate, C8, D – decanoate, C10) and the shape corresponds to either rods (R), diabolos (D) or platelets (P). The synthesis details of cobalt precursors and samples are gathered in the Annex, in part A.2.1.

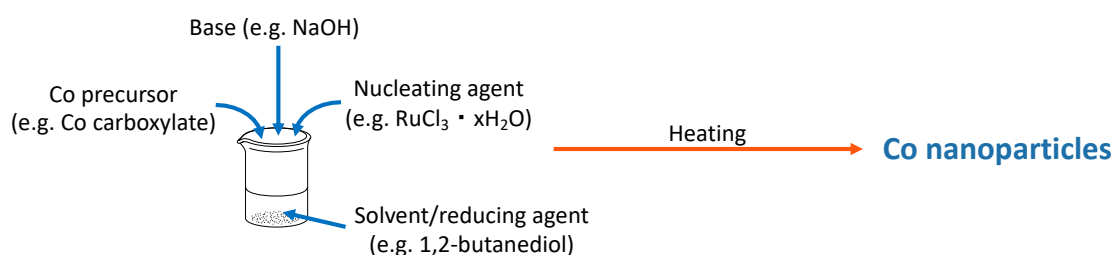


Figure 2.1. Schematic illustration of polyol synthesis method

2.3. Characterization techniques

2.3.1. Elemental analysis by ICP-OES

Inductively coupled plasma optical emission spectroscopy (ICP-OES) is an analytic technique allowing for the quantitative measurement of inorganic atoms or ions in solid and liquid samples. When the elements are placed in plasma stream, they gain energy and jump into an excited state. Then, when their electrons go back to ground state, they emit energy of characteristic wavelength, which is measured. The position of photon rays allows to identify elements and the intensity of rays allows to quantify their content.

ICP-OES analysis was used to evaluate the final Co content in supported catalysts and to verify the metal leaching during the reaction. The catalysts were analyzed after reduction and passivation. And the examined reaction solutions were the ones collected at the end of reaction. The materials were digested in a mixture of H₂SO₄, HNO₃ and HF and heated

in the temperature of 250-300°C. The analysis was performed with an “Activa” Jobin Yvon apparatus, for which the detection limit is equal to 0.2 mg L⁻¹.

2.3.2. Specific surface area measurement

Specific surface area (SSA) is a feature of a substance, dependent on type of material, size of particles and their porosity. BET (Brunauer-Emmett-Teller) theory³ is most commonly used to measure SSA and porosity of substances. The measurements are conducted with a gas, which is chemically inert for the investigated material (usually N₂), at the boiling temperature of this given gas (for N₂ -196°C).

The linear form of the BET isotherm equation is used to analyze the results collected during the measurements.

$$\frac{\frac{p}{p_0}}{V_a(p_0-p)} = \frac{1}{V_a C} + \frac{(C-1) p}{V_m C p_0}$$

p – equilibrium pressure

p_0 – saturation pressure

V_a – adsorbed gas quantity (e.g. in volume)

V_m – monolayer adsorbed gas quantity

C – BET constant

Knowing the volume of gas adsorbed in the first monolayer, at a given temperature, we know its amount (n_{gas}). With this, it is possible to estimate the surface of the investigated material, by multiplying n_{gas} with the surface occupied by one molecule of gas.

The measurements of specific surface area for supports, supported catalysts and some unsupported Co samples were conducted with ASAP 2020 apparatus. N₂ was used as adsorbing gas, and the analysis were conducted at -196°C. Before the analysis, the supports and supported catalysts were desorbed for 3 h at 250°C (heating rate 4 °C min⁻¹) under high vacuum ($p < 1.5 \cdot 10^{-5}$ atm). Whereas unsupported catalysts were desorbed for 12 h at 120°C (heating rate 5 °C min⁻¹), also under high vacuum ($p < 1.5 \cdot 10^{-5}$ atm). The SSA measured in N₂ physisorption experiment is marked as SSA_{BET}.

2.3.3. X-ray diffraction

X-ray diffraction is a non-destructive analytical technique, providing information on crystallography and composition of a solid sample. It is based on the observation of diffraction patterns coming from X-ray beam scattered by sample.

When monochromatic X-ray beam hits the surface of crystalline sample (sample with regular structure), the scattered rays undergo constructive and destructive interferences, called diffraction. Size and shape of the unit cell of the material determine the directions of diffraction. The kind and arrangements of atoms in crystal structure influence the intensity of diffraction waves. Usually powders are composed of many tiny crystallites, oriented in all possible directions. When such powder is placed in the beam of X-rays, the beam will detect all of the crystal planes. By changing the experimental angle systematically all the possible diffraction signals will be noticed.

The XRD measurements are performed with diffractometers. X-rays are generated by a cathode ray tube, filtered to produce monochromatic beam. After concentration, the rays are directed toward the sample, placed in a goniometer (allowing the rotation of the sample). They undergo diffraction and are then detected, processed and counted.

The particle size can be calculated with Scherrer equation, which correlates it with the broadening of the signal from a given element, visible on the diffraction pattern. It can be written as:

$$\tau = \frac{K\lambda}{\beta \cos\theta}$$

where:

τ – mean size of metal nanoparticle

K – shape factor, which value is close to 0.89

λ – X-ray wavelength

β – line broadening at half of the maximum intensity of signal

θ – Bragg angle

Powder XRD patterns were registered with BRUKER Advance D8A25 equipment. Copper tube was used as a source of X-rays ($\lambda_{K\alpha} = 1.54184 \text{ \AA}$) and nickel filter was used to eliminate $K\beta$ lines of the radiation. Multi-channel fast detector LynxEye (192 channels, active length 2.947°) was used to register the diffraction signals. For the samples containing cobalt scans were

performed in the angle range $15^\circ < 2\theta < 86^\circ$, and for the supports, scans were performed in the range of angles $15^\circ < 2\theta < 90^\circ$. When it was possible the Scherrer equation was used to calculate the crystallite size.

2.3.4. Thermogravimetric analysis

Thermogravimetric analysis (TGA) is a thermal analysis in which the change of the sample mass is recorded in function of time and temperature. Temperature during the measurement can be kept fixed or can be increased with a given heating rate. The changes of mass can occur due to desorption, absorption, sublimation, vaporization, oxidation, reduction and decomposition of the sample.

TGA analysis can be conducted under the atmosphere of:

- inert gases, for which thermal decomposition of sample is observed (TGA-N₂ or TGA-Ar)
- air – oxidative conditions, change of mass is due to sample oxidation (TGA-air)
- H₂ – reductive conditions, change of mass results from the reduction of the sample (TGA-H₂)

The equipment is composed of: furnace, high-precision balance, temperature programmer and recorder. It can be also coupled with mass spectrometer (MS), what allows to analyze and identify the evolved gases.

TGA-N₂ measurements were performed with Mettler Toledo Thermobalance MX1 equipment. For each measurement 5-15 mg of samples were placed in a 70 μ L alumina crucible. The flow of gas (N₂) was equal to 50 mL min⁻¹. Analysis was performed in the temperature range of 20-1000°C, with heating rate 10 °C min⁻¹.

TGA-H₂ analysis was conducted with Setaram Setsys Evolution 12 apparatus, coupled with Pfeiffer Omnistar mass spectrometer. For each measurement 20-40 mg of sample was placed in 100 μ L platinum crucible. All the measurements were conducted under the flow of the mixture of 5% H₂ and 95% of Ar, with total flow of 50 mL min⁻¹, in the temperature range of 25-600°C. Mass spectra were collected during the analysis for $m/z = 2$ (signal from H₂), 14 (N⁺), 15 (NH⁺ or CH₃⁺), 16 (NH₂⁺ or CH₄⁺), 17 (OH⁺), 18 (H₂O⁺), 28 (N₂²⁺), 30 (CH₃NH₂⁺ or NO⁺), 32 (N₂H₄⁺), 44 (NO₂).

2.3.5. Transmission Electron Microscopy

Transmission Electron Microscopy (TEM) is an analytical technique allowing to study the crystallographic structure and features of a solid sample. Crystal structure, defects, grain boundaries, as well as chemical composition, can be investigated with it.

Three main parts of the apparatus can be distinguished. The first part consists of an electron gun, which is responsible for producing the highly energetic electron beam, and a condenser system, which focuses the beam onto the sample. Second part of the apparatus is an image-producing system. It consists of objective lenses and projector lenses; the later ones focus the electrons which passed through the sample. The third part of microscope is an image-recording system. It converts the electron beam into an image recognizable for human eye. Usually it consists of a fluorescent screen, for focusing the image, and a digital camera, for permanent registration. Additionally, the system of vacuum pumps and power supplier are necessary to make the measurement possible.

The TEM measurements for supported Co catalysts were performed with JEOL 2010 apparatus, operating at an acceleration voltage of 200 kV, and equipped with an EDX (energy dispersive spectroscopy) system, allowing for the chemical analysis of a sample.

For the unsupported samples, the analysis was performed with Jeol JEM-2010 transmission electron microscope equipped with a LaB₆ filament and operating at 200 kV. The images were collected with a 4008 × 2672 pixels CCD camera (Gatan Orius SC1000). All samples were prepared by evaporating a drop of diluted suspension in ethanol on a carbon-coated copper grid. The mean particle sizes were determined by a statistical analysis of at least 200 particles. And the specific surface areas (SSA_C) and proportions between different surfaces exposed by Co in the samples were calculated using the mean dimensions found by TEM and assuming simple geometrical models, as explained in the part A.2.2. in Annex.

2.3.6. Surface coverage with ligands for unsupported Co particles

For a given unsupported catalyst sample, the surface coverage with organic ligands was evaluated as the ratio between the amount of ligands (in mol) per a given mass, as quantified by TGA-N₂, and the surface exposed by metallic Co (in m²), for the same mass of sample, as derived from the TEM images analysis.

$$\text{Surface coverage} = \frac{n_{\text{ligands}}}{SA}$$
$$n_{\text{ligands}} = \frac{\frac{\Delta m_{\text{TGA-N}_2}}{100} \times m_{\text{sample}}}{M_{\text{ligands}}}$$
$$SA = SSA_C \times \left(\frac{(100 - \Delta m_{\text{TGA-N}_2})}{100} \times m_{\text{sample}} \right)$$

The establish accuracy of it is equal to 2.5·10⁻⁶ mol m⁻². For the example see Annex, part A.2.3.

2.3.7. X-ray Photoelectron Spectroscopy

X-ray Photoelectron Spectroscopy (XPS) is a surface analysis technique which reveals the relative composition of a sample in the surface region, usually in the depth up to 5 nm. The apparatus operates under ultra-high vacuum. The surface of a sample is excited with mono-energetic X-ray beam, which in return causes the emission of photoelectrons from the sample. Their energy is measured by energy analyzer. Based on the binding energy and the intensity of the peaks it is possible to identify the chemical states of the element and their distribution.

The analysis was performed with AXIS Ultra DLD KRATOS instrument. X-ray beam was coming from monochromatized Al K source (hν = 1486.6 eV).

2.4. Catalytic tests

2.4.1. Reaction equipment and catalytic tests conditions

The reactor consists of (Figure 2.2):

- flow-meters regulating the flow of gases through the reactor (Bronkhorst High-Tech EL-FLOW Select mass flow meters for N₂, Ar and H₂),
- semi-batch glass reactor (100 mL),
- mechanical stirring system,
- gases tight agitation turret (PFA material),
- vapor condenser,
- heater and oil bath,
- gas chromatograph coupled with the outlet of gases.

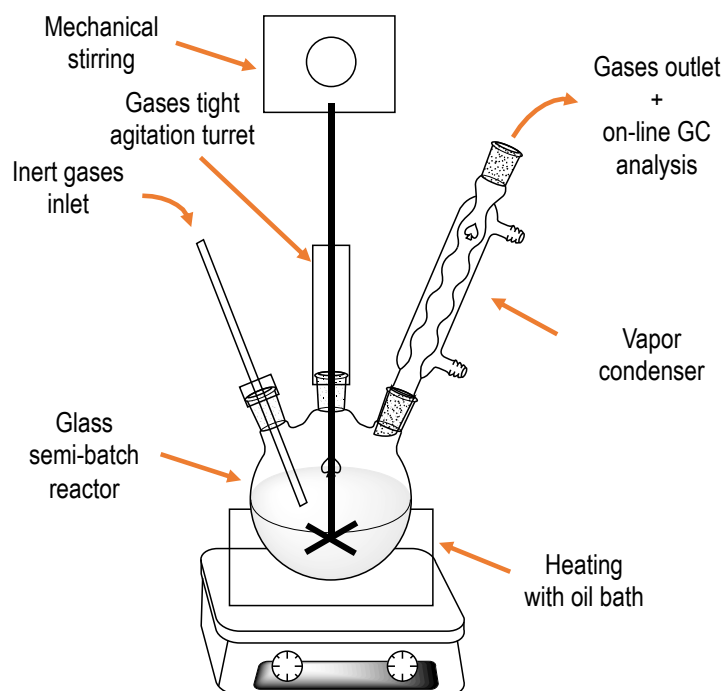


Figure 2.2. Schematic of semi-batch glass reactor

The catalytic tests of alcohol dehydrogenation were conducted for 24 h at 145°C. 25 mg of unsupported cobalt catalysts or 500 mg of supported cobalt catalysts were used in the reactions, aiming to have 1 mol% of cobalt towards alcohol. The total volume of reaction

solution was equal to 45 mL and the alcohol concentration was equal to 0.95 mol L⁻¹. As primary alcohol 1-octanol was used, as secondary alcohol 2-octanol was used and as diol 1,2-octanediol was used. For most reactions n-decane served as a solvent. Typically, a given mass of catalyst and 30 mL of solvent were placed in the reactor. The equipment was connected and the mixture was heated. When it reached the desired reaction temperature, the mixture of an alcohol (appropriate volume, e.g. 6.746 mL of 2-octanol) and remaining solvent (e.g. 8.254 mL) were added through the septum. Since that moment the reaction was considered as started. The flow of inert gases, being a mixture of 10% N₂ and 90% Ar, was constant and equal to 30 mL min⁻¹. Mechanical stirring was performed with a speed of 750 rpm.

The reaction products were analyzed in two ways: by on-line GC analysis of reaction gases mixture (inert gases inserted into the reactor and produced H₂) and by the analysis of liquid aliquots collected periodically during the course of an experiment. The outlet of gases from the reactor was coupled with gas chromatograph (Shimadzu GC-2010, Supelco Carboxen-1010 PLOT column; thermal program: isotherm, 50°C, Ar used as a carrier gas, TCD detector). The signal from H₂ appeared at retention time of 2.5 min after the injection, whereas the signal from N₂ (internal standard) appeared at retention time of 3.0 min after the injection. The H₂ quantification was based on the ratio between integrations of H₂ and N₂ signals and the performed calibration, for which both gases were considered as perfect gases. Thanks to the H₂ flow-meter (coupled with reactor) it was possible to precisely regulate its flow rate (and by this amount - in mol - entering the reactor per minute). The calibration was performed by flowing the mixture of inert gases (3 mL min⁻¹ N₂ and 27 mL min⁻¹ Ar) and H₂ (given volume per min) through reactor containing 45 mL of decane and heated up to 145°C, to resemble as much as possible the reaction conditions. The measurements were done for 9 different flows of H₂, at least 3 times for each of them. The correlation line was obtained by relating the ratio between %H₂ and %N₂ in the mixture of gases with the ratio of H₂ and N₂ signals integrations and is presented on Figure 2.3. The measurement data are collected in Table 2.1.

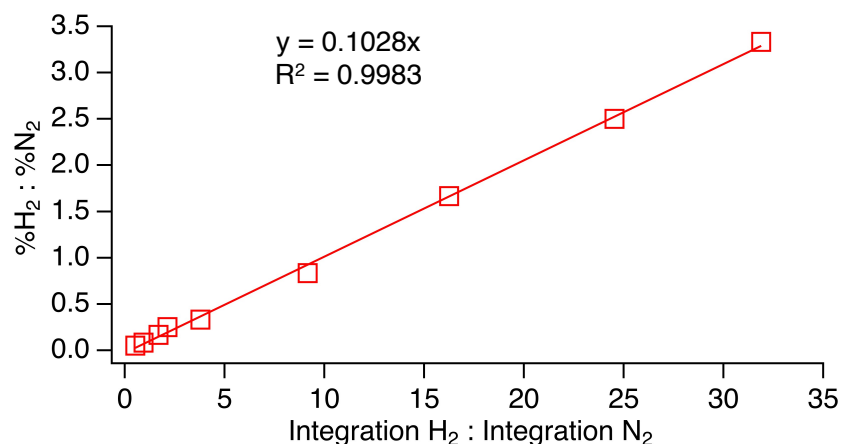


Figure 2.3. H₂ calibration graph.

Table 2.1. Measurement data for H₂ calibration line.

H ₂ flow rate (mL min ⁻¹)	H ₂ integration (a.u.)	N ₂ integration (a.u.)	Integration H ₂ : Integration N ₂	%H ₂ : %N ₂
10.00	1382330	43347	31.89	3.33
7.50	1134145	46213	24.54	2.50
5.00	808562	49776	16.24	1.67
2.50	478342	52240	9.16	0.83
1.00	214399	56566	3.79	0.33
0.75	121927	56931	2.14	0.25
0.50	96117	57018	1.69	0.17
0.25	53120	56817	0.93	0.08
0.15	30073	57874	0.52	0.05

Liquid aliquots were also collected during the reaction, to analyze the concentration of alcohol and product(s) in liquid phase. They were analyzed with gas chromatography (Shimadzu, GC-2010, column ZB-FFAP, thermal program: gradient 40°C → 230°C, 20 °C min⁻¹, isothermal 230°C, 10 min, N₂ used as carrier gas, FID detector). As the substrates 1-octanol (retention time 7.2 min), 2-octanol (6.3 min) and 1,2-octanediol (10.3 min) were used. For all of them the calibration was performed by relating the signals integration with the concentration of the solution of alcohol in decane. For each alcohol, at least 5 solutions of different concentrations were prepared. The obtain calibration lines are presented on Figure 2.4.

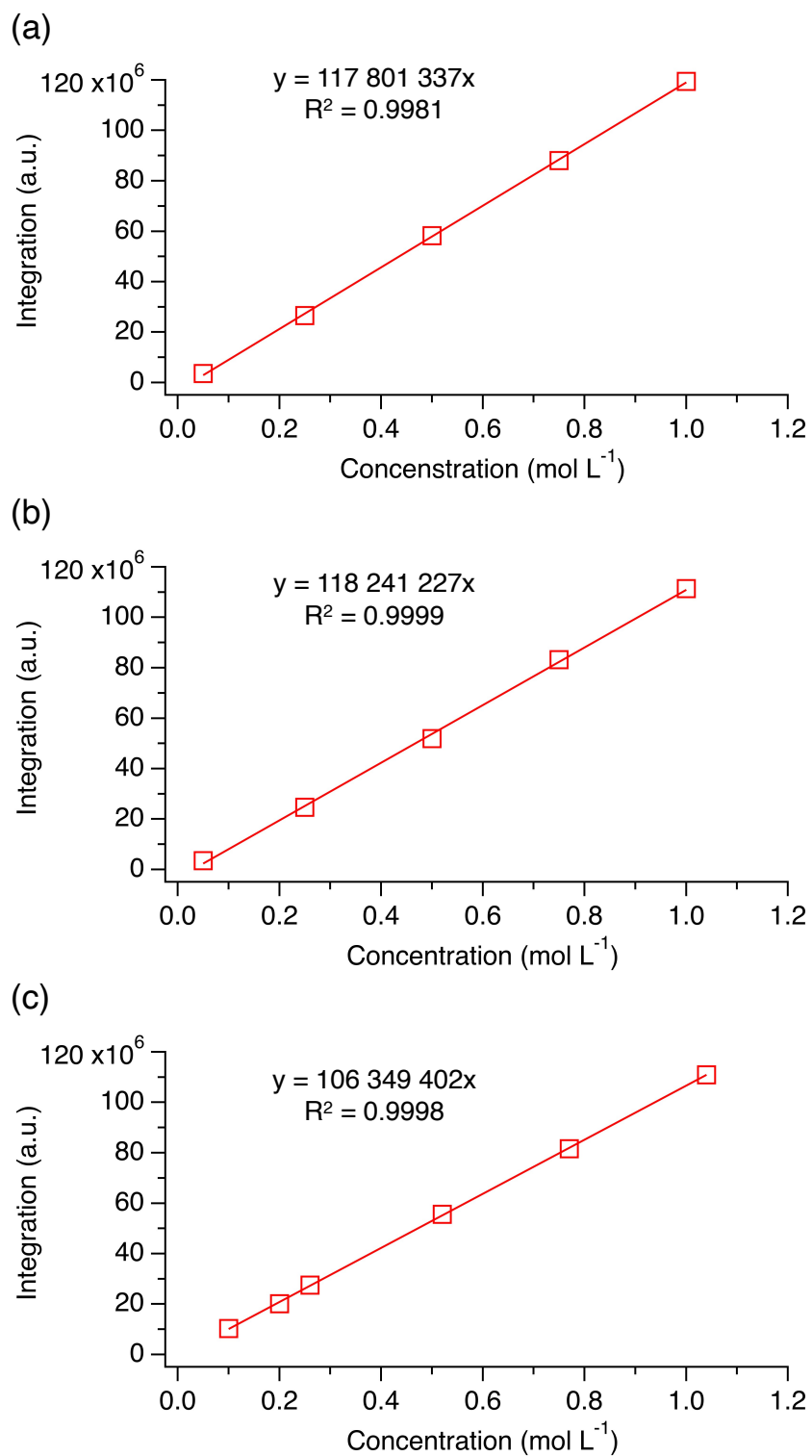


Figure 2.4. Calibration graphs for: (a) 1-octanol, (b) 2-octanol, (c) 1,2-octanediol. a.u. stands for arbitrary units.

The main (expected) reaction products were octanal (retention time 5.5 min), 2-octanone (5.4 min) and 1-hydroxy-2-octanone (8.4 min) from 1-octanol, 2-octanol and 1,2-octanediol, respectively. For octanal and 2-octanone the calibration was performed for at least 5 solutions of different concentrations in decane. The obtained calibration lines are presented on Figure 2.5. 1-hydroxy-2-octanone is not commercially available, hence to measure its concentration we used the same calibration line as obtained for 1,2-octanediol.

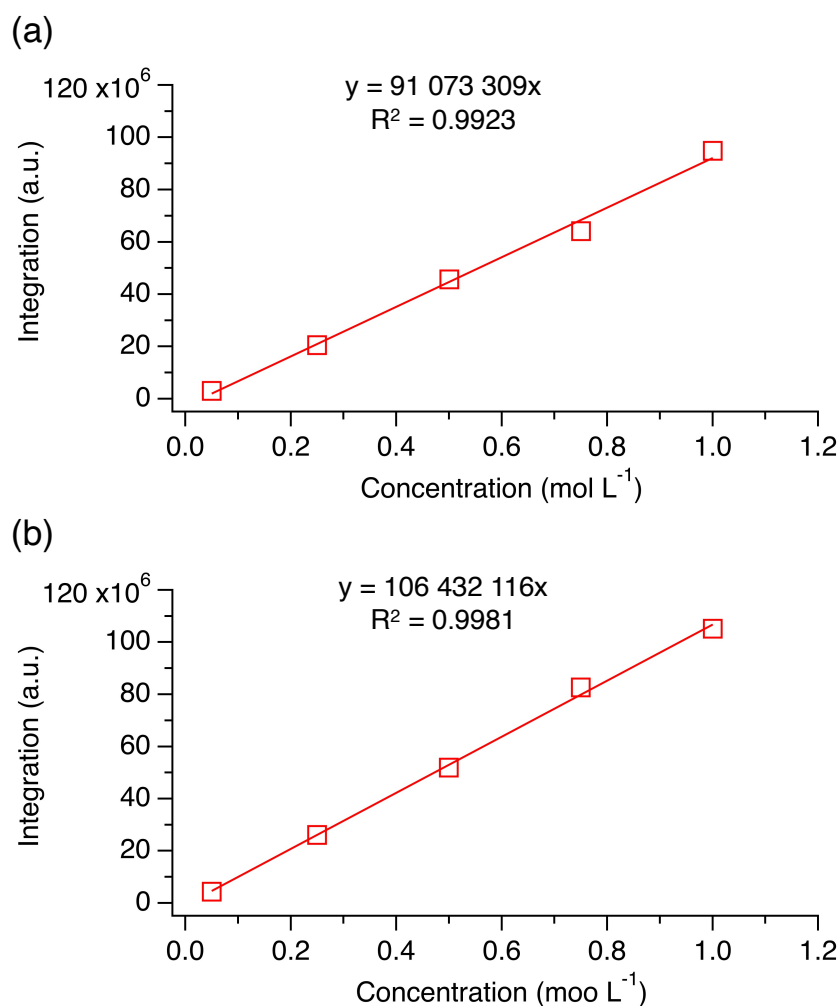


Figure 2.5. Calibration graphs for: (a) octanol, (b) 2-octanone. a.u. stands for arbitrary units.

Despite of the main carbonyl product, also some C16 by-products were observed (retention time 9.0 min to 11.0 min). As the exact structure of by-products could not be identified and any of the possible products are not commercially available, the calibration was performed

with the similar in mass and composition 5-hexadodecanon. 5 solutions of different concentration in decane were prepared to obtain the correlation line and the corresponding graph is presented on Figure 2.6.

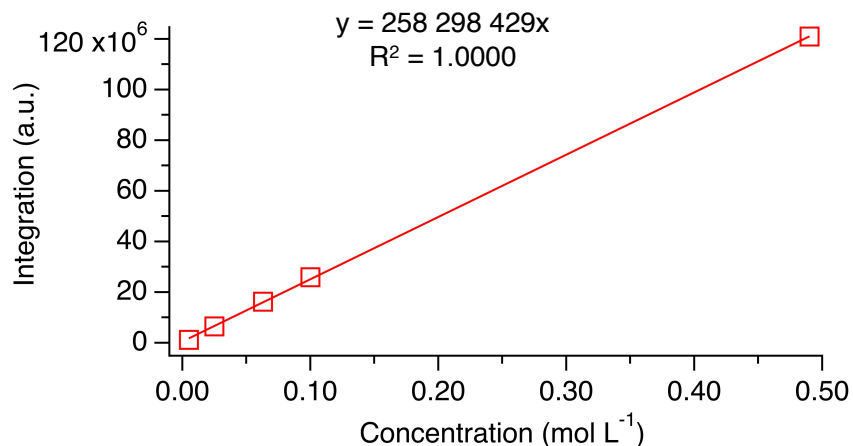


Figure 2.6. Calibration graph for 5-hexadodecanon. a.u. stands for arbitrary units.

2.4.2. Reaction results analysis

Conversion of the substrate X is defined as

$$X = \left(1 - \frac{C_x}{C_0}\right) \cdot 100\%$$

where:

C_x – concentration of alcohol at a given time in liquid aliquots

C_0 – concentration of alcohol at the beginning of reaction

Selectivity is defined as:

$$S = \frac{C_{\text{carbonyl}}}{C_{\text{carbonyl}} + \sum n \cdot C_{\text{by-product}}}$$

C_{carbonyl} – concentration of desired carbonyl compound (aldehyde, ketone, and hydroxyketone respectively for primary alcohol, secondary alcohol, and diol) at a given time in liquid aliquots

$C_{\text{by-product}}$ – concentration of byproduct(s) at a given time in liquid aliquots

n – coefficient factor, for C8 molecules equal to 1, and for C16 molecules equal to 2

Reaction yield Y in product is given by:

$$Y = X \cdot S$$

The yield in H₂ was also evaluated as

$$Y_{\text{H}_2} = \frac{n_{\text{H}_2}}{n_{\text{theor}}} \cdot 100\%$$

where:

n_{H_2} – accumulated amount of H₂, produced after given time of reaction

n_{theor} – theoretical amount of H₂ possibly produced during alcohol dehydrogenation reaction, based on a concentration of the alcohol in the solution at the beginning of the reaction.

For the unsupported cobalt catalysts, the turnover number (TON) is calculated as:

$$\text{TON} = \frac{n_{\text{converted substrate}}}{n_{\text{surface Co atoms}}}$$

with:

$n_{\text{converted substrate}}$ – amount of alcohol converted into product(s) during the reaction, counted based on its concentration in liquid samples at the beginning (C_0) and at the end of the reaction (C_x)

$n_{\text{surface Co atoms}}$ – amount of surface Co (1st layer of metal) in the catalyst sample used in the reaction. This number is evaluated taking into account that different exposed facets expose different amount of Co atoms per surface unit. Establish uncertainty of TON values is equal to 25 mol mol⁻¹. For the example see Annex, part A.2.4.

2.4.3. Catalyst pre-treatment

To increase the catalytic activity different pre-treatment procedures were applied:

1. Thermal treatment under vacuum

Around 100 mg of dry unsupported Co catalyst was placed into a glass cell, which subsequently was connected to the vacuum system. After reaching a high vacuum ($p < 1.5 \cdot 10^{-5}$ atm), the temperature program was started (10 °C min⁻¹, 120°C, 12 h) to desorb the ligands from the catalyst.

2. Washing with EtOH

Around 100 mg of dried unsupported Co catalyst was placed into a centrifugation vial (5.0 mL volume). 3.0 mL of EtOH was added to the sample. After few minutes of shaking, the sample was centrifugated (5 000 rpm, 10 min) and the supernatant was collected. The washing was repeated 3 times. Then, the sample was placed for 24 h in the oven under the temperature of 80°C and N₂ flow for drying.

3. H₂ *in situ* pre-treatment

The appropriate mass of dried catalyst (25 mg or 500 mg for unsupported and supported cobalt catalysts, respectively) and 30.0 mL of decane were placed into the reactor. All the reaction equipment was connected and the reactor was heated up to 145°C. After the target temperature was reached, the solution was treated for 1 h with a mixture of flowing gases: 10 mL min⁻¹ H₂ + 30 mL min⁻¹ inert gases, and for the next 1 h only with 30 mL min⁻¹ of inert gases, to remove the remaining H₂ from the reactor. After this, 15 mL of a solution of alcohol in decane were added into the reactor to reach a final volume of a reaction solution of a concentration of 0.95 mol L⁻¹ of alcohol in decane and the reaction was started.

4. Modified washing procedure before sample drying

The chosen catalysts (P-R-1 and P-P) were re-synthesized and the modified washing procedure before drying were applied for them. P-R-1 catalyst was washed 6 times with MeOH, and P-P sample was washed 12 x MeOH (both instead of 3 x EtOH).

2.5. Density Functional Theory

Density Functional Theory (DFT) is a computational quantum chemistry modeling method, used to investigate electronic properties of molecules and materials. It provides the energy of a given structure (linking it with electronic density by functional), with a certain accuracy that depends on the choice of the level of approximation, on the numerical parameters and on the system under consideration. In the catalysis field, it can be applied to determine the energy of molecules, intermediates and transitions states, to investigate reaction mechanisms and then predict activity of different catalysts.⁴ To model metallic nanoparticles, typically a periodic slab model that mimics the exposed facet by an ideal surface is used. The quality of

the obtained results relies on numerical parameters, choice of the functional and choice of the slab model.

In this work, periodic DFT computations were performed with Vienna *Ab initio* Simulation Package (VASP) computer program.^{5,6} As cobalt is magnetic metal, performed calculations were spin polarized. The exchange-correlation energy and potential were calculated with the generalized gradient approximation using the PBE functional⁷ with dDc dispersion correction,^{8,9} a combination which was proved to be the most accurate to describe the adsorption of molecules on metal surfaces¹⁰. The projector augmented wave method (PAW)^{11,12} was used to describe the electron-ion interactions. A cut-off energy of 400 eV was applied to obtain a tight convergence of the plane-wave expansion. Electronic energies were obtained with a convergence criterium of 10^{-6} eV.

The optimal interatomic Co-Co distance was established for bulk hcp Co and was found to be equal to 2.47 Å (what is in good agreement of the experimental value of 2.51 Å), and further used for all the surfaces. The catalyst surfaces were represented by supercells, composed of few metal layers (usually 4) over which the vacuum was placed (over 10 Å). Half of the layers (bottom layers) were fixed in bulk truncated positions, whereas the remaining half (upper layers) were allowed to relax. Such surface model is called asymmetrical slab (Figure 2.3). It is repeated periodically to mimic the extended metal surface. 5 hcp type surfaces and 4 fcc type facets of Co were considered in computations. For hcp type facets the following supercells were used: p(3x3) of 4 layers for Co(0001), p(4x4) of 4 layers for Co(10-11), p(4x4) of 6 layers for Co(10-10), p(3x3) of 4 layers for Co(10-12) and p(4x4) of 4 layers for Co(11-20). Whereas for fcc type surfaces they were: p(3x3) of 4 layers for Co(111), p(3x3) of 4 layers for Co(100), p(3x4) of 4 layers for Co(110) and p(3x3) of 4 layers for Co(211) facets. For the Brillouin zone integration, a Monkhorst-Pack mesh of 3 x 3 x 1 K-points was used.¹³ 1.63 μB per atom was used initially as magnetic moment value for Co and it tuned slightly to: 1.58 μB for (0001), 1.70 μB for (10-11), 1.71 μB for (10-10), 1.73 μB for (10-12), 1.78 μB for (11-20), 1.60 μB for (111), 1.69 for (100), 1.69 μB for (110) and 1.69 μB for (211).

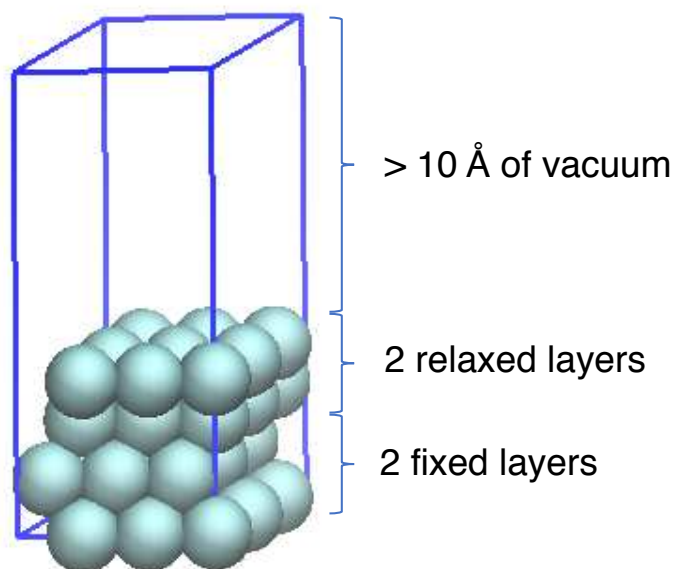


Figure 2.3. Asymmetric slab model, on the example of p(3x3) Co(111) supercell.

Adsorption and reaction processes were realized on the upper surface of the slab. Structures were allowed to relax until the forces were lower than $0.015 \text{ eV } \text{\AA}^{-1}$. Frequencies were computed numerically within the harmonic approximation. Reaction path generator developed by P.Fleurat-Lessard, Opt'n Path,¹⁴ together with nudge elastic band procedures (NEB),^{15,16} allowed to determine the transition state structure, between two given ground states structures. It was further optimized using the dimer method,^{17,18} which minimalizes the forces (not energy) in a given state, and confirmed by the presence of a single imaginary frequency which normal model corresponds to the reaction coordinate.

Adsorption energy of molecules was considered as difference between the energy of the molecule adsorbed on the surface and the energy of pristine surface and molecule in gas phase. A negative energy means stabilizing adsorption.

$$E_{\text{ads}} = E_{\text{molecule@slab}} - E_{\text{slab}} - E_{\text{molecule}}$$

E_{ads} – adsorption energy

$E_{\text{molecule@slab}}$ – energy of the molecule adsorbed on the slab

E_{slab} – energy of the slab

E_{molecule} – energy of molecule in the gas phase

In most of the cases the energies were considered as electronic energies. They were considered as Gibbs Free Energies while the comparison with the experimental results was intended and counted with the home-made script. In such cases, the computations were performed with the dipole correction in z direction. The Gibbs energies are derived from the electronic energies within the perfect gas model for molecules and the lattice gas for adsorbate and the rigid rotator and harmonic oscillator approximations. In other words, for molecules in gas phase, Gibbs Free Energy is calculated as follow:

$$G = E_{\text{ele}} + nk_{\text{B}}T + \text{ZPE} - T \times (S_{\text{t}} + S_{\text{r}} + S_{\text{vib}})$$

with:

E_{ele} – electronic energy

$n = 4$ for non-linear molecules and $n = 3.5$ for linear molecules

k_{B} – Boltzmann constant

T – temperature (in K)

ZPE – zero-point energy

$S_{\text{t}}, S_{\text{r}}, S_{\text{vib}}$ – translational, rotational and vibrational entropy components

Entropy components were considered for molecules in gas state.

Adsorbates are considered to lose their rotational and translational degrees of freedom and have a diffusion energy that is higher than the thermal energy. Hence, their Gibbs Free Energies are considered as follow:

$$G_{\text{slab}} = E_{\text{ele}} + \text{ZPE} - T \times S_{\text{vib}}$$

$$G_{\text{ads/slab}} = E_{\text{ele}} + \text{ZPE} - T \times S_{\text{vib}}$$

G_{slab} – Gibbs Free Energy of slab

$G_{\text{ads/slab}}$ – Gibbs Free Energy of the species adsorbed on a slab

ZPE and S_{vib} are based on the harmonic vibration of the adsorbate. Frequencies lower than 50 cm^{-1} were neglected for them.

EtOH, 1-PrOH and iPrOH were used as model primary and secondary alcohols, chosen to mimic the alcohols used in the catalytic experiments. However, they carbon chain length is shorter, to minimize the computational costs.

Bibliography

1. Bosc, F., Ayral, A., Keller, N. & Keller, V. Room temperature visible light oxidation of CO by high surface area rutile TiO₂-supported metal photocatalyst. *Appl. Catal. B-Environ.* **69**, 133–137 (2007).
2. Soumare, Y. *et al.* Kinetically controlled synthesis of hexagonally close-packed cobalt nanorods with high magnetic coercivity. *Adv. Funct. Mater.* **19**, 1971–1977 (2009).
3. Brunauer, S., Emmett, P. H. & Teller, E. Adsorption of gases in multimolecular layers. *J. Am. Chem. Soc.* **60**, 309–319 (1938).
4. Van Santen, R. A. & Sautet, P. *Computational Methods in Catalysis and Materials Science: An Introduction for Scientists and Engineers.* (Wiley-VCH Verlag GmbH & Co. KGaA, 2009).
5. Kresse, G. & Hafner, J. Ab initio molecular dynamics for liquid metals. *Phys. Rev. B* **47**, 558–561 (1993).
6. Kresse, G. & Furthmüller, J. Efficient iterative schemes for ab initio total-energy calculations using a plane-wave basis set. *Phys. Rev. B* **54**, 11169–11186 (1996).
7. Perdew, J. P., Burke, K. & Ernzerhof, M. Generalized gradient approximation made simple. *Phys. Rev. Lett.* **77**, 3865–3868 (1996).
8. Steinmann, S. N. & Corminboeuf, C. A generalized-gradient approximation exchange hole model for dispersion coefficients. *J. Chem. Phys.* **134**, 044117 (2011).
9. Steinmann, S. N. & Corminboeuf, C. Comprehensive benchmarking of a density-dependent dispersion correction. *J. Chem. Theory Comput.* **7**, 3567–3577 (2011).
10. Gautier, S., Steinmann, S. N., Michel, C., Fleurat-Lessard, P. & Sautet, P. Molecular adsorption at Pt(111). How accurate are DFT functionals? *Phys. Chem. Chem. Phys.* **17**, 28921–28930 (2015).
11. Blöchl, P. E. Projector augmented-wave method. *Phys. Rev. B* **50**, 17953–17979 (1994).
12. Kresse, G. & Joubert, D. From ultrasoft pseudopotentials to the projector augmented-wave method. *Phys. Rev. B* **59**, 1758–1775 (1999).
13. Monkhorst, H. J. & Pack, J. D. Special points for Brillouin-zone integrations. *Phys. Rev. B* **13**, 5188–5192 (1976).
14. Fleurat-Lessard, P. A chemist view on reaction path determination.

15. Henkelman, G., Uberuaga, B. P. & Jónsson, H. A climbing image nudged elastic band method for finding saddle points and minimum energy paths. *J. Chem. Phys.* **113**, 9901–9904 (2000).
16. Sheppard, D., Terrell, R. & Henkelman, G. Optimization methods for finding minimum energy paths. *J. Chem. Phys.* **128**, 134106 (2008).
17. Henkelman, G. & Jónsson, H. A dimer method for finding saddle points on high dimensional potential surfaces using only first derivatives. *J. Chem. Phys.* **111**, 7010–7022 (1999).
18. Kästner, J. & Sherwood, P. Superlinearly converging dimer method for transition state search. *J. Chem. Phys.* **128**, 014106 (2008).

Chapter 3

Activity of cobalt supported catalysts towards alcohol dehydrogenation

Acceptor-less alcohol dehydrogenation (AAD) is an atom efficient reaction, which can be applied to biomass derived (poly)alcohols as substrates. It is leading to products (molecules containing a carbonyl group and H₂) of high interest. However, it has some constraints, like the high temperature of reaction, inert atmosphere, which assure the acceptor-less reaction conditions, and necessity of removing the gaseous H₂ from the reaction environment to switch reaction equilibria towards products.

The use of catalyst allows to conduct the reaction with good efficiency. In the literature many supported metal catalysts have been reported for this reaction. Among them Co/TiO₂ can be found,¹ which is non-noble, abundant metal catalyst. To begin with, we had to establish the reaction conditions and we performed some benchmark investigations about the activity of supported Co catalyst.

While conducting the reaction in liquid phase, the use of solvent allows to keep reasonable ratio between metal and alcohol (e.g. 1 mol%), and to avoid using significant mass of catalyst. However, the choice of appropriate solvent is important, as it is interacting with reactants (substrate and products) and catalyst surface.^{2,3} Hence, it should be as inert as possible for the reaction. Also, as was reported for different catalysts used in AAD reaction, the nature of metallic catalyst support is important for its activity.^{1,4,5} It can as well influence the metal reducibility^{6,7,8} and NPs size,^{9,10} that can affect the catalytic performance. Cobalt is an oxophilic metal,¹¹ which easily undergoes oxidation with air, by this being deactivated.¹² Therefore, it requires protection (e.g. passivation)¹³ and precaution (inert atmosphere) while handling it and/or re-activation before the catalytic tests.¹⁴

First aim of our work was to establish the reaction conditions and to reproduce the results reported by Shimizu et al. for Co/TiO₂ catalyst.¹ To be consistent with literature we decided to

use 1 mol% of metal in the reaction, 145°C as reaction temperature, and o-xylene as a solvent. With these parameters, we first established the appropriate flow of inert gases (N₂ and Ar mixture, 30 mL min⁻¹, from the 30-60 mL min⁻¹ range) and speed of stirring (750 rpm, from the range of 300-1 000 rpm). (The results for establishing the reaction conditions are not included in this Chapter.) Then, we decided to investigate the effect of solvent for the studied reaction. Subsequently, we evolved the influence of different parameters on the activity of cobalt supported catalysts. We paid attention on catalyst post-treatment (passivation), aging, *in situ* H₂ pre-treatment before the reaction, support and metal precursor effects. To begin with, we conducted the dehydrogenation of 2-octanol (the model secondary alcohol), as the activity towards its dehydrogenation was expected to be higher than towards dehydrogenation of primary alcohol. This allowed us to determine the most active catalysts and check their recyclability (to assess their stability in the reaction conditions), and activity towards dehydrogenation of primary alcohol (1-octanol, to examine their chemoselectivity). As our final step, we tested the chosen catalysts towards dehydrogenation of 1,2-octanediol, what put us closer towards the investigations of desired biomass derived polyalcohols.

3.1. Characterization of supported catalysts

Wet impregnation method is one of the most commonly known and simplest method for preparation of catalysts.¹⁵ It consists of few steps. At first the excess of solution containing metal precursor (usually metal salt) is contacted with solid (catalyst support). After a certain time, in which the solution diffuses into pores of solid, the excess of solution is removed by filtration or evaporation. Subsequently, the solid is calcined and/or reduced to the catalyst active species. 5 wt% supported cobalt catalysts were synthesized with this method. An aqueous solution of Co(NO₃)₂ · 6H₂O salt was used (0.16 mol L⁻¹) as metal precursor, unless stated otherwise. Supports of different nature (TiO₂ P25, ZrO₂, γ-Al₂O₃, C, ZnO), and TiO₂ with different crystallographic composition (anatase to rutile ratio; TiO₂ P25, TiO₂ P90, TiO₂ DT51D, TiO₂ SGNH and TiO₂ home made) were utilized for the synthesis. All the obtained catalyst precursors, after drying, were calcined in air at 300°C for 1 h, with the heating rate of 1 °C min⁻¹ (except for Co/C, which was not calcined at all). They were then reduced in flowing H₂, at 400°C, for 0.5 h (heating rate 1 °C min⁻¹; to obtain the metal), and passivated in 1%O₂/N₂ for 0.5 h at room temperature (to create a tiny protective layer of oxide on the metal NPs surface), unless stated otherwise.

Their physicochemical characterization was conducted by: elemental analysis (ICP-OES), specific surface area measurements, X-ray diffraction (XRD), thermogravimetry analysis under H₂ (TGA-H₂), TEM and XPS.

3.1.1. Elemental analysis of metal content and specific surface area measurements

Inductively coupled plasma optical emission spectroscopy (ICP-OES) allowed us to determine the actual cobalt content in the synthesized catalysts. For all of them the values were close to the theoretical value equal to 5 wt% of Co (Table 3.1).

N₂ physisorption was performed to measure the specific surface area of the catalysts; the BET theory was applied and the results are included in Table 3.1.

Table 3.1. Co content and BET surface area for the catalysts.

Catalyst ^a	Co content (wt%) ^c	Surface area (m ² g ⁻¹)
Co/TiO₂ P25	4.7	61
Co/ZrO₂	4.9	131
Co/C^b	4.8	1067
Co/γ-Al₂O₃	4.8	111
Co/ZnO	4.9	15
Co/TiO₂ P90	4.8	118
Co/TiO₂ DT51D	5.0	84
Co/TiO₂ SGNH	4.7	98
Co/TiO₂ home made	4.9	111

^a All the catalysts were calcined in air at 300°C, subsequently reduced in H₂ at 400°C, and passivated in 1%O₂/N₂

^b Catalyst was not calcined

^c Determined by ICP-OES analysis

While comparing the values of specific surface area of the catalysts with the ones of supports (see experimental section, Chapter 2.3.2), we observe that they are always a bit lower for the catalysts. This indicates blocking of some pores of the support, but the changes are not significant.

3.1.2. X-ray diffraction analysis

XRD analysis was performed to assess the formation of metal nanoparticles, get information on their crystallographic structure and investigate their crystallite size. The influence of different parameters such as the thermal treatment, used metal precursor and the type of support were investigated.

3.1.2.1. Catalyst treatment

The influence of different thermal treatments was investigated for Co/TiO₂ P25 catalyst. In Figure 3.1. are presented the diffractograms for: catalyst only calcined in air at 300°C (a, in red); and catalyst calcined at 300°C, reduced at 400°C and passivated (b, in green).

TiO₂ can exist in different crystallographic forms: rutile, anatase, brookite. Rutile is the most thermodynamically stable, hence, its formation is preferred at elevated temperatures.¹⁶ TiO₂ P25 support contains two crystallographic phases: 25% of rutile and 75% of anatase. In XRD measurements the main signals from rutile are located at the 2θ angle equal to 27.5° (80% of relative intensity, (110) crystallographic plane), 36.0° (60%, (101)), 54.2° (100%, (211)) (PDF 00-001-1292). The main signals from anatase are located at: 23.3° (100% of relative intensity, (101) crystallographic plane), 37.9° (22%, (004)), 48.0° (32%, (200)) (PDF 00-064-0863). The presence of these signals on the diffractograms confirms the presence of rutile and anatase TiO₂ in the material.

The calcination under air of the impregnated catalyst aims to decompose the metal precursor (Co(NO₃)₂ · 6H₂O) and forms the metal oxide (Co₃O₄ and/or CoO). In XRD analysis, the main signals from Co₃O₄ are expected to appear at 2θ of 31.2° (40% relative intensity, (220) crystallographic plane), 36.8° (100%, (311)), 65.2° (45%, (440)) (PDF 00-009-0418), and from CoO at 36.5° (65%, (111)), 42.4° (100%, (200)), 61.5° (54%, (220)) (PDF 00-048-1719). For the catalyst after calcination only signals from Co₃O₄ were observed (Figure 3.1.a). The signals at 31.2° and 65.2° are clearly visible. The (main) signal at 36.8° superimpose with the signal from TiO₂ anatase. However, its intensification is visible, therefore, confirming the presence of signal from Co₃O₄. The average crystallite size, established with Scherrer equation, is equal to 13 nm. After reduction and passivation, the signals coming from Co₃O₄ are not present anymore. As the catalyst was passivated (in a flow of 1% v/v O₂/N₂) the formation of

a monolayer of CoO on the surface is expected. Because the signals from CoO are not visible on the diffraction pattern, we can assume that only the surface was oxidized in the passivation process, whereas in bulk, Co is in metallic state.⁷

Cobalt nanoparticles can exist in two crystallographic forms: hexagonal close packed (hcp) and face centered cubic (fcc). The thermal transition between them (hcp → fcc) occurs around 450°C for bulk metal,¹⁷ hence for catalysts reduced at 400°C, we cannot exclude the coexistence of these two phases. For hcp Co the main signals appear at 2θ equal to 47.6° (100% relative intensity, (101) facet), 75.9° (80%, (110)), 84.2° (80%, (103)) (PDF 00-005-0727), and for fcc Co at 44.2° (100%, (111)), 51.5° (40%, (200)), 75.8° (25%, (220)) (PDF 00-015-0806). However, no signals from metallic Co are visible. They can be unnoticeable due to the superimposing with the signals from support (like Co hcp signal at 47.6° and signal from TiO₂ anatase at 48.0°) and/or due to the small size of metal crystallites (< 10 nm). Hence, based on the obtained XRD results we cannot conclude about the crystallographic phase of Co⁰ after reduction.

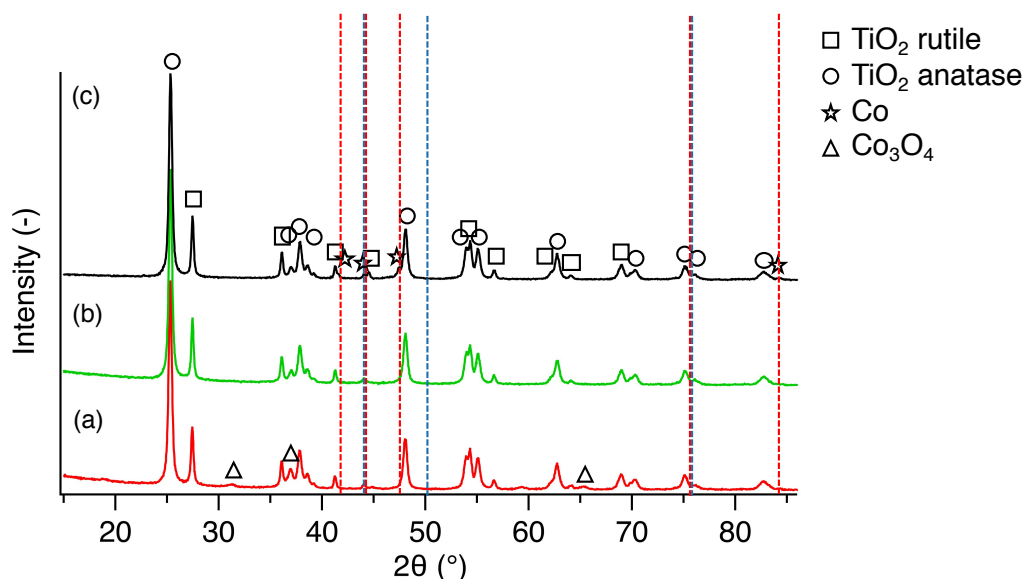


Figure 3.1. XRD diffraction patterns associated with Co/TiO₂ P25 (a) after calcination (in red), (b) Co/TiO₂ P25 catalyst after additional reduction and passivation (in green), and (c) CoCl/TiO₂ P25 after calcination, reduction and passivation (in black). The vertical dashed lines indicate the expected 2θ angles for appearance of Co signals: red – hcp Co and blue – fcc Co.

3.1.2.2. Different metal precursors

Different metal precursors can be used in the preparation of Co supported catalysts. We prepared a second Co/TiO₂ P25 with a different metal salt - CoCl₂ · 6H₂O. It will be named Co_{Cl}/TiO₂ P25 from now on. As previously, the catalyst was calcined at 300°C, reduced at 400°C and subsequently passivated. The corresponding diffraction pattern is presented on Figure 3.1.c (in black); the catalyst can be compared with the one obtained with Co(NO₃)₂ · 6H₂O (b, in green).

For the catalyst obtained from CoCl₂ the signals from hcp Co nanoparticles are clearly visible, even though they partly overlap with the signals from TiO₂ support. The established average crystallites size (Scherrer equation, measurements of 3 signals) is equal to 54 nm. Based on these results we can conclude that the use of cobalt chloride leads to the formation of bigger nanoparticles than the use of cobalt nitrate, while the same thermal treatment is applied.

Panpranot et al. investigated the influence of the cobalt precursor on the metallic dispersion on MCM-41 (Mobil Composition of Matter No. 41, mesoporous material from silicate and aluminosilicate family of solids), for catalysts with 8 wt% Co loading.¹⁸ When cobalt nitrate and cobalt chloride were used as metal precursors the nanoparticles of Co₃O₄ obtained after calcination at 500°C exhibit mean size of 6.3 nm and 15.0 nm, respectively. Cobalt nitrate appeared to be the most suitable Co precursor, as it allowed to obtain NPs of smaller size. Big nanoparticles possess smaller exposed surface area, that diminishes the amount of available active sites and metal-support interface. Additionally, when cobalt chloride was used, the metal active sites obtained after reduction were blocked by residual Cl⁻.

3.1.2.3. Different supports

Cobalt catalysts with different supports were synthesized from Co(NO₃)₂ · 6H₂O precursor salt by wet impregnation method. All of them were calcined in air at 300°C, reduced under H₂ flow at 400°C and subsequently passivated. The diffractograms for Co supported on: ZrO₂ (a, red), γ-Al₂O₃ (b, green), C (c, blue) and ZnO (d, black) are presented on Figure 3.2.

ZrO₂ used in the synthesis is composed in 90% from ZrO₂ monoclinic and in 10% from ZrO₂ tetragonal. The main signals from ZrO₂ monoclinic are located at 2θ equal to 28.2° (relative intensity of 100%, (-111) facet), 31.5° (66%, (111)), and 50.2 (22%, (022)) (PDF 00-065-0687),

and the main signals from ZrO₂ tetragonal are located at 29.8° (100%, (101)), 34.0 (39%, (002)), 50.1 (38%, (200)) (PDF 00-042-1164). Most of the expected signals from hcp and fcc Co are located at the same places as signals from ZrO₂. However, if the metal will be in hcp state, then the signal at 47.6° should be visible. As it is not observed, we can assume that either Co is in fcc state, or the metal crystallites are too small.

Main diffraction signals from cubic γ -Al₂O₃ are located at 2 θ equal to 39.4° (60% relative intensity, (222) facet), 45.8° (64%, (400)), and 66.8° (100%, (440)) (PDF 00-056-0457). Moreover, a tetragonal (δ) phase is also present, for which the main signals occur at 2 θ of 36.5° (69%, (312)), 45.5° (65%, (400)) and 67.1° (100%, (4012)) (PDF 00-056-1186). For Co/ γ -Al₂O₃ catalyst the signals from metallic Co are not visible. In the literature, the formation of cubic CoAl₂O₄ has also been reported for 10 wt% Co/ γ -Al₂O₃, prepared by wet impregnation method and calcined in static air at 400°C.⁸ Hence, its presence could be suspected. However, the main peak at 36.7° overlap with the support (PDF 00-044-0160). Therefore, we cannot make conclusions about its presence.

The diffractogram of Co/C is presented on Figure 3.2.c. The peaks at 26.7° and 42.9° can be attributed to the activated carbon support. On the diffractogram only the signal from Co₃O₄ species is visible, that implies that the catalyst was not reduced at 400°C.

The main signals from ZnO (hexagonal) occur at 2 θ equal to 31.8° (relative intensity 56%, (100) crystallographic facet), 34.4° (41%, (002)), 36.3° (100%, (101)) (PDF 01-070-8070). For cobalt supported on ZnO the main peak at 44.2° and attributed to (111) plan of fcc Co was recognizable. Based on this peak, the crystallite size is equal to 17 nm. The visibility of this signal is in agreement with literature, as for 10 wt% Co/ZnO it was the only signal from metallic Co observed (at the same place) and the remaining signals were overlapping with signals from highly crystalline ZnO.¹⁹ However, authors did not ascribe it neither to hcp, neither to fcc Co. The visibility of the Co signal for this catalyst is connected with the formation of bigger metal crystallites. Such change in size, in comparison with catalyst on other supports, is favored by the low surface area of Co/ZnO, equal only to 16 m² g⁻¹ (vs over 60 m² g⁻¹ for other catalysts).

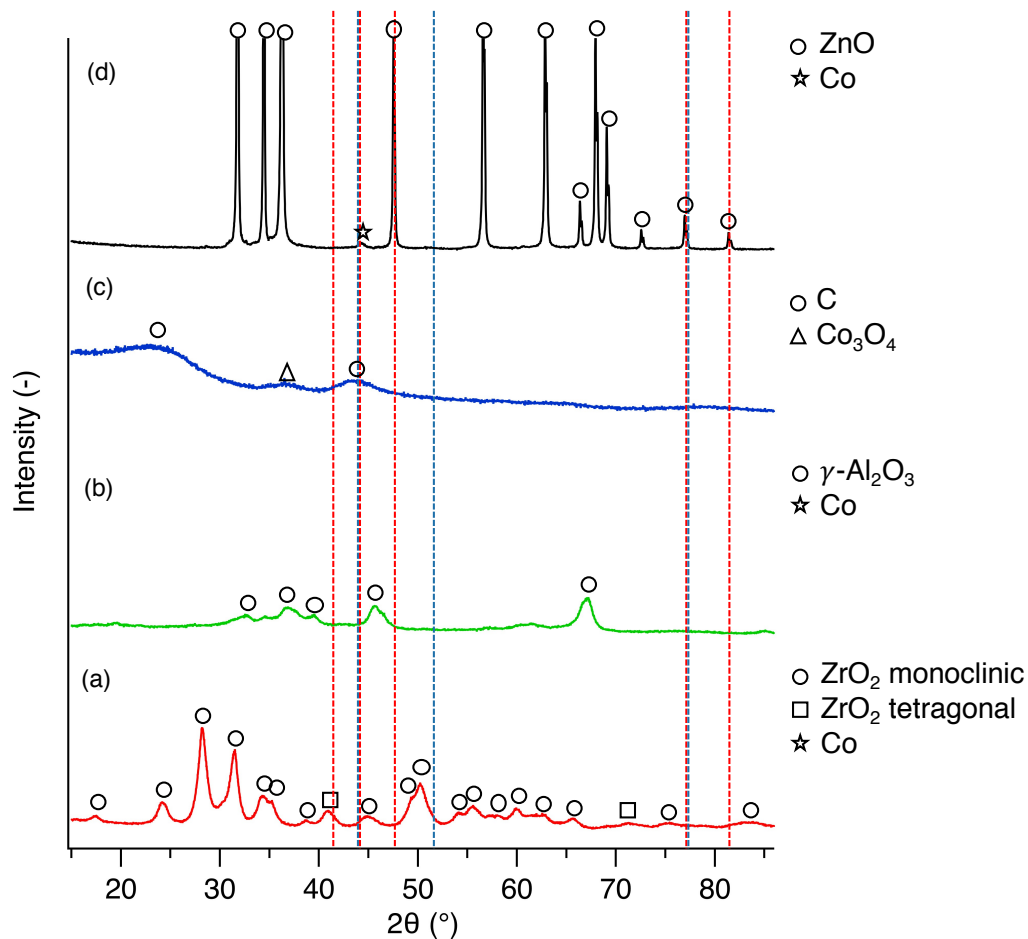


Figure 3.2. XRD diffractograms associated with (a) Co/ZrO₂ (red), (b) Co/ γ -Al₂O₃ (green), (c) Co/C (blue), and (d) Co/ZnO (black). The vertical dashed lines indicate the expected 2θ angles for appearance of Co signals: red – hcp Co and blue – fcc Co.

In the previous part we presented Co supported on TiO₂ P25 (25% rutile + 75% anatase). To dig more into the support effect, we checked the influence of other types of TiO₂ on the crystallographic properties of cobalt species. We used commercially available TiO₂ P90 (10% rutile + 90% anatase) and TiO₂ DT51D (100% anatase). We also used a TiO₂ synthesized by sol-gel non-hydrolytic method (SGNH), obtained thanks to the kindness of H. Mutin, J. Alauzun and M. Bouchneb from Institut Charles Gerhardt Montpellier (TiO₂ SGNH, 100% anatase). Furthermore, we conducted the synthesis of a TiO₂ sample in our laboratory (TiO₂ home made) by low temperature sol-gel method,²⁰ aiming to obtain TiO₂ in pure rutile

phase. However, as a result we obtain the oxide in mixed rutile (20%) and anatase (80%) phases. The composition of all the TiO₂ materials was confirmed by XRD analysis.

Figure 3.3. presents the diffractograms for cobalt supported on different types of TiO₂. For most of them, the signals associated with metallic Co are not visible, indicating that the cobalt crystallite sizes are below 10 nm. Only for Co/TiO₂ (SGNH) it was possible to see the main peak associated with Co cubic at 44.2°, for which the crystallite size is equal to 13 nm.

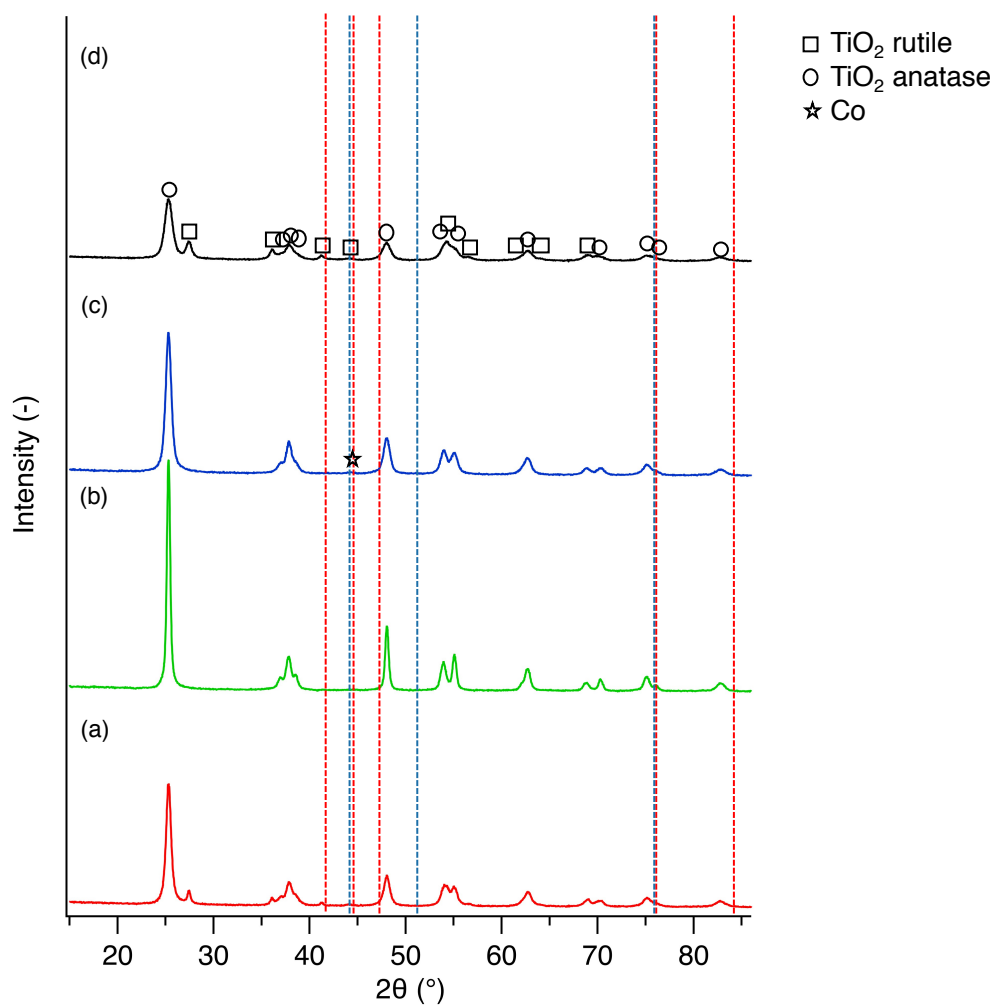


Figure 3.3. XRD diffractograms for cobalt catalysts supported on different types of TiO₂: (a) Co/TiO₂ P90 (in red), (b) Co/TiO₂ DT51D (in green), (c) Co/TiO₂ SGNH (in blue), and (d) Co/TiO₂ home made (in black). The vertical dashed lines indicate the expected 2θ angles for appearance of Co signals: red – hcp Co and blue – fcc Co.

The XRD analysis was performed for the Co catalysts on different supports, which were calcined at 300°C, reduced at 400°C, and passivated. However, the results did not allow to confirm if the catalysts were all fully reduced, neither to assess the crystallographic phase and size of metal NPs. Therefore, to get more information about the reducibility and crystallinity of NPs, we decided to investigate the temperature of reduction of the catalyst, by TGA-H₂, and perform some TEM and XPS measurements, that will be described in the following sections.

3.1.3. Thermogravimetry analysis under H₂

TGA-H₂ analysis of cobalt catalysts was performed to investigate the reducibility and stability of the Co catalysts samples. It was conducted on all of the samples after calcination in order to compare the temperature of reduction of the materials. As the analysis was not conducted in the same condition as during the reduction protocol, we also considered the influence of heating rate on metal oxide reducibility. Moreover, after the passivation, a layer of Co oxide is present at the surface of the catalyst and has to be removed before reaction.¹³ The stability of a catalyst was investigated for a series of Co/TiO₂ P25 catalysts reduced and passivated at different times before reactivation.

All the measurements were conducted under the flow of the mixture of 5% H₂ and 95% of Ar, with total flow of 50 mL min⁻¹, in the temperature range of 25-600°C. Some mass spectra were collected during the analysis ($m/z = 2, 14, 15, 16, 17, 18, 28, 30, 32, 40, 41, 44$).

3.1.3.1. Influence of heating rate on the catalyst reducibility

At first, we checked the influence of heating rate on the catalyst reducibility, as the measurements were conducted with another heating rate than used during the catalyst reduction. Co₃O₄/TiO₂ P25 catalyst was subjected to TGA-H₂ analysis with two different heating rates: 2 °C min⁻¹ and 5 °C min⁻¹. The weight loss during the thermal reduction is presented in Figure 3.4.

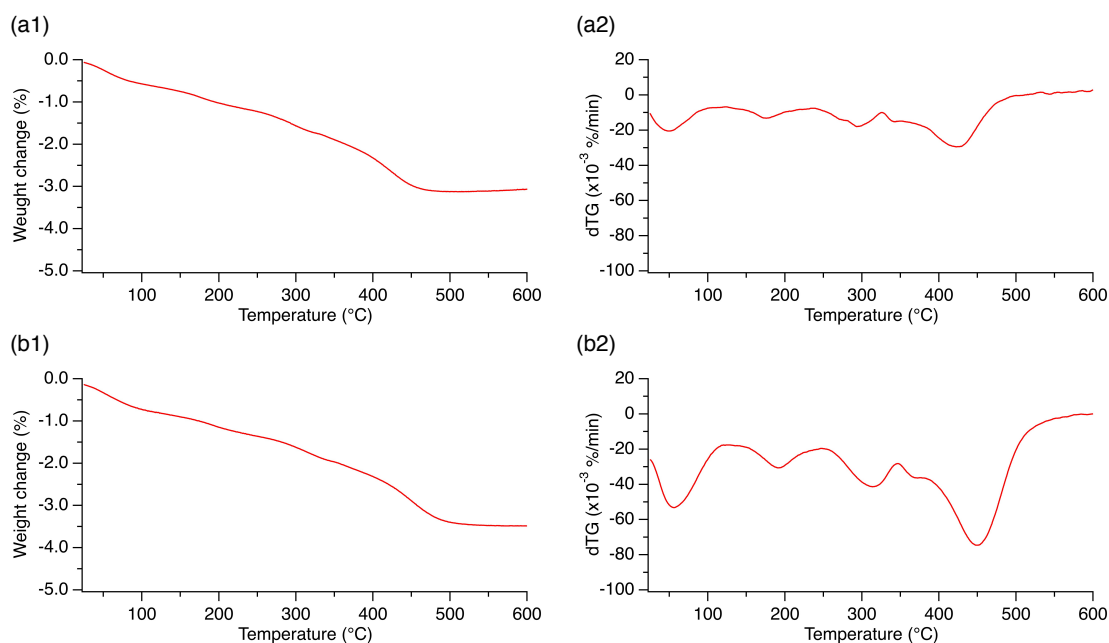


Figure 3.4. Thermal reduction of $\text{Co}_3\text{O}_4/\text{TiO}_2$ P25 at (a) $2\text{ }^\circ\text{C min}^{-1}$ and (b) $5\text{ }^\circ\text{C min}^{-1}$. Graphs marked with number 1 represent the weight loss vs temperature and marked with number 2 the derivate of weight loss vs temperature.

For both measurements the direct analysis of mass change vs temperature is not very informative, as the mass decreases continuously (Figure 3.4. a1 and b1). Graphs a2 and b2 on Figure 3.4. represent the derivatives from mass change in function of temperature, where five mass drops can be noticed. The first one (maximum at 60°C) can be ascribed to moisture desorption. The second drop at $175\text{-}200^\circ\text{C}$ may come from the elimination of crystalline water, from undecomposed metal precursor, or from chemisorbed water.²¹ The third decrease can be associated with the reduction of Co_3O_4 to CoO . The mass drop is consistent with the theoretical value of 0.4%. It takes place in the temperatures range of $300\text{-}320^\circ\text{C}$, which is consistent with the literature for Co/TiO_2 ^{10,22} catalysts. Also this temperatures are in agreement with the reduction temperature of bulk Co_3O_4 (320°C).²³ The fourth small mass change (at $330\text{-}350^\circ\text{C}$) is connected with the decomposition of NO_3^- , coming from the cobalt precursor, which was not fully decomposed during the catalyst calcination at 300°C . The last mass drop (at $420\text{-}450^\circ\text{C}$) represents the transformation of CoO into metallic Co . Its value is consistent with the theoretical weight loss of 1.3% for this transformation, and the temperature of transformation is in agreement with the one reported in the literature for

Co/TiO₂ (450°C).^{10,22} However, it is higher (by 30-60°C) than the temperature reported for reduction of bulk CoO.²³ This is due to metal-support interactions, which hinder the reduction. All of the transformations are endothermic, which means that they required some energy input to take place.

The changes were confirmed by the collected mass spectra (Figure 3.5). For $m/z = 2$, representing H₂ consumption, it is hard to notice any changes, as the analysis was conducted with an excess of the reductive gas. The signals associated with $m/z = 17$ and $m/z = 18$ confirm the water production for all the material transformations. Moreover, the 4th transformation – decomposition of NO₃ is confirmed by the signals from $m/z = 15$ and $m/z = 16$ (ascribed to NH⁺ and NH₂⁺ ions) at temperatures of 350-375°C. The results indicate that calcination of Co/TiO₂ P25 at 300°C was not completely efficient to decompose Co(NO₃)₂ · 6H₂O, used as a metal precursor. It is in agreement with literature,^{24,25} where it is reported that complete decomposition of (unsupported) cobalt nitrate hexahydrate under air takes place at 325-350°C. However, the remaining metal precursor will be decomposed during the reduction process, conducted at 400°C. Hence, it will be no more present on the catalyst used for the catalytic test.

The comparison of the TGA-H₂ measurement results under different heating rates (2 °C min⁻¹ vs 5 °C min⁻¹) showed that complete reduction is reached at lower temperature when the sample is reduced with lower heating rate (450°C, instead of 475°C). Such dependency is in agreement with literature.²⁶ Therefore, as the catalyst reduction before the reaction is conducted with heating rate of 1 °C min⁻¹, we can expect that at 400°C the cobalt oxide should be completely or almost completely reduced to metallic Co. (The TGA-H₂ measurement with 1 °C min⁻¹ heating rate was not conducted only due to technical reasons.) Knowing this rule, further TGA-H₂ experiments were conducted with heating rate of 5 °C min⁻¹.

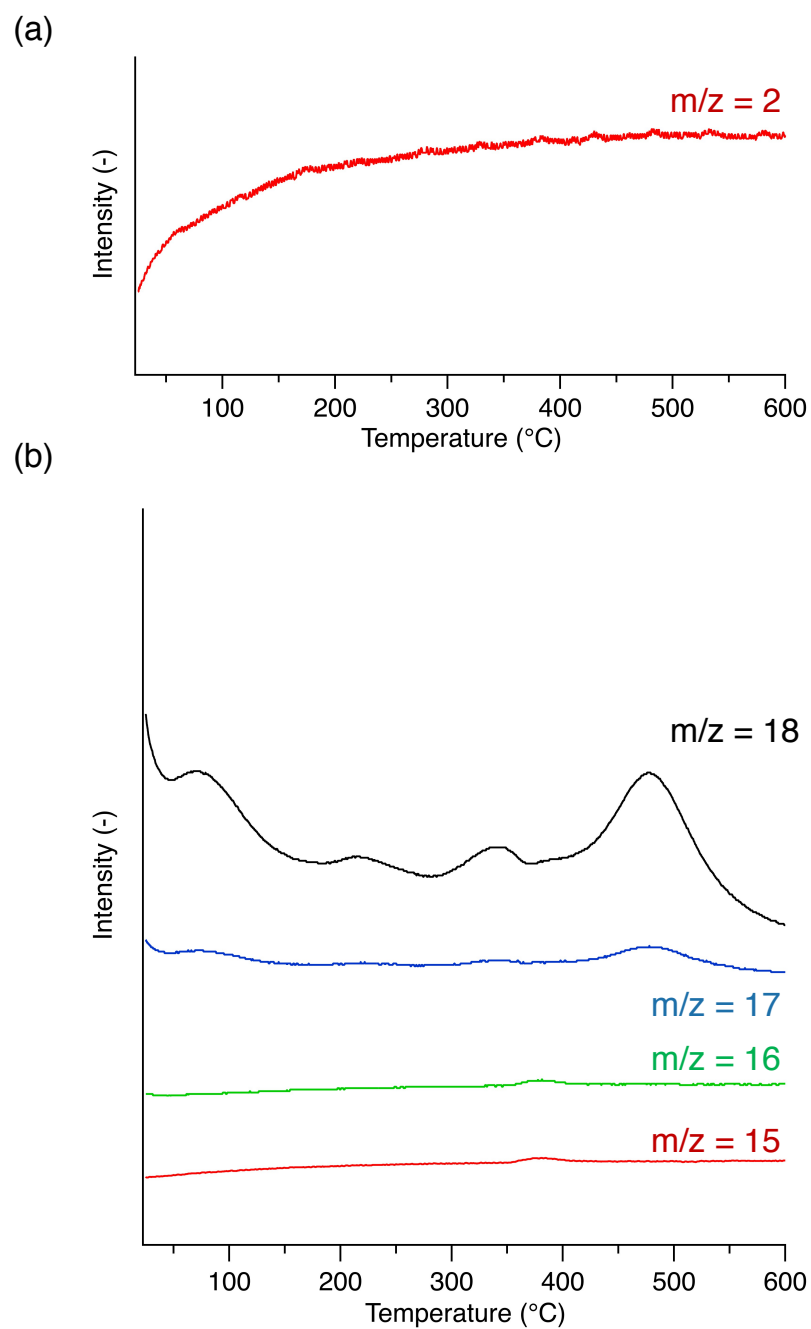


Figure 3.5. Chosen mass spectra, collected during the analysis of $\text{Co}_3\text{O}_4/\text{TiO}_2$ P25 catalyst, with the heating rate of $5\text{ }^\circ\text{C min}^{-1}$: (a) H_2 ($m/z = 2$) and (b) NH^+ and NH_2^+ ($m/z = 15$ and 16), and H_2O ($m/z = 17$ and 18).

3.1.3.2. Influence of the support on cobalt reducibility

Cobalt catalysts were prepared with supports of different nature: TiO₂ P25, ZrO₂, C, γ -Al₂O₃, ZnO. The reducibility of cobalt oxides supported on different materials was checked by TGA-H₂ with 5 °C min⁻¹ heating rate up to 600°C. Before the analysis, all the catalysts were calcined under air flow at 300°C, except C. The results are collected in Table 3.2. The graphs of weight loss vs temperature, derivative of weight loss vs temperature, and chosen mass spectra vs temperature, for different catalysts are presented in Annex, on Figures A.3.1-4.

For all of the catalysts with different supports the first mass drop, at 60°C, is connected with desorption of moisture. Next transformation, around 200°C, is mainly connected with elimination of chemisorbed H₂O. However, for some of the catalysts another change takes place around this temperature that will be described later. The TGA-H₂ of Co/TiO₂ P25 was already described in details in subchapter 3.1.3.1. For this catalyst, the reduction of Co₃O₄ into CoO occurs at 350°C, and the reduction of CoO into metallic Co at 450°C. Additionally, we observed that the cobalt precursor was not completely decomposed during the calcination performed at 300°C.

Co/ZrO₂ catalyst showed a similar mass loss profile to Co/TiO₂ P25 (see Annex, Figure A.3.1). Co₃O₄ is decomposed into CoO at 260°C and the cobalt monoxide is reduced to metallic Co at 440°C. In the case of this catalyst we do not observe any signal of undecomposed metal precursor after calcination. The complete reduction of CoO on ZrO₂ is taking place at very similar temperature as on TiO₂ (440°C and 450°C, respectively). This is not in line with the literature, where the reported reduction temperature for Co/TiO₂ is higher by around 50°C than the temperature reported for Co/ZrO₂.²⁷

Reducibility of cobalt oxides on carbon is more complex (Figure A.3.2.). The signal at 110°C probably comes from the reduction of some organic groups containing nitrogen. The signal at 190°C can be associated with decomposition of metal precursor, what is in agreement with the literature, where for the decomposition of bulk Co(NO₃)₂ · 6H₂O under H₂ the temperature of 240±20°C is reported.²⁴ This is confirmed by the presence of mass spectrometry signal of m/z = 30 at these temperatures. It is usually associated with the presence of CH₃NH₂⁺ or NO⁺ ions. The following signal at 350°C indicates reduction of Co₃O₄ into CoO. Even though we do not observe any further signal on the graph of derivative of mass change, a continuous mass loss is still observed. This means that the catalyst reduction is still on-going at 600°C. It is

connected with CoO reduction into Co, but also with reduction of some organic functional groups on the support. This is confirmed by the presence of mass spectrometry signals of $m/z = 15$ and 16 which can be ascribed to the NH^+ or CH_3^+ and NH_2^+ or CH_4^+ ions, respectively. In the literature it is reported that the CoO reduction on C is taking place even up to 900°C .²⁸ The authors investigated three different activated carbons as catalyst supports. For two of them they identified the $\text{CoO} \rightarrow \text{Co}$ reduction maxima at 550°C and 575°C , respectively, but for the third catalyst the clear maximum was not visible. However, the reduction continued as the H_2 uptake during H_2 -TPR measurement was still significant.

Cobalt supported on $\gamma\text{-Al}_2\text{O}_3$ is also not completely reduced at 600°C (Figure A.3.3). The signal at 160°C results from the decomposition of species containing nitrogen, what is indicated by the MS signal of $m/z = 30$. They are probably coming from not completely decomposed cobalt nitrate. The reduction of Co_3O_4 into CoO takes place at 300°C , what is in good agreement with the literature (308°C).⁸ We do not observe any further straightforward material transition. However, a loss of mass still occurs, which indicates reduction of CoO into Co. This is as well in line with the literature report, where this transformation was reported to occur in a broad range of temperatures ($450\text{-}700^\circ\text{C}$).^{29,30}

Co/ZnO exhibits the simplest reduction profile of all the investigated types of support (Figure A.3.4). Only two signals, at 250°C and 390°C , are observed, and they come from the transformation of $\text{Co}_3\text{O}_4 \rightarrow \text{CoO} \rightarrow \text{Co}$. It can be assumed that the reduction is facilitated for this catalyst, as the temperature of reduction is lower for it. It was already reported in the literature, that when comparing 10 wt% Co/ZnO and 15 wt% Co/ZnO, the oxide species were reduced more easily for the later one as they were bigger (due to the higher metal content).²⁹ This might also be the case for this catalyst in comparison with the others. According to XRD results the measured mean metal crystallite size for Co/ZnO is equal to 17 nm, whereas for the other catalysts the Co signals on diffractograms were not visible, indicating the crystallites sizes below 10 nm. This suggests that the oxide species might exhibit different size depending on the support, which could explain the shift in reduction temperature.

Table 3.2. Temperatures of transformations for Co catalysts during TGA-H₂ measurements at 5 °C min⁻¹, up to 600°C, under 50 mL min⁻¹ of H₂.

Calcined catalyst	H ₂ O (moisture) desorption (°C)	Elimination of chemisorbed H ₂ O (°C)	Co ₃ O ₄ → CoO (°C)	NO ₃ ⁻ decomposition (°C)	CoO → Co (°C)
Co₃O₄/TiO₂ P25	60	200	320	350	450
Co₃O₄/ZrO₂	60	200	260	Not visible	440
Co(NO₃)₂·6H₂O/C *	60	110 and 190 – decomposition of N-containing species	350	Not visible	>600
Co₃O₄/γ-Al₂O₃	60	160 – decomposition of N-containing species 225 – chemisorbed H ₂ O	300	Not visible	>600
Co₃O₄/ZnO	Not visible	Not visible	250	Not visible	390
Co₃O₄/TiO₂ P90	60	210	310	Not visible	500
Co₃O₄/TiO₂ DT51D	60	190	320	Not visible	375
Co₃O₄/TiO₂ SGNH	60	200	300	Not visible	425
Co₃O₄/TiO₂ home made	60	200	310	Not visible	410

* Catalyst was not calcined

Additionally, we investigated the influence of different types of TiO₂ on cobalt reducibility (see Table 3.2. and Figure A.3.5. in Annex). After calcination at 300°C, the TGA-H₂ experiments were conducted on Co/TiO₂ P90, Co/TiO₂ DT51D, Co/TiO₂ SGNH and Co/TiO₂ home made.

For all the Co/TiO₂ samples, four reduction signals were visible. First mass drop, around 60°C comes from the moisture desorption. The second, at 190-210°C, comes from the elimination of chemisorbed water. The transformation of Co₃O₄ into CoO occurs in the range of 300 to 325°C. The reduction is the easiest on TiO₂ P25 and TiO₂ SGNH and the hardest on home made TiO₂. The change of CoO into Co takes place between 375 and 500°C. The strength of the metal-support interaction, expressed by increasing reduction temperature, is increasing in the following order: DT51D < home made < SGNH < P25 < P90. As the temperatures for this transformation differ significantly (in the range of 125°C), we can expect Co being reduced in different extent depending on TiO₂ support.

3.1.3.3. Influence of aging on the removal of the passivation layer

Co/TiO₂ P25 was obtained by wet impregnation, and subsequently calcined, reduced, and passivated. After synthesis the catalyst was stored inside a glovebox for various periods of time. Our aim was to investigate the stability of catalyst – to check if the passivation layer evolves with time, even if the catalyst is stored in closed vessel under inert (N₂) atmosphere. The TGA-H₂ analysis was done the same day as the passivation (1 day old), 2 weeks after passivation (2 weeks old) and 6 months after passivation (6 months old). All the measurements were performed with the heating rate of 5 °C min⁻¹. The corresponding graphs are presented in Figure 3.6.

For the catalyst which was 1 day old two mass drops were evident: the first one with a maximum intensity at 60°C and the second one with maximum intensity at 200°C. The first one can be ascribed to the moisture and the second one to the reduction of the passivation layer, i.e. monolayer of CoO. This signal is shifted towards lower temperature in comparison with the reduction of CoO during the H₂ treatment of the calcined catalyst (450°C, as shown in section 3.1.3.1.). This indicates that the reduction of the monolayer is easier, in agreement with the literature,³¹ where it is reported that CoO formed during the passivation of Co/TiO₂ catalyst was reduced at 225°C, instead of 450°C. After 2 weeks (Figure 3.6.b) the same two

signals were observed. Moreover, the mass loss is similar after 1 day and two weeks, suggesting that the catalyst did not evolve during this time.

In contrary, the results obtained after keeping the catalyst for 6 months suggest that the catalyst has changed. In Figure 3.6.c a third signal with a maximum temperature at 380°C is observed, and it can be associated with the reduction of bulk CoO. The temperature and the weight loss are higher in comparison to the removal of the passivation layer, which suggests the formation of thick(er) CoO layer overtime.

Comparing the three catalysts we can conclude that the activity of the catalysts being 1 day old and 2 weeks old should be similar, whereas, in the absence of any pre-treatment, the catalyst being 6 months old may not be active due to the formation of thicker CoO layer.

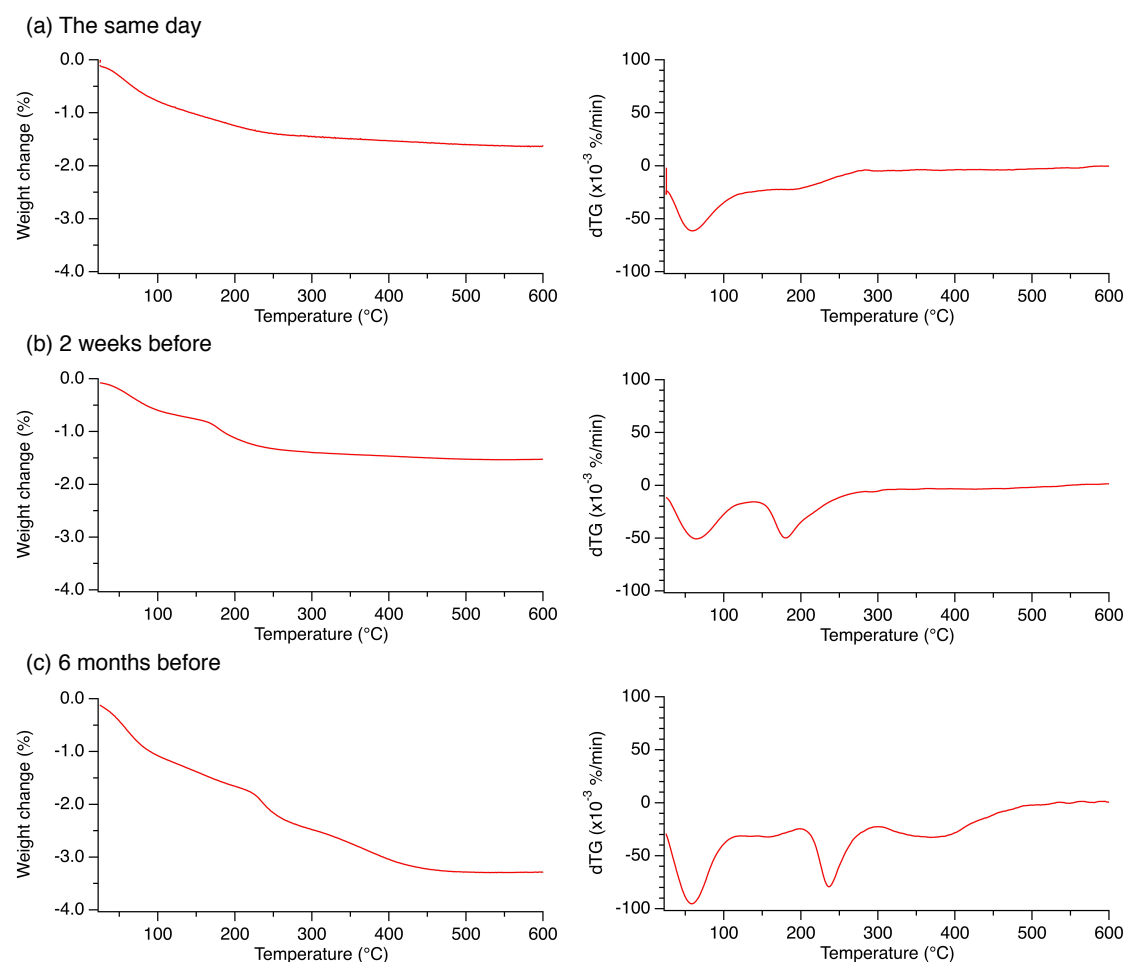


Figure 3.6. Weight loss (on left) and derivative from mass change (on right) as a function of the temperature for Co/TiO₂ P25 catalysts reduced and passivated (a) the same day, (b) 2 weeks before (c) 6 months before.

3.1.4. Transmission Electron Microscopy imaging

Transmission Electron Microscopy (TEM) imaging was performed for one of the catalysts – Co/TiO₂ P25. A representative picture is shown in Figure 3.7. The presence of cobalt particles on TiO₂ was confirmed. However, due to the low contrast between metal and support it was not possible to establish a size distribution, nor to determine their crystallographic structure.

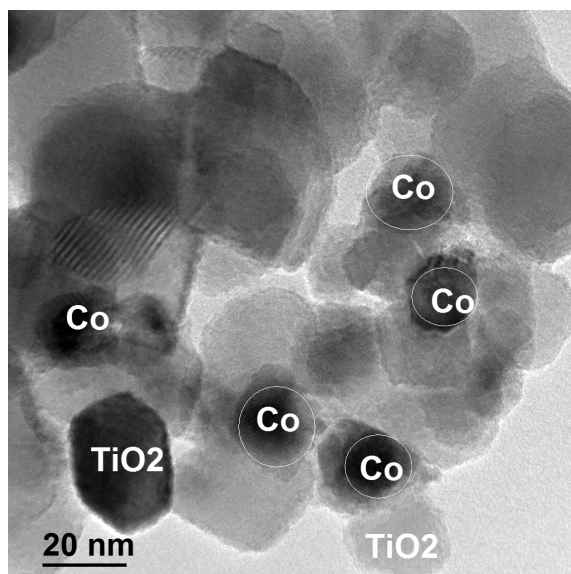


Figure 3.7. Representative TEM image of Co/TiO₂ P25 catalyst

3.1.5. X-ray Photoelectron Spectroscopy analysis

X-ray Photoelectron Spectroscopy (XPS) analysis was performed for the cobalt catalysts supported on TiO₂ P25 (Co/TiO₂ P25), to compare the influence of the different thermal treatments on the surface compositions. They differ as follow:

- (a) Sample after calcination under air (300°C, 1 h, 1 °C min⁻¹) – Co₃O₄/TiO₂
- (b) Sample after calcination, reduced in an auxiliary reaction chamber (400°C, 1 h) and transferred into the XPS chamber to avoid exposure to air
- (c) Sample calcined and reduced before the analysis (400°C, 0.5 h, 1 °C min⁻¹) not passivated, analyzed the same day as the thermal treatment was performed
- (d) Sample calcined and reduced before the analysis, passivated (1%O₂/N₂, 0.5 h, room temperature)

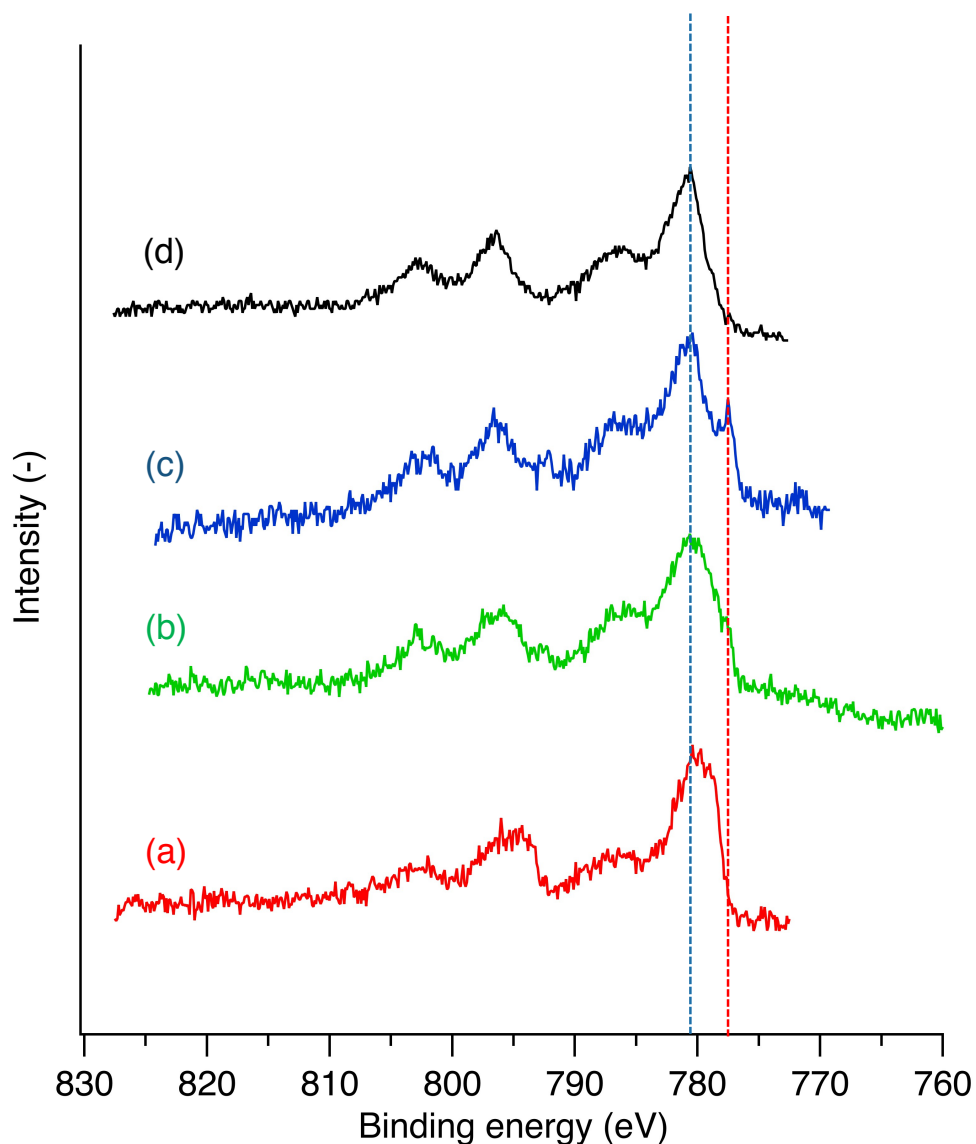


Figure 3.8. Co 2p XPS spectra of catalysts: (a) only calcined (in red), (b) calcined and reduced in the XPS auxiliary reaction chamber (in green), (c) calcined and reduced (in blue) and (d) calcined, reduced and passivated (in black). The vertical dashed blue line indicates the binding energies of Co^{2+} and Co^{3+} , and the red line indicates the expected binding energy of Co^0 .

The binding energies of Co 2p signals of different Co species are located around 780 eV: at 781.5 eV for Co^{2+} , at 779.8 eV for Co^{3+} and at 778.0 eV for Co^0 .^{32,30} For the calcined sample (a) only the Co^{2+} and Co^{3+} signals are visible. For the sample reduced *in situ* (b) still the $\text{Co}^{2+}/\text{Co}^{3+}$ signal is visible and intensive, but a broadening towards lower binding energies

is noticed. It indicates the presence of some Co^0 species. For sample (c), which was reduced the same day as the analysis was performed, and was not passivated, on the spectra the Co^0 signal is clearly visible. However, still Co^{2+} and Co^{3+} components are present. The spectra for sample (d), which was calcined, reduced and passivated before the analysis, looks similar to the spectra of sample (a), indicating that the Co^0 species formed during reduction re-oxidized into $\text{Co}^{2+}/\text{Co}^{3+}$ species.

For samples (b) and (c) we would expect only the signals from Co^0 , which is not the case. As XPS is a surface technique, and Co is oxophilic metal, even short contact with air (unavoidable during catalyst manipulation) causes the oxidation of metal NPs on the surface. Hence, Co^{2+} and Co^{3+} signals may appear in the spectra. Another explanation of the presence of these species may be that they come from non-saturated cobalt species, on metal-support interface. Also, at 400°C the metal reduction might not be complete, and the cationic cobalt species may come from non-reduced cobalt oxide. No strong evidence exists for any of these possibilities.

The spectra deconvolution is in progress, however the analysis already allowed us to confirm the partial reduction of cobalt oxide to metallic cobalt species at 400°C . Also, it proved the formation of cobalt oxide protecting layer during the catalyst passivation.

3.1.6. Characterization – summary

Different characterization techniques allowed us to investigate the physico-chemical properties of the catalysts. The 5 wt% metal loading of the samples was confirmed by ICP-OES elemental analysis. N_2 physisorption indicated that the specific surface area of the materials does not evolve during thermal treatment.

Based on XRD analysis for Co catalysts supported on different types of TiO_2 , ZrO_2 and ZnO we can conclude that they were reduced to metallic Co. In most of the cases the signals from metallic Co and support are overlapping, but main signals from Co_3O_4 and/or CoO were not visible, indicating the formation of metallic species. For $\text{Co}/\gamma\text{-Al}_2\text{O}_3$ such assessment was not possible as the signals from support overlap with signals from cobalt oxides and metallic Co. On the other hand, the analysis of Co/C confirmed that it was not reduced to metal at 400°C .

To investigate more the reducibility of different catalysts TGA-H₂ analysis was conducted. It showed that Co/C and Co/ γ -Al₂O₃ were not reduced in 400°C, which is in agreement with the XRD results. On the contrary, the other catalysts showed easier reducibility. The temperature of reduction depends on the support, even for the different TiO₂. This analysis also revealed, that the CoO passivation layer is evolving with time, and may lead to catalyst oxidation, hence lower activity and even deactivation.

Due to low contrast between Co NPs and TiO₂ support it was not possible to assess the nanoparticle size distribution, neither crystallographic phase by TEM. XPS analysis proved that during the reduction some Co⁰ species are formed. However, they are re-oxidized into cobalt oxide during the passivation treatment.

All in all, the characterization results showed that Co/TiO₂, Co/ZrO₂ and Co/ZnO should be good candidates for catalysts in acceptor-less alcohol dehydrogenation reaction, due to the presence of metallic Co NPs. The results also revealed, that for Co/C and Co/ γ -Al₂O₃ higher reduction temperature than 400°C are required. Moreover, due to the oxophilicity of the metal, care should be taken about the catalyst handling and holding (aging).

3.2. Catalytic tests results

The aim of acceptor-less alcohol dehydrogenation is to obtain selectively carbonyl product (aldehyde or ketone) and H₂ from the corresponding primary or secondary alcohol. Catalytic reactions were conducted in a semi-batch glass reactor (see Chapter 2.4.1. for details). The necessary inert atmosphere during the reaction was assured by constant flow of inert gases (30 mL min⁻¹, 10% N₂/Ar). In this way it was also possible to remove the produced H₂ from the reaction environment, and thus push the reaction equilibria towards products. The experiments were conducted for 24 h, at 145°C, and with mechanical stirring (750 rpm). 500 mg of supported catalysts were used (1 mol% of metal to alcohol) for all the catalytic tests in this Chapter.

Co/TiO₂ P25 was used as our benchmark catalyst. It was prepared by wet impregnation method, and subsequently calcined at 300°C in air flow, reduced under H₂ flow at 400°C, and passivated in 1%O₂/N₂. First, the effects of the solvent, catalyst aging and activation by

in situ H₂ pre-treatment were investigated in the dehydrogenation of 2-octanol. Afterwards, the support effect on the activity of secondary alcohol dehydrogenation was studied. For the most active catalysts, we examined their recyclability and activity towards the dehydrogenation of 1-octanol. As a final stage of our investigation, catalytic activity towards 1,2-octanediol dehydrogenation of chosen catalysts was investigated, closing us to the aimed dehydrogenation of (biomass-derived) polyols.

3.2.1. Solvent effect

Solvent effect was investigated using the benchmark Co/TiO₂ P25 catalyst for 2-octanol dehydrogenation reaction. At first, the catalytic tests to establish the reaction conditions were conducted with *o*-xylene, as it is a solvent reported in the literature for acceptor-less alcohol dehydrogenation.^{4,1} However, due to the encountered issues with one batch of supplied *o*-xylene (solvent impurities were poisoning our catalyst), we decided to investigate if the choice of solvent has an effect on the catalyst activity and selectivity. The other tested solvents were: decane, diisopentyl ether, γ -valerolactone (GVL), dimethyl sulfoxide (DMSO). They were chosen because of their high boiling temperatures, allowing to conduct the reaction in liquid phase at temperature around 150°C, and because of their miscibility with the studied alcohol(s).

The progress of the reaction was monitored by the analysis of liquid samples collected periodically during the reaction (analysis of alcohol conversion and carbonyl product yield), and by measuring the H₂ production during the reaction (by on-line GC analysis). The integration of H₂ signals with time allowed also to calculate the H₂ yield. The results for 2-octanol dehydrogenation using Co/TiO₂ P25 catalyst, and *o*-xylene as solvent are gathered in Figure 3.9. They represent the typical plots obtained during the catalytic tests.

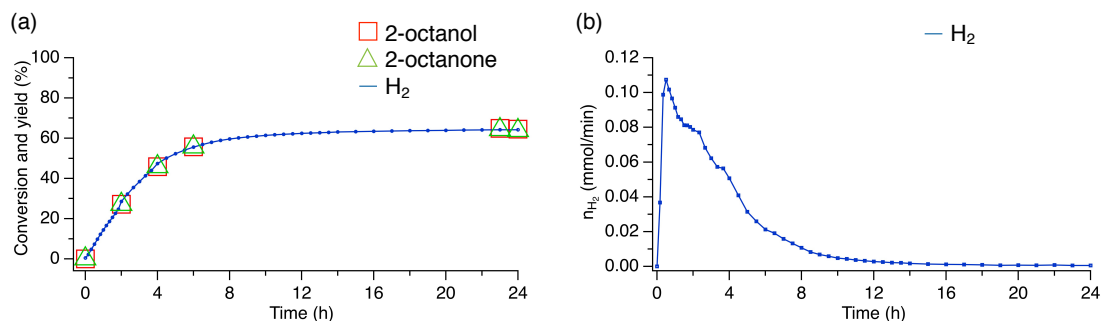


Figure 3.9. (a) Conversion of alcohol (□) and yields of ketone (△) and H₂ (—) vs time, (b) H₂ production vs time, for 2-octanol dehydrogenation over Co/TiO₂ P25 catalyst, in o-xylene solvent.

As visible on the graph, the accuracy between 2-octanol conversion (65% in this case), 2-octanone yield (64%) and H₂ yield (64%) is very good, confirming the acceptor-less mechanism of alcohol dehydrogenation. The reaction progresses intensively, until it starts to be close to the equilibria. But it will never reach it, as we are working in a system where one of the products is constantly removed from the reactor. Considering H₂ production a short induction time (in here 20 min) is observed until the catalyst reaches the maximum activity (expressed by maximal intensity of H₂ production). Then it gradually decreases, to become only traces at the end of the reaction.

Table 3.3. Conversion, selectivity and yields of 2-octanone and H₂ for the dehydrogenation of 2-octanol in different solvents. Reaction conditions: 500 mg of Co/TiO₂ P25, 0.95 mol L⁻¹ 2-octanol, 24 h, 145°C, V_{total} = 45 mL.

Solvent	X (%)	S (%)	Y (%)	Y _{H₂} (%)
Decane	70	98	69	64
Diisopentyl ether	64	>99.9	64	65
o-Xylene	65	99.0	64	64
GVL	0	n.a.	0	0
DMSO	0	n.a.	0	0

n.a. - not applicable

The results obtained after 24 h of 2-octanol dehydrogenation with Co/TiO₂ P25 in different solvents are gathered in Table 3.3. The highest conversion was observed when decane was used as the solvent. Slightly lower conversions were obtained with diisopentyl ether and o-xylene. In diisopentyl ether no by-products formation was observed, whereas in decane and o-xylene small amounts of additional substances were noticed. In the literature it is reported that the by-products are coming from the aldol condensation reaction.^{33,34} Also, the esterification reaction is possible.^{35,36} Moreover, the subsequent hydrogenation of condensation and/or esterification product with H₂ obtained in alcohol dehydrogenation cannot be excluded. All the observed by-products are C16 substances. However, it was not possible to identify exactly their structures (by GC-MS), due to their low amounts, the fact that there are not commercially available and their high similarity between them. In GVL and DMSO no conversion occurred. Moreover, while the test was conducted in GVL the reaction solution changed color from colorless to blue, suggesting that the catalyst was not stable and formation of cobalt-solvent complexes took place. After the reaction in DMSO the characteristic aroma of sulfates were noticeable from the reaction medium, also indicating that the catalyst and/or solvent were not stable in this reaction conditions.

To the best of our knowledge the solvent effect had never been investigated in the acceptor-less alcohol dehydrogenation. Based on these results we observe that the chosen solvent can influence the activity and/or selectivity of the catalyst. As decane occurred to be the most inert solvent, we decided to use it for further catalytic tests.

3.2.2. Catalyst post-treatment, aging and activation

Cobalt is an oxophilic metal, which easily interacts with O₂. Passivation of catalysts is conducted in order to create a tiny (ideally 1 monolayer thin) layer of oxide on the metal NPs surfaces, protecting it against the uncontrolled oxidation by air and (complete) deactivation.³⁷ Hence, our aim was to check: if and how the duration of catalyst post-treatment (passivation) can influence the catalyst activity and/or selectivity; if the protecting oxide layer can evolve with time (influence of catalyst aging); and if the *in situ* H₂ pre-treatment (pointing at removing the protecting layer of oxide) can enhance the catalysts performance. Co/TiO₂ P25 catalysts, for which different lengths of post-treatment and different aging times were applied, were tested in 2-octanol dehydrogenation, with decane as the solvent.

Table 3.4. Conversion, selectivity and yields of 2-octanone and H₂ in dehydrogenation of 2-octanol after catalyst aging. Reaction conditions: 500 mg of Co/TiO₂ P25, 0.95 mol L⁻¹ 2-octanol, decane, 24 h, 145°C, V_{total} = 45 mL.

Entry	Passivation (h)	Time between reduction and reaction	<i>In situ</i> H ₂ pre-treatment	X (%)	S (%)	Y (%)	Y _{H₂} (%)
0 - blank reaction	n.a.	n.a.	n.a.	4	n.a.	n.a.	0
1	none	1 week	No	70	95	66	58
2	0.5	The same day	No	70	98	69	64
3			Yes	69	99	69	66
4		2 weeks	No	73	96	70	63
5			Yes	77	98	76	75
6		6 months	No	1	n.a.	n.a.	0
7			Yes	65	94	61	59
8	2	The same day	No	71	96	68	66
9		2 weeks	No	50	99	50	45
10			Yes	64	98	63	61

n.a. - not applicable

Catalyst passivation was conducted at room temperature in 1%O₂/N₂ after reduction. When we compare the activity of catalyst passivated for 0.5 h (entry 2) and 2 h (entry 8), tested directly after synthesis, we do not observe differences in their activity (conversion 70-71%). Moreover, the non-passivated catalyst (entry 1), transferred to the reactor via a glovebox, exhibit similar results. This suggests that the passivation treatment does not affect the catalytic results when the catalyst is used directly after synthesis. However, when the catalyst is stored for two weeks before testing, the catalyst passivated for 2 h (entry 9) showed lower activity than the catalyst passivated only for 0.5 h (entry 4). This indicates that the CoO layer is thickening with time and this phenomenon is more important when the passivation was conducted for longer time.

Considering the influence of aging on catalytic activity, when the time between the catalyst reduction-passivation and reaction is really long (i.e. few months), then the catalytic activity decreases. Indeed, for the catalyst passivated for 0.5 h and tested 6 months after reduction-passivation (entry 6), complete loss of activity is observed. It is in agreement with TGA-H₂ results, where there were no significant differences between the catalyst tested the same day and after 2 weeks. However, the thermogravimetry analysis revealed the presence of bulk

CoO on the catalyst reduced 6 months earlier, which must be the cause for the absence of activity.

Wolf et al. showed that the passivation in diluted oxygen (1%O₂/N₂) leads to the creation of CoO layer on the surface of Co/SiO₂ catalyst, even at 30°C.¹³ However, this treatment was not suitable for long-term protection, due to on-going slow oxidation of catalyst. Moreover, they observed, that the re-reduction of partially oxidized Co NPs was easier than the reduction of calcined catalyst. The re-reduction requires much shorter time (0.5 h instead of 10 h, at 400°C, with heating rate of 2 °C min⁻¹) to re-gain the catalyst activity. These observations are in agreement with ours. Also, as it was reported in the literature by Vu et al., *in situ* H₂ pre-treatment can re-activate the catalyst.³⁸ During the dehydrogenation of vicinal diol in liquid phase with Ru/C and Ru/Al₂O₃ catalysts, they observed that the catalysts started to be active only after few hours of reaction (4-5 h). Hence, they decided to treat them with H₂, under the reaction conditions (atmospheric pressure of H₂, 1 h, 175°C). This re-activated the catalyst, which resulted in the immediate observation of activity.

Motivated by the above described findings we also wanted to check if it would be possible to re-activate the Co/TiO₂ P25 catalyst by *in situ* H₂ pre-treatment, under the reaction conditions. The catalyst and part of the solvent (30 mL) were heated up to 145°C and treated with a mixture of H₂ (10 mL min⁻¹) and inert gases (30 mL min⁻¹). The catalyst with a thin CoO layer (passivated 0.5 h and tested the same day and 2 weeks later, entries 3 and 5) did not show any improvement of activity. However, for the catalyst with thicker oxide layer on the surface the change was noticeable. H₂ pre-treatment of the catalyst passivated for 2 h and tested 2 weeks after reduction (entry 10), allowed to increase the conversion up to 64%, which is close to the one obtained with the catalyst tested on the same day. And the catalyst passivated for 0.5 h and reduced 6 months before the reaction it allowed to re-gain activity. In this reaction 65% of conversion was obtained. What is worth to notice, the H₂ production for the *in situ* pre-treated catalysts started immediately, whereas for the non-pre-treated catalysts it was increasing gradually.

Passivation is associated with the formation of a monolayer of CoO layer. However, oxidation of the catalyst proceeds with time. This phenomenon is more intensive when the passivation is conducted for longer time. It is possible to re-activate the catalyst by performing *in situ* H₂ pre-treatment. But still freshly reduced catalyst is the most active towards 2-octanol

dehydrogenation. The further catalytic tests were performed with the catalysts reduced and passivated for 0.5 h no longer than 2 weeks before the reaction. The additional H₂ pre-treatment was not applied for them.

3.2.3. Cobalt precursor

We looked at the effect of the metal precursor on Co/TiO₂ P25, as it can influence the metal NPs size, and their activity (by the presence or absence of remained precursor ions). The Co/TiO₂ P25 synthesized with Co(NO₃)₂ · 6H₂O and with CoCl₂ · 6H₂O (named respectively Co/TiO₂ P25 and Co_{Cl}/TiO₂ P25) were tested towards 2-octanol dehydrogenation. The second catalyst was hardly active (Table 3.5), strictly indicating the importance of metal precursor used in the synthesis. By XRD analysis we observed the formation of much bigger metal nanoparticles from cobalt chloride than from cobalt nitrite (54 nm vs <10 nm), that must have influenced the catalyst activity (by decreasing the available NPs surface and/or interface between NPs and support). We also have to take into consideration that despite the treatment at 400°C, Cl⁻ ions may still be present on the catalyst surface and poison it by blocking the active sites.³⁹

Table 3.5. Influence of used metal precursor. Reaction conditions: 500 mg of catalyst, 0.95 mol L⁻¹ 2-octanol, decane, 24 h, 145°C, V_{total} = 45 mL.

Catalyst	X (%)	S (%)	Y (%)	Y _{H₂} (%)
Co/TiO ₂ P25	70	98	69	64
Co _{Cl} /TiO ₂ P25	5	n.a.	n.a.	1

n.a. - not applicable

3.2.4. Support effect in catalytic dehydrogenation of 2-octanol

Another factor which may influence the metal catalyst activity is the type of support. As it was already described in Chapter 1, the nature of the support can greatly influence the activity of supported catalysts in acceptor-less alcohol dehydrogenation. Shimizu et al. showed that Co/TiO₂ outperforms the Co catalysts supported on different carriers in the dehydrogenation of cyclododecanol.¹ At first, we used supports of different nature (Table 3.6): amphoteric (TiO₂ P25, ZrO₂, γ-Al₂O₃), neutral (C), and basic (ZnO). Among these catalysts Co/TiO₂ P25 gave

the highest conversion of 2-octanol (70%), with very good selectivity towards 2-octanone and H₂. Co/ZrO₂ catalyst was only slightly active, with 10% of conversion. By TGA-H₂ analysis it was observed that the reduction of CoO into Co occurs around 440°C on that support. However, the XRD analysis did not allow to confirm the formation of metal nanoparticles of Co, which are supposed to be the active species in the reaction. Therefore, it is hard to conclude if the lower activity is purely the effect of support, or the effect of not reduced enough metal NPs.

Co/C and Co/γ-Al₂O₃ were not active for this reaction. The TGA-H₂ analysis showed that a reduction at 400°C is not enough to reduce the cobalt oxides. Therefore, the Co/C and Co/γ-Al₂O₃ catalysts were also tested after reduction at 600°C (named Co₆₀₀/C and Co₆₀₀/γ-Al₂O₃). However, no improvement was observed and the conversion remained negligible. Different reasons may explain this absence of activity: either the Co oxides are still not fully reduced at 600°C, and hence NPs are still not active, or large particles are formed due to the higher reduction temperature.

Co/ZnO was neither active in the catalytic test. Even though complete reduction of CoO into Co is reached at 400°C, large particles of Co were formed, as shown by XRD ($d_{Co} = 17$ nm), which might not be active for dehydrogenation reaction. Another reason may be the basic character of the ZnO support, and hence it may not be favoring the reaction.

Shimizu et al. investigated the influence of the support on the catalytic activity in the dehydrogenation of cyclododecanol.¹ According to their results Co/TiO₂ was the most active catalyst, giving 39% of alcohol conversion. It was followed by Co/γ-Al₂O₃, Co/C and Co/ZrO₂, which gave 15%, 10% and 9% of alcohol conversion, respectively. On one side, this confirms our findings that Co/TiO₂ is the best performing catalyst, and that Co/ZrO₂, another catalyst with amphoteric support, is also active in this reaction. On the other hand, Co/γ-Al₂O₃ and Co/C were not active in the reaction of 2-octanol, in contrast to the results in the paper. The reason is not the reduction thermal treatment of the catalysts, which in both studies were performed at 400°C for 0.5 h before the reaction. The activity difference may come from the different properties of the supports. Shimizu et al. obtained γ-Al₂O₃ by calcination of γ-AlOOH, whereas we used the commercially available γ-Al₂O₃ from Degussa. Hence, we suppose that the two Al₂O₃ differ in the crystallographic composition, what could influence the activity of catalysts. Considering activated carbon as a support, they possess different

specific surface areas of 296 m² g⁻¹ and 1095 m² g⁻¹, which signalizes that the materials differ in porosity (meso- and microporosity, respectively). It could influence the dispersion, reducibility and crystallinity of metal species on these supports, and by this vary their activity. Size effect was not investigated in the literature for cobalt supported catalysts. However, some examples are reported for other metals: Pt/ γ -Al₂O₃,⁴⁰ Au/HT,^{41,42,43} Ag/Al₂O₃,⁴⁴ Ni/ θ -Al₂O₃.⁴ With the increase of metal NPs size, their activity was decreasing. In the alcohol dehydrogenation reaction mechanism both metal NPs and support take part (see Chapter 1.2.2). Hence, while the size of metal NP increases, its surface area decreases, and by this fewer active sites are available. Also, for larger metal nanoparticles the available metal-support interface is decreased, what as well diminishes the amount of available active sites. For Co/ZnO we observed the formation of larger metal NPs (17 nm vs <10 nm for the other catalysts). Hence, it can justify the lack of its catalyst activity in the reaction. However, the effect of the basic nature of ZnO support cannot be excluded.

Table 3.6. Support effect in 2-octanol dehydrogenation. Reaction conditions: 500 mg of catalyst, 0.95 mol L⁻¹ 2-octanol, decane, 24 h, 145°C, V_{total} = 45 mL.

Catalyst	X (%)	S (%)	Y (%)	Y _{H₂} (%)
Co/TiO₂ P25	70	98	69	64
Co/ZrO₂	10	>99.9	10	7
Co/C	3	n.a.	n.a.	0
Co₆₀₀/C	3	n.a.	n.a.	0
Co/γ-Al₂O₃	2	n.a.	n.a.	0
Co₆₀₀/γ-Al₂O₃	2	n.a.	n.a.	0
Co/ZnO	3	n.a.	n.a.	0
Co/TiO₂ P90	72	90	65	62
Co/TiO₂ home made	66	95	63	62
Co/TiO₂ DT51D	3	n.a.	n.a.	0
Co/TiO₂ SGNH	30	99.5	30	29

n.a. - not applicable

To better understand the reason of the high activity of Co/TiO₂ P25, the catalytic performance of Co supported on different types of TiO₂ (Table 3.6) were examined. Beside TiO₂ P25 (containing: 25% of rutile and 75% of anatase), we used also TiO₂ home made (20% rutile + 80% anatase), TiO₂ P90 (10% rutile + 90% anatase), TiO₂ DT51D (100% anatase) and TiO₂ SGNH

(100% anatase). Co supported on TiO₂ being a mixture of rutile and anatase showed good catalytic activity, between 66% and 72%. Co supported on anatase SGNH gave 30% of 2-octanol conversion, whereas Co supported on TiO₂ anatase DT51D was not active. No significant differences between these catalysts were observed by XRD and TGA-H₂ analysis. We suspect that the support preparation plays a crucial role. Indeed, TiO₂ SGNH was obtained by sol-gel non-hydrolytic method, using chloride precursor, whereas TiO₂ DT51D is obtained by precipitation from sulfates. The final SO₃⁻ ions content of the commercial support is <0.6%. We cannot exclude that the residual SO₃⁻ ions may poison the Co metal.¹² The selectivities reported in Table 3.6 are the ones at final reaction time (24h). It is worth to notice that at low conversion all the catalysts were fully selective towards 2-octanone and H₂, whereas, at high conversions the selectivity decreased (in the worst case to 90%). By-products started to be observed at conversion exceeding around 30%. For comparison Shimizu et al.¹ reported a selectivity of 92% after 12h of reaction, at conversion of 85%. However, they did not consider the evaluation of selectivity with increasing conversion.

3.2.5. Catalyst recyclability

Recyclability tests were conducted using Co/TiO₂ P25 and Co/TiO₂ P90 catalysts, the most active catalysts in 2-octanol dehydrogenation (model secondary alcohol). At first, the catalytic tests were conducted with doubled amount of catalysts (1000 mg) to get enough material for recyclability test. After reactions, the solids were recovered by filtration, subsequently washed with ethanol and dried under N₂ atmosphere. For the recyclability tests, 500 mg of them were used. The *in situ* H₂ pre-treatments were conducted to re-activate the used materials before the reactions.

In the second run, the used Co/TiO₂ P25 catalyst gave lower conversion of 2-octanol than in the first run (with standard 500 mg mass of catalyst, 70% vs 49%). However, this difference may be caused by not complete re-activation of the catalyst. Probably 1 h of treatment with flowing H₂ was not enough to re-reduced the formed cobalt oxide(s) into metallic Co. Co/TiO₂ P90 also gave lower conversion in the second catalytic run (72% vs 23%). Moreover, whereas the activity of both catalysts in the first run was comparable, the used Co/TiO₂ P25 gave much better performance than the used Co/TiO₂ P90, indicating its better stability in the reaction conditions.

Table 3.7. Catalytic recyclability test for Co/TiO₂ catalysts. Reaction conditions: 500 mg of catalyst, 0.95 mol L⁻¹ 2-octanol, decane, 24 h, 145°C, V_{total} = 45 mL.

Catalyst	Reaction run	X (%)	S (%)	Y (%)	Y _{H₂} (%)
Co/TiO ₂ P25	1 st	70	98	69	64
	2 nd	51	>99.9	51	47
Co/TiO ₂ P90	1 st	72	90	65	62
	2 nd	23	>99.9	23	19

3.2.6. Catalytic dehydrogenation of 1-octanol

For the two catalysts which were the most active in 2-octanol dehydrogenation, namely Co/TiO₂ P25 and Co/TiO₂ P90, we conducted the catalytic dehydrogenation of 1-octanol (chosen primary alcohol), under the same reaction conditions as for the secondary alcohol. The results are included in Table 3.8.

As reported in the literature, catalysts usually show lower activity towards dehydrogenation of primary alcohols vs secondary alcohols. This difference in activity is visible especially for the dehydrogenation of aliphatic linear alcohols (See Chapter 1.1.3). Co/TiO₂ P25 catalyst showed low activity (10% conversion) in dehydrogenation of 1-octanol, and not complete selectivity towards octanal and H₂. Some alcohol condensation C16 products were additionally observed as side products (mixture of them; originating from aldol condensation and/or esterification and possible sequential hydrogenation). Co/TiO₂ P90 catalyst was almost not active for this reaction, but some traces of formed by-products were already observed at a few percent of conversion.

Table 3.8. Catalytic dehydrogenation of 1-octanol. Reaction conditions: 500 mg of catalyst, 0.95 mol L⁻¹ 1-octanol, decane, 24 h, 145°C, V_{total} = 45 mL.

Catalyst	X (%)	S (%)	Y (%)	Y _{H₂} (%)
Co/TiO ₂ P25	10	86	9	9
Co/TiO ₂ P90	2	n.a.	2	2

n.a. - not applicable

3.2.7. Catalytic dehydrogenation of 1,2-octanediol

The dehydrogenation of 1,2-octanediol was performed using doubled mass of catalyst (1000 mg) due to the presence of 2 hydroxyl groups in the alcohol structure. 1-hydroxy-2-octanone (product of secondary OH group dehydrogenation) was expected as the main, desired product, due to the better activity of catalysts in 2-octanol dehydrogenation. However, the formation of 2-hydroxyoctanal (primary OH dehydrogenation product) and 2-oxooctanal (product of primary and secondary OH group dehydrogenation) could not be excluded.

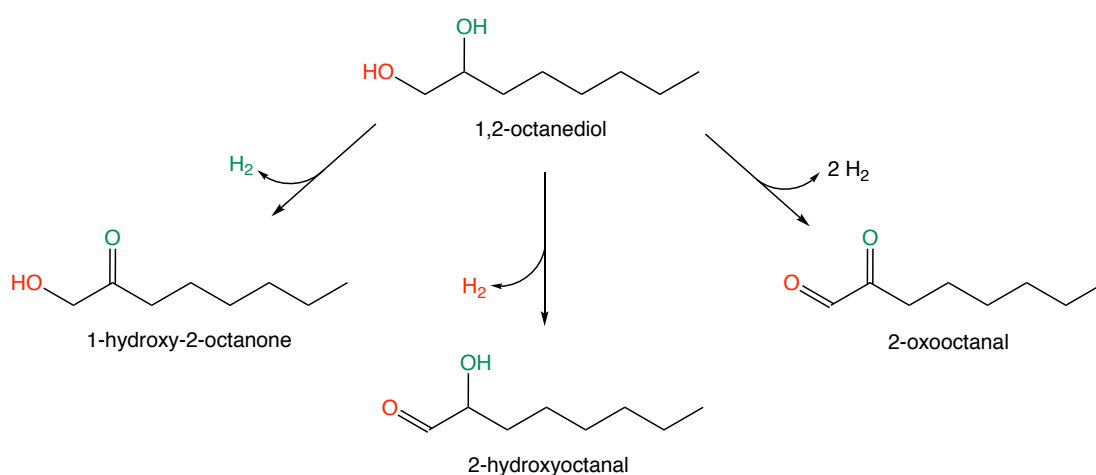


Figure 3.10. Scheme of the possible 1,2-octanediol dehydrogenations.

Co/TiO₂ P25 and Co/TiO₂ P90 gave 33% and 25% of alcohol conversion, respectively. The main reaction product was 1-hydroxy-2-octanone, but none of the catalysts were totally selective towards its formation (90% and 69% for Co/TiO₂ P25 and Co/TiO₂ P90, respectively). However, the observed by products were C16 condensation products, not the simple OH group dehydrogenation products.

Based on the conversion and selectivity to the desired product, we can conclude that Co/TiO₂ P25 is the best catalyst for diol dehydrogenation. In the literature only one example of 1,2-octanediol dehydrogenation is available.⁴⁵ The reported reaction was conducted in solvent-free conditions at 175°C, using 0.35 mol% of Ni/SiO₂ catalyst: a conversion of 28% and a selectivity of 64% were reported. 2-octanone was observed as a by-product. The Co/TiO₂ P25 catalyst exhibits similar conversion, however for a higher metal to alcohol

ratio (1 mol% vs. 0.35 mol%). Nonetheless, it is more selective to the desired secondary OH group dehydrogenation product (90% vs 64% of selectivity reported in the paper).

Table 3.9. Catalytic dehydrogenation of 1,2-octanediol. Reaction conditions: 1000 mg of catalyst, 0.95 mol L⁻¹ 1,2-octanediol, decane, 24 h, 145°C, V_{total} = 45 mL.

Catalyst	X (%)	S (%)	Y (%)	Y _{H₂} (%)
Co/TiO ₂ P25	33	90	30	28
Co/TiO ₂ P90	25	69	18	21

3.2.8. Towards dehydrogenation of other diols

By screening (and understanding) the activity of different catalysts in dehydrogenation of model secondary and primary alcohols we aimed to determine the most active and selective catalysts in acceptor-less alcohol dehydrogenation reaction. Subsequently, in the reaction with model diol we verified their performance (activity and chemoselectivity), while two hydroxyl groups (primary and secondary) were present in the alcohol molecule at the same time. As our long-term goal was directed towards dehydrogenation of biomass-derived polyols, we wanted to broaden the scope of diols. 1,2-butanediol (1,2-BDO) and 1,3-butanediol (1,3-BDO) were selected as good candidates for this purpose. They were shorter chain aliphatic diols (more resembling the biomass-derived polyalcohols). Also, they differ in the distance between the OH groups, what will allow to assess if this alcohol structural parameter influences the catalyst performance.

However, the catalytic tests with 1,2-BDO and 1,3-BDO required the change of reaction solvent, as these diols were not miscible with decane. Among the other possible solvents (due to their high boiling point and inertness, see subchapter 3.2.1) only diisopentyl ether revealed to have potential. At room temperature none of the diols were miscible with it, but at elevated (reaction) temperature this property improved to an acceptable level. However, when collecting the liquid samples, the problem of miscibility of 1,3-BDO with diisopentyl ether prevented us to properly conduct the GC analysis; hence the result is not reported. The catalytic test result for 1,2-BDO dehydrogenation is presented in Table 3.10.

Table 3.10. Catalytic dehydrogenation of 1,2-butanediol. Reaction conditions: 500 mg of catalyst, 0.95 mol L⁻¹ 1,2-butanediol, diisopentyl ether, 24 h, 145°C, V_{total} = 45 mL.

Catalyst	X (%)	S (%)	Y (%)	Y _{H₂} (%)
Co/TiO ₂ P25	38	n.a.	7	33

n.a. - not applicable

According to the liquid sample analysis the conversion of 1,2-BDO was equal to 38%, in quite good agreement with H₂ production yield (33%), assuming that only one OH group was dehydrogenated. The only observed product in the liquid phase was 1-hydroxy-2-butanone, but its yield was only 7%. This was not in line with the rest of the analysis results. Probably, the formation of secondary (sequential) product from dimerization/polymerization of 1-hydroxy-2-butanone took place, resulting in the formation of products which were not observed by the used analytical methods. Hence, we see that broadening the scope of diol substrates is challenging at the moment.

3.3. Conclusions

Catalytic alcohol dehydrogenation requires elevated temperatures and inert atmosphere to proceed via the acceptor-less pathway. We established the catalytic tests conditions using a benchmark Co/TiO₂ catalyst, and proved the quantitative H₂ production during the reactions.

Cobalt is an oxophilic metal, and hence it can evolve (oxidize), depending on the treatment and handling. In the catalyst post-treatment (passivation) a CoO protecting layer is created, and assures the stability of catalyst for at least 2 weeks. However, this oxide layer is expanding with time, leading to the catalyst deactivation. But, it is possible to re-activate the catalyst by *in situ* H₂ pre-treatment before reaction. Also, the metal precursor used for the synthesis can dramatically influence the catalyst activity. Using cobalt chloride instead of cobalt nitrate, as the precursor the catalyst activity was suppressed almost entirely.

Motivated by the literature, we examined also the influence of the nature of support on the performance of Co catalysts. Supports of amphoteric nature appeared to favor the reaction, and TiO₂ outperformed ZrO₂. However, the activity of TiO₂ was influenced by its crystallographic composition, being the best for mixed anatase and rutile phases.

The 2-octanol dehydrogenation allowed to determine the most active catalysts: Co/TiO₂ P25 and Co/TiO₂ P90. In the recyclability tests their activity diminished, showing that they were not stable in the reaction conditions or not re-activated properly.

Still aiming at the dehydrogenation of biomass-derived polyalcohols, we determined the activity of some chosen catalysts towards dehydrogenation of model primary alcohol (1-octanol), to examine their chemoselectivity. The catalysts proved to be highly selective towards secondary alcohol dehydrogenation. This was also true in the dehydrogenation of 1,2-octanediol, the model diol. We wanted to further broaden the scope of diols, however, due to encountered problems with miscibility of solvent and alcohols, it still remains a challenge.

Bibliography

1. Shimizu, K. *et al.* Heterogeneous cobalt catalysts for the acceptorless dehydrogenation of alcohols. *Green Chem.* **15**, 418–424 (2013).
2. Dyson, P. J. & Jessop, P. G. Solvent effects in catalysis: rational improvements of catalysts via manipulation of solvent interactions. *Catal. Sci. Technol.* **6**, 3302–3316 (2016).
3. Singh, U. K. & Vannice, M. A. Kinetics of liquid-phase hydrogenation reactions over supported metal catalysts — a review. *Appl. Catal. A-Gen.* **213**, 1–24 (2001).
4. Shimizu, K., Kon, K., Shimura, K. & Hakim, S. S. M. A. Acceptor-free dehydrogenation of secondary alcohols by heterogeneous cooperative catalysis between Ni nanoparticles and acid–base sites of alumina supports. *J. Catal.* **300**, 242–250 (2013).
5. Mitsudome, T. *et al.* Copper nanoparticles on hydrotalcite as a heterogeneous catalyst for oxidant-free dehydrogenation of alcohols. *Chem. Commun.* 4804–4806 (2008). doi:10.1039/b809012b
6. Jacobs, G. *et al.* Fischer–Tropsch synthesis: support, loading, and promoter effects on the reducibility of cobalt catalysts. *Appl. Catal. A-Gen.* **233**, 263–281 (2002).
7. Riva, R., Miessner, H., Vitali, R. & Del Piero, G. Metal–support interaction in Co/SiO₂ and Co/TiO₂. *Appl. Catal. A-Gen.* **196**, 111–123 (2000).
8. Ji, L., Lin, J. & Zeng, H. C. Metal–support Interactions in Co/Al₂O₃ catalysts: a comparative study on reactivity of support. *J. Phys. Chem. B* **104**, 1783–1790 (2000).
9. Storsater, S., Totdal, B., Walmsley, J., Tanem, B. & Holmen, A. Characterization of alumina-, silica-, and titania-supported cobalt Fischer–Tropsch catalysts. *J. Catal.* **236**, 139–152 (2005).
10. Xaba, B. M. & de Villiers, J. P. R. Sintering behavior of TiO₂-supported model cobalt Fischer–Tropsch catalysts under H₂ reducing conditions and elevated temperature. *Ind. Eng. Chem. Res.* **55**, 9397–9407 (2016).
11. Kepp, K. P. A quantitative scale of oxophilicity and thiophilicity. *Inorg. Chem.* **55**, 9461–9470 (2016).
12. Tsakoumis, N. E., Rønning, M., Borg, Ø., Rytter, E. & Holmen, A. Deactivation of cobalt based Fischer–Tropsch catalysts: A review. *Catal. Today* **154**, 162–182 (2010).
13. Wolf, M., Fischer, N. & Claeys, M. Effectiveness of catalyst passivation techniques studied in situ with a magnetometer. *Catal. Today* **275**, 135–140 (2016).

14. Cai, J., Jiang, F. & Liu, X. Exploring pretreatment effects in Co/SiO₂ Fischer-Tropsch catalysts: different oxidizing gases applied to oxidation-reduction process. *Appl. Catal. B-Environ.* **210**, 1–13 (2017).
15. Perego, C. & Villa, P. Catalyst preparation methods. *Catal. Today* **34**, 281–305 (1997).
16. Hanaor, D. A. H., Assadi, M. H. N., Li, S., Yu, A. & Sorrell, C. C. Ab initio study of phase stability in doped TiO₂. *Comput. Mech.* **50**, 185–194 (2012).
17. Lee, B. W., Alsenz, R., Ignatiev, A. & Van Hove, M. A. Surface structures of the two allotropic phases of cobalt. *Phys. Rev. B* **17**, 1510–1520 (1978).
18. Panpranot, J., Kaewkun, S., Praserttham, P. & Goodwin, Jr., J. G. Effect of cobalt precursors on the dispersion of cobalt on MCM-41. *Catal Lett* **91**, 95–102 (2003).
19. Pan, Z. & Bukur, D. B. Fischer–Tropsch synthesis on Co/ZnO catalyst - effect of pretreatment procedure. *Appl. Catal. A-Gen.* **404**, 74–80 (2011).
20. Bosc, F., Ayral, A., Keller, N. & Keller, V. Room temperature visible light oxidation of CO by high surface area rutile TiO₂-supported metal photocatalyst. *Appl. Catal. B-Environ.* **69**, 133–137 (2007).
21. Morimoto, T., Nagao, M. & Tokuda, F. Desorbability of chemisorbed water on metal oxide surfaces. I. Desorption temperature of chemisorbed water on hematite, rutile and zinc oxide. *B. Chem. Soc. Jpn.* **41**, 1533–1537 (1968).
22. Yung, M., Holmgren, E. & Ozkan, U. Cobalt-based catalysts supported on titania and zirconia for the oxidation of nitric oxide to nitrogen dioxide. *J. Catal.* **247**, 356–367 (2007).
23. Paryjczak, T., Rynkowski, J. & Karski, S. Thermoprogrammed reduction of cobalt oxide catalysts. *J. Chromatogr.* 254–256 (1980).
24. Yuvaraj, S., Fan-Yuan, L., Tsong-Huei, C. & Chuin-Tih, Y. Thermal decomposition of metal nitrates in air and hydrogen environments. *J. Phys. Chem. B* **107**, 1044–1047 (2003).
25. Keely, W. M. & Maynor, H. W. Thermal studies of nickel, cobalt, iron and copper oxides and nitrates. *J. Chem. Eng. Data* **8**, 297–300 (1963).
26. Monti, D. A. M. & Baiker, A. Temperature-programmed reduction. Parametric sensitivity and estimation of kinetic parameters. *J. Catal.* 323–335 (1983).
27. Le, T. A., Kim, M. S., Lee, S. H. & Park, E. D. CO and CO₂ methanation over supported cobalt catalysts. *Top Catal* **60**, 714–720 (2017).
28. Sun, Y. *et al.* Effect of different activated carbon support on CH₄CO₂ reforming over Co-based catalysts. *International Journal of Hydrogen Energy* **43**, 1497–1507 (2018).

29. Goicoechea, S. *et al.* Support effect on structure and performance of Co and Ni catalysts for steam reforming of acetic acid. *Applied Catalysis A: General* **514**, 182–191 (2016).
30. Ferencz, Zs. *et al.* Reforming of ethanol on Co/Al₂O₃ catalysts reduced at different temperatures. *J. Catal.* **358**, 118–130 (2018).
31. H.F.J. Van't Blik, J.H.A. Martens, R. Prins. Characterization of supported cobalt and cobalt-rhodium catalysts. *J. Catal.* 200–209 (1986).
32. Zhu, J., Kailasam, K., Fischer, A. & Thomas, A. Supported cobalt oxide nanoparticles as catalyst for aerobic oxidation of alcohols in liquid phase. *ACS Catal.* **1**, 342–347 (2011).
33. Yi, J. *et al.* A reusable unsupported rhenium nanocrystalline catalyst for acceptorless dehydrogenation of alcohols through γ -C-H activation. *Angew. Chem. Int. Edit.* **53**, 833–836 (2014).
34. Sushkevich, V. L., Ivanova, I. I. & Taarning, E. Mechanistic study of ethanol dehydrogenation over silica-supported silver. *ChemCatChem* **5**, 2367–2373 (2013).
35. Neurock, M., Tao, Z., Chemburkar, A., Hibbitts, D. D. & Iglesia, E. Theoretical insights into the sites and mechanisms for base catalyzed esterification and aldol condensation reactions over Cu. *Faraday Discussions* **197**, 59–86 (2017).
36. Sad, M. E., Neurock, M. & Iglesia, E. Formation of C–C and C–O bonds and oxygen removal in reactions of alkanediols, alkanols, and alkanals on copper catalysts. *J. Am. Chem. Soc.* **133**, 20384–20398 (2011).
37. Huber, F. *et al.* Remarks on the passivation of reduced Cu-, Ni-, Fe-, Co-based catalysts. *Catal Lett* **110**, 211–220 (2006).
38. Vu, N. D., Guicheret, B., Duguet, N., Méta y, E. & Lemaire, M. Homogeneous and heterogeneous catalytic (dehydrogenative) oxidation of oleochemical 1,2-diols to α -hydroxyketones. *Green Chem.* **19**, 3390–3399 (2017).
39. Argyle, M. & Bartholomew, C. Heterogeneous catalyst deactivation and regeneration: a review. *Catalysts* **5**, 145–269 (2015).
40. Kon, K., Hakim Siddiki, S. M. A. & Shimizu, K. Size- and support-dependent Pt nanocluster catalysis for oxidant-free dehydrogenation of alcohols. *J. Catal.* **304**, 63–71 (2013).
41. Fang, W., Zhang, Q., Chen, J., Deng, W. & Wang, Y. Gold nanoparticles on hydrotalcites as efficient catalysts for oxidant-free dehydrogenation of alcohols. *Chem. Commun.* **46**, 1547–1549 (2010).

42. Fang, W., Chen, J., Zhang, Q., Deng, W. & Wang, Y. Hydrotalcite-supported gold catalyst for the oxidant-free dehydrogenation of benzyl alcohol: studies on support and gold size effects. *Chem-Eur J.* **17**, 1247–1256 (2011).
43. Chen, J., Fang, W., Zhang, Q., Deng, W. & Wang, Y. A comparative study of size effects in the Au-catalyzed oxidative and non-oxidative dehydrogenation of benzyl alcohol. *Chem. Asian J.* **9**, 2187–2196 (2014).
44. Shimizu, K. & Satsuma, A. Silver cluster catalysts for green organic synthesis. *J. Jpn. Petrol. Inst.* **54**, 347–360 (2011).
45. Guicheret, B. *et al.* A two-step oxidative cleavage of 1,2-diol fatty esters into acids or nitriles by a dehydrogenation-oxidative cleavage sequence. *ChemSusChem* **11**, 3431–3437 (2018).

Chapter 4

Activity of different cobalt hcp and fcc type surfaces toward alcohol dehydrogenation – DFT investigations

To achieve good catalytic performance, it is important to find an active metal in a given reaction. But to improve it, it is essential to understand the factors guiding the activity. As it was demonstrated in the literature, some reactions, like benzene hydrogenation¹ and styrene oxidation,² are structure (shape) sensitive. The type of exposed facet can influence the activity and/or selectivity of the catalyst.

Not much is known, up to now, about the shape sensitivity of acceptor-less alcohol dehydrogenation. Very recently two reports on Cu were published. In 2018, Hoyt et al. reported the DFT results,³ according to which the (100) and (111) steps exhibit superior activity in alcohol dehydrogenation over Cu(111) close-packed facet. In the next (2019) year, the report of He et al. appeared,⁴ in which the restructured Cu NPs, supported over SiO₂, shown higher activity over the non-modified NPs in catalytic EtOH dehydrogenation. This effect was ascribed to the transformation of NPs surfaces from the more faceted shape, into more spherical shape. DFT computations confirmed such hypothesis. According to the modeling Cu(111) facet was less active than the stepped (211) surface.

As we have shown in Chapter 3, Co supported catalysts are active in the acceptor-less alcohol dehydrogenation reaction. Nowadays, it is also possible to synthesize Co unsupported NPs, of well-defined shapes.⁵ By this, they are exposing defined and known crystallographic facets, which can exhibit different activity in alcohol dehydrogenation, what will be discussed in Chapter 5.

To shed light on the structure sensitivity of alcohol dehydrogenation with Co catalysts, the reaction was modeled by DFT on chosen hcp and fcc type metal surfaces. By the comparison of the adsorption energies for reaction species (thermochemistry), and the activation energies for bond breakings (kinetic), it was possible to determine the preferred reaction mechanism and also compare the activity of different facets. To better understand our results, we analyzed if the thermochemistry of elementary reactions correlates with their kinetics (BEP type relations), and if the adsorption energies of reaction species is conditioned by the geometry properties of surfaces (expressed with generalized coordination number, as surface geometry descriptor). In the last part of this chapter, the chemoselectivity, observed in the preliminary catalytic tests by our project partners from ITODYS in Paris, will be explained thanks to DFT calculations.

4.1. Population of different surfaces on unsupported Co NPs

Cobalt nanoparticles (Co NPs) can exist in two crystallographic forms: hexagonal close packed (hcp) or face centered cubic (fcc). The thermal transition between them (hcp \rightarrow fcc) is reported to take place around 450°C for bulk metal.⁶ Also by using different preparation methods it is possible to obtain hcp and/or fcc type NPs.^{7,8,9} The final shape and size of NPs depend on thermodynamic (stability of surfaces) and kinetic (rate of facets growing) factors.

Wulff construction¹⁰ is a method, which allows to determine the equilibrium shape of crystals of a given volume. It is based on the thermodynamic stability of facets and uses energy minimization arguments. Liu et al.¹¹ and Chen et al.¹² modeled free cobalt spherical NPs using this method. Based on the facets surface energies, they determined which ones are exposed and in which extent. Their results are collected in Table 4.1.

Table 4.1. Exposed facets, their surface energy and surface area participation in the total surface area of free Co hcp and fcc NPs, obtained by Wulff construction, according to the literature.^{11,12}

hcp Co NP					fcc Co NP		
Facet	E _s (meV Å ⁻²)		SA (%)		Facet	E _s (meV Å ⁻²)	SA (%)
	Liu et al. ¹¹	Chen et al. ¹²	Liu et al. ¹¹	Chen et al. ¹²		Liu et al. ¹¹	
(10-11)	149	152	35	29	(111)	127	70
(10-10)	140	143	28	28	(100)	154	12
(0001)	131	134	18	14	(311)	156	10
(10-12)	156	159	12	9	(110)	151	8
(11-20)	155	157	6	6			
(11-21)	163	166	1	1			
(10-15)	n.d.	154	n.d.	6			
(11-22)	n.d.	164	n.d.	6			
(11-24)	n.d.	165	n.d.	2			

E_s – surface energy

SA – surface area participation

n.d. – not determined

From the thermodynamic point of view the most exposed should be the most stable surface – surface of the lowest surface energy. For hcp and fcc NPs they are the close packed (the most densely packed) (0001) and (111) facets, respectively. Indeed, for fcc type Co NP the most exposed facet is close packed (111) surface, as favored by the thermochemistry, and it occupies 70% of total surface area of NP. Other, open type (100), (311) and (110) facets, occupy the rest of NP surface, each around 10% of total surface area. However, as appearing from the results, for hcp type Co NP the most exposed are open type (10-11) and (10-10) surfaces, occupying around 60% of particle surface, even though they are not the most stable facets. Close packed (0001) facet is occupying only around 14-18% of hcp Co NP surface. Also, other open type surfaces are present in noticeable amount, namely (10-12), (11-20), (10-15) and (11-22) facets.

Attempting to investigate the structure sensitivity of acceptor-less alcohol dehydrogenation, we choose the most exposed facets on hcp and fcc type cobalt NPs for modeling of our reaction. We computed the alcohol dehydrogenation pathways on five hcp type surfaces: (0001), (10-11), (10-10), (10-12) and (11-20), and on four fcc type facets: (111), (100), (110)

and (211) (which is a stepped surface similarly as (311)). On Figures 4.1-4. the images of them are presented, and the adsorption sites are marked.

For all of the surfaces two adsorption sites are common: top site and bridge site. By top site we name the adsorption at the top of a single metal atom, and by bridge position we mean the adsorption between two metal atoms distant by lattice constant value (for Co it is equal to 2.47 \AA , according to our computations). In the following paragraphs the appearance of different surfaces will be described shortly.

The hcp Co(0001) and fcc Co(111) are close-packed type surfaces (Figure 4.1). They resemble each other, as both possess 3-fold adsorption sites: hcp and fcc. However, they are not identical. In hcp type (0001) surface the metal layers are ordered as AB AB AB, and for fcc type (111) surface, layers are arranged as ABC ABC. Hence, for fcc site on (0001) facet no atom is present underneath, whereas for fcc site on (111) surface the metal atom from the 3rd layer is present. Due to the high similarities between Co(0001) and Co(111) they are expected to exhibit the same (or very similar) activity.

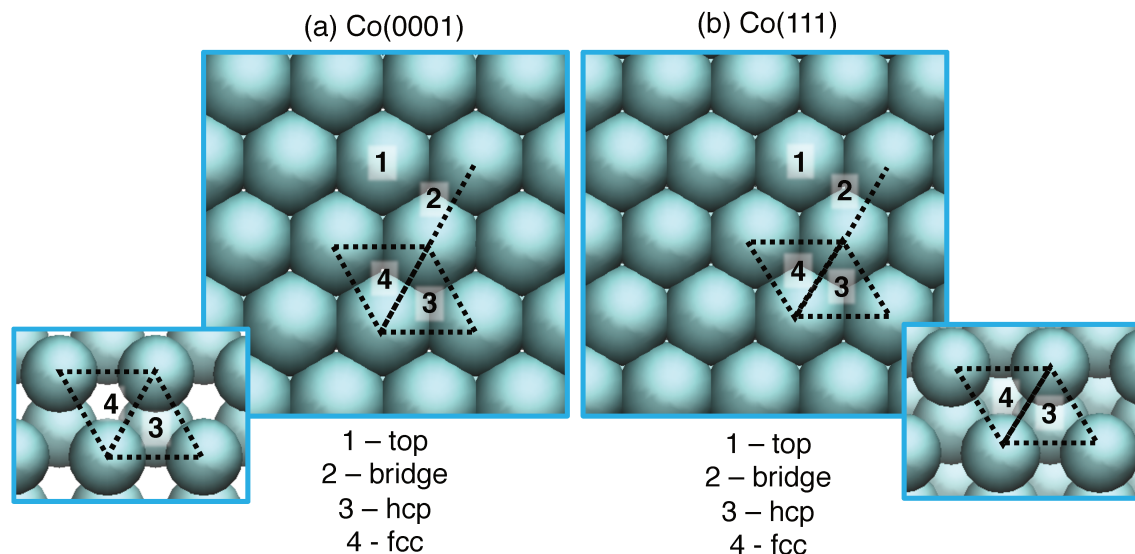


Figure 4.1. Close packed (a) hcp Co(0001) and (b) fcc Co(111) surfaces from the top view. Adsorption sites are marked on the pictures with numbers and explained below them. The insets refer to 3-fold adsorption sites and are presented with smaller atom radius, to highlight the differences.

Among the open type surfaces, hcp Co(10-11) and fcc Co(100) are the first possessing 4-fold (square) adsorption sites (Figure 4.2). The (100) is the most populated open type facet for fcc Co NP. When we take a look on its surface from top view, we will see that it is actually composed only from squares attached to each other, which are on the same altitude (see inset on Figure 4.2.b, representing the side view of the surface). (10-11) facet, despite 4-fold sites, possess also 3-fold fcc and hcp type sites. When we take a look on it from side view (inset on Figure 4.2.a) we will see that the atoms in the 1st layer do not have the same altitude. This reveals the similarity of this surface with the stepped (10-12) facet (Figure 4.4).

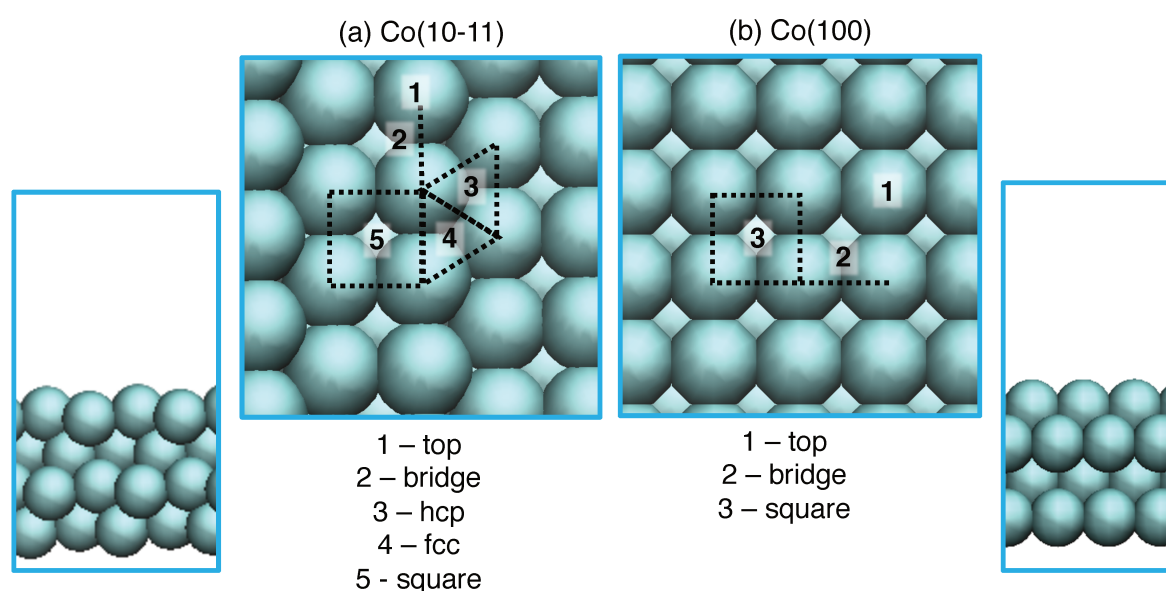


Figure 4.2. Open type (a) hcp Co(10-11) and (b) fcc Co(100) surfaces from the top view. Adsorption sites are marked on the pictures with numbers and explained below them. The insets refer to the side views of the surfaces.

Another group among the open type surfaces constitute the facets exposing rows, namely hcp (10-10) and (11-20), and fcc (110) (Figure 4.3). (10-10) and (110) facets are similar to each other, as they both expose straight rows. However, while comparing the altitudes of their rows, they are more exposed for the fcc (110) facet. Also, the surfaces differ in the intervals between rows. For (10-10) the interval between them is equal to ~ 1.6 times of metal interatomic distance, whereas for (110) this interval is equal to ~ 1.4 times the metal

interatomic distance. Hcp (11-20) surface is exposing the zig-zag type rows, which are shifted towards each other. It means that the corner of one row is in the opposite of the concave of another row. What is characteristic for all of these surfaces, they possess the adsorption position between the rows, which we call bridge between rows (bbr).

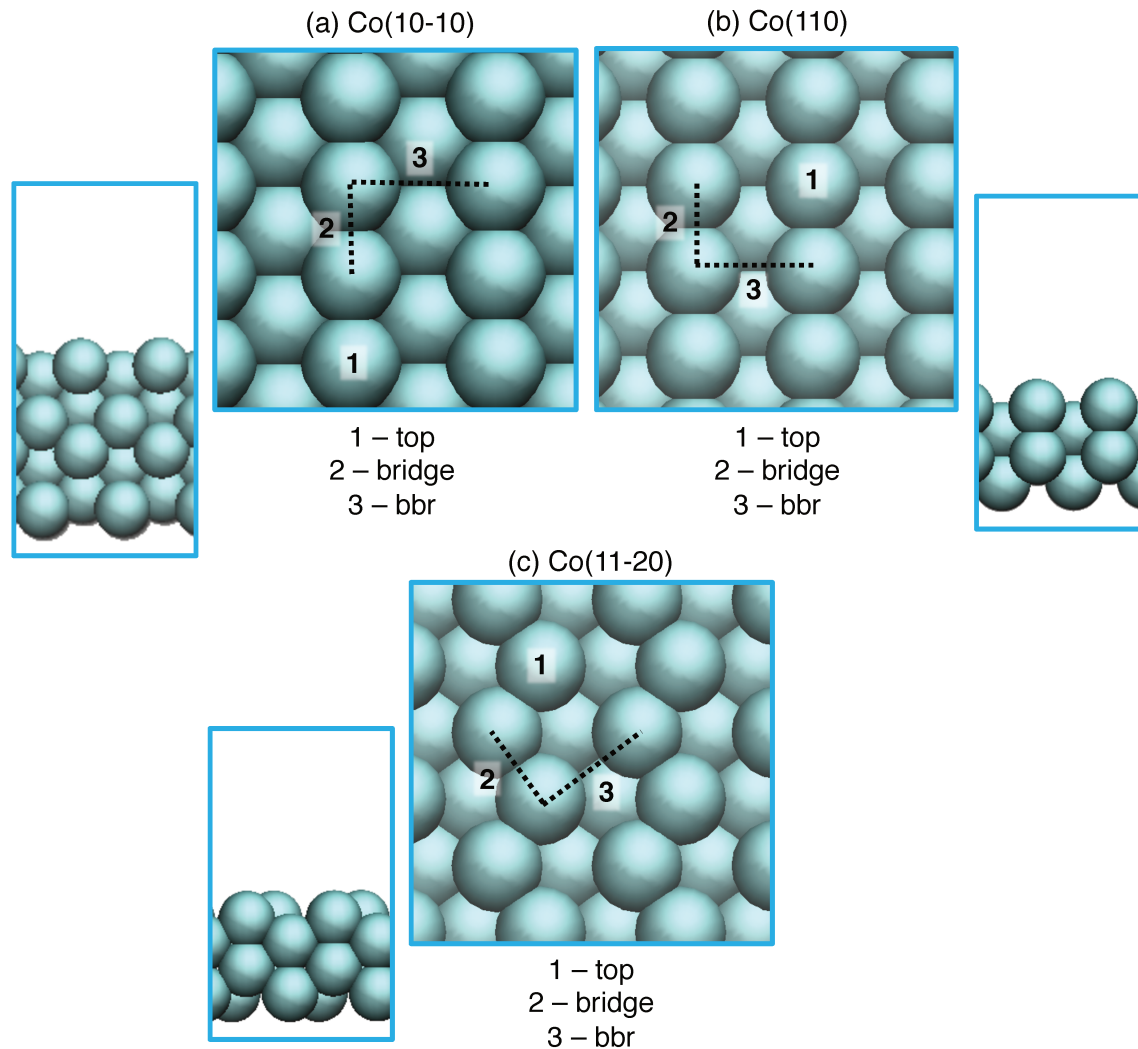


Figure 4.3. Open type (a) hcp Co(10-10), (b) fcc Co(110) and (c) hcp Co(11-20) surfaces from the top view. Adsorption sites are marked on the pictures with numbers and explained below them. The insets refer to the side views of the surfaces. 'bbr' stands for bridge between rows adsorption position.

Last, also the stepped hcp (10-12) and fcc (211) facets were considered. For them, the exposed metal layer is composed of rows attached to each other, which differ in the altitude – the 2nd row is lower than the 1st (the most exposed) row, and the 3rd row is located lower than the 2nd one. By top and bridge position on these surfaces we understand the ones on the 1st, the highest in altitude, row. The facets possess also the 3-fold and 4-fold coordinated sites. However, they are not between the same rows. For example, the square position for (10-12) facet is located between 1st and 2nd row, whereas for (211) surface it occurs between 1st and 3rd row (on the other side of 1st row). Hence, as it can be seen, they expose variety of sites.

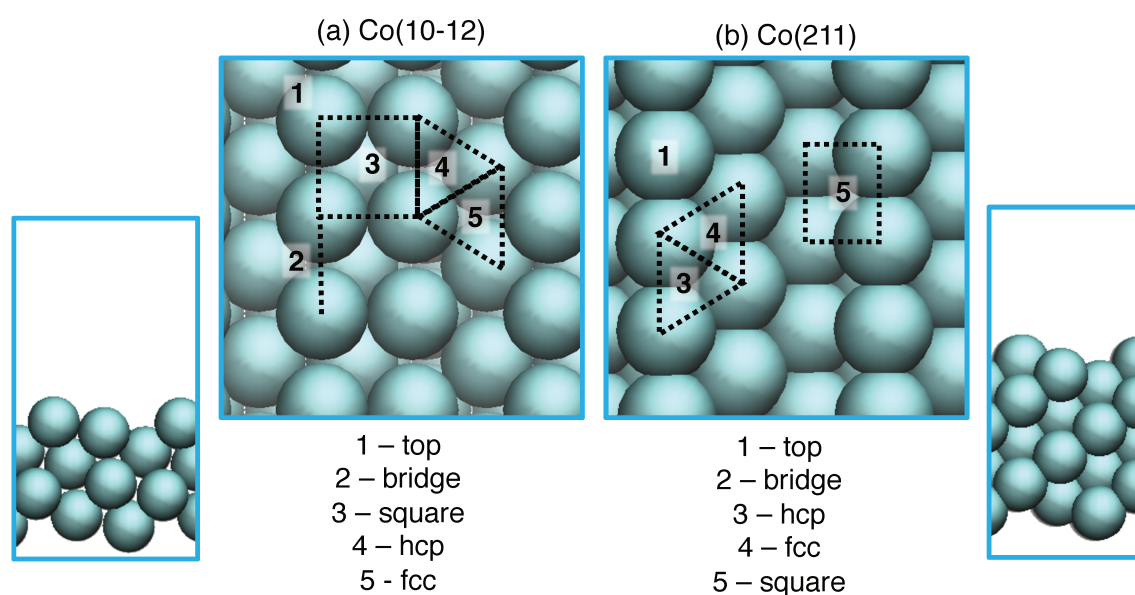


Figure 4.4. Open type (a) hcp Co(10-12) and (b) fcc Co(211) stepped surfaces from the top view. Adsorption sites are marked on the pictures with numbers and explained below them. The insets refer to the side views of the surfaces.

4.2. Alcohol dehydrogenation mechanisms

4.2.1. Mechanisms description

Catalytic acceptor-less dehydrogenation of alcohols can proceed through two mechanisms: alkoxy or hydroxyalkyl (Figure 4.5). Both of them start with the adsorption of alcohol molecule on the metal surface. Subsequently OH (alkoxy pathway) or CH (hydroxyalkyl pathway) bond

scissions are possible (on Figure 4.5 they structures are marked as TS OH and TS CH, respectively). In the alkoxy mechanism, breaking of OH bond leads to the formation of alkoxy intermediate, for which in the next step CH bond scission occurs (through TS OH-CH). It results in the formation of corresponding carbonyl product. In the hydroxyalkyl mechanism, after the CH bond dissociation, hydroxyalkyl intermediate is formed. It is followed by OH bond breaking (TS CH-OH), leading to the formation of final (the same) carbonyl product. The catalytic cycle is finished by desorption of carbonyl product and H₂ from the metal surface. In our computations, EtOH was used as a model primary alcohol and iPrOH was used as a model secondary alcohol.

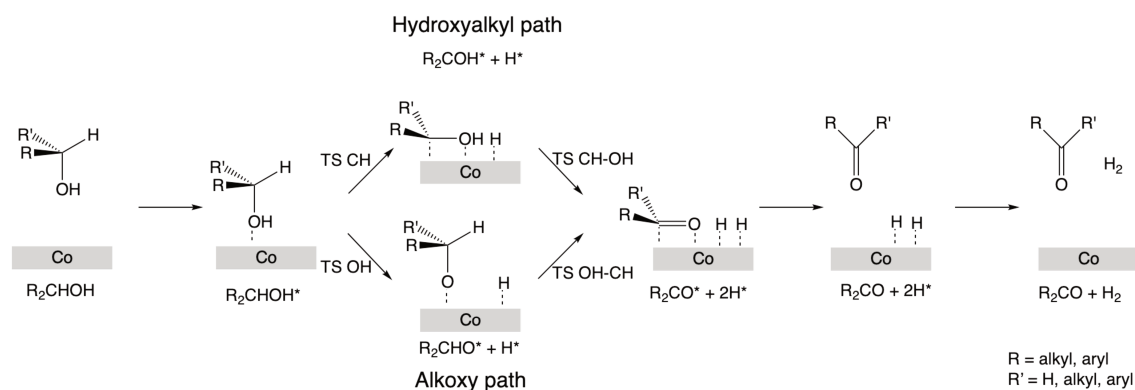


Figure 4.5. Schematic of alcohol dehydrogenation mechanisms.

4.2.2. EtOH dehydrogenation on Co (0001) – determining the preferred reaction mechanism

To determine the preferred reaction mechanism, it is necessary to compare the energies of the reaction species between the possible pathways, and to compare the activation energies for the corresponding bond breakings. The selection process will be described in details on the example of EtOH dehydrogenation on Co(0001) close packed facet. The obtained energy profiles for alkoxy and hydroxyalkyl pathways are presented on Figure 4.6, and for the structures of reaction species see Figure 4.7.

To assess the energy changes during the reaction, as a reference we chose the sum of energy of bare metal surface and alcohol molecule in gas phase. In our present case it is a sum of Co(0001) p(3x3) slab unit cell energy and energy of EtOH molecule in gas phase.

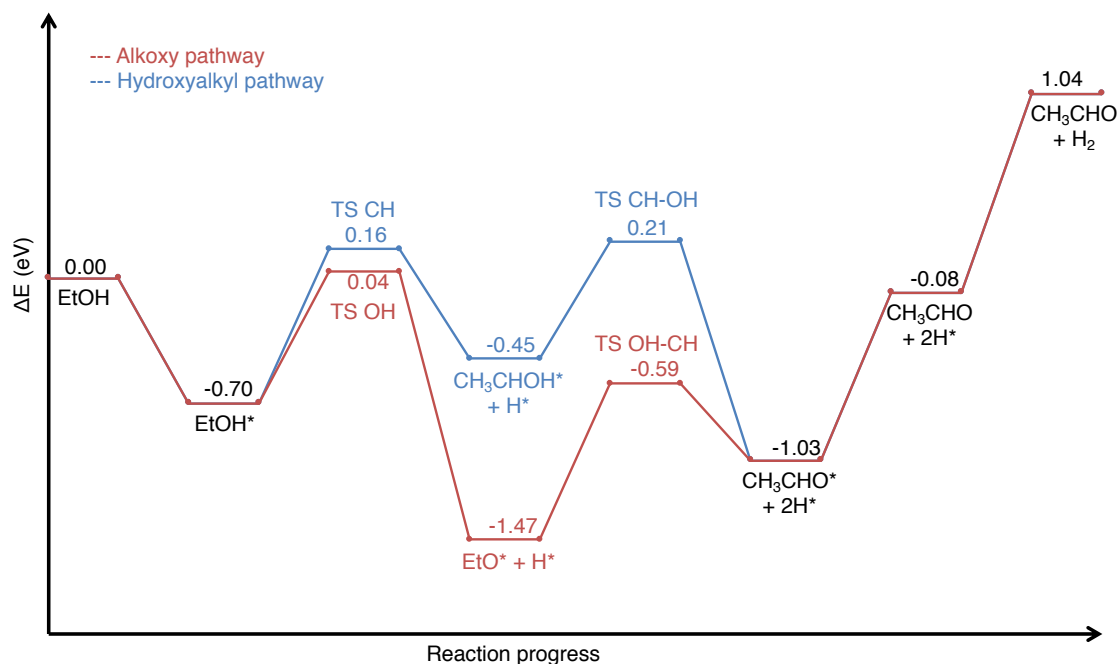


Figure 4.6. EtOH dehydrogenation on Co(0001) surface. In red dehydrogenation via alkoxy pathway and in blue dehydrogenation via hydroxyalkyl pathway. All the energies are given in eV, '*' stands for the adsorption of species on the surface.

EtOH adsorption is exothermic by -0.70 eV and the molecule is bounded to the surface through O atom, adsorbed in top position. It can be followed by OH or CH bond breaking, which require 0.74 eV and 0.87 eV of activation energy, respectively. This indicates that OH bond scission is kinetically preferred over CH bond dissociation. During the transformation, OH bond is elongated from 0.98 Å to 1.26 Å (Figure 4.7.a and 4.7.b), that indicates early transition state. However, in geometry it resembles more the resulting intermediate, what indicates it to be late transition state. Hence, it can be assumed that it is neither early, neither late transition state. During the dissociation, the CH bond length changes from 1.10 Å to 1.56 Å (Figure 4.7.a and 4.7.c), and the geometry of transition state resembles more the geometry of resulting intermediate. Together it indicates the late nature of the transition state. These elementary reactions lead to the formation of alkoxy (EtO*, CH₃CH₂O*) and hydroxyalkyl (CH₃CHOH*) intermediates, respectively, together with H* atom, being consider as adsorbed on the nearby surface. The adsorption of EtO* occurs through O atom, which is bounded in hcp position,

whereas, $\text{CH}_3\text{CHOH}^\bullet$ interacts with the surface by O (in top position) and C (in bridge position) atoms. While comparing the adsorption strength of these two reaction intermediates, it is clear that EtO^\bullet is more stable, as it is bounded stronger with the surface by 1.02 eV. Additionally, it is the most stable intermediate among all occurring during the reaction. This means that reaching this state is thermodynamically preferred by the system (it is resting state of the reaction). From the intermediate state, second bond breaking is necessary to obtain desired reaction products – aldehyde and H_2 . Along the alkoxy pathway OH-CH bond scission occurs, and among the hydroxyalkyl pathway CH-OH bond dissociation takes place. They require 0.88 eV and 0.66 eV of activation energy, respectively. The CH bond of EtO^\bullet is elongated to 1.57 Å (Figure 4.7.g), indicating late transition state. The OH bond of $\text{CH}_3\text{CHOH}^\bullet$ is extended to 1.35 Å (Figure 4.7.h), which is longer than the length of OH bond dissociation from EtOH. This implies the different nature of this bond dissociation – TS CH-OH is later transition state than TS OH. These elementary reactions are leading to the formation of corresponding aldehyde (CH_3CHO , acetaldehyde) and 2 H^\bullet atoms, adsorbed on the surface. CH_3CHO adsorbs to the surface via O (hcp) and C (top) atoms. The desorption of acetaldehyde and H_2 from the surface (final stage of the catalytic cycle) is endothermic – it requires the input of energy to the system.

Concluding, alkoxy mechanism is the preferred reaction pathway for alcohol dehydrogenation on cobalt (0001) surface. The initial OH bond breaking is less demanding than CH bond scission. Additionally, it is leading to the formation of alkoxy intermediate, which is the most stable among all the reaction species. Hence, making this mechanism thermodynamically and kinetically favored. Our findings are in line with the one from Luo and Asthagiri¹³ and Sutton and Vlachos¹⁴, what validates our computations.

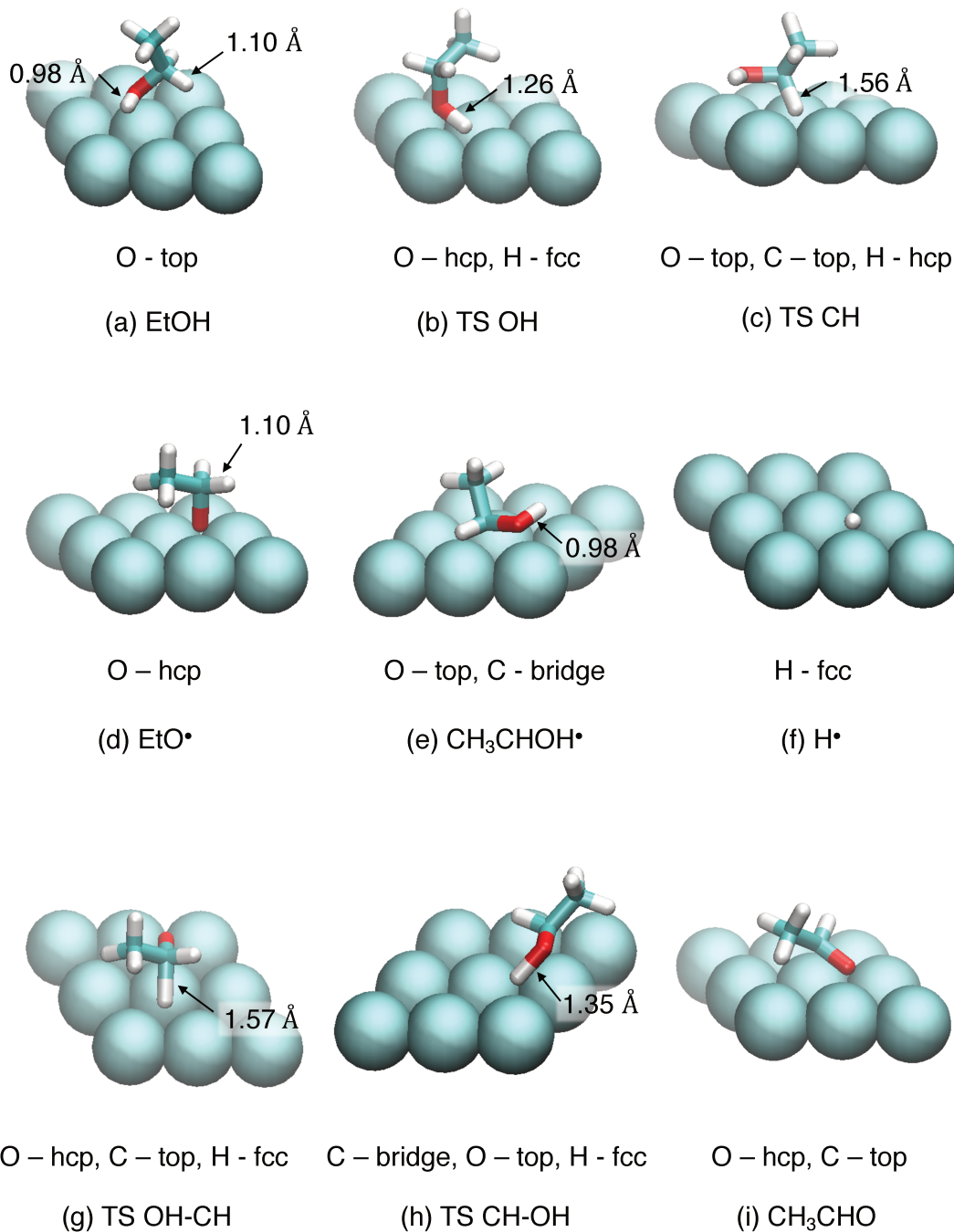


Figure 4.7. Structures of reaction species for EtOH dehydrogenation on Co(0001) facet: (a) EtOH, (b) TS OH, (c) TS CH, (d) EtO*, (e) CH₃CHOH*, (f) H*, (g) TS OH-CH, (h) TS CH-OH, (i) CH₃CHO. Element coding on picture is as follow: light blue (cyan) balls – Co, light blue (cyan) sticks – C, red sticks – O and white sticks – H. The OH and CH bond lengths are given on the pictures (in Å).

4.3. Alcohol dehydrogenation on different surfaces

Aiming at investigating structure sensitivity of alcohol dehydrogenation on cobalt surfaces, we modeled the dehydrogenation of primary (EtOH) and secondary (iPrOH) alcohol on different Co hcp and fcc type facets. Among hcp type surfaces we investigated the activity of close packed (0001), and open type (10-11), (10-10), (10-12), (11-20) facets, and among fcc type surfaces we studied the activity of close packed (111) facet, and open type (100), (110) and (211) surfaces. The conclusions about the activity of different surfaces are independent of the type of alcohol, hence, for simplicity, in this chapter only the results for EtOH dehydrogenation are presented and discussed, and the results for iPrOH can be found in the Annex. The selectivity towards primary vs secondary alcohol dehydrogenation will be discussed in part 4.5.

4.3.1. Adsorption of molecules and intermediates

To compare the activity of different surfaces toward alcohol dehydrogenation, at first, we will pay attention to the adsorption of reaction species. The adsorption positions and adsorption energies of the most stable molecules and intermediates on different facets are listed in Table A.4.1 in Annex. The preferred reaction mechanism may be different depending on the surface. Hence, adsorption of intermediates on both pathways will be discussed, starting with the ones along alkoxy pathway.

EtOH is adsorbed stronger on open type surfaces than on close packed facets, by 0.09-0.34 eV. It tends to adsorb by O atom, bounded in top position to metal. However, for open type surfaces O adsorption in bridge position is close in energy, only 0.05 eV higher. Ethoxy intermediate tends to bind to the surface with the maximum number of Co. It binds in bridge, three-fold (hcp or fcc) or square position, depending on the availability (existence) of the site on different surfaces. The adsorption strength seems not to depend on the type of surface by itself. It differs in the range of 0.30 eV, but no pattern of adsorption strength is noticeable. Carbonyl product (CH_3CHO) preferentially binds to the surface via O and C atoms, what assures the interaction of π electrons from C=O group with surface metal atoms. They adsorb stronger on open type surfaces (up to 0.68 eV). The last of intermediates present along the reaction pathway is H^* atom. It tends to adsorb in positions coordinated by multiple cobalt atoms,

to maximize the interactions with metal. Similarly as for alkoxy intermediate, its adsorption seems to be not influenced by the type of facet.

Considering dehydrogenation of alcohol proceeding via hydroxyalkyl pathway, in many cases the C-H bond dissociation is possible from the most stable adsorption position of alcohol. It is conditioned by the presence of H (bonded with C_{α} - the same C as OH group) pointing towards metal surface. However, even if such alcohol configuration is not the most stable among all possible, it differs only slightly in energy (by less than 0.10 eV) from the most stable one. Hydroxyalkyl intermediate (CH_3CHOH^*) binds to the surface similarly as carbonyl product – via O and C atoms. It tends to adsorb in top positions on metal atoms, favoring σ type interactions. On open type surfaces it is stronger than on close packed surfaces, by 0.28-0.59 eV.

Among different types of surfaces similar adsorption configurations are kept. For some of the species (alcohol, carbonyl product, hydroxyalkyl intermediate) the strength of adsorption is influenced by the type of facet. It tends to be weaker on close packed (0001) and (111) surfaces and stronger on open type facets.

4.3.2. Bonds dissociation

Another, very important factor affecting the surface activity, is the activation energy necessary for different bond breakings. Again, as the preferred reaction mechanism may differ depending on the surface, bond scissions along both alkoxy and hydroxyalkyl pathway will be considered. The transition state configurations, lengths of breaking bonds, and activation energies for given bonds scissions are listed in Table 4.2. for EtOH and Table A.4.2. in Annex for iPrOH. The geometries of transition states are conditioned by the type of surface. However, some observations can be made.

Along the alkoxy pathway OH bond breaking occurs as the first one. For molecule in transition state, O tends to be coordinated by few Co atoms. The OH bond is elongated to 1.25-1.38 Å, from 0.98 Å in alcohol molecule. Hence, it is in between early and late transition state. Activation energy for this bond dissociation is equal to ~0.7 eV for close packed surfaces, (10-11) and (10-10) facets. And for the remaining open type surfaces it requires 0.34-0.46 eV of energy input, which are significantly lower values. The energy variations can be related to

the geometries of transition states. On (0001), (111) and (10-11) surfaces O is coordinated by 3 Co atoms, whereas on the open surfaces it is bounded only by 2 Co atoms. Hence, the changes in O coordination between alcohol adsorption and TS are bigger in the former, than in the later case, resulting in increase of activation energy. The exception is (10-10) facet, for which O is also coordinated by 2 Co atoms, but H is in transfer position to another metal row, what requires additional energy input.

The alkoxy intermediate is an initial state for OH-CH bond dissociation. In this transition state, O still tends to be coordinated by few Co atoms, similarly as alkoxy intermediate. However, C is also adsorbed on the surface (usually on top site) and H tends to be adsorbed on highly coordinated position. Such geometry starts to resemble the configuration of carbonyl product. CH bond is elongated to 1.50-1.73 Å, from 1.10 Å in alkoxy intermediate. It is the longest on (10-10) facet, where the dissociated H has to be transferred to another metal row. Based on these similarities, it can be named late transition state. Activation energy necessary for OH-CH bond scission is equal to 0.65-0.94 eV, and shows no dependency on the type of surface.

Among the hydroxyalkyl pathway CH bond breaking occurs as the first one. In transition state, alcohol molecule adsorbs to the surface via O (in top position) and C (in top position), H tends to bind in position coordinated by few metal atoms. Such configuration resembles the geometry of hydroxyalkyl intermediate, which indicates, that this transition state is late transition state. CH bond is elongated to 1.44-1.56 Å, from 1.10 Å in alcohol. The activation energy is equal to 0.68-0.88 eV, being the highest for close packed surfaces.

The following bond dissociation is the CH-OH bond breaking. In transition state, the hydroxyalkyl intermediate adsorbs to the surface by C atom, O atom (in top position) and H atom (in position highly coordinated by metal atoms). Again, the transition state can be called late transition state, as its geometry resembles the product of bond scission – carbonyl molecule. The OH bond is elongated to 1.35-1.40 Å, from 0.98 Å in hydroxyalkyl intermediate. To occur, it requires an energy input of 0.45-0.69 eV. It is not showing a clear tendency to be facilitated on open type surfaces, what was noticeable among alkoxy dehydrogenation pathway. We observe the highest value for it on (110) facet, when H is in the transfer position to another metal row.

Comparison of the configurations of different transition states allowed us to assume, that even though the surfaces are very different, molecules are adopting similar geometries for bond breakings. OH bond scission along the alkoxy pathway turns out to be facilitated on open type surfaces, that is not straightforward for CH-OH bond dissociation along the hydroxyalkyl pathway. For CH and OH-CH bond breaking no clear tendencies for structure sensitivity are visible.

Table 4.2. Transition states configurations, dissociated bonds lengths and activation energies for different bond breakings, and energy differences between the state preceding (initial state, IS) and following (final state, FS) given TS along the EtOH dehydrogenation pathways. E_{act} stands for the activation energy of a given transition state, ΔE_{FS-IS} stands for the energy of elementary reaction (energy difference between the state following and preceding given transition state). Species signified with '*' are considered as adsorbed on the surfaces. All the adsorption positions refer to the 1st layer of metal, unless stated otherwise. All the energies are given in eV.

Surface	TS OH configuration	O-H bond length (Å)	E_{act} OH	$\Delta E_{EtO^*+H^*-EtOH^*}$	$\Delta E_{EtO^*+\frac{1}{2}H_2-EtOH^*}$	TS OH-CH configuration	C-H bond length (Å)	E_{act} OH-CH	$\Delta E_{CH_3CHO+H^*-EtO^*}$	$\Delta E_{CH_3CHO+\frac{1}{2}H_2-EtO^*}$
(0001)	O – hcp, H - fcc	1.26	0.74	-0.77	-0.21	O – hcp, C – top, H - fcc	1.57	0.88	0.44	1.00
(10-11)	O – fcc, H – hcp	1.26	0.70	-0.91	-0.25	O – fcc, C – top, H - bridge	1.54	0.80	0.19	0.84
(10-10)	O – bridge, H – bridge (between 1 st and 2 nd layer)	1.38	0.72	-0.59	0.00	O – bridge, C – bridge between rows, H – bridge (another row)	1.73	0.75	0.17	0.77
(10-12)	O – bridge, H – top (3 rd step)	1.34	0.42	-0.69	-0.16	O – bridge, C – top, H - bridge	1.51	0.70	0.06	0.59
(11-20)	O – bridge, H - bridge	1.31	0.46	-0.69	-0.18	O – bridge, C – top, H – bridge (between 1 st and 2 nd layer)	1.60	0.89	0.15	0.65
(111)	O – hcp, H – fcc	1.25	0.74	-0.78	-0.20	O – hcp, C – top, H – fcc	1.55	0.90	0.44	1.02
(100)	O – bridge, H - bridge	1.31	0.42	-0.72	-0.24	O – bridge, C – top, H – bridge	1.53	0.94	0.13	0.61
(110)	O – bridge, H – bridge between rows	1.33	0.34	-0.68	-0.18	O – bridge, C – top, H – bridge	1.54	0.65	0.13	0.63
(211)	O – bridge, H – bridge (3 rd step)	1.33	0.36	-0.72	-0.15	O – bridge, C – top, H - bridge	1.50	0.65	0.21	0.78

Table 4.2. cont.

Surface	TS CH configuration	C-H bond length (Å)	$E_{\text{act}}^{\text{CH}}$	$\Delta E_{\text{CH}_3\text{CHOH}^+ + \text{H}^* - \text{EtOH}^*}$	$\Delta E_{\text{CH}_3\text{CHOH}^+ + \frac{1}{2}\text{H}_2 - \text{EtOH}^*}$	TS CH-OH configuration	O-H bond length (Å)	$E_{\text{act}}^{\text{CH-OH}}$	$\Delta E_{\text{CH}_3\text{CHO}^+ + \text{H}^* - \text{CH}_3\text{CHOH}^*}$	$\Delta E_{\text{CH}_3\text{CHO}^+ + \frac{1}{2}\text{H}_2 - \text{CH}_3\text{CHOH}^*}$
(0001)	O – top, C – top, H - hcp	1.56	0.87	0.25	0.81	C – bridge, O – top, H - fcc	1.35	0.66	-0.57	-0.02
(10-11)	O – top, C – top, H – hcp	1.55	0.79	0.04	0.70	C – bridge, O – top, H – bridge	1.35	0.56	-0.76	-0.10
(10-10)	O – top, C – bridge, H - bridge	1.47	0.82	0.11	0.70	C – bridge, O – top, H – bridge between rows	1.37	0.55	-0.52	0.08
(10-12)	O – top, C – top, H - bridge	1.45	0.76	0.09	0.62	C – bridge, O – top, H – bridge (between 1 st and 2 nd step)	1.38	0.61	-0.72	-0.19
(11-20)	O – top, C – top, H - bridge	1.53	0.80	0.19	0.70	C – top, O – top, H – bridge between rows	1.39	0.60	-0.68	-0.17
(111)	O – top, C – top, H - hcp	1.56	0.88	0.24	0.81	C – bridge, O – top, H - fcc	1.35	0.66	-0.57	0.00
(100)	O – top, C – top, H - bridge	1.50	0.83	0.13	0.61	C – top, O – top, H - bridge	1.40	0.69	-0.72	-0.24
(110)	O – top, C – top, H - bridge	1.45	0.71	0.18	0.68	C – bridge, O – top, H – bridge between rows	1.36	0.45	-0.74	-0.24
(211)	O – top, C – top, H - bridge	1.44	0.68	-0.01	0.56	C – bridge, O – top, H – top (3 rd step)	1.39	0.58	-0.51	0.06

4.3.3. Activity of different surfaces

To assess the relative activity of different surfaces we have to take a look on all the obtained results together, what can be done comparing reaction energy profiles. As it was mentioned, the preferred reaction mechanism may depend on the type of surface, hence at first it has to be determined. The dehydrogenation of EtOH via alkoxy and hydroxyalkyl pathways are presented on Figures 4.5 and 4.6. (For iPrOH the profiles are gathered on Figure A.4.1 and A.4.2 in Annex.)

While comparing the two dehydrogenation pathways for different surfaces, it is clearly visible that the reaction proceeds preferentially via alkoxy mechanism on all of them. The activation energy for OH bond breaking is lower than the energy necessary to break the CH bond in the alcohol molecule (it is kinetically favored). Additionally, it leads to the formation of alkoxy intermediate, which is the most stable intermediate on all the surfaces (it is favored thermodynamically). Further, from alkoxy intermediate the following OH-CH bond scission is preferred over recombination to alcohol substrate, due to the activation energy differences for elementary reactions. This is not the case for hydroxyalkyl intermediate, for which, even if it will be formed, it is kinetically and thermodynamically preferred to reconstruct the alcohol. Kinetically, because the activation energy to form carbonyl product is higher than the activation energy of hydrogenation to form alcohol, and thermodynamically because alcohol molecule is adsorbed stronger than hydroxyalkyl intermediate (and H[•]), what is preferential for the system.

Owing to the fact that we already know which reaction pathway is preferred, to assess the relative activity of different surfaces we can compare their energy profiles for alcohol dehydrogenation via alkoxy mechanism. As it is illustrated on Figure 4.8, and which was mentioned before, the adsorption of alcohols and carbonyl products is stronger on the open type surfaces. Moreover, the OH bond dissociation energy barriers are lower for them than for close packed (0001) and (111) facets. From the profiles we cannot directly compare the adsorption strength of alkoxy intermediate, as it is shaded by H[•] adsorption. But, as it was already stated, neither the adsorption of alkoxy intermediate, neither adsorption of H[•] show a regular structure dependency.

Taking all the findings into account, we can conclude that the alcohol dehydrogenation is a structure sensitive reaction, and it is supposed to proceed preferentially on open type surfaces over close packed facets, especially due to decreased OH bond scission activation energies for them. Making a prediction, we can name (10-12) and (211) stepped facets, together with (11-20) zig-zag type surface, as the most active cobalt surfaces for acceptor-less alcohol dehydrogenation reaction.

To the best of our knowledge, the structure sensitivity of alcohol dehydrogenation was not investigated yet on cobalt surfaces. However, He et al. reported the EtOH dehydrogenation on close-packed Cu(111) and stepped Cu(211) facets, modeled by DFT computations.⁴ Their results revealed that adsorption of reaction species is enhanced on the stepped surface. And the activation energies of OH and OH-CH bond scissions are lower on the stepped surface than on close packed facet (by 0.46 eV and 0.31 eV, respectively). While we compare exclusively the adsorption of species on Co(111) and Co(211) surfaces, our findings agree with the literature. We observed stronger adsorption of species on (211) facet, and found OH and OH-CH bond dissociations being easier by 0.38 eV and 0.25 eV, respectively, between these two fcc type surfaces.

Another report, being in line with our findings, is given by Hoyt et al.³ They performed the modeling of EtOH dehydrogenation on Cu close-packed (111) surface and (100) and (111) steps, modeled with (553) and (533) surfaces, which can be consider as other stepped surfaces. According to their results, the adsorption of reaction species is stronger on steps than on close packed facet, and the activation energies for OH and OH-CH bonds dissociations are lower for steps. Therefore, the steps are expected to be more active than (111) facet.

Even though the available reports concern another metal, they strengthen our finding that the type of metal surface plays a role for the activity in alcohol dehydrogenation.

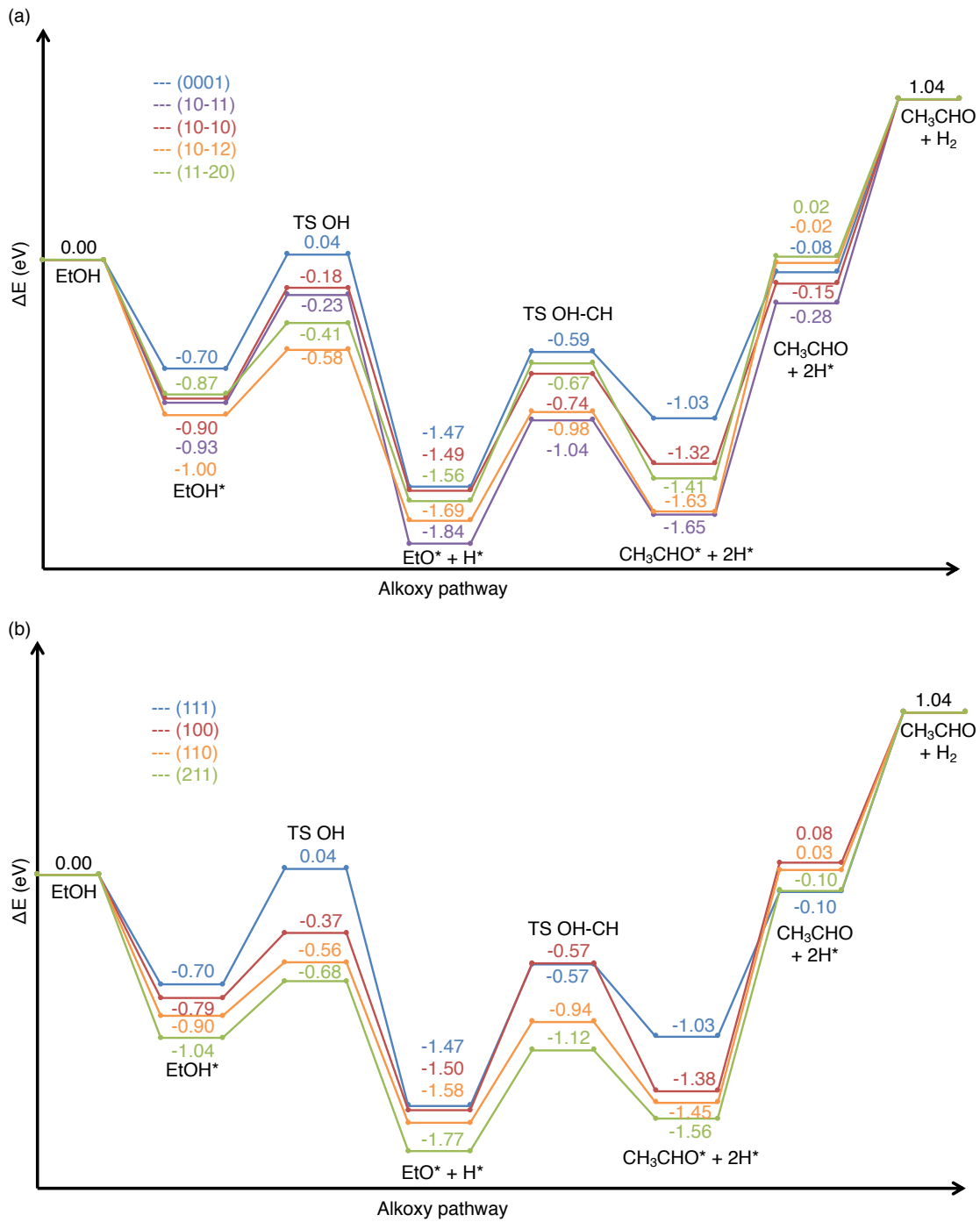


Figure 4.8. Energetic profiles for EtOH dehydrogenation via alkoxy pathway on different (a) hcp and (b) fcc surfaces. All the energies are given in eV, '*' stands for the adsorption of the species on the surface.

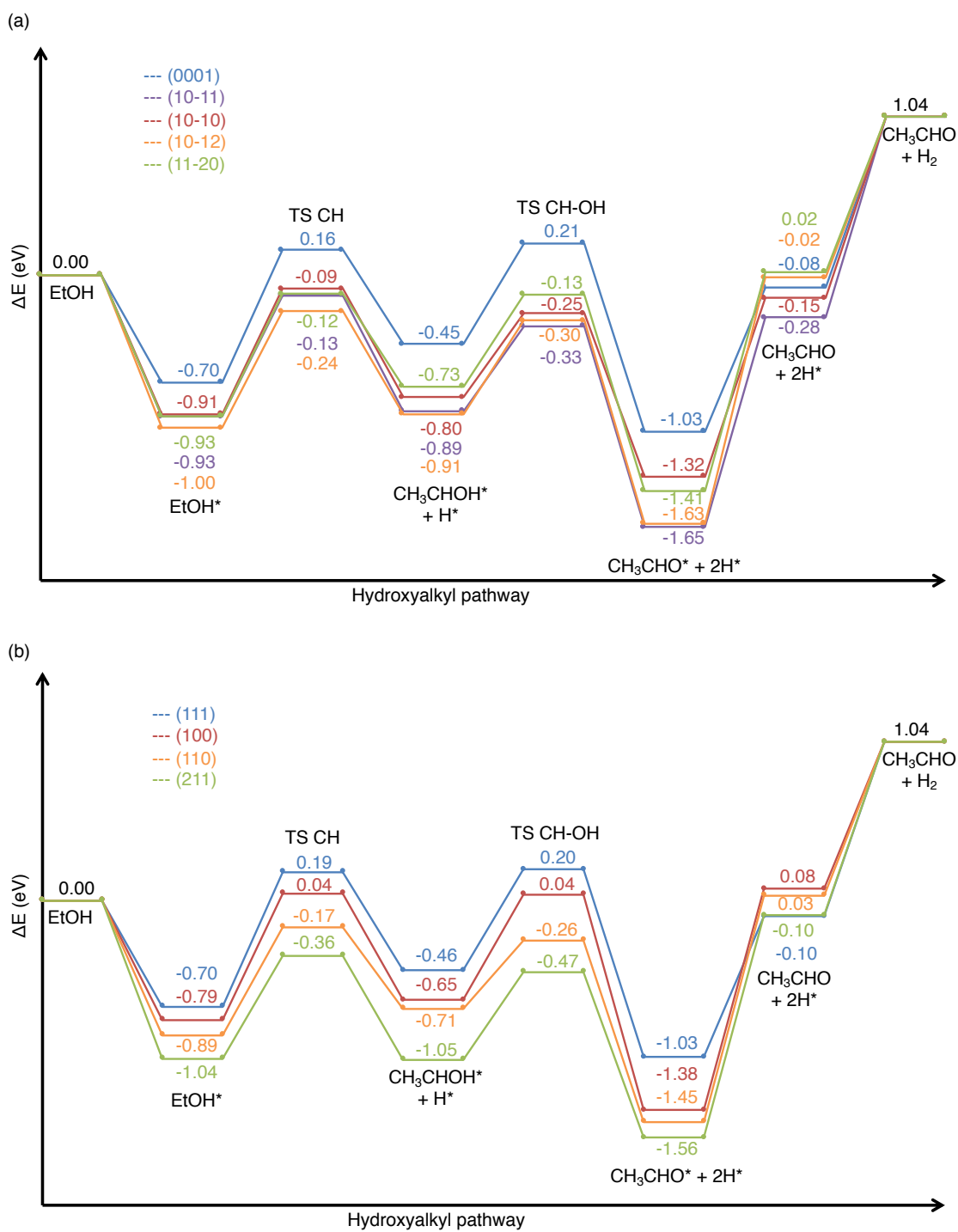


Figure 4.9. Energetic profiles for EtOH dehydrogenation via hydroxyalkyl pathway on different (a) hcp and (b) fcc surfaces. All the energies are given in eV, '*' stands for the adsorption of the species on the surface.

4.4. Towards understanding and predicting(?) catalytic activity

Having a set of computational data, it is possible to analyze them in terms of the relations between energy and geometry, to better understand the catalytic activity and possibly predict the most active metals and surfaces. At first, the possible correlation between thermochemistry and activation energy of an elementary reaction can be analyzed (thermochemistry vs kinetics, Brønsted-Evans-Polanyi type relations), which allows to assess if one is conditioned by the other.^{15,16} Also, the relation between the adsorption strength of species and the type of adsorption position, expressed by a geometry descriptor, can be investigated. It allows to assess if the adsorption strength is conditioned by the type of given site. Generalized coordination number is a relatively new geometry descriptor.^{17,18,19} It allows to better distinguish the adsorption sites, as it includes the amount of second neighbors for a given position (what is not taken into account for the coordination number), and hence it allows to better describe the adsorption positions on the variety of our investigated surfaces.

4.4.1. Kinetics vs thermochemistry of elementary reaction

4.4.1.1. Bell-Evans-Polanyi (BEP) principle

Brønsted-Evans-Polanyi (or Bell-Evans-Polanyi, BEP) principle^{20,21} states that in the same family of reactions (elementary reactions, transformations) the activation energies of the reactions are proportional to their reaction enthalpies.

$$E_{\text{act}} = \alpha \Delta H + E_0$$

E_{act} – activation energy

α – factor

ΔH – enthalpy of reaction

E_0 – constant, equal to activation energy when reaction is athermic

In heterogeneous catalysis the elementary reaction (Figure 4.10), according to Langmuir-Hinshelwood mechanism, is considered as the transformation from the initial state (IS), which is a species adsorbed on the surface, and whose energy is the local minimum, proceeding through transition state (TS), towards the final state (FS), which is another species adsorbed

on the surface, whose energy is also a local energy minimum. The energy necessary for bond breaking is called activation energy (E_{act}) and the energy difference between IS and FS is the energy of elementary reaction (ΔE).

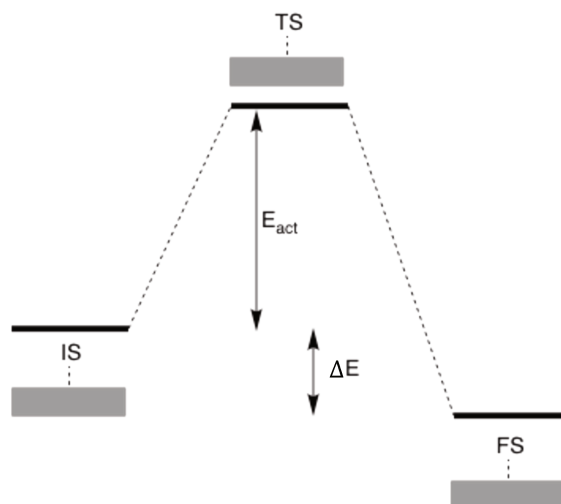


Figure 4.10. Schematic of elementary reaction in heterogeneous catalysis, according to Langmuir-Hinshelwood mechanism.

Therefore, for the heterogeneous catalytic system the BEP equation changes into:

$$E_{\text{act}} = \alpha\Delta E + E_0$$

E_{act} – activation energy

α – factor, characterizing the earliness of TS (the smaller the value the earlier is TS)

ΔE – elementary reaction energy

E_0 – constant, equal to activation energy when reaction is athermic

If in investigation of a group of elementary reactions (e.g. OH or CH bond breakings in alcohol molecule on different metals¹⁵), the obtained relation between E_{act} and ΔE is linear, it confirms that they belong to the same family of reactions (they are reactions of the same nature). If such relation is not behaving linearly, it signals that the transformations may be of different nature. The values of mean absolute error below 0.10 eV and maximal absolute error lower than 0.20 eV (which is an accuracy border of DFT-GGA calculations)²² between the data

and linear fitting indicate their good accuracy. Moreover, by the slope of the line it is possible to assess the earliness of the transition state. The bigger the α value is, the later (more product-like) is the transition state. This we would like to check for OH and CH bond dissociations in alcohol dehydrogenation on different cobalt surfaces.

4.4.1.2. Checking the relations between E_{act} and ΔE for OH and CH bond breakings on different Co surfaces

Plotting the relations between E_{act} and ΔE for OH and CH bond scissions allowed us to analyze some properties of our systems in quicker and more generalized way. In such analysis the bigger the data set, the more relevant are the conclusions. Hence, the results concerning both EtOH and iPrOH dehydrogenation are considered simultaneously in this section. The corresponding plots for OH, CH, OH-CH and CH-OH transitions are presented on Figure 4.11. For the raw data, refer to the Tables 4.2. for EtOH and Table A.4.2 in Annex for iPrOH. To avoid misleading influence of H^* adsorption (it differs up to 0.18 eV for different surfaces), ΔE are considered for the states where $\frac{1}{2}H_2$ is already desorbed from the surface.

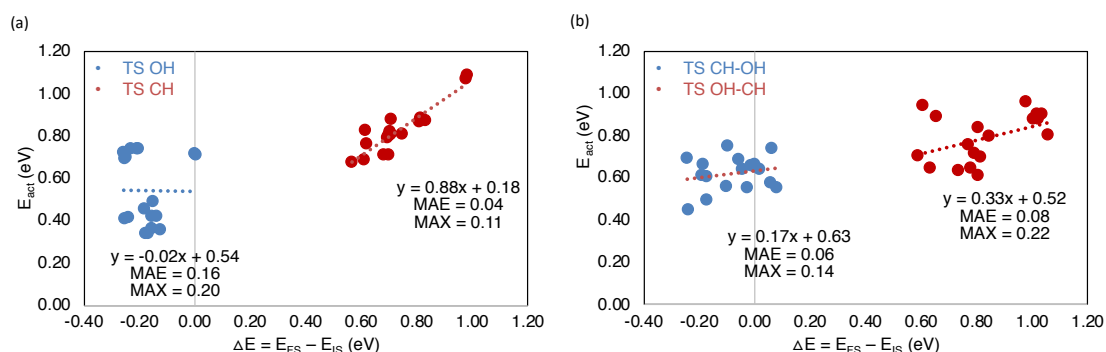


Figure 4.11. Graphs presenting relations between E_{act} and ΔE for: (a) OH and CH bond scissions, (b) for OH-CH and CH-OH bonds dissociation on different cobalt surfaces. MAE stands for the mean absolute error and MAX stands for maximum absolute error. Their values are given in eV.

Generally speaking, OH bond dissociation is exothermic transformation ($\Delta E < 0$) and CH bond breaking is endothermic transformation ($\Delta E > 0$) (Figure 4.11.a). As well, breaking of OH bond requires less energy (E_{act}) than breaking of CH bond on a given surface.

For OH bond scission among the alkoxy pathway (TS OH) the correlation between E_{act} and ΔE does not exist, what is confirmed by the MAE (mean average error) value of 0.16 eV. However, at least two groups of transformation can be distinguished. One with high activation energy (~ 0.70 eV), and the second with lower activation energy (~ 0.35 - 0.50 eV). While we come back to their geometries, as it was described in part 4.3.2, we will see that, indeed, this bond dissociation on close packed surfaces proceeds through the transition state in which O was coordinated to 3 Co atoms and required more energy, whereas for open type surface O was bounded with 2 Co atoms, and it required less energy. The exception was OH bond breaking on (10-10) facet, for which O was bounded with 2 Co atoms, but H atom was moved to another metal row, what required more energy (two points with $\Delta E \sim 0.0$ eV on Figure 4.11.a). That explains the observed groups.

CH bond dissociation on hydroxyalkyl pathway (TS CH) shows good correlation between its activation energy and transformation energy (MAE = 0.04 eV, MAX = 0.11 eV). The α factor is equal to 0.88, what indicates the similarity of transition state configuration to the final state structure (late nature of this transition state). We already assumed this in subchapter 4.3.2, while we were analyzing the configurations of different transition states. Based on these properties we can assume that CH bond breaking on different Co surfaces has the same nature – belongs to the same family of elementary reactions. This is confirmed by the transition states configurations, which in every case include O and C adsorbed in top positions and H adsorbed in position coordinated by few metal atoms (H is adsorbed at 3-fold sites on (0001), (111) and (10-11) facets, and at bridge position on the rest of surfaces).

For OH-CH and CH-OH the MAE values are equal respectively to 0.06 eV (MAX = 0.14 eV) and 0.08 eV (MAX = 0.22 eV), what indicates quite good correlation between E_{act} and ΔE . However, according to the line slopes they are expected to be early transition states, what is not in line with our previous observations (part 4.3.2), as they were assessed to be late transition states.

To sum up, CH, CH-OH and OH-CH bond dissociations showed the dependency between the kinetic (E_{act}) and thermochemistry (ΔE). Based on the line slope TS CH it is predicted to be late transition state, what is in agreement with our earlier assumptions. However, TS OH-CH

and TS CH-OH are predicted to be early transition states, what is in contrary to our earlier conclusions. E_{act} of OH bond scission was not dependent on ΔE , but plotting them allowed to visualize that the transformation does not belong to the same family on different surfaces.

Sutton and Vlachos investigated the EtOH activation (including dehydrogenation pathways) on the compact planes of different metals,¹⁴ and studied the correlation between activation energy and thermochemistry (BEP type relations) for the elementary reactions. According to their results CH bond breaking is late transition state and OH bond dissociation is an early transition state. What is in line with the findings of Zaffran et al.¹⁵ The above-mentioned results, together with our findings, imply that the nature of CH bond breaking is insensitive neither to the metal, neither to the type of surface. On close packed facets of different metals OH bond breaking is of early nature, but it is not straightforward to assess it on different Co surfaces.

4.4.2. Linking surface geometric arrangements with their adsorption properties

4.4.2.1. Geometry descriptors

To investigate and correlate the type of adsorption position with its strength for different species, it is necessary to use a geometry descriptor, which can be expressed by numbers. It can be coordination number¹⁸ (cn) or generalized coordination number (\overline{CN}).¹⁹ Coordination number is defined as the number of nearest neighbors (neighbors remote by the metal interatomic distance) for chosen atom or position (i.e. the atom(s) to which a molecule or intermediate is adsorbed). It is simple surface descriptor, but it does not allow to distinguish between some adsorption sites, like hcp and fcc 3-fold positions on (111) surface. This can be reached using generalized coordination number.¹⁷ It is relatively new surface geometry descriptor, introduced in 2014. It is first order extension of coordination number, what means that the second-nearest neighbors are taken into consideration to quantify the adsorption positions. Hence, it allows to distinguish the 3-fold adsorption sites on (111) facet, but also is efficient to differentiate the sites on metal nanoparticles,^{17,19} and different types of surfaces.^{18,23,24}

Generalized coordination number is defined as:

$$\overline{\text{CN}} = \frac{\sum_{i=1}^{n} \text{cn}(i)}{n_{\text{MAX}}}$$

$\overline{\text{CN}}$ – generalized coordination number

$\text{cn}(i)$ – coordination number of i^{th} atom neighboring with the chosen atom or ensemble of atoms (avoiding double counting)

n_{MAX} – maximum number of nearest neighbors for chosen atom or ensemble of atoms in bulk (avoiding double counting)

n – amount of nearest neighbors for chosen atom or ensemble of atoms

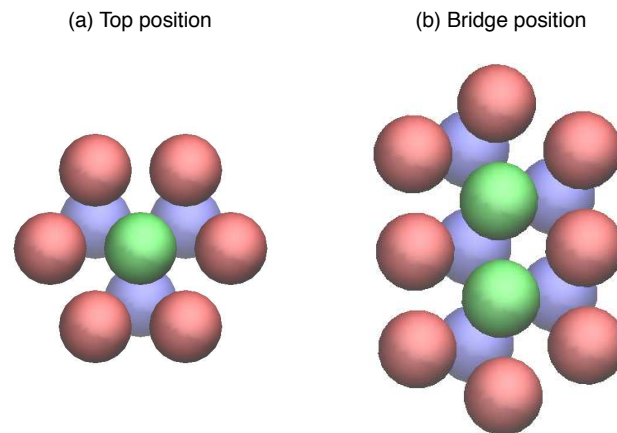


Figure 4.12. Example of top and bridge position for close packed (0001) facet. In green – the atom(s) of a given position, in red – nearest neighbors in the same layer, in blue – nearest neighbors in the layer underneath. For better visualization atoms are presented with smaller radius (than the atomic radius).

For example, to calculate the generalized coordination number for top position on (0001) close packed facet, the formula will be as follow:

$$\overline{\text{CN}} = \frac{6 \cdot 9 + 3 \cdot 12}{12} = 7.5$$

The sum of coordination numbers for the nearest neighbors will consist of 6 nearest neighbors in the same (surface) layer of the coordination number equal 9, and 3 nearest neighbors in the layer underneath of the coordination number equal 12. The maximum amount of nearest

neighbors in bulk for one atom is equal 12, hence, the sum is divided by it. This gives $\overline{\text{CN}}$ equal 7.5, whereas cn for this position is equal 9.

For bridge position the equation will be as follow:

$$\overline{\text{CN}} = \frac{8 \cdot 9 + 5 \cdot 12}{18} = 7.33$$

The ensemble of two neighboring atoms, which constitute the bridge position, has 8 nearest neighbors in the same layer of the coordination number equal 9, and 5 nearest neighbors in the layer underneath of the coordination number equal 12. The maximum number of nearest neighbors for the ensemble of 2 atoms in bulk (avoiding double counting) is equal to 18. Hence, the obtained $\overline{\text{CN}}$ is equal to 7.33.

Generalized coordination numbers for different adsorption positions on variety of our chosen hcp (5) and fcc (4) type surfaces were counted with the script written by our colleague Paul Clabaut from Laboratoire de Chimie, ENS de Lyon. In the script, at first, for the chosen atom/position the nearest neighbors are defined. In the next step, neighbors of the neighbors are identified. Subsequently, double counted nearest neighboring atoms are eliminated and the $\overline{\text{CN}}$ is counted according to the equation. The obtained $\overline{\text{CN}}$ for different surfaces ranges between 5.4 and 9.2, and are characteristic for the adsorption sites. The relations between adsorption position and adsorption energy of different species along the alcohol dehydrogenation pathways will be discussed in the following section.

4.4.2.2. Relation between adsorption strength and geometry properties of adsorption site

The scaling relation between the adsorption energy and the geometry descriptor is supposed to have a linear form:

$$E_{\text{ads}} = a\overline{\text{CN}} + b$$

E_{ads} – adsorption energy

a – slope

$\overline{\text{CN}}$ – generalized coordination number

b – offset

The accuracy of linear fitting and E_{ads} values is indicated by MAE (mean absolute error) and MAX (maximal absolute error). If the MAE and MAX do not exceed 0.10 eV and 0.20 eV, it indicates good fitting accuracy. Then it allows to make some reliable conclusions about structure sensitivity of adsorption of molecules and intermediates on metal surfaces. The value of the slope indicates how strongly adsorption strength is influenced by the geometric properties of the adsorption site (high value of the slope – big adsorption energy changes, small value of the slope – small adsorption energy changes).

In our analysis, the adsorption of species was considered only in the most stable positions and their adsorption energies were considered as electronic energies. The results are collected in Table A.4.1 in Annex, and the obtained corresponding graphs are presented on Figure 4.13. Adsorption of reaction intermediates was evaluated without H^* co-adsorption (as alcohol \rightarrow intermediate or carbonyl product + $n \text{H}_2$, where $n = \frac{1}{2}$ or 1), to avoid its misleading influence. For the species adsorbed to the surface by several atoms, the average from the $\overline{\text{CN}}$ s of different positions was taken as $\overline{\text{CN}}$. For example, CH_3CHO on Co(10-10) is adsorbed by O in bridge position ($\overline{\text{CN}} = 6.23$) and C in top position ($\overline{\text{CN}} = 6.68$). Hence the $\overline{\text{CN}}$ for this species is equal to $(6.23 + 6.68) / 2 = 6.46$.

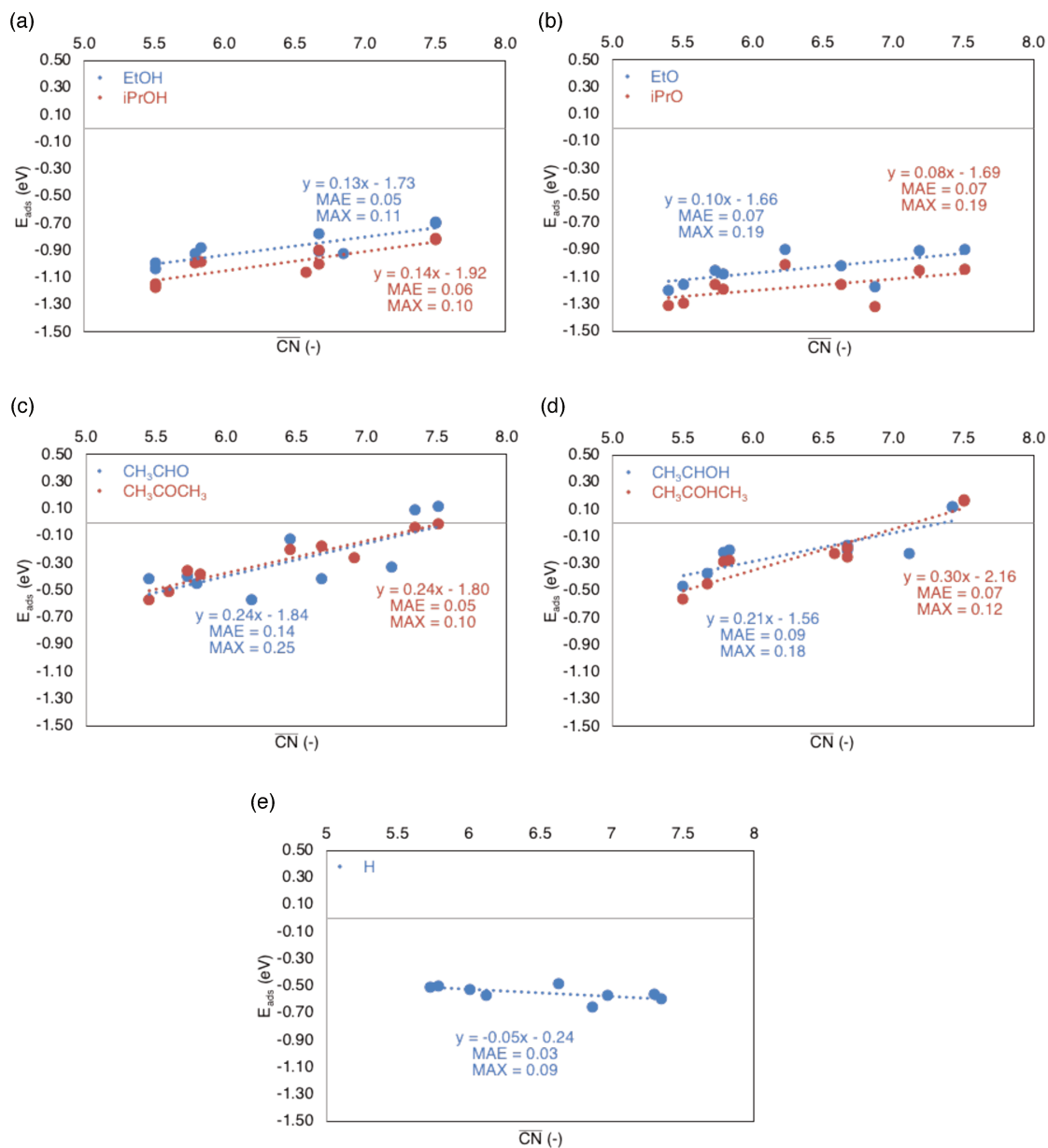


Figure 4.13. Graphs representing the relations between E_{ads} and $\overline{\text{CN}}$ for the most stable reaction species: (a) alcohol, (b) alkoxy intermediate, (c) carbonyl product, (d) hydroxyalkyl intermediate, (e) H^* . Energies are given in eV, $\overline{\text{CN}}$ are unitless. MAE stands for mean absolute error and MAX stands for maximal absolute error. Their values are given in eV.

Table 4.3. Slope (a), intercept (b), mean absolute error (MAE) and maximum absolute error (MAX) values for the linear fitting of data.

Species	a (eV)	b (eV)	MAE (eV)	MAX (eV)
EtOH	0.13	-1.73	0.05	0.11
iPrOH	0.14	-1.92	0.06	0.10
EtO	0.10	-1.66	0.07	0.19
iPrO	0.08	-1.69	0.07	0.19
CH ₃ CHO	0.24	-1.84	0.14	0.25
CH ₃ COCH ₃	0.24	-1.80	0.05	0.10
CH ₃ CHOH	0.21	-1.56	0.09	0.18
CH ₃ COHCH ₃	0.30	-2.16	0.07	0.12
H [•]	-0.05	-0.24	0.03	0.09

For almost all the cases MAE and MAX do not exceed 0.10 eV and 0.20 eV (except CH₃CHO), what confirms the good accuracy between the values and linear fitting. This allows to make some reliable conclusions about structure sensitivity of adsorption of molecules and intermediates, occurring along the alcohol dehydrogenation mechanisms, on different cobalt surfaces.

From the analyzed species, the adsorption of carbonyl products (aldehyde and ketone), and adsorption of hydroxyalkyl intermediates are the most structure sensitive. For all of them the slope value is over 0.2. Adsorption of alcohols on different surfaces is also structure dependent (slope of 0.13-0.14), but less than the before mentioned species. On the contrary adsorption of H[•] and alkoxy intermediates is not sensitive to the type of the surface, what is indicated by the slope value below 0.1. These conclusions are in agreement with our previous analysis from subchapter 4.3.1. of adsorption of species on different surfaces.

The additional analysis of our computational results in term of thermochemistry vs kinetic, and adsorption energy vs geometry relations allowed to identify the structure sensitive elementary reactions and structure sensitive species. These confirm that the alcohol dehydrogenation reaction can be facilitated, when appropriate metal surface is exposed and available.

4.5. Selectivity – primary vs secondary alcohol dehydrogenation

Until now we did not compare the selectivity of primary vs secondary alcohol dehydrogenation on Co surfaces. It will be done in this part of the Chapter and it will be combined with the experimental results. Before my thesis started, our project partners from ITODYS in Paris synthesized unsupported Co nanorods and performed preliminary catalytic tests with secondary and primary alcohols. DFT computations allowed to explain the observed results, what was published in 2017 in the paper entitled “Unsupported shaped cobalt nanoparticles as efficient and recyclable catalysts for the solvent-free acceptorless dehydrogenation of alcohols”.²⁵

4.5.1. Activity of Co nanorods

Unsupported cobalt nanorods (Co NRs) were obtained by our partners by polyol method²⁶. In the synthesis protocol, cobalt (II) dodecanoate (laurate) was a metal precursor, NaOH was used to assure the basic conditions, 1,2-butanediol served as a solvent and reducing agent and $\text{RuCl}_3 \cdot x \text{H}_2\text{O}$ was used as nucleating agent. During heating NPs of well-defined shapes were formed. The TEM image of obtained Co NRs is presented on Figure 4.14. HRTEM analysis revealed that the nanorods were exposing mainly (11-20) facets (on the side walls) and small amounts of (0001) surface on tips.

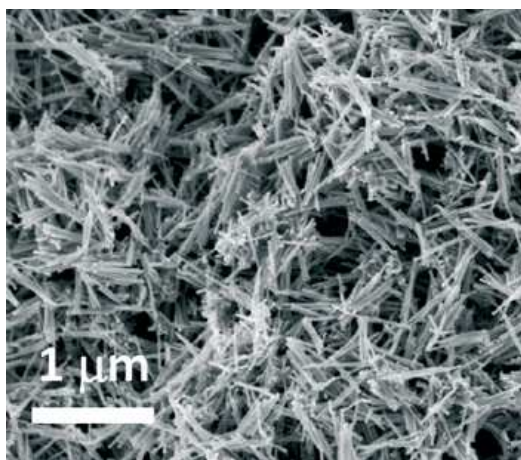


Figure 4.14. TEM image of Co NRs obtained by polyol method.

The preliminary catalytic tests were also conducted by our partners in Paris. As model secondary alcohol 2-octanol was used, and 1-octanol served as model primary alcohol. The reactions were solvent-free, performed at 180°C (boiling temperature of substrates), with 20 mg of Co NRs. Alcohol conversion was measured by ^1H NMR and GC-MS analysis, and H_2 production was monitored by volumetry. For 2-octanol 85% of conversion, with 95% selectivity was obtained, whereas, for 1-octanol conversion was only 4%, with 43% selectivity. What showed very good chemoselectivity of Co NRs towards secondary alcohol dehydrogenation.

Similar activity trends were already reported in the literature. Shimizu et al.²⁷ tested Co/TiO₂ catalyst in dehydrogenation of 2-octanol and 1-octanol, and obtained 85% and 12% of conversion, respectively. However, as the reactions were conducted in different temperature (144°C) and with solvent (o-xylene), we cannot directly compare their results with the results of preliminary tests with Co NRs. But it can be concluded that the observed chemoselectivity has the same trend. Yi et al.²⁸ tested unsupported Re NPs towards dehydrogenation of 2-octanol and 1-octanol in the solvent-free conditions, at boiling temperatures of substrates. The complete conversion of secondary alcohol, and no conversion of primary alcohol was reported. Even though their results are a bit better, we still can consider Co NRs as very good catalysts. Especially that they were easy to handle (it was possible to separate them with external magnet) and that Co is cheaper than Re, what makes our catalyst more attractive.

4.5.2. Towards explanation of the chemoselectivity

4.5.2.1. Electronic Energy vs Gibbs Free Energy profiles

In the previous parts of this chapter, all the energies were reported as electronic energies. However, to properly express the thermochemistry of reaction the energies have to be considered as Gibbs Free Energies, for which entropy at temperature of experiment is taken into consideration. Also, the zero-point energy (ZPE) correction is reported as important for aldehyde hydrogenation,²⁹ hence we assume that it will be important for the alcohol dehydrogenation modeling. As the used slab model is not symmetric, the dipol correction in z direction was included at this point to improve the electronic energy values.

Gibbs energies are derived from the electronic energies within the perfect gas model for molecules and the lattice gas for adsorbate and the rigid rotator and harmonic oscillator approximations. In other words, for molecules in gas phase, Gibbs free energy G is calculated as follow:

$$G = E_{\text{ele}} + nk_{\text{B}}T + \text{ZPE} - T \times (S_{\text{t}} + S_{\text{r}} + S_{\text{vib}})$$

with:

E_{ele} – electronic energy

$n = 4$ for non-linear molecules and $n = 3.5$ for linear molecules

k_{B} – Boltzmann constant

T – temperature, equal to 180°C (453 K, as the reaction temperature)

ZPE – zero-point energy

$S_{\text{t}}, S_{\text{r}}, S_{\text{vib}}$ – translational, rotational and vibrational entropy components

Adsorbates are considered to lose their rotational and translational degrees of freedom and have a diffusion energy that is higher than the thermal energy. Hence, their Gibbs free energies are considered as follow:

$$G_{\text{slab}} = E_{\text{ele}} + \text{ZPE} - T \times S_{\text{vib}}$$

$$G_{\text{ads/slab}} = E_{\text{ele}} + \text{ZPE} - T \times S_{\text{vib}}$$

G_{slab} – Gibbs Free Energy of slab

$G_{\text{ads/slab}}$ – Gibbs Free Energy of the species adsorbed on a slab.

ZPE and S_{vib} are based on the harmonic vibration of the adsorbate. Frequencies lower than 50 cm^{-1} were neglected for them.

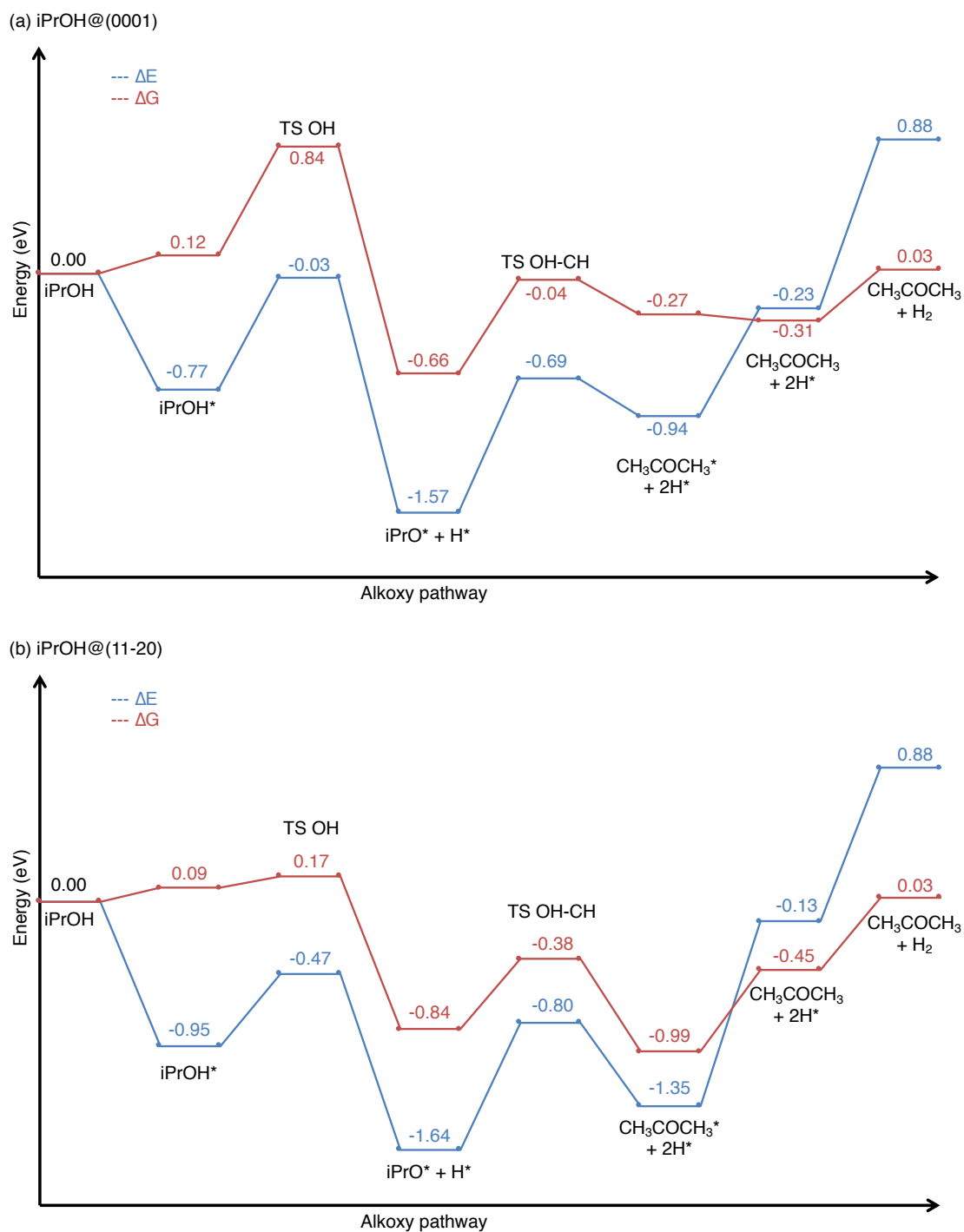


Figure 4.15. Reaction energy profiles for iPrOH dehydrogenation via alkoxy pathway on (a) (0001) and (b) (11-20) cobalt surfaces. In blue profile in electronic energy differences (ΔE ; without dipol correction) and in red in Gibbs Free Energy differences (ΔG). All the energy values are given in eV. '*' stands for the adsorption of the species on the surface.

Table 4.4. Activation energies for the bond breakings occurring among the alcohol dehydrogenation pathways, expressed as electronic energies and Gibbs Free Energies.

Bond breaking	Activation energy			
	(0001)		(11-20)	
	E (eV)	G (eV)	E (eV)	G (eV)
OH	0.74	0.72	0.48	0.08
OH-CH	0.88	0.62	0.84	0.46
CH	1.07	0.94	0.80	0.39
CH-OH	0.65	0.50	0.68	0.37

The energy profiles, expressed as electronic energy differences (ΔE) and as Gibbs Free Energy differences (ΔG), for iPrOH dehydrogenation on (0001) and (11-20) facets are presented on Figure 4.12 for alkoxy pathway and on Figure A.4.3. in Annex for hydroxyalkyl pathway. As the reference state the sum of energy of surface and alcohol is taken, expressed respectively in electronic energies and Gibbs Free Energies. These two surfaces were chosen for the comparison, as they are present on the Co nanorods, used in experiments. Moreover, the dehydrogenation of model secondary alcohol (iPrOH) is presented, as dehydrogenation of secondary alcohol (2-octanol) was effective in catalytic tests.

It is globally observed that while the energies are expressed as Gibbs Free Energies then the adsorption is weaker. Hence, the contact time between species and surface is shorter, but also the probability of blocking the active sites is lower. As it can be seen in Table A.4.3, the change results from the entropy correction. The activation energies for different bond scissions possess lower values, while the corrections are included (Table 4.4). This trend is especially visible for open type (11-20) facet. For example, the activation energy of OH bond breaking diminished from 0.48 eV to only 0.08 eV. It again results mostly from the entropy correction, but also ZPE correction is important. Further, from the corrected profiles, we can clearly read that in the temperature of 180°C, the reaction is almost athermic ($\Delta G = 0.03$ eV). Hence, it can efficiently proceed, if the substrate-product equilibrium is switched towards products, for example by removing H_2 from the reaction space. With this knowledge, for the comparison of experimental results with computational results, only corrected energy values will be used in further considerations.

As the computations showed the (11-20) surface is supposed to be more active than the (0001) facet. It is also the most exposed facet on the Co NRs surface, and therefore, it can be assumed to be responsible for their catalytic activity. Hence, it will be used in the DFT

modeling to explain the observed chemoselectivity towards secondary alcohol dehydrogenation.

4.5.2.2. Primary vs secondary alcohol dehydrogenation

To shed the light on the superior activity of Co NRs towards dehydrogenation of secondary alcohol vs primary one, DFT modeling was conducted. 1-PrOH was used in computations as a model of primary alcohol, and iPrOH was used as a model of secondary alcohol. The chosen alcohols were of the same carbon chain length, to avoid the misleading influence of dispersion, coming from the additional $-CH_2-$ group. The reaction was modeled on (11-20) facet, as it is occupying the biggest part of surface area of nanorods. The energies were considered as Gibbs Free Energies, and the applied temperature was equal to 180°C , which is the reaction temperature. Negative energy means stabilizing interactions.

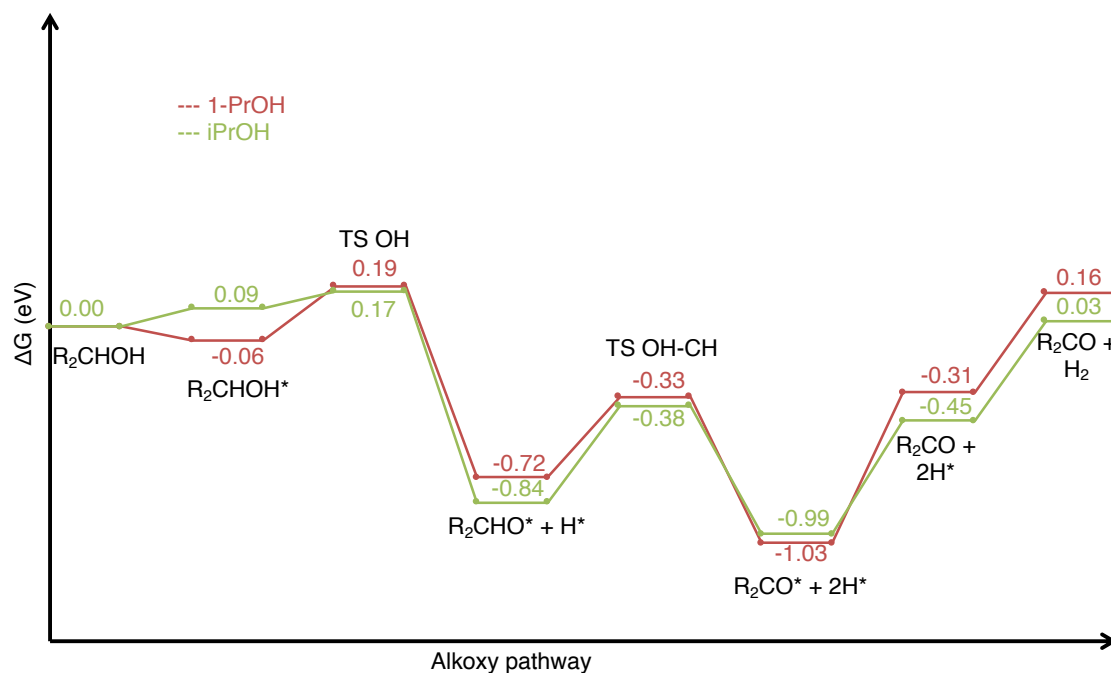


Figure 4.16. Gibbs Free Energy profile for 1-PrOH (red) and iPrOH (green) dehydrogenation on Co(11-20) facet via alkoxy pathway. '*' means the adsorption of species on the surface. All the energies are given in eV.

As we already demonstrated in part 4.2, and confirmed in part 4.3 of this chapter, the alcohol dehydrogenation reaction proceeds preferentially by alkoxy mechanism on different Co surfaces and only it will be discussed in the main text. The Gibbs Free Energy profiles for 1-PrOH and iPrOH dehydrogenation via alkoxy pathway are presented on Figure 4.16, and via hydroxyalkyl pathway on Figure A.4.4. in the Annex.

1-PrOH adsorption on the surface is exothermic by -0.06 eV, whereas the adsorption of iPrOH is endothermic by 0.09 eV. Such energy values in both of the cases imply short contact time between alcohol molecule and the metal surface. Both alcohols are contacting with the surface via O in top position to the metal atom. Alkoxy intermediates are strongly adsorbed on the surface. They are bounded by O atom in bridge position. However, iPrO* is adsorbed stronger by 0.12 eV than 1-PrO*. Adsorption of carbonyl products (aldehyde vs ketone) differs only by 0.04 eV, which is not a significant difference. Both molecules adsorb via C and O atoms in bridge positions, in which π electrons from C=O bond are interacting with the metal surface.

Considering the activation energies for bond breakings, OH dissociation requires 0.17 eV for 1-PrOH and 0.08 eV for iPrOH. In the transition state, the OH bond length is equal to 1.30 Å for 1-PrOH and iPrOH (elongated from 0.98 Å). Subsequent OH-CH bond breaking, requires 0.39 eV and 0.46 eV for primary and secondary alcohols, respectively. The CH bond length in the transition state is equal to 1.61 Å for 1-PrO* and 1.66 Å for iPrO* (elongated from 1.10 Å).

The lower activation energy for OH bond dissociation is in favor of iPrOH dehydrogenation over 1-PrOH. On the other hand, alkoxy intermediate from secondary alcohol adsorbs stronger than alkoxy intermediate from primary alcohol, what is in favor of 1-PrOH dehydrogenation, due to lower possibility of active sites blocking. As well in favor of 1-PrOH dehydrogenation is lower energy barrier for OH-CH bond scission. However, these differences are not significant enough to explain the chemoselectivity exhibited by nanorods towards secondary alcohol dehydrogenation.

The noticeable difference on the dehydrogenation pathway between primary and secondary alcohol is the amount of energy necessary to desorb carbonyl product from the metal surface (desorption energy). Desorption of CH₃CH₂CHO requires 0.72 eV, whereas desorption of CH₃COCH₃ requires 0.54 eV. As well we have to keep in mind that 1-PrOH dehydrogenation is

endothermic by 0.16 eV, whereas iPrOH dehydrogenation is endothermic only by 0.03 eV. What as well favors dehydrogenation of secondary alcohol over primary one.

To sum up, the selectivity of nanorods towards secondary alcohol dehydrogenation over primary alcohol is not caused by the differences among the dehydrogenation pathway. It is caused by the difference in energy for carbonyl product desorption and thermochemical preference for secondary alcohol dehydrogenation.

4.6. Conclusions

Investigation of structure (shape) sensitivity of acceptor-less alcohol dehydrogenation was possible by Density Functional Theory (DFT) calculations. The activity of different close packed and open type hcp and fcc Co surfaces were studied towards primary and secondary alcohol dehydrogenation. The computations revealed that among the two possible reaction mechanisms, alkoxy pathway is preferred for all the Co surfaces. It is favored kinetically due to lower activation energy for OH bond breaking vs CH bond scission, and thermodynamically, as the alkoxy intermediate, present along it, is the most stable of all reaction species. The comparison of reaction energy profiles for different surfaces revealed that the OH bond breaking is easier on open type facets. Further, adsorption of alcohol and carbonyl product molecules occurred to be surface sensitive, whereas, the adsorption of alkoxy intermediate and H^{\bullet} was not. Among all the surfaces, (10-12), (211) and (11-20) were predicted to be the most active.

Additional analysis of kinetic (E_{act}) vs thermochemistry (ΔE) of reaction allowed to visualize that OH bond dissociation proceeds through transition states of different geometries, whereas CH, OH-CH and CH-OH transition states are similar in nature. It confirmed the CH bond breaking being late transition state, but it led to the misleading conclusions about the CH-OH and OH-CH transition state nature. Analysis of adsorption vs geometry relations revealed alcohol, carbonyl product and hydroxyalkyl intermediate being surface sensitive, whereas alkoxy intermediate and H^{\bullet} were not, what agreed with our earlier observations.

The above findings open the gate towards guiding the acceptor-less alcohol dehydrogenation reaction using Co NPs of different shapes as catalysts. It will be further verified by joined experimental and theoretical investigations, described in the following Chapter 5.

As the preliminary tests in Paris demonstrated, alcohol dehydrogenation was also chemoselective. Co nanorods, exposing mainly (11-20) facet, were highly active towards secondary alcohol dehydrogenation (2-octanol), and almost not active towards primary alcohol dehydrogenation (1-octanol). DFT calculations allowed to explain that this selectivity comes from the difference in the reaction thermochemistry, and easier desorption of ketone than aldehyde from the catalyst surface. The proper comparison between computational and experimental results was possible while the energies were considered as Gibbs Free Energies.

Bibliography

1. Bratlie, K. M., Lee, H., Komvopoulos, K., Yang, P. & Somorjai, G. A. Platinum nanoparticle shape effects on benzene hydrogenation selectivity. *Nano Lett.* **7**, 3097–3101 (2007).
2. Xu, R., Wang, D., Zhang, J. & Li, Y. Shape-dependent catalytic activity of silver nanoparticles for the oxidation of styrene. *Chem. Asian J.* **1**, 888–893 (2006).
3. Hoyt, R. A., Montemore, M. M., Sykes, E. C. H. & Kaxiras, E. Anhydrous methanol and ethanol dehydrogenation at Cu(111) step edges. *J. Phys. Chem. C* **122**, 21952–21962 (2018).
4. He, X. *et al.* Controllable in situ surface restructuring of Cu catalysts and remarkable enhancement of their catalytic activity. *ACS Catal.* **9**, 2213–2221 (2019).
5. Atmane, K. A. *et al.* Control of the anisotropic shape of cobalt nanorods in the liquid phase: from experiment to theory... and back. *Nanoscale* **6**, 2682–2692 (2014).
6. Lee, B. W., Alsenz, R., Ignatiev, A. & Van Hove, M. A. Surface structures of the two allotropic phases of cobalt. *Phys. Rev. B* **17**, 1510–1520 (1978).
7. Dumestre, F. *et al.* Unprecedented crystalline super-lattices of monodisperse cobalt nanorods. *Angew. Chem. Int. Edit.* **42**, 5213–5216 (2003).
8. Liu, Q. *et al.* Synthesis of shape-controllable cobalt nanoparticles and their shape-dependent performance in glycerol hydrogenolysis. *RSC Advances* **5**, 4861–4871 (2015).
9. Fischer, N., van Steen, E. & Claeys, M. Preparation of supported nano-sized cobalt oxide and fcc cobalt crystallites. *Catal. Today* **171**, 174–179 (2011).
10. Wulff, G. XXV. Zur Frage der Geschwindigkeit des Wachstums und der Auflösung der Kristallflächen. *Zeitschrift für Kristallographie und Mineralogie* **34**, 449–530 (1901).
11. Liu, J.-X., Su, H.-Y., Sun, D.-P., Zhang, B.-Y. & Li, W.-X. Crystallographic dependence of CO activation on cobalt catalysts: HCP versus FCC. *J. Am. Chem. Soc.* **135**, 16284–16287 (2013).
12. Chen, Q. *et al.* Potassium adsorption behavior on hcp cobalt as model systems for the Fischer–Tropsch synthesis: a density functional theory study. *Phys. Chem. Chem. Phys.* **19**, 12246–12254 (2017).
13. Luo, W. & Asthagiri, A. Density Functional Theory study of methanol steam reforming on Co(0001) and Co(111) surfaces. *J. Phys. Chem. C* **118**, 15274–15285 (2014).
14. Sutton, J. E. & Vlachos, D. G. Ethanol activation on closed-packed surfaces. *Ind. Eng. Chem. Res.* **54**, 4213–4225 (2015).

15. Zaffran, J., Michel, C., Delbecq, F. & Sautet, P. Trade-off between accuracy and universality in linear energy relations for alcohol dehydrogenation on transition metals. *J. Phys. Chem. C* **119**, 12988–12998 (2015).
16. Sutton, J. E. & Vlachos, D. G. Ethanol activation on closed-packed surfaces. *Ind. Eng. Chem. Res.* **54**, 4213–4225 (2015).
17. Calle-Vallejo, F., Martínez, J. I., García-Lastra, J. M., Sautet, P. & Loffreda, D. Fast prediction of adsorption properties for platinum nanocatalysts with generalized coordination numbers. *Angew. Chem. Int. Edit.* **53**, 8316–8319 (2014).
18. Calle-Vallejo, F., Loffreda, D., Koper, M. T. M. & Sautet, P. Introducing structural sensitivity into adsorption–energy scaling relations by means of coordination numbers. *Nature Chemistry* **7**, 403–410 (2015).
19. Calle-Vallejo, F. *et al.* Finding optimal surface sites on heterogeneous catalysts by counting nearest neighbors. *Science* **350**, 185–189 (2015).
20. Bell, R. P. Relations between the energy and entropy of solution and their significance. *Transactions of the Faraday Society* **33**, 496–501 (1937).
21. Evans, M. G. & Polanyi, M. Further considerations on the thermodynamics of chemical equilibria and reaction rates. *Transactions of the Faraday Society* **32**, 1333–1360 (1936).
22. Kurth, S., Perdew, J. P. & Blaha, P. Molecular and solid-state tests of density functional approximations: LSD, GGAs, and meta-GGAs. *Int. J. Quantum Chem.* **75**, 889–909 (1999).
23. Zhao, Z., Chen, Z., Zhang, X. & Lu, G. Generalized surface coordination number as an activity descriptor for CO₂ reduction on Cu surfaces. *J. Phys. Chem. C* **120**, 28125–28130 (2016).
24. Yang, K., Zhang, M. & Yu, Y. Theoretical insights into the effect of terrace width and step edge coverage on CO adsorption and dissociation over stepped Ni surfaces. *Phys. Chem. Chem. Phys.* **19**, 17918–17927 (2017).
25. Viola, A. *et al.* Unsupported shaped cobalt nanoparticles as efficient and recyclable catalysts for the solvent-free acceptorless dehydrogenation of alcohols. *Catal. Sci. Technol.* **8**, 562–572 (2018).
26. Dong, H., Chen, Y.-C. & Feldmann, C. Polyol synthesis of nanoparticles: status and options regarding metals, oxides, chalcogenides, and non-metal elements. *Green Chem.* **17**, 4107–4132 (2015).

27. Shimizu, K. *et al.* Heterogeneous cobalt catalysts for the acceptorless dehydrogenation of alcohols. *Green Chem.* **15**, 418–424 (2013).
28. Yi, J. *et al.* A reusable unsupported rhenium nanocrystalline catalyst for acceptorless dehydrogenation of alcohols through γ -C-H activation. *Angew. Chem. Int. Edit.* **53**, 833–836 (2014).
29. Cao, X.-M., Burch, R., Hardacre, C. & Hu, P. An understanding of chemoselective hydrogenation on crotonaldehyde over Pt(111) in the free energy landscape: The microkinetics study based on first-principles calculations. *Catalysis Today* **165**, 71–79 (2011).

Chapter 5

Activity of cobalt unsupported nanoparticles of well-defined shapes towards alcohol dehydrogenation

The experimental investigations on the supported Co catalysts showed us that this metal is active in the acceptor-less alcohol dehydrogenation (see Chapter 3), in agreement with the literature.¹ Also, the preliminary reactions conducted by our project partners from ITODYS in Paris showed, that Co nanorods are highly active towards secondary alcohol dehydrogenation.² Furthermore, DFT computations lead us to the conclusion that this reaction should be structure (surface) sensitive (see Chapter 4). The structure sensitivity of alcohol dehydrogenation was already reported in the literature for Cu catalysts.^{3,4} Therefore, arises the question: “Is the alcohol dehydrogenation a structure sensitive reaction with cobalt catalysts?”

The synthesis of shaped Co NPs⁵ is possible by polyol method,⁶ which is a mild synthesis protocol. By varying the preparation conditions it is possible to obtain NPs of various shapes,⁷ which are exposing different and well-defined crystallographic facets. Hence, they are good model catalysts to investigate the structure sensitivity of the reaction. To stabilize the crystallographic facets, the presence of ligands is helpful, as it can favor the formation and growth of thermodynamically less stable (without ligands) surfaces.⁷ However, as the ligands remain on the surfaces after the synthesis, they can modify the activity and/or selectivity of the samples,^{8,9,10,11,12,13} and their presence should be taken into account.

As it can be seen in the literature, different approaches have to be combined to investigate the shape sensitivity^{4,3,14,15} of the reaction and the role of ligands^{8,9,10,11}: controlled synthesis, extensive characterization, theoretical modeling. Aiming at investigating and understanding

the activity of the shaped Co NPs in acceptor-less alcohol dehydrogenation, we also combined different approaches. Our project partners from LPCNO in Toulouse and ITODYS in Paris synthesized 14 Co samples of different shapes and protected with carboxylic ligands of different lengths, using polyol synthesis method. Catalytic testing of the samples allowed us to assess their activity towards model aliphatic secondary alcohol (2-octanol) dehydrogenation. Different characterization techniques (TEM, N₂ physisorption, XRD, TGA-N₂) revealed their properties (i.e. shape, type and ratio of exposed facets, surface coverage with ligands). By DFT computations it was possible to explain its nature. Analysis of the gathered information allowed us to determine the most decisive factor for the activity.

5.1. Preparation and characterization of Co NPs of different shapes

Our partners from LPCNO in Toulouse and ITODYS in Paris chose the polyol synthesis method¹⁶ to obtain cobalt nanoparticles of different shapes,^{5,7,17} by varying the preparation conditions. (For details see Chapter 2.2.3 and Annex, part A.2.1.) During the synthesis, a polyol is used both as a solvent and as a reducing agent. In our synthesis protocols 1,2-butanediol or 1,2-propanediol were used. NaOH was used to ensure basic conditions (0.075 or 0.160 mol L⁻¹). And RuCl₃ · xH₂O or RuCl₃ were used as nucleating agents. The synthesis proceeded with or without stirring. Different cobalt carboxylates (cobalt laurate – C12, palmitate – C16, heptanoate – C7, octanoate – C8 and decanoate – C10) were used as cobalt precursors. The carboxylic ligands served also as stabilizing agents for the NPs surfaces. For each sample the synthesis protocol differed.

Three series (14 samples together) of Co NPs were prepared by our project partners. First series consisted of samples covered with laurate ligands (L), possessing different shapes. They were: nanorods (R) of different lengths, diabolos (D) and platelets (P). Second series of catalysts was protected with palmitate ligands (P) and it also contained samples of different shapes. The third series was composed of Co nanorods protected by carboxylic ligands of different lengths: heptanoates (H), octanoates (O) and decanoates (D). Samples are named according to the role: type of ligand – shape – order number (if necessary). For example, sample L-R-1 is a sample protected with laurate ligands (L), being nanorods (R) in shape, with the order number of 1.

TEM measurements allowed to identify the morphology of prepared samples. On Figure 5.1 are given typical TEM images of Co particles prepared with the laurate ligand (nanorods (a), diabolos (b) and platelets (c)), together with their corresponding geometrical models. The TEM images of all the other Co samples are shown in Figures A.5.1-3 in the Annex. Depending on the preparation conditions, nanorods can possess different length (marked as L_{TEM} on the Figures). For example, L-R-1 sample is 175 nm long, whereas L-R-3 sample is over 3 times shorter (51 nm), although the shape is the same. Among nanorods we can also find some with conical tips (like L-R-2 sample) and others without them (like sample L-R-4). Along the same axes direction, the length of diabolos (L_{TEM}) and the thickness of platelets (t_{TEM}) are smaller than the length of nanorods (e.g. 39 nm for L-D and 8 nm for L-P samples, respectively), but their width (D_{TEM}) is larger (e.g. 46 nm for L-D and 56 nm for L-P samples, respectively). These differences influence the proportion of the exposed crystallographic surfaces.

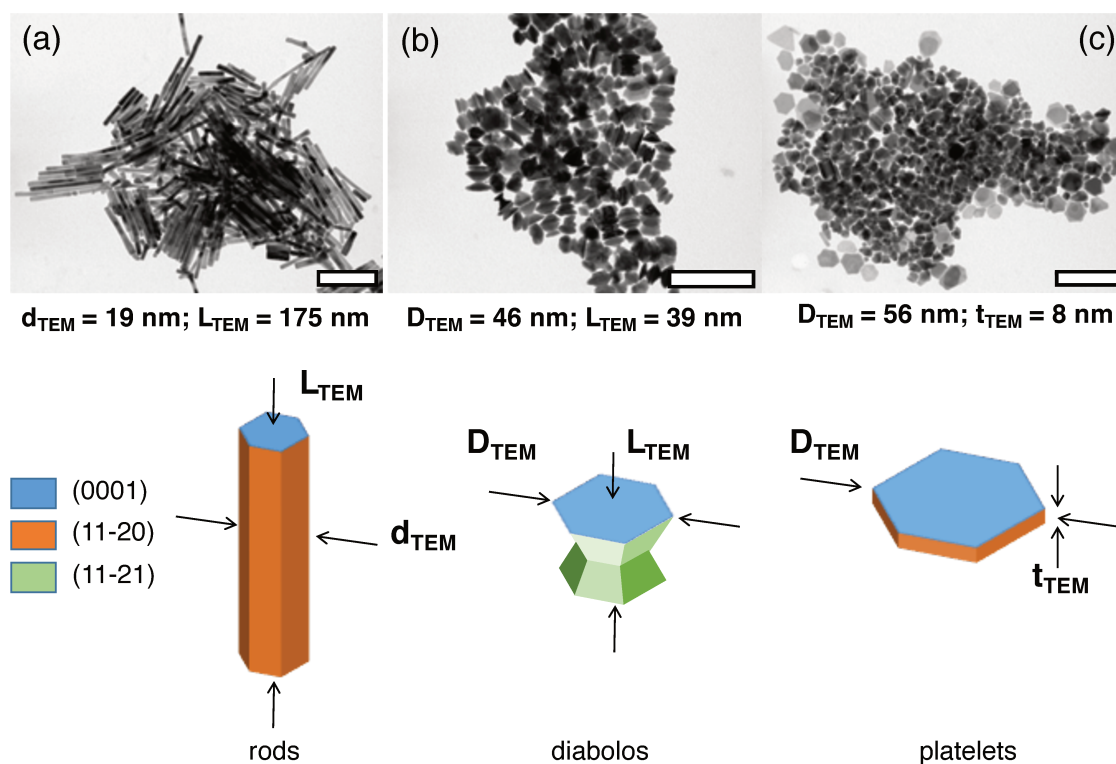


Figure 5.1. TEM images for Co NPs with different shapes, protected with laurate ligands and their respective geometrical model: (a) rods, L-R-1, (b) diabolos, L-D and (c) platelets, L-P. The scale bar stands for 200 nm. L_{TEM} - mean length; D_{TEM} - mean diameter of the diabolos tips and of the platelets; d_{TEM} - mean diameter of the rods and of the central column in the diabolos; t_{TEM} - mean thickness of the platelets.

Three types of crystal facets are encountered in these particles: (0001) compact planes and open (11-20) and (11-21) facets. Their relative proportions depend on the nanocrystal morphology and can be calculated combining the shape approximation and TEM dimension measurement (see Chapter 2.3.5 and Annex, part A.2.2 for technical details, and Table 5.1 for the outcome of surface proportions). Typically, about 90% of the surface of Co rods correspond to (11-20) facets, and the last 10% to (0001) planes, while the surface corresponding to (11-21) facets, if any, can be neglected. The distinction between rods and diabolos is not straightforward since diabolos can be seen as rods with extended conical tips. Particles with a high proportion of (11-21) and (0001) facets are denoted diabolos while the rods mainly exhibit (11-20) planes. For diabolos, two different type of facets are mainly exposed: (0001) and (11-21), corresponding respectively to about 35-38% and 62-65% of the total surface of NPs. Platelets expose close packed (0001) facets, corresponding to ~70-80% of the NP surface, while the lateral walls correspond to (11-20) facets and occupy the rest of the particle surface.

Table 5.1. Characterizations of unsupported shaped Co nanoparticles obtained by polyol synthesis method.

Sample ¹	Ligand	Shape	Exposed facets			SSA _c ² (m ² g ⁻¹)	$\Delta m_{\text{TGA-N}_2}$ ³ (wt%)	Surface coverage (mol m ⁻² 10 ⁻⁶)
			(0001) (%)	(11-20) (%)	(11-21) (%)			
L-R-1	C12 - Laurate	Nanorods	5	95	0	29	9.6	18
L-R-2	C12 - Laurate	Nanorods	6	94	0	26	10.2	22
L-R-3	C12 - Laurate	Short nanorods	35	20	45	39	28.4	51
L-R-4	C12 - Laurate	Nanorods without tips	6	94	0	39	11.4	17
L-D	C12 - Laurate	Diabolos	38	0	62	27	10.9	23
L-P	C12 - Laurate	Platelets	78	22	0	36	12.0	19
P-R-1	C16 – Palmitate	Long nanorods	5	95	0	27	41.2	102
P-R-2	C16 – Palmitate	Short nanorods	8	92	0	35	31.9	52
P-R-3	C16 – Palmitate	Very short nanorods	14	86	0	47	59.7	123
P-D	C16 – Palmitate	Diabolos	35	0	65	39	62.5	167
P-P	C16 – Palmitate	Platelets	67	33	0	28	44.4	112
H-R	C7 – Heptanoate	Nanorods	-	-	-	-	9.7	-
O-R	C8 – Octanoate	Nanorods	8	92	0	22	6.4	22
D-R	C10 – Decanoate	Nanorods	5	95	0	23	8.4	23

¹ Naming of the samples according to the role: type of ligand – shape – order number (if necessary)

² SSA_c – Calculated specific surface area of exposed metal facets, based on TEM geometric measurements

³ Weight loss according to TGA-N₂ measurements, equal to the mass of organic ligands in the sample

The particles were further characterized by powder X-ray diffraction (see Figure A.5.4. in Annex). Co rods crystallize with the pure hcp structure, diabolos and platelets crystallize mainly with the hcp structure, but the fcc phase can also be detected, especially for the platelets. During post-synthesis sample manipulation a surface CoO phase was created. It can be hardly detected, what suggests its very low thickness. It was already shown in the literature, that this phase has a thickness of about 1.5 nm.¹⁸

To measure the specific surface area of samples N₂ physisorption technique can be used (SSA_{BET}). However, as our NPs are composed of metal NPs covered with organic ligands, which will influence the gas physisorption, this method is not appropriate to obtain the specific surface area exposed only by metallic Co. This one can be calculated using the NPs dimensions extracted from the TEM images (SSA_C; see Chapter 2.3.5, and Annex, part A.2.2). To compare SSA_{BET} and SSA_C, the N₂ physisorption was performed on L-R-1 and L-R-2 samples. The obtained SSA_{BET} are equal to 29 m² g⁻¹ and 32 m² g⁻¹, respectively, whereas, their SSA_C have the values of 29 m² g⁻¹ and 26 m² g⁻¹. The result difference for L-R-2 particles confirms that, indeed, the presence of ligands influences the specific surface area value. Later in this chapter only the values of specific surface area exposed by metal (SSA_C) will be used. The calculated values of SSA_C are in the range 22-47 m² g⁻¹ (per g of Co, see Table 5.1). No connection between the shape and the exposed surface area is visible.

Since carboxylate ligands are adsorbed onto the particle surface,¹⁹ TGA experiments were performed in order to determine the different amounts of organic matter for all the Co particles. The decomposition of carboxylate ligands occurs at about 300°C and is associated with an endothermic peak (see Figure A.5.5). The weight loss is in the range 6.5-62.5%, depending on the nature of the sample (see Table 5.1). These data indicate that the particles display different thicknesses of ligand layers. To determine them, we combined TGA results with TEM geometric measurements. Knowing the weight loss for a given sample ($\Delta m_{\text{TGA-N}_2}$) and the type of ligands present on the surface it is possible to calculate the molar amount of ligands (n_{ligands}) per given mass of sample (m_{sample} ; see equation (1) below). Also, knowing the mass of sample, the mass of pure Co in it is known (m_{Co}), and by it the exposed metal surface area (SA, thanks to SSA_C; equation (2)). The ratio of these two values constitutes the ligand surface coverage value (equation 3).

$$n_{\text{ligands}} = \frac{\frac{\Delta m_{\text{TGA-N}_2}}{100} \times m_{\text{sample}}}{M_{\text{ligands}}} \quad (1)$$

$$SA = SSA_C \times \left(\frac{m_{\text{Co}}}{100} \times m_{\text{sample}} \right) = SSA_C \times \left(\frac{(100 - \Delta m_{\text{TGA-N}_2})}{100} \times m_{\text{sample}} \right) \quad (2)$$

$$\text{Surface coverage} = \frac{n_{\text{ligands}}}{SA} \quad (3)$$

The calculated ligand surface coverages values are in the range $17\text{-}167 \cdot 10^{-6} \text{ mol m}^{-2}$. Based on the area of surface unit cell for a given facet (from the crystallographic cleavage of bulk metal) and maximum number of ligands adsorbed per it (1 carboxylic ligand is considered as adsorbed per 2 surface Co atoms), 1 monolayer (ML) of ligands on the close packed (0001) surface is equivalent to $16 \cdot 10^{-6} \text{ mol m}^{-2}$, and to $10 \cdot 10^{-6} \text{ mol m}^{-2}$ on open type (11-20) facet. This clearly indicates that the ligand protecting layer on the samples corresponds to at least 1-2 ML (or one bilayer), and in some cases, is even larger than 10 ML.

To summarize, adjusting of the conditions in the polyol synthesis protocol allowed to obtain Co NPs of various shapes. They were exposing three types of facets, namely (0001), (11-20) and (11-21), in different proportions. They were covered with different types and amounts of carboxylic ligands, what was quantified by the extensive characterization of sample. This knowledge will allow to rationalize the catalytic tests results and determine the factor(s) guiding the activity.

5.2. Catalytic activity of shaped Co NPs

The catalytic activity of decorated shaped Co nanoparticles was studied for the 2-octanol dehydrogenation reaction. The reactions were conducted in acceptor-less conditions (atmosphere of inert gases), at 145°C , for 24 h. The used mass of catalyst was equal to 0.025 g, as the aim was to have the $n_{\text{alc}} : n_{\text{cat}} = 100$. The corresponding catalytic tests results are presented in Table 5.2.

Figure 5.2. gathers two graphs which illustrate typical results of a catalytic test on the sample L-R-1: (a) intensity of H_2 production during the course of the reaction and (b) conversion based on change of substrate concentration (X), yield in H_2 (Y_{H_2}) and yield in 2-octanone (Y) as

a function of time. Before the H₂ production started, short induction time (10-20 min) was required. It can be explained by the presence of the tiny CoO layer on the catalyst surface, and the necessity of its reduction, to activate the catalyst. As the H₂ production begun, it was increasing gradually, to reach maximum after few hours (around 4 h) of reaction and then dropped gradually, once the reaction equilibrium is approached. For all the catalytic tests, the yields of 2-octanone and H₂ are in good agreement, within 6%, and also the selectivity towards the production of the ketone and hydrogen is quantitative (no by-products formation was observed). Moreover, the observed H₂ production is in line with ketone formation, what confirms the acceptor-less mechanism of the reaction.

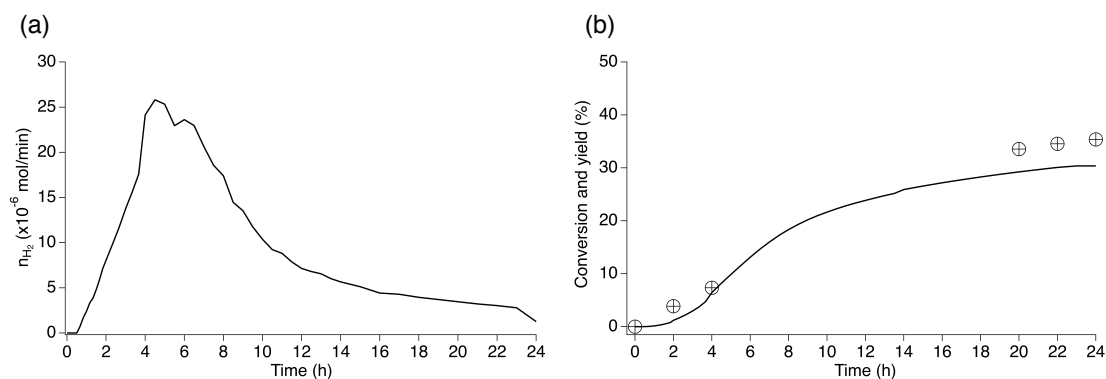


Figure 5.2. Catalytic test results for 2-octanol dehydrogenation with L-R-1 catalyst. (a) H₂ production (black line) vs time (b) Conversion of the 2-octanol X (○), yield in hydrogen Y_{H_2} (black line), and in ketone (+) vs time,

The catalytic test results after 24 h for all the samples are presented in Table 5.2. The first series of samples – Co NPs of different shapes protected with laurate ligands, showed similar catalytic activity towards secondary alcohol dehydrogenation. They all gave 32-35% of conversion, except for short nanorods (L-R-3), which gave a conversion of 4% only. It prevailed making any straightforward correlation between structure and activity. The samples from the second series (NPs of different shapes, protected with palmitate ligands) were poorly or not active towards 2-octanol dehydrogenation. Only platelets (P-P) gave 16% of conversion and very short nanorods (P-R-3) gave 9% of alcohol conversion. The last series of catalysts (nanorods, protected with carboxylic ligands of different lengths) gave similar 2-octanol conversion, ranging from 22% to 25%. This conversion is lower than the one obtained with

the laurate nanorods (L-R-1, L-R-2 and L-R-4, above 30%) or other shaped nanoparticles covered by laurate (L-D, L-P, above 30%). In summary, nanorods with laurate ligands demonstrated the best performance, giving conversions of over 10% higher than nanorods protected with ligands of other chain lengths.

Table 5.2. Catalytic 2-octanol dehydrogenation using Co shaped nanoparticles decorated with carboxylate ligands. Reaction conditions: $m_{\text{cat}} = 0.025$ g, $n_{\text{alc}} : n_{\text{cat}} = 100$, 0.95 mol L^{-1} 2-octanol, decane, 24 h, 145°C , $V_{\text{total}} = 45$ mL.

Sample	X (%)	Y (%)	Y_{H_2} (%)	TON (mol mol^{-1})
L-R-1	35	35	30	1140
L-R-2	32	32	27	1170
L-R-3	4	4	2	70
L-R-4	34	34	28	830
L-D	32	32	30	610
L-P	35	35	33	600
P-R-1	2	2	1	90
P-R-2	3	3	1	100
P-R-3	9	9	7	350
P-D	1	1	1	70
P-P	16	16	15	430
H-R	22	22	17	n.a.
O-R	23	23	19	890
D-R	25	25	23	970

n.a. - not applicable

To conclude, 2-octanol dehydrogenation with unsupported Co NPs is completely selective towards the corresponding ketone (2-octanone) and H_2 production. Among all the tested samples Co NPs with laurate ligands demonstrated the best performance, giving conversions of over 30%. However, some of the samples appeared to be not active.

5.3. Importance of the ligand decoration

5.3.1. Factor(s) guiding the catalytic activity

To explain the catalytic behavior of different Co NPs we started to look for the factor(s) guiding their performance. To better express their activity, as the samples differ in intrinsic properties like specific surface area exposed by metal, we decided to use turnover numbers (TON) for this purpose. TON is equal to the ratio between amount of converted substrate to the total amount of surface Co atoms. It allows to express the activity per surface active site.

$$\text{TON} = \frac{n_{\text{converted substrate}}}{n_{\text{surface Co atoms}}}$$

The TON values are reported in Table 5.2. and details for TON calculations for the other samples are gathered in Table A.5.1. The exact example of TON counting is presented in part A.2.4 in Annex.

Our main question was if acceptor-less alcohol dehydrogenation is a structure sensitive reaction with Co catalysts. Hence, at first, we checked the relation between type and amount of exposed facet (expressed by the amount of Co atoms in the first layer of a given type of facet in a given mass of sample used in the reaction) and the catalytic activity, expressed by TON. Two graphs were prepared: the first one gathers the relation between TON and the amount of Co atoms exposed by close packed (0001) surface in the sample (Figure 5.3.a), and the second one relates the catalytic activity with the amount of Co atoms exposed by open type facets ((11-20) and (11-21)) in the catalysts (Figure 5.3.b). If the reaction will be structure sensitive, the activity should correlate with the amount of facet(s) of given type. However, no such tendency was visible. Therefore, we assume that there has to be a more important factor, guiding the catalyst activity than the type and amount of exposed surface.

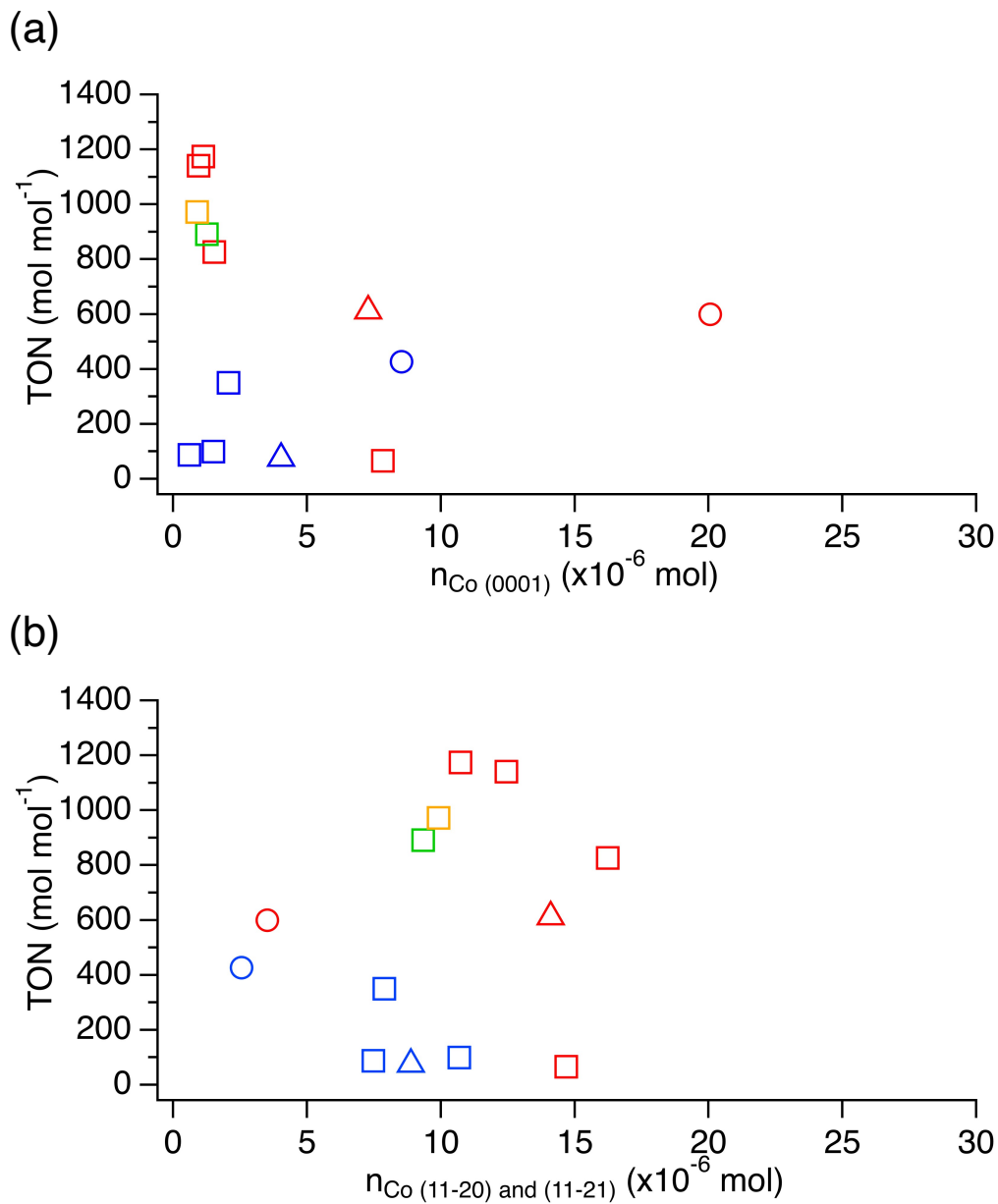


Figure 5.3. Catalytic activity (TON) as a function of type and amount of exposed facet in a given mass of sample used in the reaction: (a) for close packed (0001) facet, (b) for open type (11-20) and (11-21) surfaces. Each point corresponds to a Co sample characterized in Table 5.1 and with its catalytic activity reported in Table 5.2. The shape of the symbol codes the shape of the Co nanoparticles: nanorods (□), diabolos (△), platelets (○). The color of the symbols codes the decorating ligand: palmitate (blue), laurate (red), decanoate (orange), octanoate (green).

Looking for the property of samples guiding their performance, we checked if the activity (TON) correlates with the amount of ligands present on the metal surface in the sample (Figure 5.4). As it was already mentioned, the organic ligands surface coverage of the Co nanoparticles was estimated combining the exposed surface area derived from the TEM images and the weight loss measured by TGA. It is reported in Table 5.1. Once compared with the catalytic activity of the nanoparticles (Table 5.2), it is easily noticed that a high coverage is detrimental to catalytic activity. For instance, P-R-2 sample has a similar shape as L-R-1, but shows a much lower activity towards 2-octanol dehydrogenation (3% vs 35% of conversion, and 100 mol mol^{-1} vs $1140 \text{ mol mol}^{-1}$, when expressed in TON, respectively). On the plot of TON vs ligands surface coverage (Figure 5.4), two groups of catalysts are evident. In the first group, the coverage is around $20 \cdot 10^{-6} \text{ mol m}^{-2}$, the conversion is above 20% and the corresponding TON is above 500 mol mol^{-1} . In the second group, the coverage is above $50 \cdot 10^{-6} \text{ mol m}^{-2}$ and the reported catalytic activities are much poorer (conversion under 20% and TON under 500 mol mol^{-1}). A too thick organic layer (over 1-2 ML) prevents the catalytic activity, probably limiting the access of the substrate to the catalytic surface. This was already reported in the literature, for the aerobic oxidation of benzyl alcohol with Au_{25} clusters supported on carbon.⁸ The Au NPs were covered with thiolate ligands. The more of them were present on the metal surface, the weaker was the activity of the catalyst, and with the full surface coverage it was entirely suppressed. Also, for Pd/ Al_2O_3 such behavior was observed.⁹ The catalysts uncoated with thiolate ligands showed higher activity than the coated ones in furfural hydrogenation. In our case it is noticeable that the activity was maintained up to 1-2 ML of ligand surface coverage.

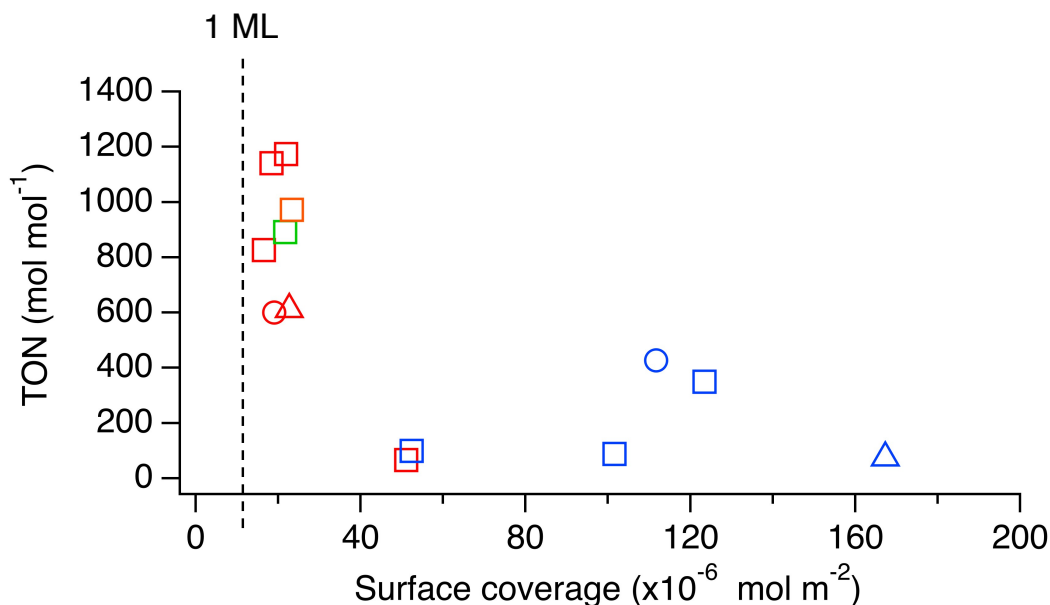


Figure 5.4. Catalytic activity (TON) as a function of the surface coverage by ligands. Each point corresponds to a Co sample characterized in Table 5.1 and with its catalytic activity reported in Table 5.2. The shape of the symbol codes the shape of the Co nanoparticles: nanorods (□), diabolos (△), platelets (○). The color of the symbols codes the decorating ligand: palmitate (blue), laurate (red), decanoate (orange), octanoate (green). The perpendicular dashed black line marks the 1 ML (monolayer) of ligand coverage.

5.3.2. Attempts to improve the catalysts activity

In the literature the removal of surface ligands was achieved by a calcination at 400-500°C.⁸ However, to preserve the morphology of the shaped Co NPs, different approaches were tried. Several pre-treatments were tested on two dried non-active catalysts (L-R-3 and P-R-2): (1) thermal treatment under vacuum, (2) additional washing with EtOH, (3) H₂ *in situ* pre-treatment before the reaction. Detailed protocols can be found in Chapter 2. None of these pre-treatments improved the catalysts activity (Table 5.3). The synthesis protocol was then modified in order to decrease the amount of ligands at the surface, by washing more intensively the nanoparticles *before* drying. This last pre-treatment (labeled #4 in Table 5.3) was performed on the P-R-2 and P-P samples, where the final washing was modified from 3 times with ethanol to 6 and 12 times with methanol, respectively. TEM was used to control that the shape was not changed after this treatment. This more intensive washing lead to a decrease in the amount of the palmitate ligands from 32 wt% to 12 wt% for P-R-2 sample,

and from 44 wt% to 16 wt% for P-P sample (see Table 5.3). When tested towards the dehydrogenation of 2-octanol, the performance improved – conversion increased from 3% up to 19%, and from 16% to 55% for P-R-2 and P-P samples, respectively - confirming the importance of the amount of ligands surrounding the catalysts in controlling their catalytic activity.

Table 5.3. Catalytic 2-octanol dehydrogenation with Co nanorods after different pre-treatments: (1) thermal treatment under vacuum, (2) washing with EtOH of the dried sample, (3) H₂ *in situ* pre-treatment, (4) modified washing procedure before sample drying. Reaction conditions: $m_{\text{cat}} = 0.025$ g, $n_{\text{alc}} : n_{\text{cat}} = 100$, 0.95 mol L⁻¹ 2-octanol, decane, 24 h, 145°C, $V_{\text{total}} = 45$ mL. The amount of ligands has been estimated before and after the pre-treatment by TGA-N₂ analysis, and the surface coverage was calculated based on the obtained results.

Sample	Pre-treatment	X (%)	$\Delta m_{\text{TGA-N}_2}^1$ (wt%)	Surface coverage (mol m ⁻² 10 ⁻⁶)
L-R-3	---	4	28	55
	1	1	31	62
P-R-2	---	3	32	52
	1	1	32	53
	2	1	30	49
	3	4	n.a.	n.a.
	4	19	12	22
P-P	---	16	44	112
	4	55	16	19

¹Weight loss according to TGA-N₂ measurements, equal to the mass of organic ligands in the sample

n.a. – not available

5.3.3. Post-reaction analysis

When the samples with a high coverage of ligands were used to perform the catalytic tests, the color of the suspension evolved from colorless to light yellow/brown, which might be an indication of Co leaching. This triggered us to perform additional post reaction characterizations. ICP-OES of the supernatant (see Table A.5.2 in Annex) confirmed the presence of Co for all samples of the second group while this leaching is under the detection limit in the case of an active catalyst (L-R-1). TGA analyses for two spent catalysts showed that the amount of organic ligands protecting the samples decreased after

the reaction: from 32 wt% to 26 wt% for the inactive P-R-1 and from 10 wt% to 6 wt% for the active L-R-1. Even though the active catalyst is as well losing some ligands it can be assessed that a monolayer is still present on the metal surfaces, whereas the decrease of ligand content for the inactive catalyst is not large enough to improve its activity. To verify if the NPs changed shape during the reaction, TEM analysis of two spent catalysts was performed. Figure 5.5 presents some TEM images for L-R-1 and P-R-3 samples before and after the reaction. Sample L-R-1 remained unchanged during the reaction course, whereas for sample P-R-3 the rounding of edges and sintering is observed.

To summarize, the inactive samples underwent structural changes during the catalytic reaction, namely the loss of ligands from the surface and modification in the shape, which is accompanied by leaching of Co into the solution. In other words, a too thick organic layer is detrimental not only to the catalytic activity, but also to the stability of the nanoparticles. To the best of our knowledge until now nobody reported such samples instability connected with the excess of ligands.

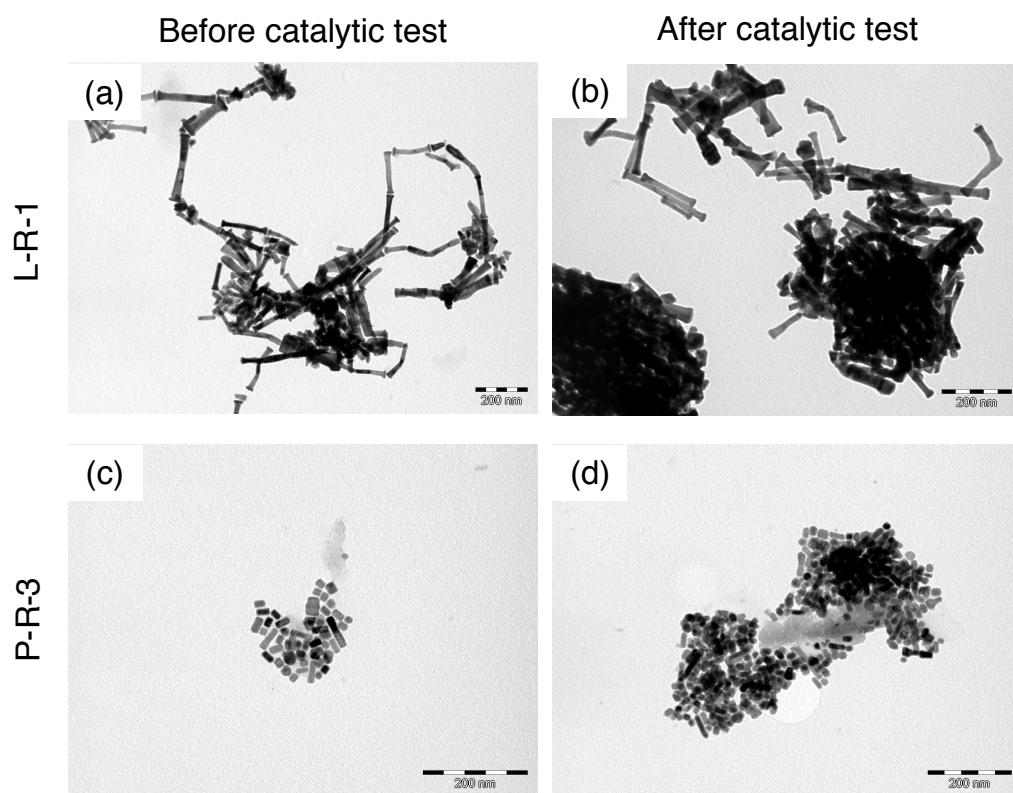


Figure 5.5. TEM images of catalysts L-R-1 (a, b) and P-R-3 (c, d), before (a, c) and after catalytic test (b, d).

5.3.4. Back to structure sensitivity

After identifying the ligand coverage as the main parameter driving the catalytic activity, we came back to the considerations about structure sensitivity. Among the active catalysts, namely those that are covered by roughly one to two monolayers, structure-activity relationships can be investigated plotting the catalytic activity per exposed site (TON) as a function of the amount of given type of facet(s) (see Figure 5.6.a for (0001) facets and Figure 5.6.b for (11-20) and (11-21) surfaces). These plots include additionally the P-R-2 and P-P re-synthesized samples, for which the activation by improved washing procedure was applied.

Based on the relations between the activity and the amount of exposed close packed (0001) facets (Figure 5.7.a) and open type facets (Figure 5.7.b) it is not possible to conclude on a trend. As we already reported, according to our DFT computations, the type of exposed facet can influence the catalytic activity of metal, and (11-20) facet was predicted to be more active than close packed (0001) surface (Chapter 4). It is also in agreement with other reports in the literature, where stepped Cu surfaces are reported as more active than (111) facet for alcohol dehydrogenation.^{4,3} However, in none of these reports the presence of surface ligands was taken into consideration. We suppose that the presence of ligands, even though limited to 1-2 monolayers, still influences the catalyst activity and does not allow to assess the shape-activity relations.

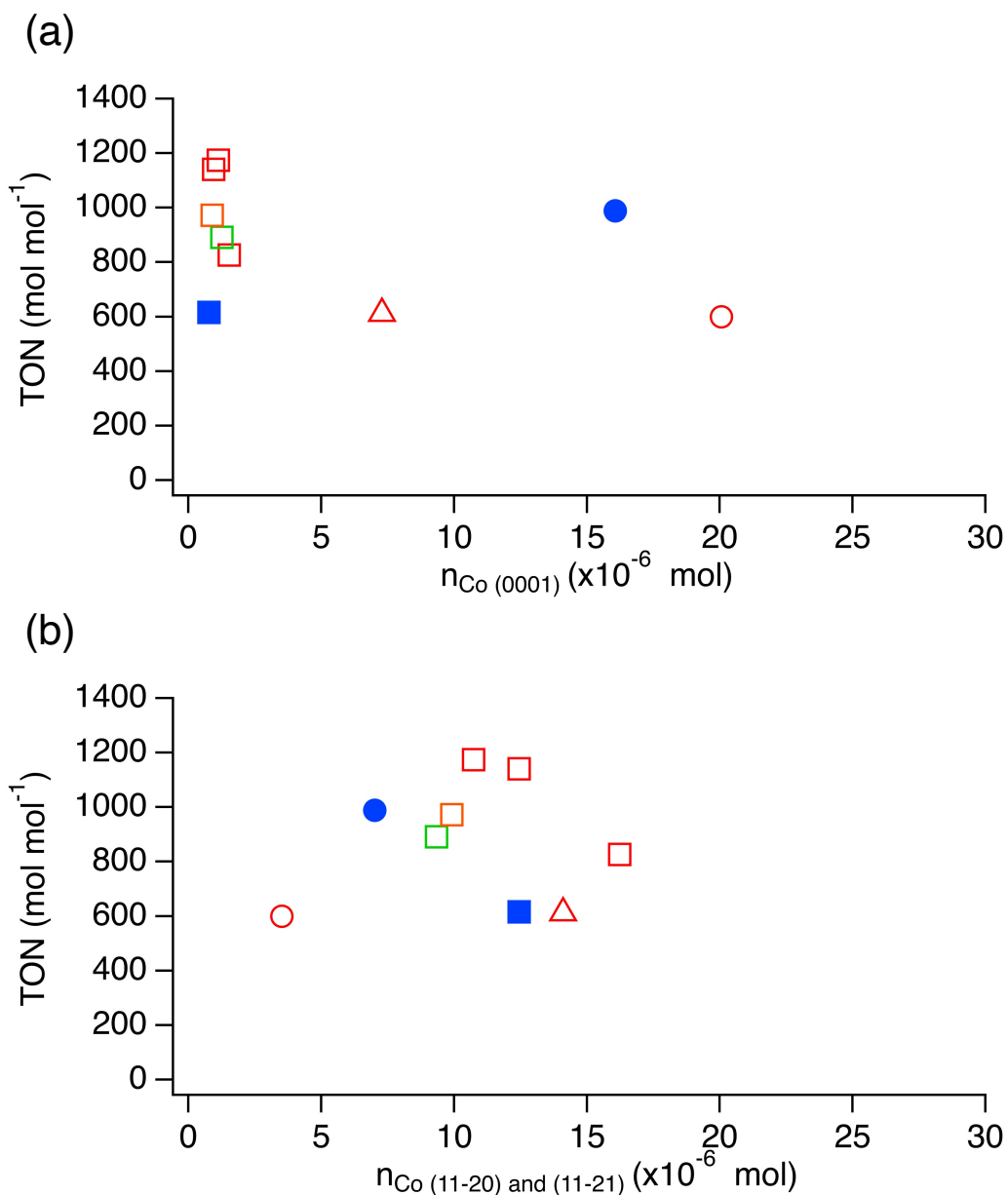


Figure 5.6. Catalytic activity (TON in mol mol⁻¹) of the catalytically active samples as a function of the number of surface exposed Co atoms (10⁻⁶ mol): (a) for the close-packed (0001) facet sites and (b) for the open facets ((11-20) and (11-21)) sites. Each point corresponds to a catalytically active Co sample (low coverage in ligands) characterized in Table 5.1 and with its catalytic activity reported in Table 5.2. The shape of the symbol codes the shape of the Co nanoparticles: nanorods (□), diabolos (△), platelets (○). The color of the symbols codes the decorating ligand: palmitate (blue), laurate (red), decanoate (orange), octanoate (green). The filled symbols refer to re-synthesized samples for which improved washing procedure was applied.

5.4. DFT computational insight – towards understanding of the role of ligands

To bring more insight into possible structure sensitivity of the alcohol dehydrogenation on Co in the presence of ligands, we investigated this reaction on the two mainly exposed facets, the (0001) and (11-20), with periodic DFT calculations.

5.4.1. Chosen molecule and surface models and preferred reaction mechanism

In the computations, isopropanol (iPrOH) was used as a model of secondary alcohol. The energies were considered as Gibbs Free Energies at 145°C, which is the experimental reaction temperature. The activities of pristine (0001) and (11-20) surfaces were compared with the ones decorated with carboxylic ligands. CH₃COO* was chosen as model ligand, to minimize the computational demands. Experimentally, the active samples are covered with 1-2 ML of ligands, but probably some defects in the covering layer are present. Hence, for the modeling, the surfaces with the ligands coverage of roughly $7 \cdot 10^{-6}$ mol m⁻² were chosen, as they resemble the most the 1 ML coverage, and still the space for alcohol molecule adsorption and proceeding of the reaction is available. It means, that per (0001) p(3x3) surface unit cell, two CH₃COO* ligands were co-adsorbed ($\theta = 4/9$ ML, 0.44 ML, $6.98 \cdot 10^{-6}$ mol m⁻², named 0.44A-Co(0001)), and per one (11-20) p(4x4) three ligands were present ($\theta = 3/4$ ML, 0.75 ML, 7.26 mol m⁻², named 0.75A-Co(11-20)).

As we already saw in Chapter 4 (for temperature of 180°C, as the preliminary reactions were performed in it), alcohol dehydrogenation is found to be slightly endergonic ($\Delta G = 0.07$ eV at 145°C) in close agreement with the experimental Gibbs reaction energy for isopropanol dehydrogenation ($\Delta G = 0.05$ eV at 145°C).²⁰ Also, as we already explained in Chapter 1 and Chapter 4, this reaction requires the scission of two bonds, OH and CH, to generate the corresponding carbonyl product (ketone). Depending on the order of these two dissociations, two pathways can be distinguished (Figure 5.7). In the alkoxy path, the OH bond breaking yields to an alkoxy intermediate, from which the OH-CH bond scission takes place. The hydroxyalkyl path starts with the CH bond dissociation, leading to the formation of hydroxyalkyl intermediate, and continues with the CH-OH bond breaking. As it was already shown in the previous Chapter 4, and in agreement with the literature,^{2,21,22} alcohol

dehydrogenation on Co surfaces proceeds preferentially via alkoxy mechanism. Hence, we will focus on it.

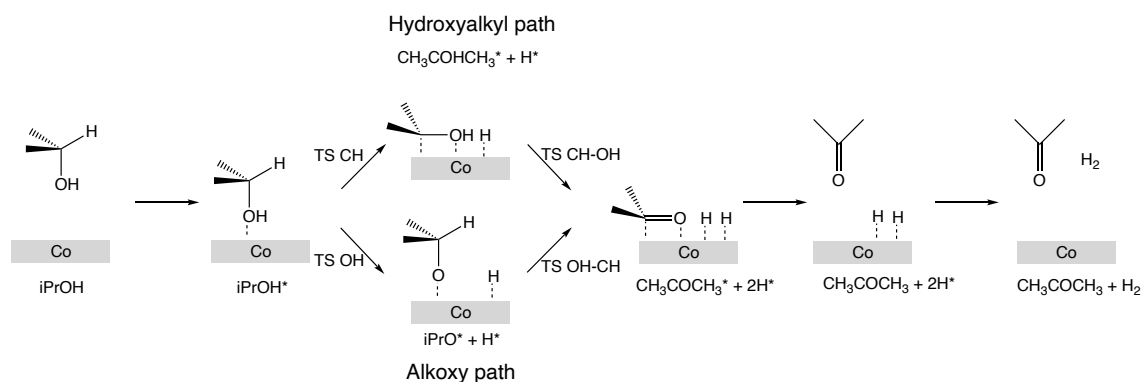


Figure 5.7. Catalytic alcohol dehydrogenation mechanism, on the example on iPrOH: top via hydroxyalkyl intermediate and bottom via alkoxy intermediate. ‘*’ means adsorption of species on the surface.

5.4.2. Activity

In Chapter 4.3. the activities (expressed in electronic energies) of different types of surfaces were already compared. Further, in Chapter 4.5, we compared the surface activity expressed in Gibbs Free Energy and electronic energy, but up to now we did not compare directly the activity of bare (0001) and (11-20) surfaces, expressed in Gibbs Free Energy at 145°C. For the sake of clarity and consistency with the following results, we will do this briefly now, focusing only on the favored alkoxy pathway. The corresponding profiles are shown with a solid line in Figure 5.9, towards the left and the right side for Co(0001) and Co(11-20) surfaces, respectively. (The corresponding profiles for hydroxyalkyl pathway are presented on Figure A.5.6 in Annex.)

On both surfaces, the adsorption of alcohol molecule is not stabilized, which will result in short contact time between the molecule and the metal surface. The OH bond breaking requires 0.70 eV and 0.10 eV of activation energy on (0001) and (11-20) facets, respectively. This scission is clearly sensitive to the structure and is favored on the open type surface. On both facets, iPrO* is the most stable intermediate. It is more strongly adsorbed on the (11-20) facet by 0.12 eV. Similarly, H* is adsorbed more strongly on this open surface

by 0.06 eV. The second OH-CH bond breaking requires 0.63 eV and 0.48 eV of activation energy on (0001) and (11-20) facets, respectively. Again, this process is favored on the open type surface. Last, comparing the adsorption of the product (acetone, in respect to the molecule in gas phase), one can notice that it is also adsorbed more strongly on the open type (11-20) facet (-0.51 eV) than on the (0001) facet (-0.06 eV), and its desorption is endergonic.

All in all, on open type (11-20) facet both the OH and OH-CH bond breakings are facilitated, in comparison with close packed (0001) surface. Also, the adsorption of products and intermediates is stronger on this open type surface, which may result in blocking of its active sites. Likewise, due to differences in adsorption strength, desorption of the products will be less hindered on close packed surface, but this is not enough to make it more active than the (11-20) facet. These observations lead to the conclusion that the alcohol dehydrogenation is sensitive to the structure of the catalyst and the sites exposed on the Co(11-20) facet are more efficient than the ones exposed on the Co(0001) surface.

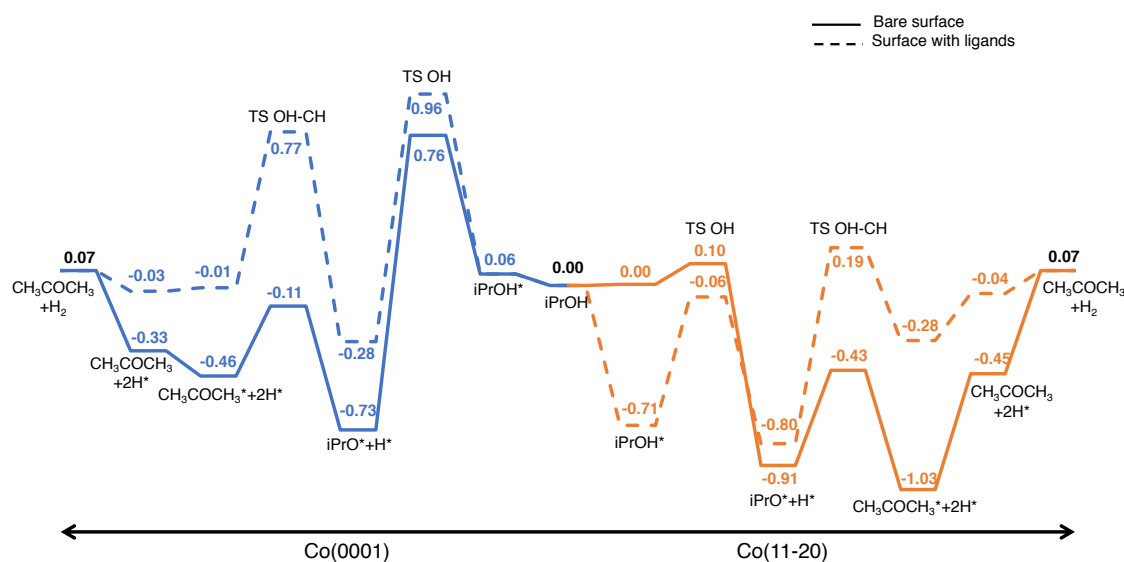


Figure 5.8. Gibbs Free Energy profiles (in eV) for iPrOH dehydrogenation via the alkoxy pathway on the Co(0001) facet (left side) and on the Co(11-20) facet (right side). Profiles with a solid lines correspond to bare surfaces, and with dashed lines to surfaces decorated with CH_3COO^* ligands (0.44A-Co(0001) and 0.75A-Co(11-20)). Adsorbed species are labelled with '*'.

Now, a question arises: does the presence of carboxylic ligands change this picture? The Gibbs Free Energy profiles of the alcohol dehydrogenation on the decorated 0.44A-Co(0001) and 0.75A-Co(11-20) facets are superimposed in dashed lines to the one of the pristine surfaces in Figure 5.8. (For the hydroxyalkyl pathway see Figure A.5.6 in Annex.) Considering the energy spans (the energy difference between the rate determining transition state and rate determining intermediate),^{23,24} for both of the surfaces the presence of ligands decreases them, which favors the reaction. For Co(0001) bare surface it is equal to 1.49 eV, whereas in the presence of ligands it reduces to 1.24 eV, and for pristine Co(11-20) facets it is equal to 1.13 eV and decreases to 0.99 eV. Taking a closer look at the adsorption of reaction species, it can be noticed that they are destabilized on (0001) facet (despite of iPrOH), and by this the contact time between them is decreased. However, on (11-20) surface the effect of ligands presence is different. Adsorption of iPrOH is enhanced, whereas adsorption of iPrO[•] and CH₃COCH₃ is destabilized. After all, this has positive effect, as it increases the contact time between the surface and substrate, and later allows to avoid the blocking of active sites by alkoxy intermediate and carbonyl product. The activation energies for OH and OH-CH bond scissions increase in the presence of ligands for both surfaces (Table 5.4). But since they are still lower for open type facet, this makes it more active than the close packed surface.

Table 5.4. Activation energies for OH and OH-CH bond breakings on bare and ligand covered Co(0001) and Co(11-20) surfaces. All the values are given in eV.

Bond breaking	Co(0001)	0.44A-Co(0001)	Co(11-20)	0.75A-Co(11-20)
OH	0.70	0.90	0.10	0.65
OH-CH	0.62	1.03	0.48	0.99

Let us now analyze in more details the origin of this differentiated influence of ligands for the two surfaces. The adsorption of iPrOH is stronger on 0.75A-Co(11-20) than on the corresponding bare surface by 0.71 eV. This stabilization appears because of the formation of H-bond and other non-covalent interactions between the alcohol molecule and the carboxylic ligands (O-H...O 1.84 Å, α-C-H...O 2.37 Å and 2.41 Å, Figure 5.9.b). The alcohol adsorption on 0.44A-Co(0001) seems not to be impacted by the presence of the ligands (0.00 eV of adsorption energy change), but a closer look at the structure shows that the

formation of H-bond and other non-covalent interaction also takes place (O-H \cdots O 1.59 Å, α -C-H \cdots O 2.80 Å, Figure 5.9.a). However, their stabilizing effect is suppressed by the destabilization caused by steric hindrance between the ligands and the iPrOH molecule.

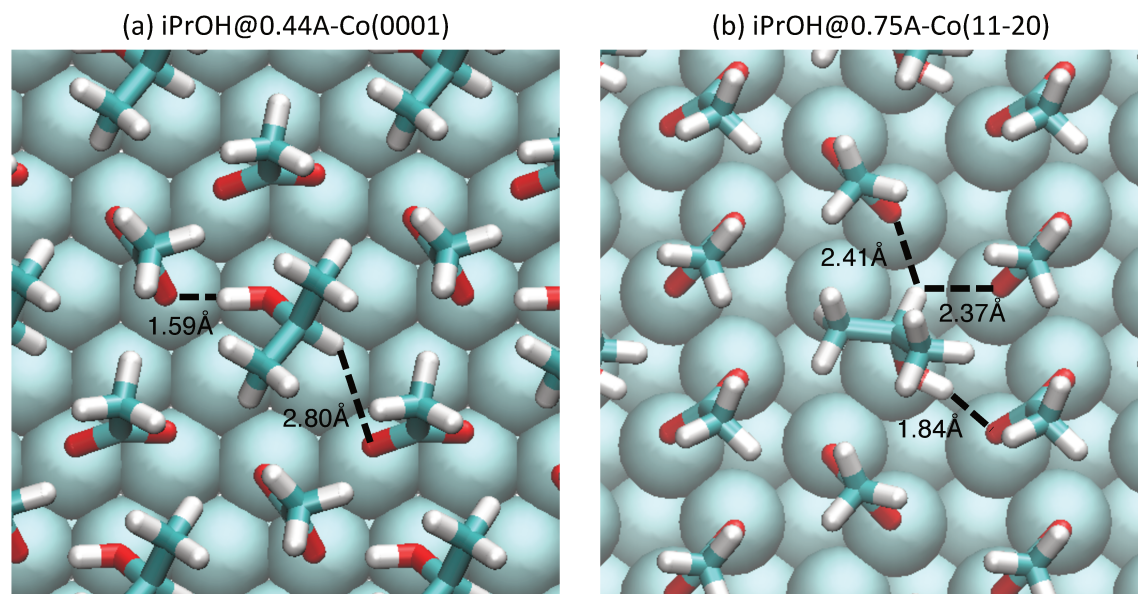


Figure 5.9. iPrOH optimized structures adsorbed on (a) 0.44A-Co(0001) and (b) 0.75A-Co(11-20). Co is shown by cyan (light blue) balls, whereas by sticks are shown: C in cyan (light blue), O in red, H in white.

These effects can be traced back through an energy decomposition into deformation and interaction. As schematically shown on Figure 5.10, the *change* in adsorption energy (ΔG , in blue) is a sum of energies of deformation (molecule, ligand, and surface; destabilizing changes), and the interaction (stabilizing effect). In Table 5.5 the corresponding results of energy change decomposition are gathered. Looking closer at iPrOH adsorption on the 0.44A-Co(0001) surface, the deformation for the molecule, ligands and surface is equal to 0.41 eV, 0.48 eV and 0.12 eV, respectively, giving 0.77 eV in total. The stabilizing interactions give 0.77 eV energy gain, what compensates the deformation energies (the total energy change is equal to 0.00 eV, as can be seen on the energy profiles). On the other hand, the energy of deformations for iPrOH adsorbed on 0.75A-Co(11-20) is equal to 0.15 eV, whereas the gain of energy from stabilizing interactions is equal to 0.86 eV. This results in better stabilization of this molecule on the surface by 0.71 eV. The main reason why the iPrOH

adsorption is weaker on (0001) surface is the deformation of ligands. The analysis also reveals the presence of well adapted reaction pocket (defect place in the ligand layer(s)) on the open type surface. Likewise, such analysis can be done for the transition states structures, showing that in the presence of ligands both the additional deformation and the decrease of interactions cause the increase in activation energies.

Comparing globally the influence of deformations and interactions on the two surfaces with ligands, it can be noticed that the influence of deformations is more significant on close packed surface. Due to smaller space available, the species experience bigger tensions. It also can be seen that the interactions have higher input on the beginning of the reaction pathway (more interactions formed), than at the end of it, especially for 0.75A-Co(11-20).

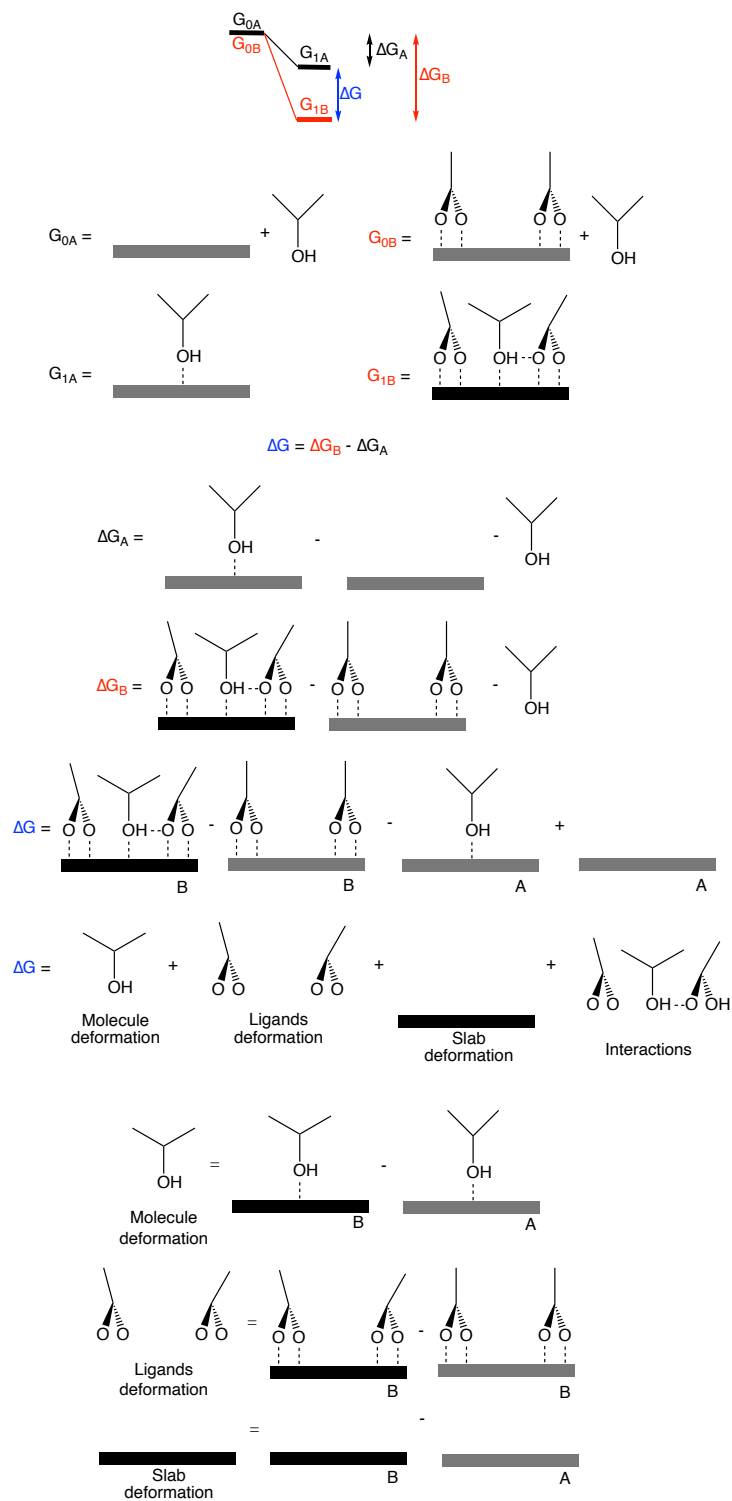


Figure 5.10. Schematic illustration of energy decomposition into stabilizing and destabilizing interactions for molecules and intermediates adsorption on the surfaces with ligands. ‘A’ refers to the adsorption on bare surface, ‘B’ refers to the adsorption on surface covered with ligands.

Table 5.5. Gibbs Free Energy change for the adsorption of molecules and intermediates, between bare surface and surface covered with ligands. The change is a sum of deformations and interactions energies (see Figure 5.10). All the energies are given in eV.

Surface	Surface species	ΔG (eV)	$\Delta G_{\text{molecule}}$ (eV)	$\Delta G_{\text{ligands}}$ (eV)	ΔG_{slab} (eV)	$\Delta G_{\text{deformations}}$ (eV)	$\Delta G_{\text{interactions}}$ (eV)
0.44A-Co(0001)	iPrOH	0.00	0.41	0.48	0.12	0.77	-0.77
	TS-OH	0.21	0.23	0.44	0.09	0.58	-0.38
	iPrO	0.30	0.24	0.49	0.05	0.68	-0.38
	H	0.15	0.04	0.19	0.00	0.23	-0.08
	TS OH-CH	0.73	0.28	0.79	0.12	0.95	-0.22
	Acetone	0.15	0.55	0.47	0.08	0.94	-0.79
0.75A-Co(11-20)	iPrOH	-0.71	0.15	0.04	0.04	0.15	-0.86
	TS-OH	-0.16	0.29	0.12	0.16	0.25	-0.41
	iPrO	-0.09	0.15	0.15	0.05	0.25	-0.34
	H	0.20	0.12	0.08	0.08	0.12	0.08
	TS OH-CH	0.41	0.58	0.43	0.15	0.86	-0.45
	Acetone	0.35	0.53	0.08	0.09	0.52	-0.17

$$\Delta G = \Delta G_{\text{molecule}} + \Delta G_{\text{ligands}} - \Delta G_{\text{slab}} + \Delta G_{\text{interactions}}$$

$$\Delta G_{\text{deformations}} = \Delta G_{\text{molecule}} + \Delta G_{\text{ligands}} - \Delta G_{\text{slab}}$$

ΔG – difference of adsorption energy between the molecule adsorbed on the bare surface and the surface covered with ligands

$\Delta G_{\text{molecule}}$ – change of Gibbs Free Energy for a molecule between its state on bare surface (BS) and surface covered with ligands (LS)

$\Delta G_{\text{ligands}}$ – change of Gibbs Free Energy for ligands between the state without and with co-adsorbed molecule

ΔG_{slab} – change of Gibbs Free Energy for slab between BS and LS

$\Delta G_{\text{interactions}}$ – change of Gibbs Free Energy of interactions between reactant molecule and ligands, between BS and LS

To sum up, the presence of carboxylic ligands improves the activity of the surfaces. The adsorption of substrate is stabilized by H-bond interactions, and thanks to the steric hindrance the desorption of carbonyl product is facilitated. A little drawback is the increase of activation energies for OH and OH-CH bond dissociations, but the barriers are still reachable at 145°C and the scissions can occur. The comparison between open type surface and close packed surface covered with ligands still shows better activity of the former, dictated by lower energy span and lower activation energies for bond dissociations. That means that even in the presence of ligands the alcohol dehydrogenation is expected to be structure sensitive reaction. Based on the analysis of catalytic tests results we could not conclude about it. These results strengthen the fact that the thickness of the ligand covering layer is crucial for the catalytic activity and to assess the shape-sensitivity of the reaction it has to be well controlled.

5.5. Activity towards primary alcohol and diol

For one of the most active catalysts in term of TON, namely L-R-1, the catalytic tests were conducted with model primary alcohol (1-octanol) and diol (1,2-octanediol). The experiments were performed in decane at 145°C under inert atmosphere, using 0.025 g of catalyst and $n_{\text{alc}} : n_{\text{cat}} = 100$. As the reaction conditions were the same as for the reaction with 2-octanol it allowed to directly assess the chemoselectivity of the catalyst. The reaction results are gathered in Table 5.6.

Table 5.6. Catalytic alcohol dehydrogenation using Co shaped nanoparticles decorated with carboxylate ligands. Reaction conditions: $m_{\text{cat}} = 0.025$ g, $n_{\text{alc}} : n_{\text{cat}} = 100$, 0.95 mol L⁻¹ 2-octanol, decane, 24 h, 145°C, $V_{\text{total}} = 45$ mL. All the catalytic tests were performed with L-R-1 sample. Y stands for the yield of the carbonyl product (2-octanone, octanal and 1-hydroxy-2-octanone, respectively for 2-octanol, 1-octanol and 1,2-octanediol).

Sample	Alcohol	X (%)	Y (%)	Y _{H₂} (%)
L-R-1	2-octanol	35	35	30
	1-octanol	10	9	7
	1,2-octanediol	20	20	19

Comparing the results of primary and secondary monoalcohols dehydrogenation it can be noticed that the catalyst was also active towards primary alcohol dehydrogenation (35% vs 10% of conversion, respectively). Moreover, it was not totally selective towards the corresponding aldehyde. Again, the observed by-products were C16 condensation and/or esterification products. However, while tested towards dehydrogenation of diol, the only observed product was 1-hydroxy-2-octanone, which is the dehydrogenation product of secondary OH group. Its exclusive formation was confirmed by GC, ^{13}C -NMR and ^1H -NMR analysis of liquid samples. The corresponding NMR spectra are presented in Figures A.5.7 and A.5.8 in Annex. Even though this was not obvious based on the monoalcohols dehydrogenation results, the catalyst occurred to be totally selective in the diol dehydrogenation.

In the literature only one paper reporting 1,2-octanediol dehydrogenation is available.²⁵ The reaction was conducted in solvent-free conditions, at 175°C, using 0.35 mol% of Ni/SiO₂ catalyst. The conversion was equal to 28% and the reported selectivity was equal to 64%. The main reaction product was 1-hydroxy-2-octanone and 2-octanone was observed as a by-product. It is not possible to directly compare the activity of our catalyst with the one reported, due to the different reaction conditions used. However, the L-R-1 catalyst demonstrated to be fully selective towards desired secondary OH group dehydrogenation product, at a comparable conversion. Also, it showed better selectivity than Co/TiO₂ P25 and Co/TiO₂ P90 catalysts, reported in Chapter 3. (The comparison of conversion is not directly possible due to different metal : substrate ratio used in the catalytic tests with supported and unsupported Co catalysts.)

5.6. Conclusions

To investigate the structure sensitivity of the acceptor-less alcohol dehydrogenation we used model shaped Co NPs as catalysts. Adjusting of the polyol synthesis method parameters allowed to obtain Co NPs of different shapes: nanorods, diabolos and platelets. The morphologies of the samples were precisely identified by TEM analysis (shape and type of exposed surfaces). By the geometric measurements from the images it was possible to calculate the specific surface area of metal in the sample and to determine the proportion of

different exposed facets. The content of organic matter (ligands) was quantified by TGA-N₂ analysis. Combination of the results from these two analytical techniques made possible the calculation of the thickness of ligand protecting layer, which ranged from 1 to over 10 ML. In the catalytic tests with 2-octanol, the samples exhibited differentiated performance (TON from 70 mol mol⁻¹ to 1170 mol mol⁻¹). When comparing the results, the most decisive factor for the activity occurred to be the thickness of ligand protecting layer, not the type and amount of exposed crystallographic facets. When the thickness of ligands was limited to 1-2 ML, the NPs were active, whereas when the layer was thicker – the activity was suppressed. Knowing this, the surface-activity relations were re-examined, but no conclusions could be drawn. This strengthens the fact that to assess the structure sensitivity of acceptor-less alcohol dehydrogenation with shaped Co NPs, the thickness of organic layer has to be precisely controlled.

As found from DFT investigations, the ligands play a dual role for the catalytic activity. From one side, they impede the reaction, due to the steric hindrance. On the other hand, their influence is positive, as they create the H-bonds with the reaction species. Both effects are acting simultaneously and can vary the activity of the metal surfaces in different ways. The results showed that the dehydrogenation is hindered on close packed Co(0001), because of the destabilization of species adsorption, whereas on open type Co(11-20) the effect of ligand is positive. The adsorption of alcohol substrate is stronger, what increases the contact time with surface, while the adsorption of the intermediate and product is destabilized, and as a result they are not poisoning the active sites.

In conclusion, thanks to controlled synthesis of Co NPs, catalytic testing, characterization of samples, together with DFT investigations it was possible to find and understand that the factor guiding the activity of obtained catalysts is the ligand decoration of the surface. With this knowledge it will be possible in the future to design improved catalysts.

One of the most active catalysts in 2-octanol dehydrogenation, L-R-1, was tested additionally towards dehydrogenation of primary alcohol (1-octanol) and diol (1,2-octanediol). It showed mild activity in 1-octanol dehydrogenation, but despite of this it occurred to be fully selective towards secondary OH group dehydrogenation in diol. This makes it good candidate for the dehydrogenation of biomass-derived polyalcohols.

Bibliography

1. Shimizu, K. *et al.* Heterogeneous cobalt catalysts for the acceptorless dehydrogenation of alcohols. *Green Chem.* **15**, 418–424 (2013).
2. Viola, A. *et al.* Unsupported shaped cobalt nanoparticles as efficient and recyclable catalysts for the solvent-free acceptorless dehydrogenation of alcohols. *Catal. Sci. Technol.* **8**, 562–572 (2018).
3. He, X. *et al.* Controllable in situ surface restructuring of Cu catalysts and remarkable enhancement of their catalytic activity. *ACS Catal.* **9**, 2213–2221 (2019).
4. Hoyt, R. A., Montemore, M. M., Sykes, E. C. H. & Kaxiras, E. Anhydrous methanol and ethanol dehydrogenation at Cu(111) step edges. *J. Phys. Chem. C* **122**, 21952–21962 (2018).
5. Soumare, Y. *et al.* Kinetically controlled synthesis of hexagonally close-packed cobalt nanorods with high magnetic coercivity. *Adv. Funct. Mater.* **19**, 1971–1977 (2009).
6. Feldmann, C. Polyol-mediated synthesis of nanoscale functional materials. *Adv. Funct. Mater.* **13**, 101–107 (2003).
7. Atmane, K. A. *et al.* Control of the anisotropic shape of cobalt nanorods in the liquid phase: from experiment to theory... and back. *Nanoscale* **6**, 2682–2692 (2014).
8. Yoskamtorn, T. *et al.* Thiolate-mediated selectivity control in aerobic alcohol oxidation by porous carbon-supported Au₂₅ clusters. *ACS Catal.* **4**, 3696–3700 (2014).
9. Schoenbaum, C. A., Schwartz, D. K. & Medlin, J. W. Controlling the surface environment of heterogeneous catalysts using self-assembled monolayers. *Accounts Chem. Res.* **47**, 1438–1445 (2014).
10. Kahsar, K. R., Schwartz, D. K. & Medlin, J. W. Control of metal catalyst selectivity through specific noncovalent molecular interactions. *J. Am. Chem. Soc.* **136**, 520–526 (2014).
11. Jin, L., Liu, B., Duay, S. & He, J. Engineering surface ligands of noble metal nanocatalysts in tuning the product selectivity. *Catalysts* **7**, 44 (2017).
12. González-Gálvez, D., Nolis, P., Philippot, K., Chaudret, B. & van Leeuwen, P. W. N. M. Phosphine-stabilized ruthenium nanoparticles: the effect of the nature of the ligand in catalysis. *ACS Catal.* **2**, 317–321 (2012).

13. Pang, S. H., Schoenbaum, C. A., Schwartz, D. K. & Medlin, J. W. Directing reaction pathways by catalyst active-site selection using self-assembled monolayers. *Nat. Commun.* **4**, 1–6 (2013).
14. Bratlie, K. M., Lee, H., Komvopoulos, K., Yang, P. & Somorjai, G. A. Platinum nanoparticle shape effects on benzene hydrogenation selectivity. *Nano Lett.* **7**, 3097–3101 (2007).
15. Xu, R., Wang, D., Zhang, J. & Li, Y. Shape-dependent catalytic activity of silver nanoparticles for the oxidation of styrene. *Chem. Asian J.* **1**, 888–893 (2006).
16. Fiévet, F. *et al.* The polyol process: a unique method for easy access to metal nanoparticles with tailored sizes, shapes and compositions. *Chem. Soc. Rev.* **47**, 5187–5233 (2018).
17. Liu, Q. *et al.* Synthesis of shape-controllable cobalt nanoparticles and their shape-dependent performance in glycerol hydrogenolysis. *RSC Advances* **5**, 4861–4871 (2015).
18. Maurer, T. *et al.* Exchange bias in Co/CoO core-shell nanowires: Role of antiferromagnetic superparamagnetic fluctuations. *Phys. Rev. B* **80**, 064427 (2009).
19. Ait Atmane, K. *et al.* High temperature structural and magnetic properties of cobalt nanorods. *J. Solid State Chem.* **197**, 297–303 (2013).
20. Buckley, E. & Herington, E. F. G. Equilibria in some secondary alcohol + hydrogen + ketone systems. *Transactions of the Faraday Society* **61**, 1618–1625 (1965).
21. Luo, W. & Asthagiri, A. Density Functional Theory study of methanol steam reforming on Co(0001) and Co(111) surfaces. *J. Phys. Chem. C* **118**, 15274–15285 (2014).
22. Sutton, J. E. & Vlachos, D. G. Ethanol activation on closed-packed surfaces. *Ind. Eng. Chem. Res.* **54**, 4213–4225 (2015).
23. Kozuch, S. & Martin, J. M. L. The rate-determining step is dead. Long live the rate-determining state! *ChemPhysChem* **12**, 1413–1418 (2011).
24. Kozuch, S. & Martin, J. M. L. “Turning over” definitions in catalytic cycles. *ACS Catal.* **2**, 2787–2794 (2012).
25. Guicheret, B. *et al.* A two-step oxidative cleavage of 1,2-diol fatty esters into acids or nitriles by a dehydrogenation-oxidative cleavage sequence. *ChemSusChem* **11**, 3431–3437 (2018).

Conclusions

Acceptor-less alcohol dehydrogenation is highly attractive, atom-efficient reaction, due to the formation of carbonyl molecule and H_2 in gaseous form as the only products. This reaction requires inert atmosphere to assure the acceptor-less mechanism and H_2 production monitoring to confirm it. In the literature many heterogeneous metal catalysts have been tested, among which supported Co was reported as active and selective towards secondary alcohols over primary alcohols dehydrogenation. To have an active and selective catalyst also its structural properties are important. It is known that parameters like nature of support, shape of NPs, presence of ligands, can influence the catalyst performance.

The purpose of this work was to investigate the structure-activity relations of Co catalysts in acceptor-less alcohol dehydrogenation. To do this, experimental and computational approaches were combined. First, we studied the effect of carriers nature for supported catalysts. Later, our partners from LPCNO in Toulouse and ITODYS in Paris synthesized unsupported ligand-decorated shaped Co NPs, by modifying the synthesis conditions using the polyol process. The different materials allowed us to investigate the surface (and ligand) sensitivity of the reaction. All the samples were tested at first towards dehydrogenation of 2-octanol taken as a model secondary alcohol. Subsequently, the most active of them were examined in the reaction with 1-octanol and 1,2-octanediol (model primary alcohol and diol, respectively), to assess their chemoselectivity. The dehydrogenation of diols was an important step towards the dehydrogenation of biomass-derived polyalcohols, our long-term goal. All of the samples were extensively characterized, and their properties were connected with the catalytic activity. The experimental investigations were completed with DFT modeling of the reaction pathways. This allowed us to compare the activity of different surfaces, determine the reason of the observed chemoselectivity, and also explain the role of ligands in the catalytic reaction.

First, it was important to establish the catalytic tests conditions, and to confirm the adapted acceptor-less reaction mechanism. This was successfully done, using semi-batch reactor, with constant flow of inert gases and monitoring the H_2 production during the reaction with GC coupled with the reactor. Experiments were conducted at 145°C with decane as a solvent.

While investigating the supported Co catalysts, the importance of catalyst post-treatment (passivation) and aging was revealed. The longer was the time of passivation (0.5 h vs 2 h) and the time between the catalyst reduction and reaction (from 1 day to 6 months) the lower was the activity. But, we proved that re-activation of the catalyst is possible by *in situ* H₂ pre-treatment. Also, the influence of the carrier nature was observed, and the Co/TiO₂ P25 with an amphoteric support appeared to be the most active catalyst, in agreement with the literature. The conversion in 2-octanol dehydrogenation was slightly lower than the one reported by Shimizu et al. (70% vs 85%, respectively), but the selectivity was better (98% vs 92%, respectively). The observed by-products were confirmed to be C16 aldol condensation and/or esterification products. The most active Co/TiO₂ P25 catalyst showed good chemoselectivity towards secondary monoalcohol dehydrogenation over primary alcohol. While tested in dehydrogenation of diol, it was entirely selective towards dehydrogenation of secondary OH group. This showed its potential in the dehydrogenation of desired biomass-derived polyalcohols. However, also the formation of some by-products was observed (C16 by-products), which may limit further applications.

To the best of our knowledge, activity of shaped Co catalysts towards acceptor-less alcohol dehydrogenation has not been reported in the literature up to now. We aimed at investigating the surface-activity dependence of the reaction, by screening non-supported Co NPs of various morphologies in 2-octanol dehydrogenation. Characterization of samples allowed to measure the surface area exposed by metallic Co (TEM) and established the thickness of ligand surface coverage (TGA-N₂ and TEM). In the catalytic tests these NPs revealed differentiated activity (in TON). The main factor guiding their performance occurred to be the thickness of organic layer, covering their surfaces, not the type and amount of exposed facets. When it was limited to 1-2 ML the activity of samples was preserved, whereas when it was thicker the activity was suppressed. To further investigate the surface-activity relations, the ligand thickness has to be precisely controlled. The chosen catalyst (L-R-1) was also tested in dehydrogenation of 1-octanol, for which it revealed mild activity, and in dehydrogenation of 1,2-octanediol, for which it was active and completely selective towards dehydrogenation of secondary OH group. This makes it very good candidate for dehydrogenation of polyols.

DFT modeling made possible the understanding of the catalytic behavior on molecular level. For the first time, predicted activity of different (5 hcp and 4 fcc) Co surfaces were compared,

revealing better performance of open type vs close packed facets. It also allowed to understand that the observed chemoselectivity of secondary vs primary alcohol comes from the differences in thermochemistry of reactions and desorption of products. Moreover, the computations showed the dual effect of carboxylic ligands. As expected, they lower the metal activity due to steric hindrance, but also improve it, by creating stabilizing H-bond interactions with reaction species. Hence, if in the ligand layer the space (pocket) for molecule adsorption exists, the catalytic activity is preserved, and can be even enhanced (this is suggested by energy span values).

To choose the best catalyst among the tested supported and unsupported Co catalyst few parameters have to be taken into account. In both groups, the active, selective and chemoselective catalysts were found. But, the supported Co catalysts deactivated with time, which was not the case for unsupported NPs, which were resistant to oxidation thanks to the ligand protection. It was not possible to determine precisely the crystallite size for supported Co/TiO₂ P25 catalyst. However, assuming their size being 5-15 nm, the activity expressed by TON will be ranging from 300 to 1300 mol mol⁻¹, which makes the supported and unsupported catalysts (TON up to ~1200 mol mol⁻¹) comparable in activity. Comparing their selectivity (by-products formation) and chemoselectivity (primary vs secondary OH dehydrogenation), shaped NPs performed better, as in secondary alcohol dehydrogenation and diol dehydrogenation the formation of C16 condensation products was not observed and the secondary OH group was dehydrogenated preferentially. Hence, they appear to be good candidates for polyol dehydrogenation. However, it will require to scale up the synthesis, as nowadays they are obtained only in small quantities. It may be also worth to try to bind them on a support, which may facilitate their manipulation, but the influence of support nature cannot be forgotten.

Some open questions still remain in this project. Considering the nature of support, the role of TiO₂ phase composition is not explained yet. Also, it will be interesting to broaden the scope of substrates to polyols. We tried to perform the experiments with long chain aliphatic diol without changing the reaction conditions. However, due to some technical limitations (such as viscosity and polarity of polyols and finding a suitable solvent with high boiling point which is not H₂ accepting), dehydrogenation of other polyalcohols may require change of reaction conditions (e.g. conducting solvent-free experiments). The thickness of ligand protecting

layer was identified to be crucial for the catalyst's activity of shaped Co NPs. Precise control of it should make possible the investigations of shape-activity relations, and by this show a way to further improve the catalyst performance. It may also be a big step forward to use them in dehydrogenation of polyols, as they were more selective than supported catalysts towards dehydrogenation of 1,2-octanediol. From DFT side, it will be worth to computationally investigate dehydrogenation of diols, paying attention to the chemoselectivity of primary vs secondary OH group dehydrogenation, and also to the influence of distance between them (1,2-diol vs 1,3-diol dehydrogenation). It will be also worth to investigate the formation of by-products, to better understand their formation mechanism. Alcohol dehydrogenation pathway can be modeled involving support participation, which will allow to better explain the experimentally observed support effect. Further, microkinetic modeling will be informative, as it will be bridging the computational and experimental results.

For a broader perspective, Co shaped NPs can be obtained by other method (e.g. organometallic), and they can be protected by ligands of other nature (e.g. amines), which might also affect their activity and/or selectivity. In the project we also already started some investigations about the activity of monometallic Ru and Cu supported catalysts and bimetallic $\text{Co}_x\text{Ru}_{100-x}$ unsupported NPs towards alcohol dehydrogenation. It would give an insight into the influence of metal oxophilicity and synergy on the performance.

Annex

A.2.1. Syntheses of unsupported Co NPs

A.2.1.1. Materials

$\text{Co}(\text{CH}_3\text{CO}_2)_2 \cdot 4\text{H}_2\text{O}$ (Aldrich, >98 %), $\text{CoCl}_2 \cdot 6\text{H}_2\text{O}$ (Alfa Aesar, 98%), $\text{RuCl}_3 \cdot x\text{H}_2\text{O}$ (Aldrich, ref. 463779, 99.98 % or Sigma Aldrich, 38.0-42.0% Ru basis), RuCl_3 (Aldrich, Ru Content 45-55%), NaOH (Acros, micropearls or Sigma Aldrich, $\geq 97\%$), 1,2-butanediol (Fluka, 98% or Sigma Aldrich, $\geq 98\%$), 1,2-propanediol (Acros, 99%), lauric (Alfa Aesar, 98%), palmitic (Alfa Aesar, 95%), heptanoic (Aldrich, $\geq 99\%$), octanoic (Aldrich, $\geq 98\%$) and decanoic (Alfa Aesar, 99%) acids, methanol (MeOH, Sigma Aldrich, $\geq 99.8\%$) and ethanol (EtOH, Sigma Aldrich, $\geq 99.5\%$) were used as received.

A.2.1.2. Preparation of cobalt precursors

Home-made cobalt carboxylates, $\text{Co}(\text{C}_n\text{H}_{2n+1}\text{CO}_2)_2$ ($n = 6-15$), were used for the following nanoparticles syntheses.

- Synthesis of $\text{Co}(\text{C}_n\text{H}_{2n+1}\text{CO}_2)_2$, $n = 6, 7, 9$

In a 1L beaker, NaOH (168 mmol) and the long-chain carboxylic acid (176 mmol) were dissolved in 160 mL of distilled water and the mixture was heated to 60°C for 30 min under mechanical stirring to yield a transparent solution. To this solution was then added dropwise under vigorous stirring (200 rpm) an aqueous solution (40 mL) of Co(II) acetate (80 mmol) preheated at 60°C for 15 min. This resulted in the formation of a pink precipitate which was left under stirring for 30 min at the same temperature. The solid was recovered by centrifugation (8 500 rpm, 15 min), washed three times with distilled water (200 mL) and dried in an oven at 50°C for three days.

- $\text{Co}(\text{C}_n\text{H}_{2n+1}\text{CO}_2)_2$, $n = 11, 15$

First, 360 mmol lauric acid (L), respectively palmitic acid (P), and 360 mmol of sodium hydroxide were added with in distilled water (300 mL) and heated at 80°C for 30 min under magnetic stirring to get a clear solution of NaL, respectively NaPa. The solutions were cooled down at room temperature. Then, an aqueous solution containing 180 mmol of $\text{CoCl}_2 \cdot 6\text{H}_2\text{O}$ was added slowly into the former solution under vigorous stirring using an Ultra-Turax homogenizer. The suspension was stirred for 30 min to obtain a pink powder of cobalt laurate, respectively cobalt palmitate, floating on the water solution. The pink powders were isolated using Buchner Funnel Filtration Process.

Several phases were obtained depending on the drying procedure. The dihydrate cobalt laurate $\text{Co}(\text{C}_{11}\text{H}_{23}\text{CO}_2)_2 \cdot 2\text{H}_2\text{O}$ and cobalt palmitate $\text{Co}(\text{C}_{15}\text{H}_{31}\text{CO}_2)_2 \cdot 2\text{H}_2\text{O}$, hereafter called L1 and P1, respectively, were obtained after a drying at 50°C for 20 hours. The anhydrous cobalt laurate called L2 was obtained drying the compound L1 at 50°C for 3 days. The anhydrous cobalt laurate called L3 was obtained drying the compound L1 at 50°C for 7 days. The anhydrous cobalt laurate called L4 was obtained drying the compound L1 at 100°C for 30 min. The anhydrous cobalt palmitate called P2 was obtained by drying the compound P1 at 65°C for 22 h. The anhydrous cobalt palmitate, called P3, was obtained drying the compound P1 at 85°C for 15 h. The anhydrous cobalt palmitate called P4 was obtained drying the compound P1 at 100°C for 30 min.

A.2.1.3. Preparation of the Co NPs

- *Rods*

Samples H-R, O-R and D-R

To 100 mL of 1,2-butanediol, were added: the cobalt (II) carboxylate precursor (80 mM), $\text{RuCl}_3 \cdot x\text{H}_2\text{O}$ ($[\text{Ru}]/[\text{Ru}+\text{Co}] = 2.5 \text{ mol}\%$) and sodium hydroxide (75 mM). The mixture was then heated under stirring at 100 rpm to 175°C with a heating rate of 8 °C min^{-1} for half an hour until the color of the solution turned black, indicating the reduction of Co(II) into metallic cobalt. After cooling down to room temperature, the cobalt particles were recovered using a permanent magnet, washed four times with 50 mL of absolute ethanol, and finally dried

overnight in an oven at 50°C. Samples prepared using heptanoate, octanoate and decanoate capping agents were labelled H-R, O-R and D-R, respectively.

Sample L-R-1

To 1 L of 1,2-butanediol, were added: the cobalt (II) laurate called L2 (80 mM), $\text{RuCl}_3 \cdot x\text{H}_2\text{O}$ ($[\text{Ru}]/[\text{Ru}+\text{Co}] = 2.5 \text{ mol\%}$) and sodium hydroxide (75 mM). The mixture was then heated under stirring at 100 rpm to 175°C with a heating rate of 8 °C min⁻¹ for half an hour until the color of the solution turned black, indicating the reduction of Co(II) into metallic cobalt. After cooling down to room temperature, the cobalt particles were recovered using a permanent magnet, washed four times with 100 mL of absolute ethanol, and finally dried overnight in an oven at 50°C.

Sample L-R-2

To 1 L of 1,2-butanediol, were added: the cobalt (II) laurate called L1 (80 mM), $\text{RuCl}_3 \cdot x\text{H}_2\text{O}$ ($[\text{Ru}]/[\text{Ru}+\text{Co}] = 2.5 \text{ mol\%}$) and sodium hydroxide (75 mM). The mixture was then heated under stirring at 100 rpm to 175°C with a heating rate of 8 °C min⁻¹ for half an hour until the color of the solution turned black, indicating the reduction of Co(II) into metallic cobalt. After cooling down to room temperature, the cobalt particles were recovered using a permanent magnet, washed four times with 100 mL absolute ethanol, and finally dried overnight in an oven at 50°C.

Sample L-R-3

To 100 mL of 1,2-butanediol, were added: the cobalt (II) laurate called L4 (80 mM), anhydrous RuCl_3 ($[\text{Ru}]/[\text{Ru}+\text{Co}] = 2.5 \text{ mol\%}$) and sodium laurate (160 mM). The mixture was then heated under stirring at 100 rpm to 175°C with a heating rate of 8 °C min⁻¹ for half an hour until the color of the solution turned black, indicating the reduction of Co(II) into metallic cobalt. After cooling down to room temperature, the cobalt particles were recovered using a permanent magnet, washed three times with 100 mL of absolute ethanol, and finally dried overnight in an oven at 50°C.

Sample L-R-4

To 100 mL of 1,2-butanediol, were added: the cobalt (II) laurate called L3 (80 mM), $\text{RuCl}_3 \cdot x\text{H}_2\text{O}$ ($[\text{Ru}]/[\text{Ru}+\text{Co}] = 2.5 \text{ mol\%}$) and sodium hydroxide (75 mM). The mixture was then heated under stirring at 100 rpm to 175°C with a heating rate of 8 °C min⁻¹ for half an hour until

the color of the solution turned black, indicating the reduction of Co(II) into metallic cobalt. After cooling down to room temperature, the cobalt particles were recovered using a permanent magnet, washed three times with 100 mL of absolute ethanol, and finally dried overnight in an oven at 50°C.

Sample P-R-1

To 100 mL of 1,2-butanediol, were added: the cobalt (II) palmitate called P4 (80 mM), $\text{RuCl}_3 \cdot x\text{H}_2\text{O}$ ($[\text{Ru}]/[\text{Ru}+\text{Co}] = 2.5 \text{ mol\%}$) and sodium hydroxide (75 mM). The mixture was then heated under stirring at 100 rpm to 175°C with a heating rate of 8 °C min⁻¹ for half an hour until the color of the solution turned black, indicating the reduction of Co(II) into metallic cobalt. After cooling down to room temperature, the cobalt particles were recovered using a permanent magnet, washed three times with 100 mL of absolute ethanol, and finally dried overnight in an oven at 50°C.

Sample P-R-2

To 100 mL of 1,2-butanediol, were added: the cobalt (II) palmitate called P2 (80 mM), $\text{RuCl}_3 \cdot x\text{H}_2\text{O}$ ($[\text{Ru}]/[\text{Ru}+\text{Co}] = 2.5 \text{ mol\%}$) and sodium hydroxide (75 mM). The mixture was then heated under stirring at 100 rpm to 175°C with a heating rate of 8 °C min⁻¹ for half an hour until the color of the solution turned black, indicating the reduction of Co(II) into metallic cobalt. After cooling down to room temperature, the cobalt particles were recovered using a permanent magnet, washed three times with 100 mL of absolute ethanol, and finally dried overnight in an oven at 50°C.

Sample P-R-3

To 100 mL of 1,2-butanediol, were added: the cobalt (II) palmitate called P4 (80 mM), anhydrous RuCl_3 ($[\text{Ru}]/[\text{Ru}+\text{Co}] = 2.5 \text{ mol\%}$) and sodium hydroxide (75 mM). The mixture was then heated under stirring at 100 rpm to 175°C with a heating rate of 8 °C min⁻¹ for half an hour until the color of the solution turned black, indicating the reduction of Co(II) into metallic cobalt. After cooling down to room temperature, the cobalt particles were recovered using a permanent magnet, washed three times with 100 mL of absolute ethanol, and finally dried overnight in an oven at 50°C.

- *Diabolos*

Sample L-D

To 100 mL of 1,2-propanediol, were added: the cobalt (II) laurate called L4 (80 mM), anhydrous RuCl_3 ($[\text{Ru}]/[\text{Ru}+\text{Co}] = 2.5 \text{ mol\%}$) and sodium hydroxide (75 mM). The mixture was then heated under stirring at 100 rpm to 175°C with a heating rate of 8 °C min⁻¹ for half an hour until the color of the solution turned black, indicating the reduction of Co(II) into metallic cobalt. After cooling down to room temperature, the cobalt particles were recovered using a permanent magnet, washed three times with 100 mL of absolute ethanol, and finally dried overnight in an oven at 50°C.

Sample P-D

To 100 mL of 1,2-butanediol, were added: the cobalt (II) palmitate called P4 (80 mM), anhydrous RuCl_3 ($[\text{Ru}]/[\text{Ru}+\text{Co}] = 2.5 \text{ mol\%}$) and sodium palmitate (160 mM). The mixture was then heated under stirring at 100 rpm to 175°C with a heating rate of 8 °C min⁻¹ for half an hour until the color of the solution turned black, indicating the reduction of Co(II) into metallic cobalt. After cooling down to room temperature, the cobalt particles were recovered using a permanent magnet, washed six times with 100 mL of methanol, and finally dried overnight in an oven at 50°C.

- *Platelets*

Sample L-P

To 100 mL of 1,2-propanediol, were added: the cobalt (II) laurate called L4 (80 mM), anhydrous RuCl_3 ($[\text{Ru}]/[\text{Ru}+\text{Co}] = 2.5 \text{ mol\%}$) and sodium laurate (160 mM). The mixture was then heated under stirring at 100 rpm to 175°C with a heating rate of 8 °C min⁻¹ for half an hour until the color of the solution turned black, indicating the reduction of Co(II) into metallic cobalt. After cooling down to room temperature, the cobalt particles were recovered using a permanent magnet, washed three times with 100 mL of absolute ethanol, and finally dried overnight in an oven at 50°C.

Sample P-P

To 100 mL of 1,2-propanediol, were added: the cobalt (II) palmitate called P4 (80 mM), anhydrous RuCl₃ ([Ru]/[Ru+Co] = 2.5 mol%) and sodium palmitate (160 mM). The mixture was then heated under stirring at 100 rpm to 175°C with a heating rate of 8 °C min⁻¹ for half an hour until the color of the solution turned black, indicating the reduction of Co(II) into metallic cobalt. After cooling down to room temperature, the cobalt particles were recovered using a permanent magnet, washed six times with 100 mL of methanol, and finally dried overnight in an oven at 50°C.

A.2.1.4. Summary of the experimental conditions for the synthesis of the different cobalt samples

Sample	Cobalt precursor	Nucleating Agent	Base	Polyol
L-R-1	Cobalt laurate "L2"	RuCl ₃ ·xH ₂ O	Sodium hydroxide 0.075 M	1,2-butanediol
L-R-2	Cobalt laurate "L1"	RuCl ₃ ·xH ₂ O	Sodium hydroxide 0.075 M	1,2-butanediol
L-R-3	Cobalt laurate "L4"	anhydrous RuCl ₃	Sodium laurate 0.16 M	1,2-butanediol
L-R-4	Cobalt laurate "L3"	RuCl ₃ ·xH ₂ O	Sodium hydroxide 0.075 M	1,2-butanediol
L-D	Cobalt laurate "L4"	anhydrous RuCl ₃	Sodium hydroxide 0.075 M	1,2-propanediol
L-P	Cobalt laurate "L4"	anhydrous RuCl ₃	Sodium laurate 0.16 M	1,2-propanediol
P-R-1	Cobalt palmitate "P4"	RuCl ₃ ·xH ₂ O	Sodium hydroxide 0.075 M	1,2-butanediol
P-R-2	Cobalt palmitate "P2"	RuCl ₃ ·xH ₂ O	Sodium hydroxide 0.075 M	1,2-butanediol
P-R-3	Cobalt palmitate "P4"	anhydrous RuCl ₃	Sodium hydroxide 0.075 M	1,2-butanediol
P-D	Cobalt palmitate "P4"	anhydrous RuCl ₃	Sodium palmitate 0.16 M	1,2-butanediol
P-P	Cobalt palmitate "P4"	anhydrous RuCl ₃	Sodium palmitate 0.16 M	1,2-propanediol
H-R	Cobalt heptanoate	RuCl ₃ ·xH ₂ O	Sodium hydroxide 0.075 M	1,2-butanediol
O-R	Cobalt octanoate	RuCl ₃ ·xH ₂ O	Sodium hydroxide 0.075 M	1,2-butanediol
D-R	Cobalt decanoate	RuCl ₃ ·xH ₂ O	Sodium hydroxide 0.075 M	1,2-butanediol

A.2.2. Evaluation of the expected specific surface area and proportion of different exposed surfaces for unsupported Co nanoparticles

A.2.2.1. Specific surface area of Co in samples

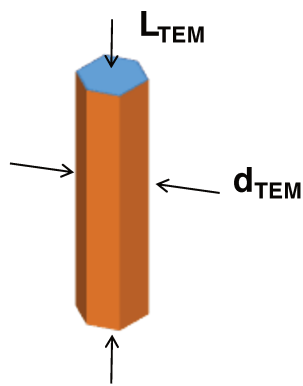
The specific surface area, SSA_C , can be calculated using the following formula:

$$SSA_C = \frac{S_{tot}}{m} = \frac{S_{tot}}{d_{Co} V}$$

with d_{Co} the density of Co (8.86 g cm^{-3}), V the volume of a NP and S_{tot} the surface area of a NP.

V and S_{tot} can be calculated, as explained below.

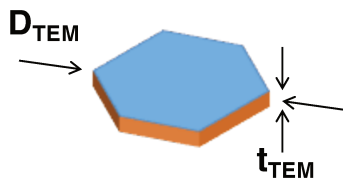
Nanorods



$$S_{tot} = 2S_{base} + S_{lateral} = 3\sqrt{3} \left(\frac{d_{TEM}}{2} \right)^2 + 6 \times L_{TEM} \times \frac{d_{TEM}}{2}$$

$$V = S_{base} \times L_{TEM} = \frac{3\sqrt{3}}{8} \times d_{TEM}^2 \times L_{TEM}$$

Nanoplatelets

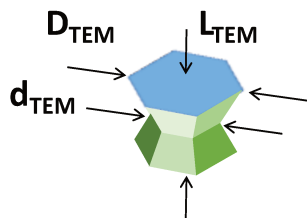


$$S_{tot} = 2S_{base} + S_{lateral} = 3\sqrt{3} \left(\frac{D_{TEM}}{2} \right)^2 + 6 \times t_{TEM} \times \frac{D_{TEM}}{2}$$

$$V = S_{base} \times t_{MET} = \frac{3\sqrt{3}}{8} \times D_{MET}^2 \times t_{MET}$$

Nanodiabolos

$$S_{tot} = 2S_{base} + S_{lateral} = 3\sqrt{3} \left(\frac{D_{TEM}}{2} \right)^2 + 6 \times \left(\frac{D_{TEM}}{2} + \frac{d_{TEM}}{2} \right) \times \sqrt{L_{TEM}^2 + \frac{3}{4} \left(\frac{D_{TEM}}{2} - \frac{d_{TEM}}{2} \right)^2}$$



$$V = \sqrt{3} L_{TEM} + \left(\left(\frac{D_{TEM}}{2} \right)^2 + \left(\frac{d_{TEM}}{2} \right)^2 + \left(\frac{D_{TEM}}{2} \times \frac{d_{TEM}}{2} \right) \right)$$

For example, for sample L-R-1:

$$L_{\text{TEM}} = 175 \text{ nm}$$

$$d_{\text{TEM}} = 19 \text{ nm}$$

$$SSA_C = \frac{S_{\text{tot}}}{m} = \frac{S_{\text{tot}}}{d_{\text{Co}} V}$$

$$\begin{aligned} S_{\text{tot}} &= 2S_{\text{base}} + S_{\text{lateral}} = 3\sqrt{3} \left(\frac{d_{\text{TEM}}}{2} \right)^2 + 6 \times L_{\text{TEM}} \times \frac{d_{\text{TEM}}}{2} = \\ &= 3\sqrt{3} \left(\frac{19 \text{ nm}}{2} \right)^2 + 6 \times 175 \text{ nm} \times \frac{19 \text{ nm}}{2} = 469 \text{ nm}^2 + 9\,975 \text{ nm}^2 = 10\,444 \text{ nm}^2 = \\ &= 10.444 \cdot 10^{-15} \text{ m}^2 \end{aligned}$$

$$V = S_{\text{base}} \times L_{\text{TEM}} = \frac{3\sqrt{3}}{8} \times d_{\text{TEM}}^2 \times L_{\text{TEM}}$$

$$\begin{aligned} V &= S_{\text{base}} \times L_{\text{TEM}} = \frac{3\sqrt{3}}{8} \times d_{\text{TEM}}^2 \times L_{\text{TEM}} = \frac{3\sqrt{3}}{8} \times (19 \text{ nm})^2 \times 175 \text{ nm} = 41\,033 \text{ nm}^3 = \\ &= 41.033 \cdot 10^{-27} \text{ m}^3 \end{aligned}$$

$$SSA_C = \frac{S_{\text{tot}}}{m} = \frac{S_{\text{tot}}}{d_{\text{Co}} V} = \frac{10.444 \cdot 10^{-15} \text{ m}^2}{8.86 \cdot 10^{-6} \text{ g m}^{-3} \times 41.033 \cdot 10^{-27} \text{ m}^3} = 29 \frac{\text{m}^2}{\text{g}}$$

A.2.2.2. Proportions of different exposed surfaces in the sample

The proportion of a given surface in the total exposed surface area of sample can be calculate with the following formula:

$$\% \text{surface} = \frac{S_{\text{surface}}}{S_{\text{total}}} \times 100\%$$

For example, sample L-R-1 is exposing (0001) and (11-20) facets. Their proportion in the sample can be calculated as follow:

$$\begin{aligned} \% \text{surface} &= \frac{S_{\text{surface}}}{S_{\text{total}}} \times 100\% \\ \% (0001) &= \frac{S_{(0001)}}{S_{\text{total}}} \times 100\% = \frac{3\sqrt{3} \left(\frac{d_{\text{TEM}}}{2} \right)^2}{S_{\text{total}}} \times 100\% = \frac{469 \text{ nm}^2}{10\,444 \text{ nm}^2} \times 100\% = 5\% \\ \% (11-20) &= \frac{S_{(11-20)}}{S_{\text{total}}} \times 100\% = \frac{6 \times L_{\text{TEM}} \times \frac{d_{\text{TEM}}}{2}}{S_{\text{total}}} \times 100\% = \frac{9\,975 \text{ nm}^2}{10\,444 \text{ nm}^2} \times 100\% = 95\% \end{aligned}$$

A.2.3. Surface coverage – example of calculations

Example concerns the L-R-1 sample (laurate protected nanorods, of the order number 1).

$$\text{Surface coverage} = \frac{n_{\text{ligands}}}{SA}$$

$$n_{\text{ligands}} = \frac{\frac{\Delta m_{\text{TGA-N}_2}}{100} \times m_{\text{sample}}}{M_{\text{ligands}}} = \frac{9.6}{100} \times \frac{0.025 \text{ g}}{199.31 \frac{\text{g}}{\text{mol}}} = 12.0 \times 10^{-6} \text{ mol}$$

$$SA = SSA_C \times \left(\frac{m_{\text{Co}}}{100} \times m_{\text{sample}} \right) = SSA_C \times \left(\frac{(100 - \Delta m_{\text{TGA-N}_2})}{100} \times m_{\text{sample}} \right) =$$

$$= 29 \frac{\text{m}^2}{\text{g}} \times \left(\frac{(100 - 9.6)}{100} \times 0.025 \text{ g} \right) = 0.6554 \text{ m}^2$$

$$\text{Surface coverage} = \frac{n_{\text{ligands}}}{SA} = \frac{12.0 \times 10^{-6} \text{ mol}}{0.6554 \text{ m}^2} = 18 \times 10^{-6} \frac{\text{mol}}{\text{m}^2}$$

A.2.4. Turnover number – example of calculations

Example concerns the L-R-1 sample (laurate protected nanorods, of the order number 1).

$$\text{TON} = \frac{n_{\text{converted substrate}}}{n_{\text{surface Co atoms}}}$$

$$n_{\text{converted substrate}} = 0.01529 \text{ mol}$$

$$n_{\text{surface Co atoms}} = SA \times \left\{ \left(\frac{\% (0001)}{100} \times \delta_{\text{Co}(0001)} \right) + \left(\frac{\% (11-20)}{100} \times \delta_{\text{Co}(11-20)} \right) + \left(\frac{\% (11-21)}{100} \times \delta_{\text{Co}(11-21)} \right) \right\}$$

$$SA = SSA_C \times m_{\text{Co}}$$

$$m_{\text{Co}} = m_{\text{cat}} \times \frac{100\% - \Delta m_{\text{TGA-N}_2}}{100\%}$$

$$m_{\text{Co}} = 0.0257 \text{ g} \times \left(\frac{(100 - 10.4)}{100} \right) = 0.0230 \text{ g}$$

$$SA = 29 \frac{\text{m}^2}{\text{g}} \times 0.0230 \text{ g} = 0.67 \text{ m}^2$$

$$n_{\text{surface Co atoms}} = 0.67 \text{ m}^2 \times \left\{ \left(\frac{5}{100} \times 31.42 \times 10^{-6} \frac{\text{mol}}{\text{m}^2} \right) + \left(\frac{95}{100} \times 19.35 \times 10^{-6} \frac{\text{mol}}{\text{m}^2} \right) + \left(\frac{0}{100} \times 37.23 \times 10^{-6} \frac{\text{mol}}{\text{m}^2} \right) \right\} =$$

$$= 13.36 \cdot 10^{-6} \text{ mol}$$

$$\text{TON} = \frac{0.01529 \text{ mol}}{13.36 \times 10^{-6} \text{ mol}} \cong 1140 \frac{\text{mol}}{\text{mol}}$$

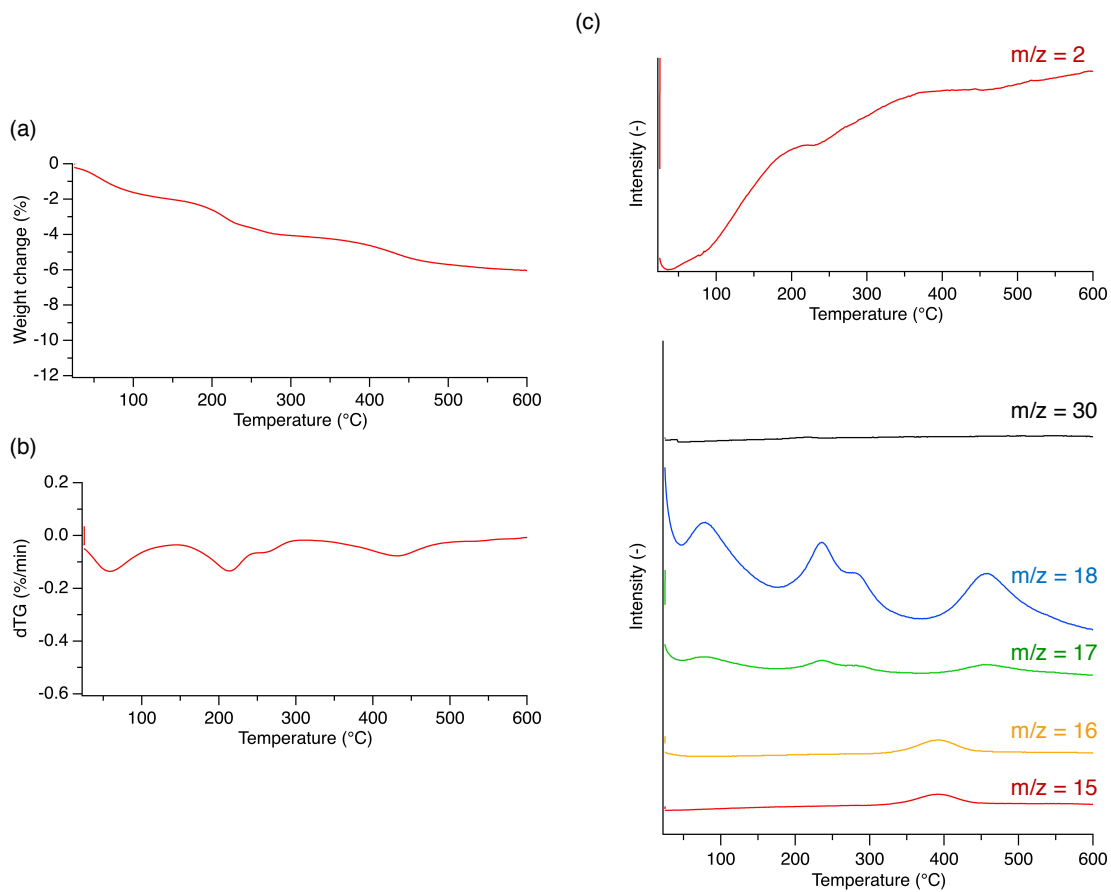


Figure A.3.1. Results of TGA-H₂ analysis for Co/ZrO₂ catalyst: (a) weight loss vs temperature, (b) derivative of weight loss vs temperature and (c) mass spectra for different ions (m/z = 2 for H₂, m/z = 15 and 16 for NH⁺ and NH₂⁺, m/z = 17 and 18 for H₂O and m/z = 30 for NO⁺)

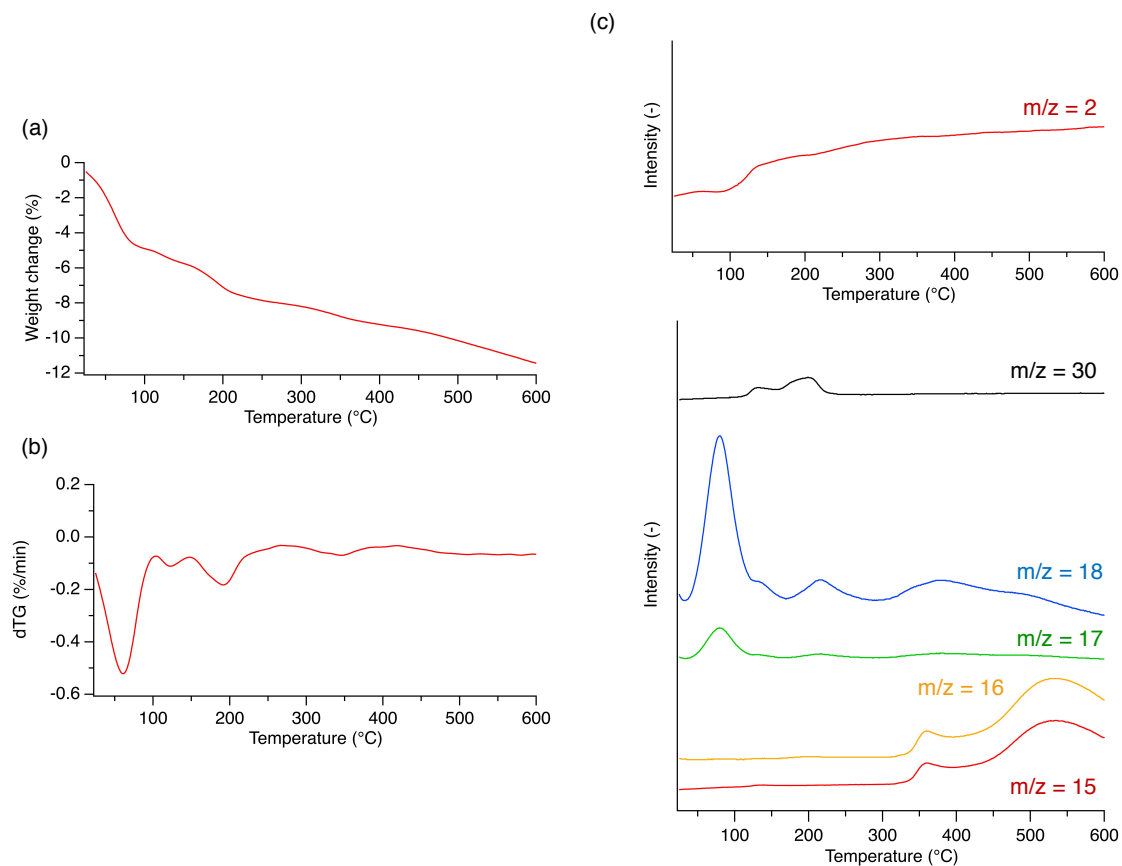


Figure A.3.2. Results of TGA-H₂ analysis for Co/C catalyst: (a) weight loss vs temperature, (b) derivative of weight loss vs temperature and (c) mass spectra for different ions ($m/z = 2$ for H₂, $m/z = 15$ and 16 for NH⁺ and NH₂⁺, $m/z = 17$ and 18 for H₂O and $m/z = 30$ for CH₃NH₂⁺ and/or NO⁺)

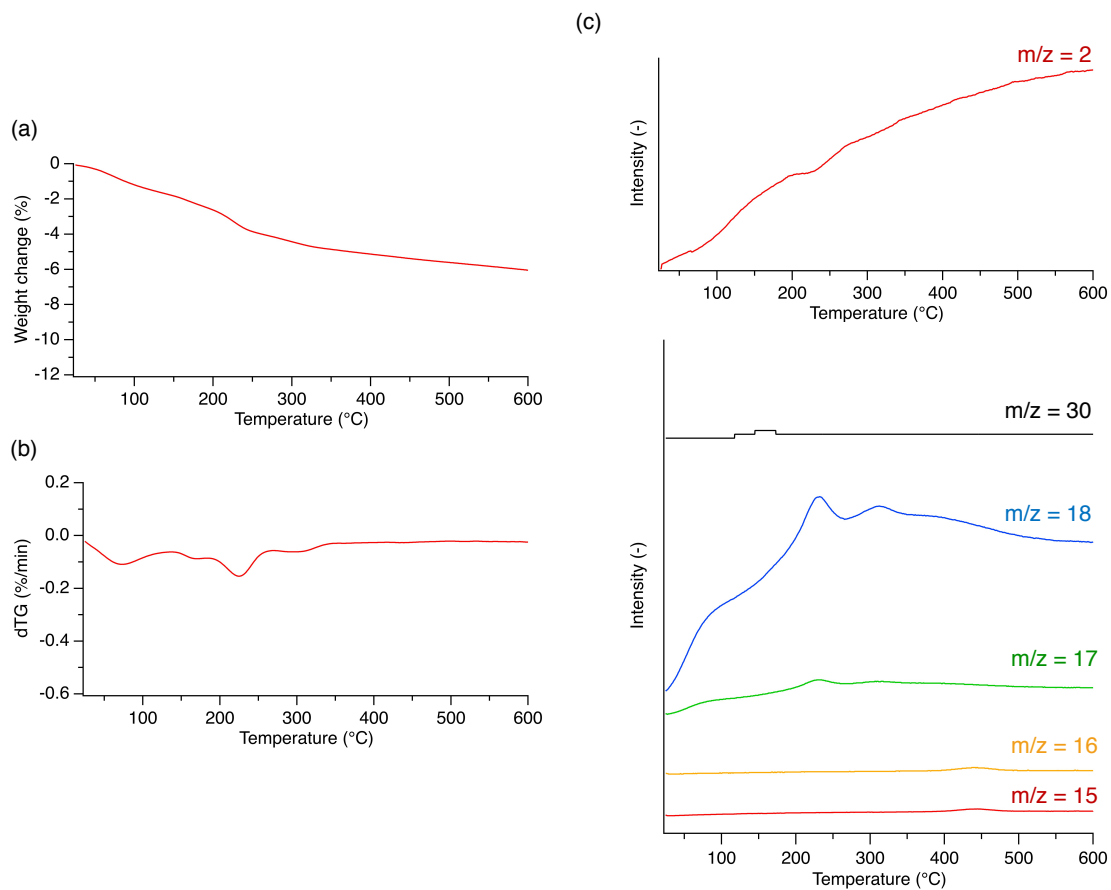


Figure A.3.3. Results of TGA-H₂ analysis for Co/ γ -Al₂O₃ catalyst: (a) weight loss vs temperature, (b) derivative of weight loss vs temperature and (c) mass spectra for different ions ($m/z = 2$ for H₂, $m/z = 15$ and 16 for NH⁺ and NH₂⁺, $m/z = 17$ and 18 for H₂O and $m/z = 30$ for NO⁺)

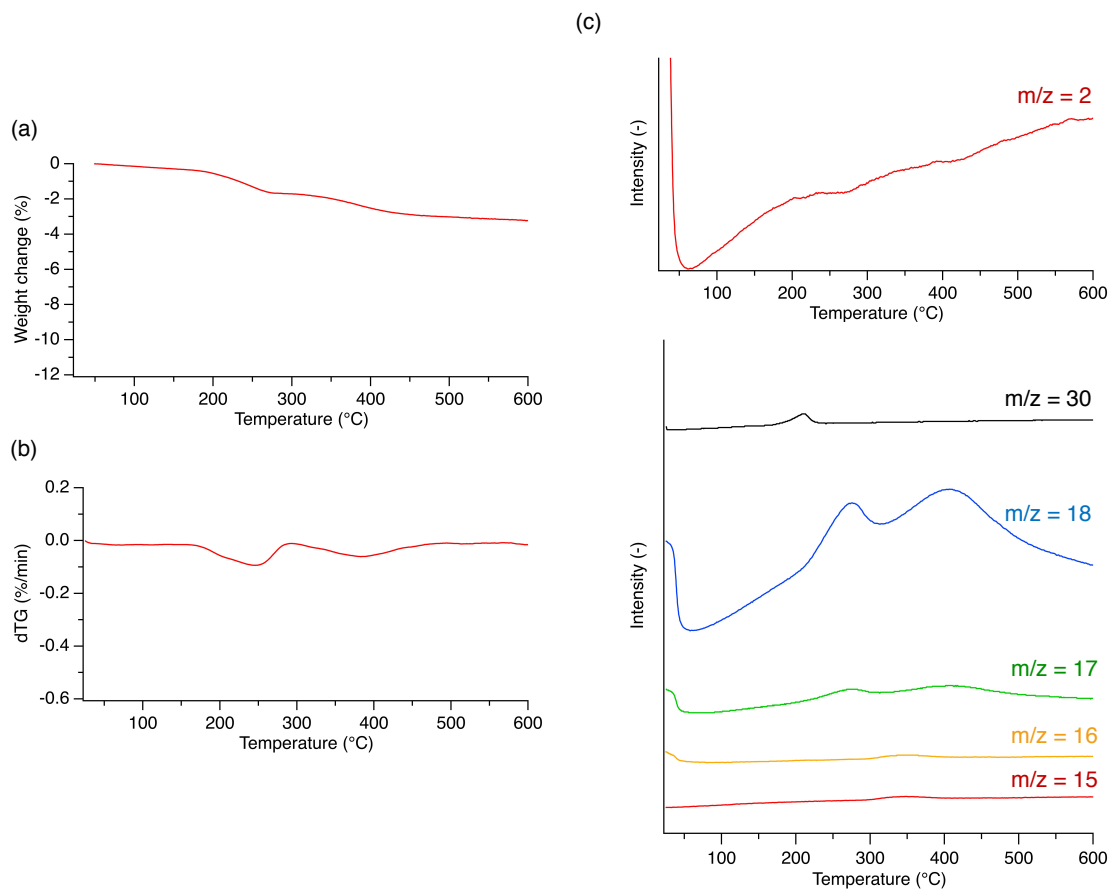


Figure A.3.4. Results of TGA-H₂ analysis for Co/ZnO catalyst: (a) weight loss vs temperature, (b) derivative of weight loss vs temperature and (c) mass spectra for different ions (m/z = 2 for H₂, m/z = 15 and 16 for NH⁺ and NH₂⁺, m/z = 17 and 18 for H₂O and m/z = 30 for NO⁺)

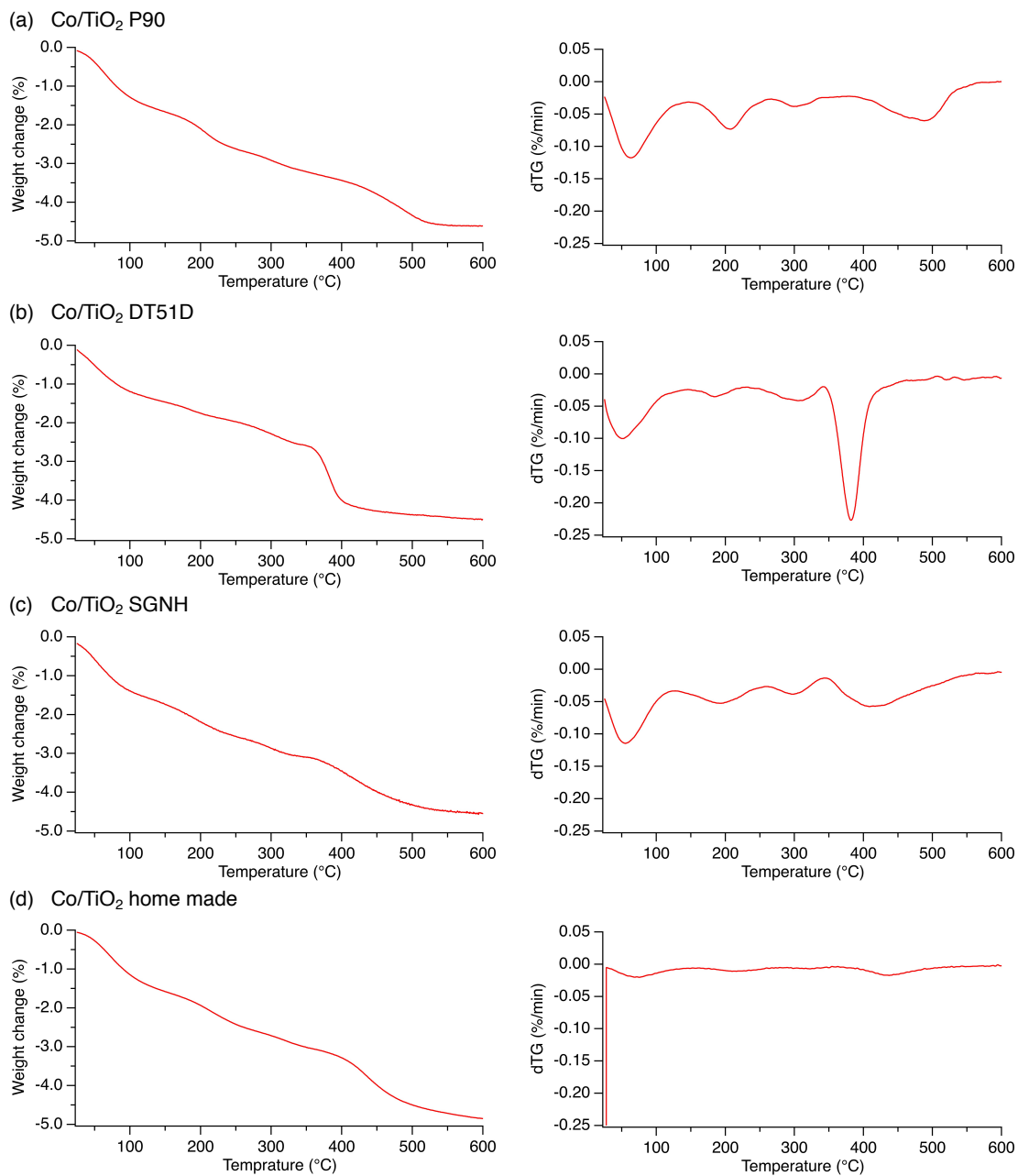


Figure A.3.5. Weight loss (on left) and derivative from mass change (on right) in function of the temperature for cobalt catalysts supported on different types of TiO₂: (a) Co/TiO₂ P90, (b) Co/TiO₂ DT51D, (c) Co/TiO₂ SGNH, (d) Co/TiO₂ home made.

Table A.4.1. Adsorption positions and energies for molecules and intermediates along the alkoxy and hydroxyalkyl dehydrogenation pathways of EtOH and iPrOH. All the energies are given in eV. Only the most stable adsorption positions are given. $\overline{\text{CN}}$ stands for generalized coordination number. When the adsorption is taking place by two atoms, $\overline{\text{CN}}$ is given as the average of the $\overline{\text{CN}}$ s for the adsorption positions.

E_{ads} is considered as follow:

(a) for alcohol

$$E_{\text{ads}} = E_{\text{alcohol@slab}} - E_{\text{slab}} - E_{\text{alcohol}}$$

Where:

$E_{\text{alcohol@slab}}$ - energy of alcohol molecule adsorbed on the surface

E_{slab} – energy of the surface

E_{alcohol} – energy of alcohol in gas phase

(b) for alkoxy intermediate

$$E_{\text{ads}} = (E_{\text{alkoxy@slab}} + \frac{1}{2} E_{\text{H}_2}) - E_{\text{slab}} - E_{\text{alcohol}}$$

$E_{\text{alkoxy@slab}}$ - energy of alkoxy intermediate adsorbed on the surface

E_{H_2} - energy of H_2 in gas phase

(c) for carbonyl product

$$E_{\text{ads}} = (E_{\text{carbonyl@slab}} + E_{\text{H}_2}) - E_{\text{slab}} - E_{\text{alcohol}}$$

$E_{\text{carbonyl@slab}}$ - energy of carbonyl product (aldehyde or ketone) adsorbed on the surface

(d) for hydroxyalkyl intermediate

$$E_{\text{ads}} = (E_{\text{hydroxyalkyl@slab}} + \frac{1}{2} E_{\text{H}_2}) - E_{\text{slab}} - E_{\text{alcohol}}$$

$E_{\text{hydroxyalkyl@slab}}$ - energy of hydroxyalkyl intermediate adsorbed on the surface

(e) for H atom

$$E_{\text{ads}} = E_{\text{H@slab}} - E_{\text{slab}} - \frac{1}{2} E_{\text{H}_2}$$

$E_{\text{H@slab}}$ - energy of hydrogen atom adsorbed on the surface

Table A.4.1. The most stable adsorption positions for the alcohol dehydrogenation reaction species, their adsorption energies (in eV) and generalized coordination numbers ($\overline{\text{CN}}$ s; unitless) of their positions, on different hcp and fcc type surfaces. When the adsorption takes place via two atoms, its $\overline{\text{CN}}$ is taken as an average of the adsorption positions $\overline{\text{CN}}$ s for these atoms.

Surface	EtOH			iPrOH		
	Position	E_{ads}	$\overline{\text{CN}}$	Position	E_{ads}	$\overline{\text{CN}}$
(0001)	O – top	-0.70	7.51	O - top	-0.82	7.51
(10-11)	O – top	-0.93	6.85	O – top	-1.07	6.59
(10-10)	O – top	-0.91	6.68	O – top	-1.01	6.68
(10-12)	O – bridge	-1.00	5.51	O – bridge	-1.16	5.51
	(O – top)	(-0.99)	(5.68)	(O – top)	-1.13	(5.68)
(11-20)	O – top	-0.93	5.80	O – top	-1.00	5.80
(111)	O – top	-0.70	7.51	O – top	-0.82	7.51
(100)	O – top	-0.79	6.68	O – top	-0.90	6.68
(110)	O – top	-0.89	5.84	O – top	-0.99	5.84
(211)	O – top	-1.04	5.51	O – top	-1.18	5.51
Surface	EtO			iPrO		
	Position	E_{ads}	$\overline{\text{CN}}$	Position	E_{ads}	$\overline{\text{CN}}$
(0001)	O - hcp	-0.91	7.19	O - hcp	-1.06	7.19
(10-11)	O – fcc	-1.18	6.87	O – fcc	-1.32	6.87
(10-10)	O – bridge	-0.90	6.23	O – bridge	-1.01	6.23
(10-12)	O – bridge	-1.16	5.51	O – bridge	-1.30	5.51
(11-20)	O - bridge	-1.05	5.73	O – bridge	-1.16	5.73
(111)	O – hcp	-0.90	7.51	O – hcp	-1.04	7.51
(100)	O – square	-1.02	6.63	O – square	-1.16	6.63
(110)	O – bridge	-1.08	5.79	O – bridge	-1.19	5.79
(211)	O – bridge	-1.20	5.40	O – bridge	-1.31	5.40

Table A.4.1. cont.

Surface	CH ₃ CHO			CH ₃ COCH ₃		
	Position	E _{ads}	\overline{CN}	Position	E _{ads}	\overline{CN}
(0001)	O – hcp, C - top	0.09	7.35	O – hcp, C - top	-0.04	7.35
(10-11)	O – bridge, C – bridge	-0.33	7.18	O - bridge, C - top	-0.26	6.92
(10-10)	O – bridge, C – top	-0.13	6.46	O – bridge, C - top	-0.20	6.46
(10-12)	O – bridge, C – bridge (2 nd step)	-0.57	6.18	O – bridge, C – top	-0.51	5.56
(11-20)	O – bridge, C - bridge	-0.40	5.73	O – bridge, C – bridge	-0.35	5.73
(111)	O – hcp, C - top	0.11	7.51	O – hcp, C – top	-0.01	7.51
(100)	O – bridge, C – bridge	-0.42	6.68	O – bridge, C – bridge	-0.18	6.68
(110)	O – bridge, C – bridge	-0.45	5.79	O – bridge, C – top	-0.39	5.82
(211)	O – bridge, C - top	-0.42	5.46	O – bridge, C - top	-0.57	5.46
Surface	CH ₃ CHOH			CH ₃ COHCH ₃		
	Position	E _{ads}	\overline{CN}	Position	E _{ads}	\overline{CN}
(0001)	O – top, C – bridge	0.11	7.43	O – top, C - top	0.15	7.51
(10-11)	O – bridge, C – bridge	-0.23	7.12	O – top, C – top	-0.24	6.59
(10-10)	O – top, C – top	-0.21	6.68	O – top, C – top	-0.26	6.68
(10-12)	O – top, C – top	-0.38	5.68	O – top, C – top	-0.46	5.68
(11-20)	O – top, C – top	-0.22	5.80	O – top, C – top	-0.29	5.80
(111)	O – top, C – bridge	0.11	7.43	O – top, C – top	0.16	7.51
(100)	O – bridge, C – bridge	-0.17	6.68	O – top, O – top	-0.19	6.68
(110)	O – top, C – top	-0.21	5.84	O – top, C – top	-0.29	5.84
(211)	O – top, C - top	-0.48	5.51	O – top, C - top	-0.57	5.51

Table A.4.1. cont.

Surface	H		
	Position	E_{ads}	$\overline{\text{CN}}$
(0001)	H – fcc	-0.56	7.30
(10-11)	H – fcc	-0.66	6.87
(10-10)	H – bridge (between 1 st and 2 nd layer)	-0.59	7.35
(10-12)	H – square	-0.53	6.01
(11-20)	H – bridge	-0.51	5.73
(111)	H – fcc	-0.57	6.97
(100)	H – square	-0.48	6.63
(110)	H – bridge	-0.50	5.79
(211)	H – bridge (between 1 st and 2 nd step)	-0.57	6.12

Table A.4.2. Transition states configurations, dissociated bonds lengths and activation energies for different bond breakings, and energy differences between the state preceding (initial state, IS) and following (final state, FS) given TS along the iPrOH dehydrogenation pathways. E_{act} stands for the activation energy of a given transition state, ΔE_{FS-IS} stands for the energy of elementary reaction (energy difference between the state following and preceding given transition state). Species signified with '*' are considered as adsorbed on the surfaces. All the adsorption positions refer to the 1st layer of metal, unless stated otherwise. All the energies are given in eV.

Surface	TS OH configuration	O-H bond length (Å)	E_{act} OH	$\Delta E_{iPrO^*+H^*}$ $-iPrOH^*$	$\Delta E_{iPrO^*+\frac{1}{2}H_2}$ $-iPrOH^*$	TS OH-CH configuration	C-H bond length (Å)	E_{act} OH-CH	$\Delta E_{CH_3COCH_3^*}$ $+H^*-iPrO^*$	$\Delta E_{CH_3COCH_3^*}$ $+\frac{1}{2}H_2-iPrO^*$
(0001)	O – hcp, H - fcc	1.29	0.73	-0.82	-0.26	O – hcp, C – top, H - fcc	1.58	0.88	0.46	1.02
(10-11)	O – fcc, H - hcp	1.24	0.69	-0.91	-0.25	O – fcc, C – top, H - bridge	1.57	0.80	0.40	1.06
(10-10)	O – bridge, H – bridge between rows	1.39	0.71	-0.59	0.00	O – bridge, C – bridge between rows, H – bridge (another row)	1.70	0.70	0.22	0.81
(10-12)	O – bridge, H – bridge (between 1 st and 2 nd step)	1.34	0.42	-0.67	-0.14	O – bridge, C – top, H – bridge	1.51	0.71	0.26	0.79
(11-20)	O – bridge, H - bridge	1.30	0.49	-0.66	-0.15	O – top, C – top, H - bridge	1.66	0.98	0.30	0.81
(111)	O – hcp, H – fcc	1.26	0.74	-0.80	-0.23	O – hcp, C – top, H – fcc	1.57	0.90	0.46	1.04
(100)	O – bridge, H – bridge	1.31	0.41	-0.73	-0.25	O – bridge, C – top, H - bridge	1.57	0.96	0.50	0.98
(110)	O – bridge, H – bridge between rows	1.32	0.34	-0.67	-0.17	O – bridge, C – top, H – bridge	1.53	0.61	0.30	0.80
(211)	O – bridge, H – bridge (2 nd step)	1.33	0.36	-0.70	-0.13	O – bridge, C – top, H – bridge	1.50	0.63	0.16	0.73

Table A.4.2. cont.

Surface	TS CH configuration	C-H bond length (Å)	E_{act} CH	$\Delta E_{CH_3COHCH_3}$ +H ⁺ -iPrOH ⁺	$\Delta E_{CH_3COHCH_3}$ $\frac{1}{2}H_1$ -iPrOH ⁺	TS CH-OH configuration	O-H bond length (Å)	E_{act} CH-OH	$\Delta E_{CH_3COCH_3}$ +H ⁺ -CH ₃ COHCH ₃ ⁺	$\Delta E_{CH_3COCH_3}$ $\frac{1}{2}H_2$ -CH ₃ COHCH ₃ ⁺
(0001)	O – top, C – top, H - bridge	1.60	1.07	0.42	0.98	C – top, O – top, H - fcc	1.40	0.53	-0.75	-0.19
(10-11)	O – top, C – top, H - top	1.51	0.87	0.17	0.83	C – top, O – bridge, H – square	1.28	0.55	-0.69	-0.03
(10-10)	O – top, C – top, H - bridge	1.51	0.81	0.36	0.75	C – top, O – top, H – bridge between rows	1.41	0.53	-0.74	0.06
(10-12)	O – top, C – top, H - bridge	1.49	0.81	0.17	0.70	C – top, O – bridge, H – bridge (between 1 st and 2 nd step)	1.31	0.64	-0.57	-0.05
(11-20)	O – top, C – top, H - bridge	1.58	0.81	0.20	0.71	C – top, O – top, H – bridge between rows	1.38	0.69	-0.57	-0.06
(111)	O – top, C – top, H - hcp	1.62	1.09	0.41	0.98	C – fcc, O – top, H - bridge	1.21	0.50	-0.75	-0.17
(100)	O – top, C – top, H - bridge	1.53	0.88	0.23	0.71	C – top, O – top, H - bridge	1.41	0.64	-0.47	0.02
(110)	O – top, C – top, H - bridge	1.48	0.71	0.20	0.70	C – bridge, O – top, H – bridge between rows	1.37	0.75	-0.60	-0.10
(211)	O – top, C – top, H - bridge	1.48	0.69	0.04	0.61	C – top, O – bridge, H – bridge (3 rd step)	1.33	0.65	-0.57	0.00

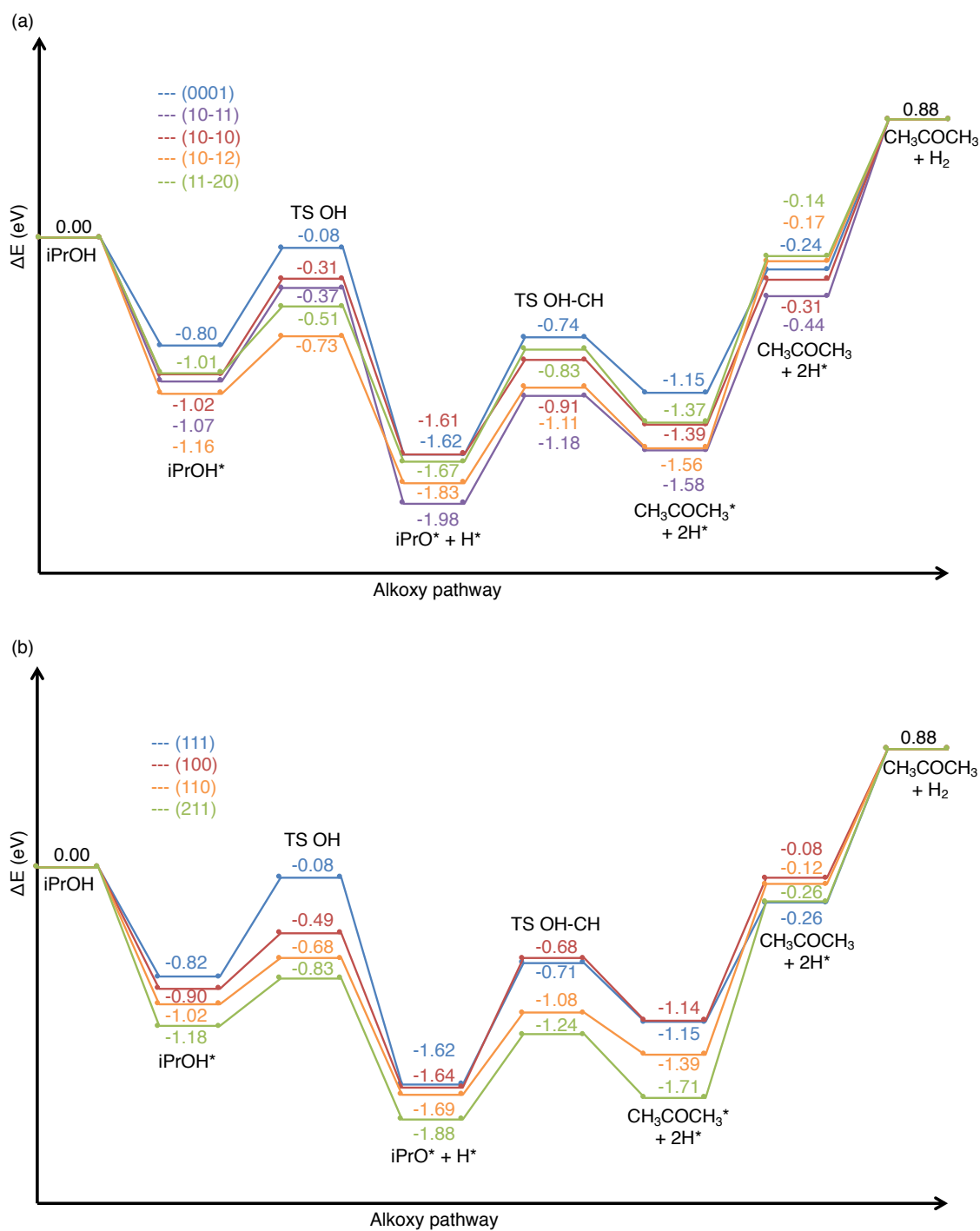


Figure A.4.1. Energetic profiles for iPrOH dehydrogenation via alkoxy pathway on different (a) hcp and (b) fcc surfaces. All the energies are given in eV, '*' stands for the adsorption of the species on the surface.

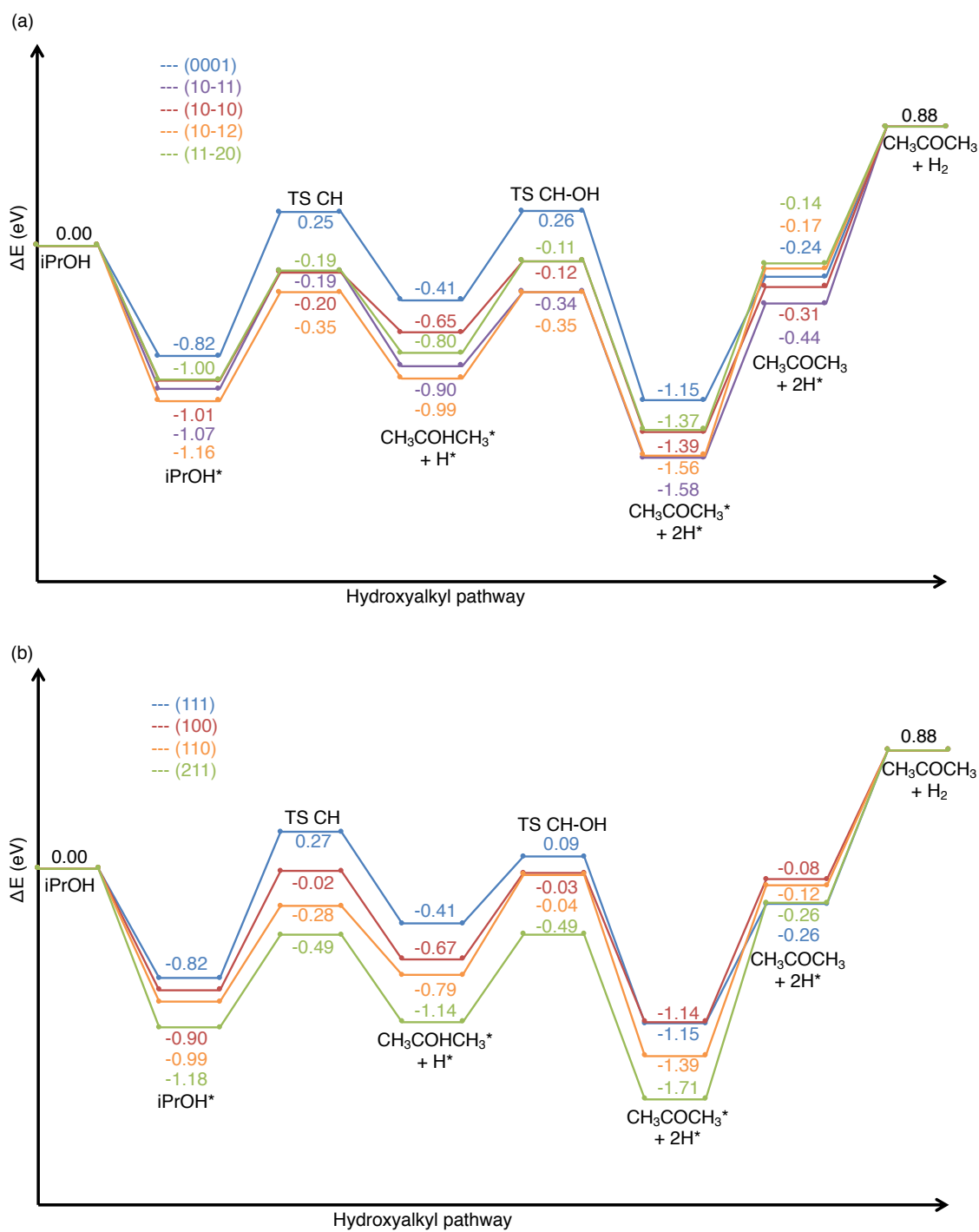


Figure A.4.2. Energetic profiles for iPrOH dehydrogenation via hydroxyalkyl pathway on different (a) hcp and (b) fcc surfaces. All the energies are given in eV, "*" stands for the adsorption of the species on the surface.

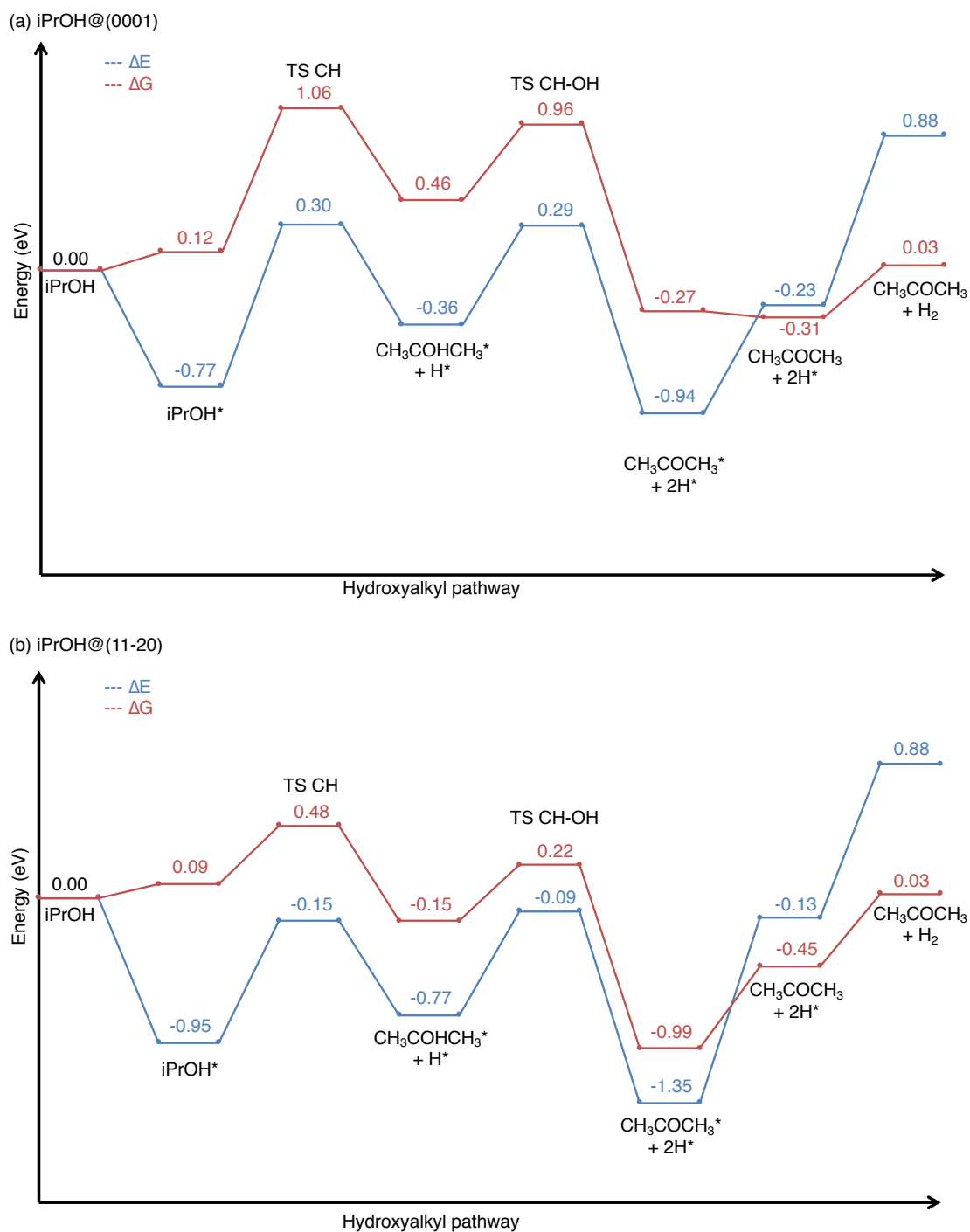


Figure A.4.3. Reaction energy profiles for iPrOH dehydrogenation via hydroxyalkyl pathway on (a) (0001) and (b) (11-20) surfaces. In blue profile in Electronic energy differences (ΔE) and in red in Gibbs Free Energy differences (ΔG). All the energy values are given in eV. '*' stands for the adsorption of the species on the surface.

Table A.4.3. iPrOH and TS OH adsorption energies on (0001) and (11-20) facets, expressed in: (a) electronic energy, (b) electronic energy with dipol correction, (c) electronic energy with dipol correction and ZPE correction, (d) Gibb Free Energy (equal to electronic energy with dipol, ZPE and entropy corrections). Values are given in eV. ZPE stands for zero point energy.

Entry	iPrOH		TS OH	
	(0001)	(11-20)	(0001)	(11-20)
a	-0.77	-0.95	-0.03	-0.47
b	-0.73	-0.94	0.01	-0.46
c	-0.71	-0.94	-0.16	-0.66
d	0.12	0.09	0.84	0.17

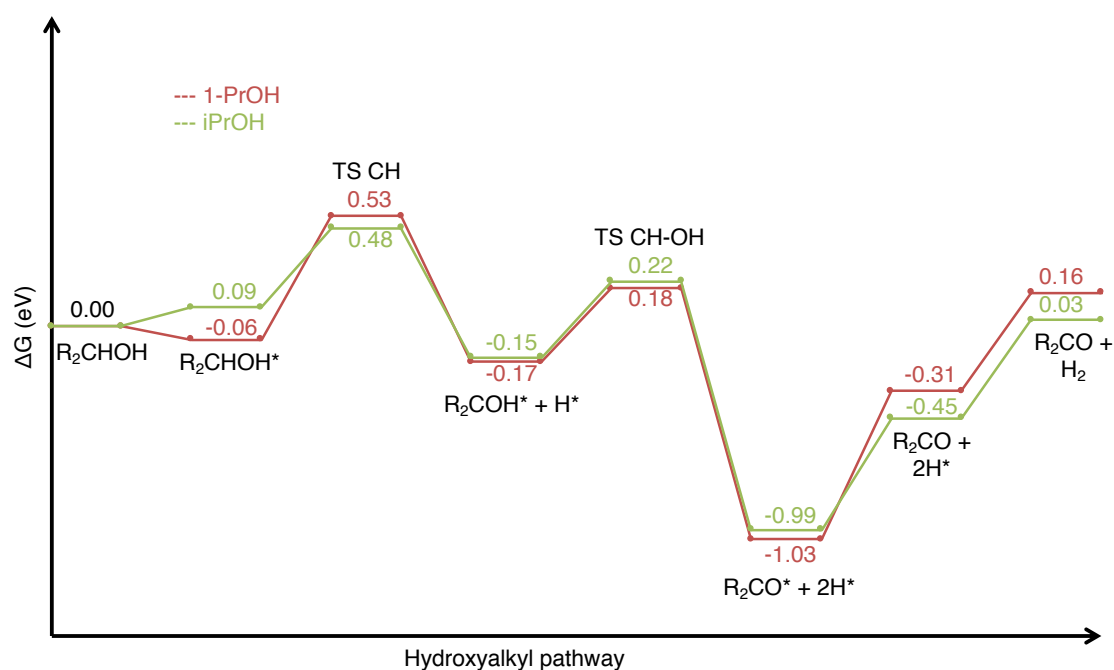


Figure A.4.4. Gibbs Free Energy profile for 1-PrOH (red) and iPrOH (green) dehydrogenation on Co(11-20) facet via hydroxyalkyl pathway. '*' means the adsorption of species on the surface. Energies are given in eV.

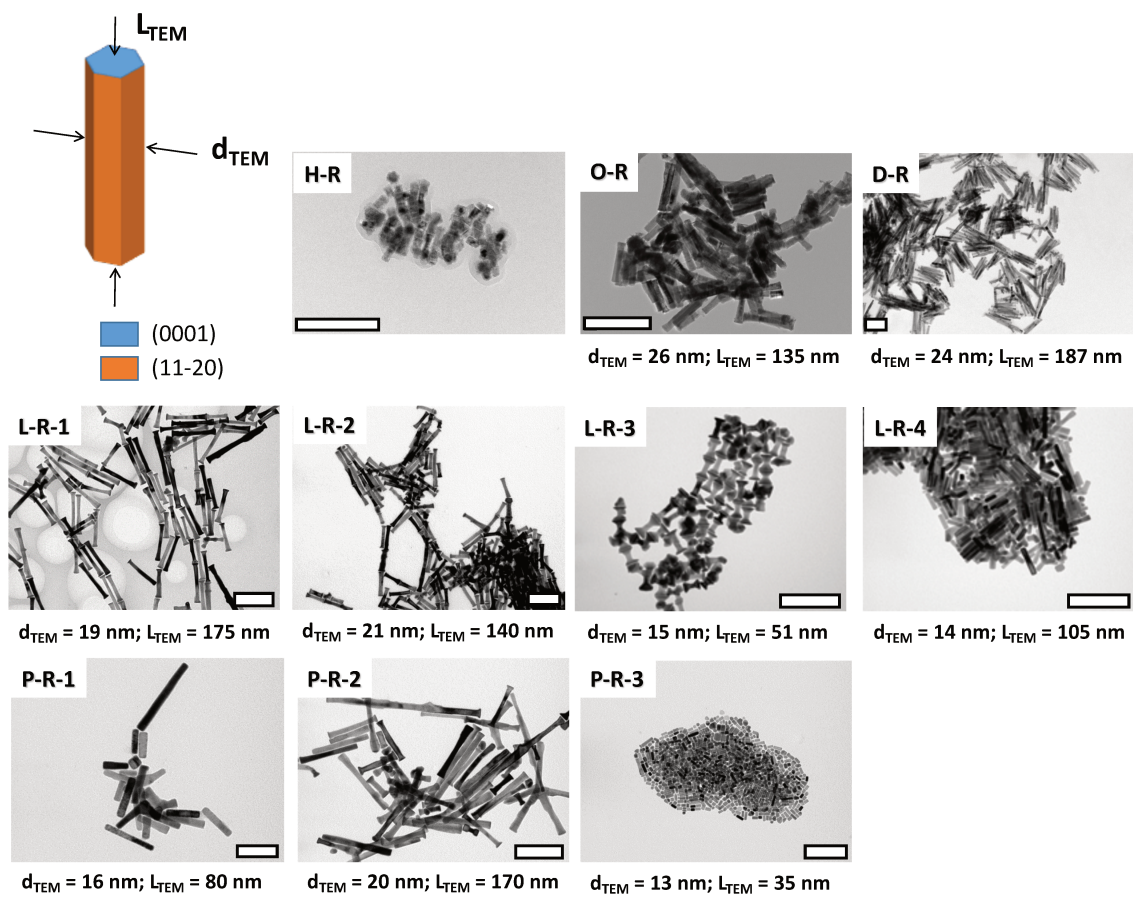


Figure A.5.1. TEM images and mean dimensions of Co nanorods. The scale bar stands for 200 nm.

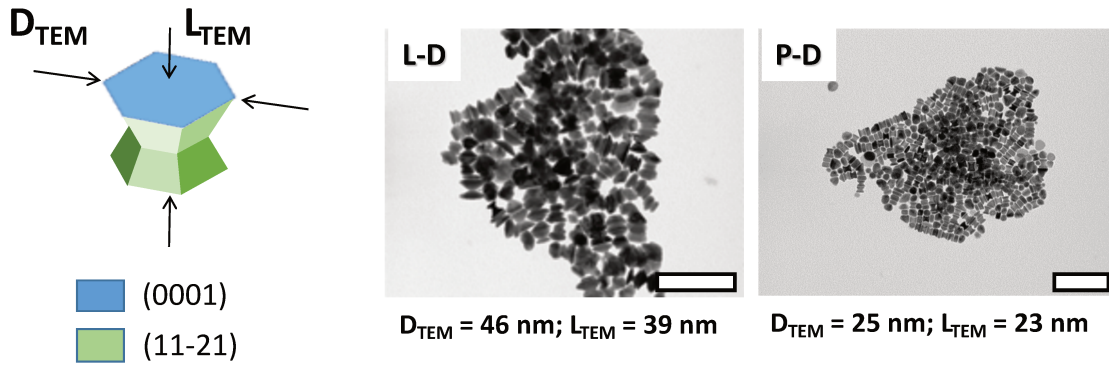


Figure A.5.2. TEM images and mean dimensions of Co nanodiabolos. The scale bar stands for 200 nm.

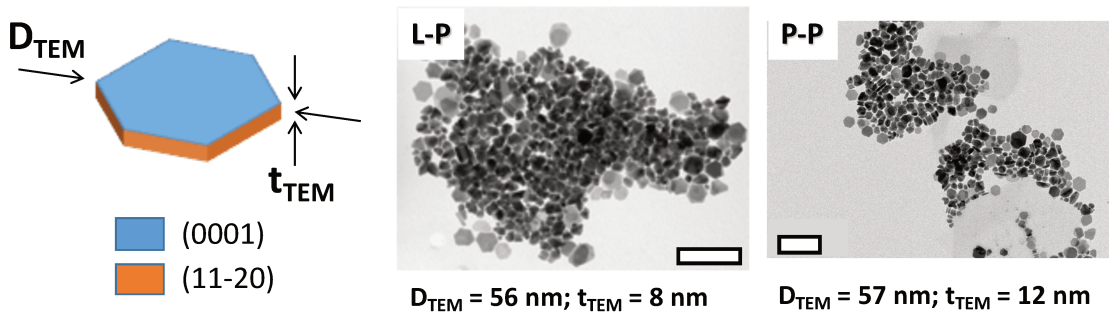


Figure A.5.3. TEM images and mean dimensions of Co nanoplatelets. The scale bar stands for 200 nm.

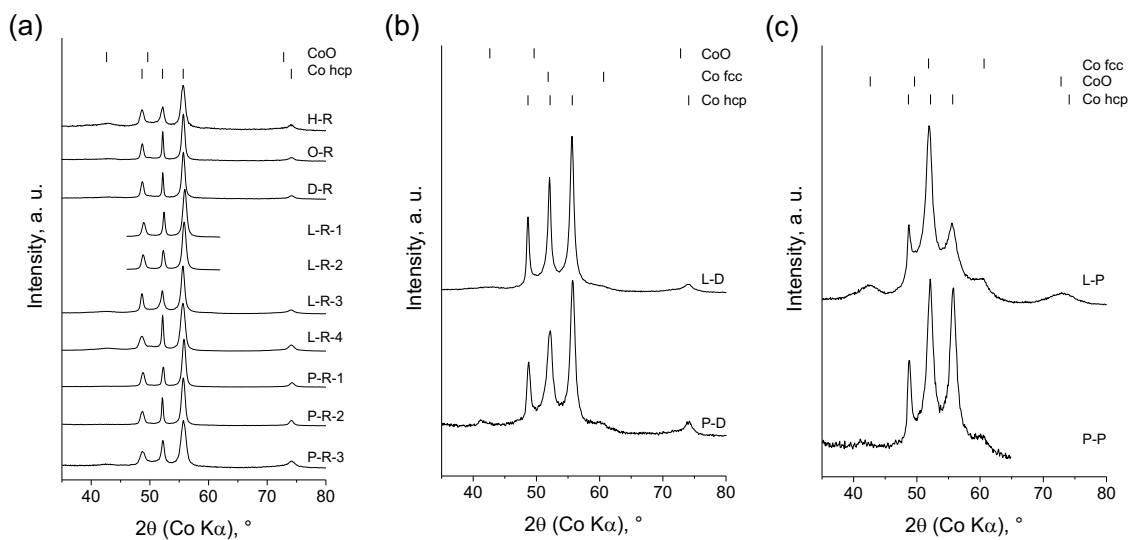


Figure A.5.4. X-ray diffraction patterns of Co (a) nanorods, (b) diabolos and (c) platelets.

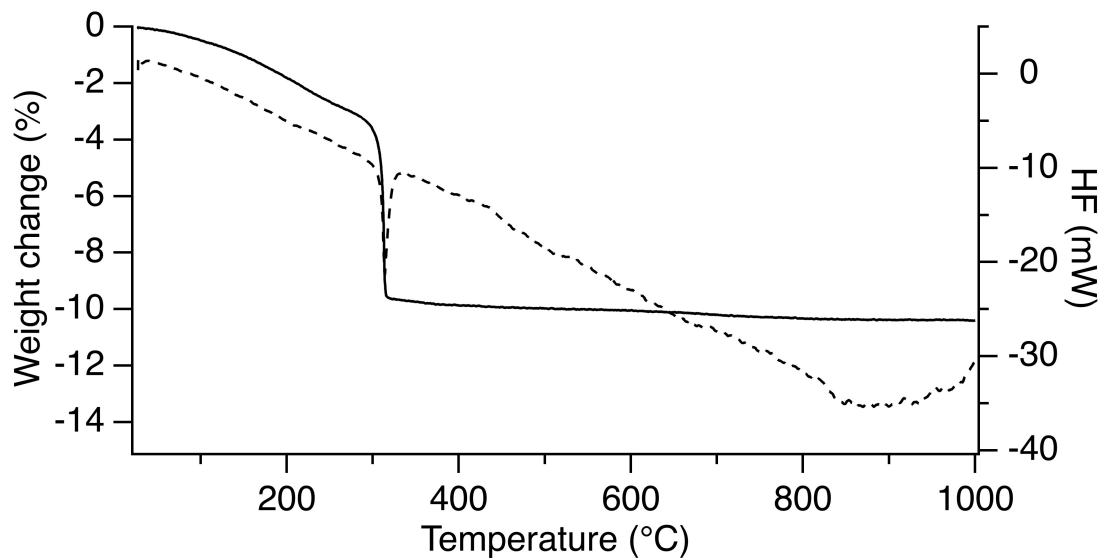


Figure A.5.5. TGA-N₂ results analysis for L-R-1 sample. By solid line the weight change is given and by dashed line the heat flow is indicated.

Table A.5.1. Data used to compute the TON values for the 2-octanol dehydrogenation reaction using decorated Co nanoparticles.

Sample ¹	$n_{\text{converted substrate}}$ (mol)	SA ² (m ²)	Exposed facets			$n_{\text{surface Co atoms}}$ ³ (10 ⁻⁶ mol)	TON ⁴ (mol mol ⁻¹)
			(0001) (%)	(11-20) (%)	(11-21) (%)		
L-R-1	0.01529	0.67	5	95	0	13.40	1140
L-R-2	0.01393	0.59	6	94	0	11.86	1170
L-R-3	0.00148	0.71	35	20	45	22.52	70
L-R-4	0.01469	0.89	6	94	0	17.77	830
L-D	0.01307	0.61	38	0	62	21.40	610
L-P	0.01414	0.82	78	22	0	23.58	600
P-R-1	0.00071	0.41	5	95	0	8.10	90
P-R-2	0.00120	0.60	8	92	0	12.20	100
P-R-3	0.00349	0.47	14	86	0	9.96	350
P-D	0.00096	0.37	35	0	65	12.92	70
P-P	0.00473	0.40	67	33	0	11.08	430
H-R	0.00866	n.a.	n.a.	n.a.	n.a.	n.a.	n.a.
O-R	0.00945	0.52	8	92	0	10.61	890
D-R	0.01052	0.54	5	95	0	10.82	970

¹Sample naming according to the role: type of ligand – shape – order number (if needed)

²SA – surface area exposed by Co in the catalyst sample used for the catalytic test: $SA = SSA_C \times m_{Co}$ with SSA_C the specific surface area calculated based on TEM geometric measurements and $m_{Co} = m_{cat} \times \frac{100\% - \Delta m_{TGA-N_2}}{100\%}$ (Δm_{TGA-N_2} can be found in Table 1, in the Chapter 5)

³the amount of Co atoms (mol) was calculated using the following formula: $n_{\text{surface Co atoms}} = SA \times \left\{ \left(\frac{\% (0001)}{100} \cdot \delta_{Co(0001)} \right) + \left(\frac{\% (11-20)}{100} \cdot \delta_{Co(11-20)} \right) + \left(\frac{\% (11-21)}{100} \cdot \delta_{Co(11-21)} \right) \right\}$, with $\delta_{Co(0001)} = 31.42 \cdot 10^{-6} \frac{\text{mol}_{Co}}{\text{m}^2}$, $\delta_{Co(11-20)} = 19.35 \cdot 10^{-6} \frac{\text{mol}_{Co}}{\text{m}^2}$, $\delta_{Co(11-21)} = 37.23 \cdot 10^{-6} \frac{\text{mol}_{Co}}{\text{m}^2}$

⁴TON values accuracy ± 25 mol/mol

n.a. – not available

Table A.5.2. ICP-OES analysis for the solutions collected after 24h of reactions.

Sample	C _{Co} ($\frac{\text{mg}}{\text{L}}$)	Co [#] (wt%)	Presence of precipitate*
L-R-1	<0.2	---	No
L-R-3	0.4	0.11	Yes
P-R-1	1.1	0.29	Yes
P-R-2	4.3	1.29	Yes
P-R-3	1.5	0.67	Yes
D-P	4.4	2.10	Yes
P-P	2.7	0.84	Yes

* After the reactions, solutions were filtered (PTFE, 0.45 μm pores filters) and put into refrigerator. After few weeks, precipitates, which probably contain cobalt, were observed. As only the supernatants from the liquid samples were used in ICP-OES analysis, thus, the established concentrations of Co are only qualitative.

[#] wt% of Co in the solution is counted in respect to the mass of Co in the catalyst sample, taken for the given reaction

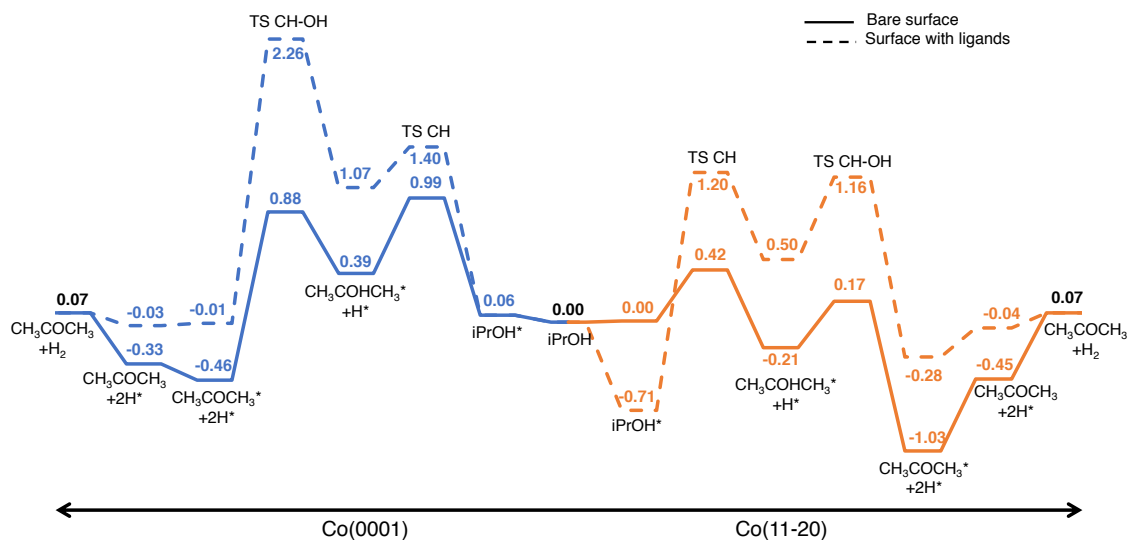


Figure A.5.6. Gibbs Free Energy profiles (in eV) for iPrOH dehydrogenation via the hydroxyalkyl pathway on the Co(0001) facet (left side) and on the Co(11-20) facet (right side). Profiles with a solid lines correspond to bare surfaces, and with dashed lines to surfaces decorated with CH₃COO* ligands (0.44A-Co(0001) and 0.75A-Co(11-20)). Adsorbed species are labelled with '*'.
 ← Co(0001) Co(11-20) →

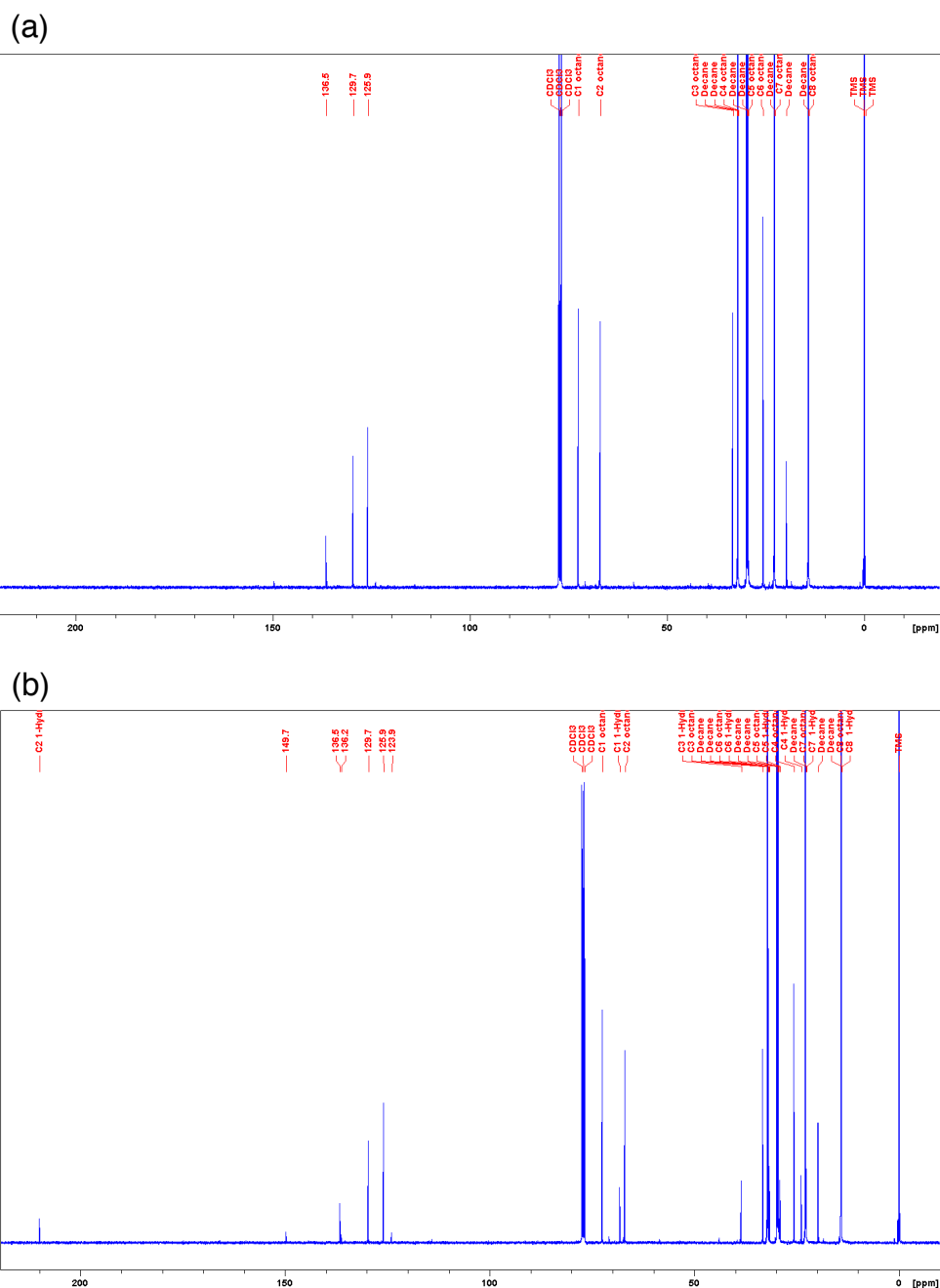


Figure A.5.7. ^{13}C -NMR spectra of the liquid samples collected (a) at the beginning and (b) at the end of the catalytic 1,2-octanediol dehydrogenation with L-R-1 catalyst. The samples are the mixture of decane (solvent) and reactants (1,2-octanediol and reaction product). The dehydrogenation of secondary OH group and formation of ketone is confirmed by the signal at chemical shift of 210 ppm, whereas the signal from aldehyde (expected at 200 ppm) is not present.

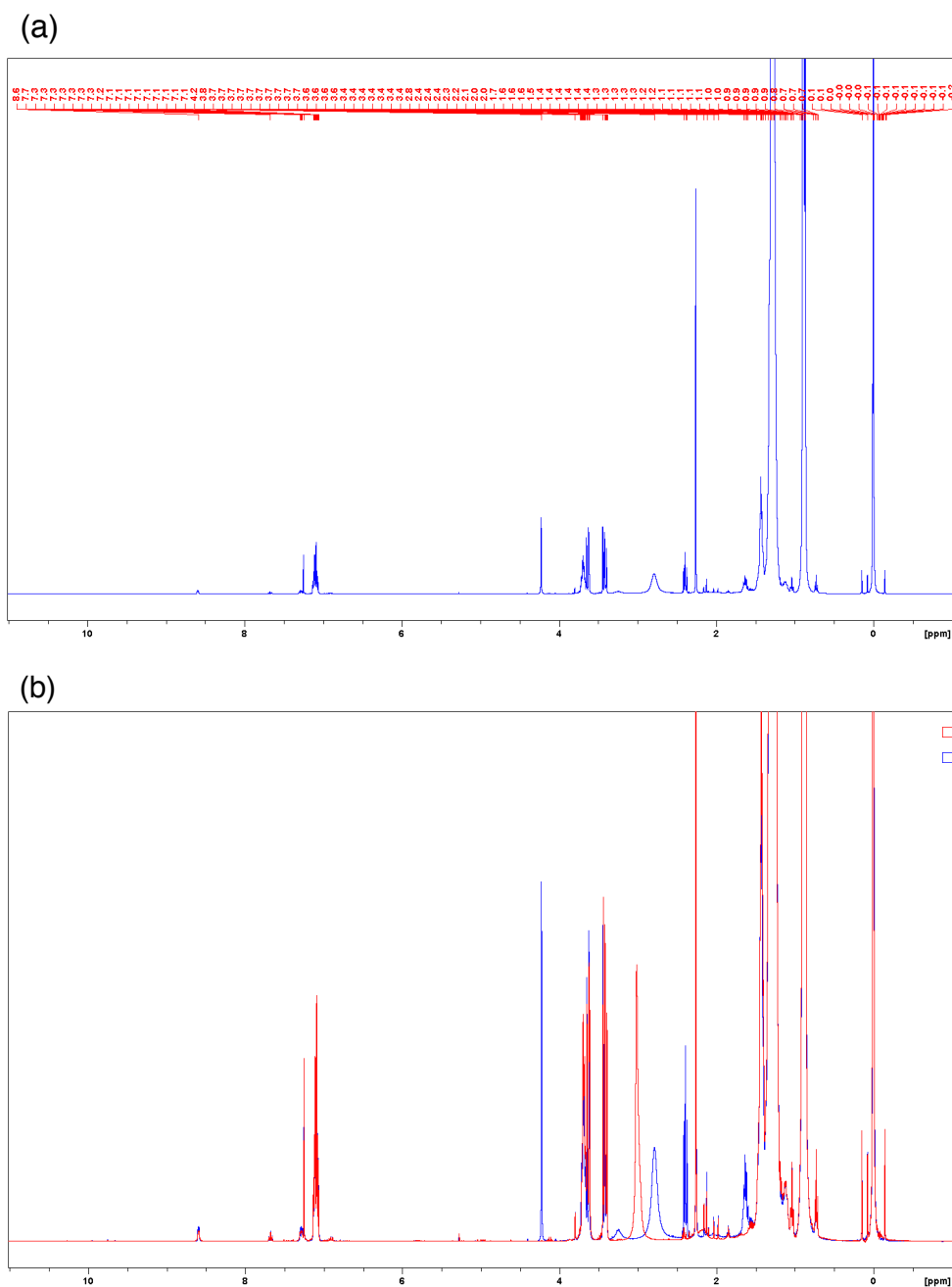


Figure A.5.8. $^1\text{H-NMR}$ spectra of the liquid samples collected from 1,2-octanediol dehydrogenation with L-R-1 catalyst: (a) at the end of the reaction and (b) superimposition of the spectra for the sample from the beginning (red) and the end (blue) of the catalytic test. The samples are the mixture of decane (solvent) and reactants (1,2-octanediol and reaction product). The dehydrogenation of secondary OH group and formation of ketone is confirmed by: singlet signal from $-\text{CH}_2\text{CH}_2\text{COCH}_2\text{OH}$ at 4.25 ppm, multiplet signal from $-\text{CH}_2\text{CH}_2\text{COCH}_2\text{OH}$ at 2.40 ppm and multiplet signal from $-\text{CH}_2\text{CH}_2\text{COCH}_2\text{OH}$ at 1.60 ppm.

Heterogeneous catalysts for acceptor-less alcohol dehydrogenation – joined experimental and theoretical studies

Acceptor-less alcohol dehydrogenation is a highly interesting reaction from the green chemistry point of view. In it, the (biomass derived) alcohols are transformed into carbonyl products, which are high value-added chemicals. Moreover, highly-energetic H₂ in gaseous form is produced as the only by-product in the reaction. The presence of catalyst facilitates the process. Cobalt heterogeneous supported catalysts and unsupported shaped nanoparticles were investigated in this reaction. To understand their catalytic performance, the experimental and theoretical approaches were joined. Catalytic testing was aiming to assess the activity and selectivity of the catalysts, towards the dehydrogenation of mono- and polyalcohols (diols) possessing primary and secondary hydroxyl groups. Extensive characterization allowed to investigate the intrinsic properties of the materials. In between the reducibility of cobalt supported on materials of different nature was examined. For unsupported nanoparticles the shape, type of exposed metal facets, and also thickness of the ligand layer protecting the nanoparticles were analyzed. Density Functional Theory (DFT) calculations gave the opportunity to understand the catalytic behavior on the molecular level. The catalytic activity and selectivity, and the influence of the co-adsorbed ligands on the catalytic performance of metal, were studied for Co surfaces of different nature. By combining all the results it was possible to identify the factors guiding the catalyst activity.

Key-words: alcohol, dehydrogenation, cobalt, catalysis, DFT

Catalyseurs hétérogènes pour la déshydrogénation d'alcool sans accepteur - études expérimentales et théoriques conjointes

La déshydrogénation d'alcool sans accepteur est une réaction extrêmement intéressante du point de vue de la chimie verte. Dans celle-ci, les alcools (dérivés de la biomasse) sont transformés en produits carbonylés, qui sont des produits chimiques à haute valeur ajoutée. De plus, de l'hydrogène est produit hautement énergétique, sous forme gazeuse, comme seul sous-produit de la réaction. La présence de catalyseur facilite le processus. Des catalyseurs hétérogènes au cobalt supportés et des nanoparticules façonnées sans support ont été étudiés dans cette réaction. Pour comprendre leurs performances catalytiques, les approches expérimentales et théoriques ont été reliées. Les tests catalytiques visaient à évaluer l'activité et la sélectivité des catalyseurs vis-à-vis de la déshydrogénation de mono- et polyalcools (diols) possédant des groupes hydroxyle primaires et secondaires. Une caractérisation poussée a permis d'évaluer les propriétés intrinsèques des matériaux. La réductibilité du cobalt sur des supports de nature différente a été examinée. Pour les nanoparticules non supportées, la forme, le type de facettes métalliques exposées et l'épaisseur de la couche de ligand protégeant les nanoparticules ont été analysés. Les calculs de la théorie fonctionnelle de la densité (DFT) ont permis de comprendre le comportement catalytique au niveau moléculaire. L'activité catalytique et la sélectivité, ont été étudiées pour des surfaces de Co de différentes natures ainsi que l'influence des ligands co-adsorbés. En combinant tous les résultats, il a été possible d'identifier les facteurs guidant l'activité du catalyseur.

Mots-clés : de l'alcool, déshydrogénation, cobalt, catalyse, DFT